Tuning Structure to Optimise Charge Transport: Nanoparticle Composites, Microcrystals and Metallopolymers

Lorraine Keane B.Sc. (Hons)

A thesis submitted for the degree of Doctor of Philosophy

Supervisor: Prof. R. J. Forster
School of Chemical Sciences
Dublin City University

August 2003

I hereby declare that this material, which I now submit for the assessment on the program study leading to the award of Doctor of Philosophy is entirely my own work and has not been taken from the work of others save and to the extent that such work has been cited and acknowledged within the text of my work

Signed _____ ID No _____

Date _____

Acknowledgements

I would sincerely like to thank my supervisor, Prof Robert Forster for his endless teaching and support for the duration of my postgraduate studies To the technical staff in the School of Chemical Sciences, Mick, Maurice, Damien, Veronica, Ann, Mary, Ambrose, Vinny and John, I appreciate all your help Thanks also to all the secretarial, faculty office and lecturing staff that were of assistance to me during my postgrad years

A special mention for all the members of the Forster Research Group, past and present – Conor, Dominic, Edna, Richard, Jenni, Darren, Mary, Johan, Sonia, Lynn, Darragh, Tommy and Andrea I will take with me fond memories of Christmas dinners and our group trip to Paris!

Thanks to all the former and present postgrads of DCU I am very grateful for your friendship over the years, especially Sandra, Mary F, Mary L, Mairead, Maire, Kathleen, Neil, Karl, Ray, Jonnie, John, Shane, Stephania, Sabine, Ger, Ian, Noel, Clare, Andrea, Scott, Adrian, Wesley and Dec and for my non DCU friends Catherine and Elaine

Last but not least, my family – Mom, Dad, Catherine, Donal and Mike You have provided me with constant support and advice I appreciate all the encouragement – thank you!

This thesis is dedicated to my parents

Table of Contents

"Tuning Structure to Optimise Charge Transport Nanoparticle Composites, Microcrystals and Metallopolymers"

Lorraine Keane, B Sc

Enhancing charge transport is important for the development of materials in devices including sensors, electronics and catalysts The focus of the work presented here is the investigation of factors that enhance charge transport in redox active materials including solid deposits, metallopolymers and metallopolymer nanoparticle composites Deposits of the osmium polypyridyl complex, $[Os(OMe\text{-}bpy)_3]^{2+}$ have been mechanically attached to a microelectrode surface Due to close packing of the material particles the internal free volume is low and solvent/counterion uptake occurs slowly Electrochemical cycling in $HClO_4$ causes changes in the deposit morphology with evidence of nucleation and crystal growth This process appears to be promoted by the protonation of the methoxy groups that encourages hydrogen bonding between adjacent complexes The rate of charge transport increases from $1\ 5\pm0\ 1 \times 10^{9}$ cm^2s^{1} for $0\ 1 \leq [HClO_4] \leq 0\ 6$ M to $13\pm1 \times 10^{9}$ cm^2s^{1} in 1 0 M $HClO_4$ For the osmium polypyridyl polymer, $[Os(bpy)_2\ (PVP)_{10}\ Cl]^{+}$ 'break in' and physical effects from the electrolyte perchlorate ion or protons were not evident Polymeric materials are rigid and rapidly swollen in electrolyte with the result of possible fast uptake of solvent/counterions Introducing gold nanoparticles forming metallopolymer nanoparticle composites increases the charge transport by approximately an order of magnitude from $5\ 3\pm2 \times 10^{10}$ to $5\ 8 \times 10^{9}$ cm^2s^{1} corresponding to electron transfer rates between the redox centres of $1\ 9 \times 10^{6}$ and $1\ 7 \times 10^{7}$ $M^{1}s^{1}$ Enhanced charge and electron transport values may indicate the formation of an interconnected network where the osmium centres mediate electron transfer between the gold nanoparticles To demonstrate the possible application of these solid state and polymeric osmium polypyridyl complexes as optical devices, it is necessary to understand their photophysical properties As a first step in elucidating these properties, the quenching of excited state Os^{2+} species by Os^{3+} has been explored using $[Os(bpy)_3](PF_6)_2$ as a model

Chapter 1

Review of Charge Transport in Microcrystals, Metallopolymers and Nanoparticle Composites

1.1 Introduction

Understanding and enhancing charge transport is important for the development of materials in a range of scientific devices. The charge transport properties of thin metal films have lead to exciting possible applications in gas sensors[1] and electronic devices.[2] Polymeric materials are to the forefront of battery[3,4] molecular electronics,[5] catalytic,[6] and electronic device research.[7] Electrodes modified with solid deposits and polymeric films allow 3-D complexes to be examined. Redox active solid materials are applied to the electrode surface by mechanical abrasion. Due to the random packing nature of the material, the particles are close together and the redox centres are at a distance that is well defined. Charge transport is defined as the movement of electrolyte counterions into and out of the redox material to compensate for the charge created during electrochemical cycling. For solid materials charge transport generally depends on electron self-exchange between the closely packed redox sites and counterion movement into and out of the material.

In contrast, for redox active polymeric materials the redox centres are fixed and the redox-to-redox distances are statistically averaged. The redox centre is bound to a rigid non-conductive backbone chain and in contrast to the solid material the redox centres are further apart. In this case charge transport is expected to depend on counterion ingress/egress with electron self exchange between the redox centres occurring slowly. To increase the rate of electron self exchange between polymer redox centres, metal nanoparticles can be introduced. Upon initial electrochemical cycling, the structural and compositional differences between these redox active solid and polymeric materials can be evident through the 'break-in' effect.

In the work presented in this thesis, new insights into the charge transport properties of redox active osmium compounds are investigated as solid deposits and within metallopolymers. The charge transport mechanism occurring with these materials is represented in Figure 1.1. Oxidation or reduction of a redox-active species at the electrode surface generates a concentration gradient between the solid layer and the bulk solution. This redox process requires electron transfer across the electrode/deposit interface. The rate at which electron transfer takes place across the interface is described

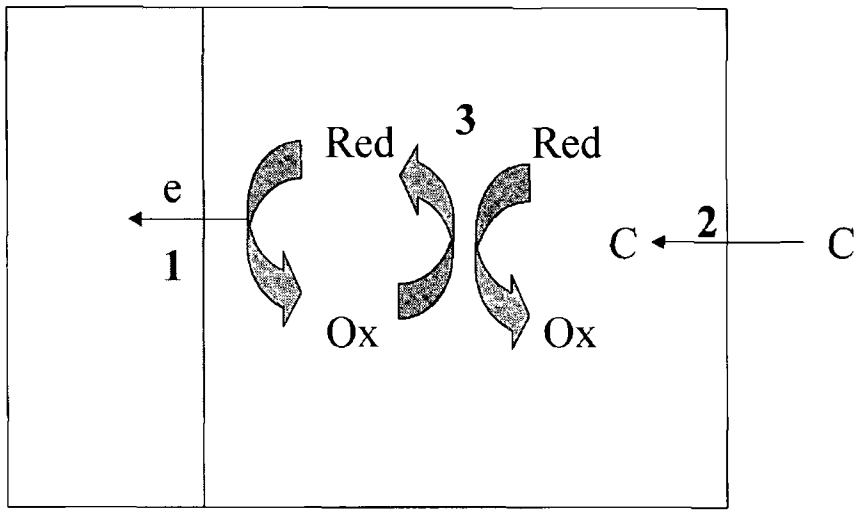

Figure 1 1 Schematic diagram of processes that can occur at a modified electrode Ox represents an oxidised substance and Red represents the reduced form in a layer on an electrode surface Processes shown are (1) heterogeneous electron transfer from Red to produce the oxidised form, Ox, (2) diffusion of counterions (C) from the electrolyte to the Ox species within the layer, (3) electron transfer from Red to another Ox in the layer (electron self exchange)

Voltammetric studies have been mostly undertaken on solution-soluble species but many compounds are insoluble in important solvents such as water leading to little electrochemical work being carried out Applying microcrystalline compounds to electrodes by mechanical attachment allows voltammetry to be undertaken The voltammetry of thin film studies of insoluble materials form part of a well-investigated area [8 9] Solid state electrochemistry has aroused much interest since the early work carried out by Scholtz and co-workers a little over ten years ago [10 11] Their work involved the analysis of metal alloys, i e tin-bismuth, through abrasive stripping voltammtery Prior to this, the majority of electrochemical studies were restricted to the

voltammtery. Prior to this, the majority of electrochemical studies were restricted to the fabrication of composite electrodes from mixtures of solid powders and conducting carbon paste.[12]

The widespread interest in polymers has been spurred by their applicability in the area of chemically modified electrodes.[13,14] Polysulfur nitride, $(SN)_n$ with its metallic nature has been exploited in the use of the polymer as an electrode in liquid electrolytes and in surface electrolcatalysis.[15,16] Doped conducting polymers such as polyacetylene and polypyrrole have relatively delocalised electronic states with properties suitable for organic storage batteries.[17] One goal of coating electrodes with electroactive polymers is the development of new materials with very active catalytic properties.[18] The bulk of the work has been with systems where the polymer itself is inert and serves only as a support for the electrocatalytic metal sites. An electrode modified with redox polymer is a means of providing the electrode with the chemical, electrochemical, optical, and other properties of the immobilised molecule. The reaction can also be controlled by the applied potential or current and monitored over a narrow potential range.

Optimising charge transport via the tuning of solid state and polymeric materials is the main focus of the work presented here. During electrochemical cycling redox active solid materials can undergo structural changes and may also enhance the charge transport properties of the material. Nucleation and crystal growth is a phenomenon identified by counterion uptake into the solid deposit and structural modification during electrochemical cycling. Due to its rigid nature, modifications to polymer structure upon counterion uptake would not be as evident. These structural changes can result in augmented diffusional charge transport properties. The introduction of metal nanoparticle fillers to polymers can provide a route for increased charge transport along with nanoparticle size control depending on the polymer mole fraction. The charge transport properties of metallopolymer:nanoparticle composites in the literature is minimal so the research findings reported in chapter 4 present some new and exciting results.

Nanoparticle:polymer composites have unique optical, electric and magnetic properties which continue to drive intense research in fields as diverse as catalytic synthesis and sensor development.

Redox active solid deposits and polymer species have the potential to exhibit interesting examples of light and electrically stimulated functions [19] To demonstrate real world applications of these materials as optical devices it is necessary to perform photoinduced processes Chapter 5 covers photoinduced electron transfer and quenching measurements of $[Os(bpy)_3]^{2+}$ as a model to demonstrate the photophysical properties of osmium polypyridyl complexes

This thesis details the following, Chapter 1 introduces the literature review that discusses aspects of charge transport in solid state and metallopolymeric materials including mass transport, 'break-in' effect, homogeneous and heterogenous charge transport, nanoparticle composite redox and optical properties Chapter 2 reports the synthesis and characterisation of the solid deposit $[Os(OMe\text{-}bpy)_3]^{2+}$, the metallopolymer $[Os(bpy)_2Cl(PVP)_{10}]^{+}$ and the nanoparticle metallopolymer composite In Chapter 3, the osmium polypyridyl microcrystalline material is mechanically attached to a microelectrode surface and electrochemically cycled in supporting electrolyte Chapter 4 describes the charge transport properties of an osmium polypyridyl polymer and the charge percolation findings of a metallopolymer nanoparticle composite Chapter 5 presents the results of lifetime and fluorescence quenching of solution phase $[Os(bpy)_3]^{2+}$

1.2 Mass Transport in Redox Active Layers

Electrochemically oxidising or reducing a redox active species at an electrode surface generates a concentration gradient between the interface and the bulk solution at a diffusion-controlled rate. For solid deposits and polymeric materials the rate of charge transport through the layer influences the voltammetric response. The equations presented below describe the diffusion rate of counterions through redox active films on the electrode surface. The current response for diffusion-only experiments depends on the flux at the electrode surface, which in turn depends on the electrode size and geometry. Fick's second law describes the diffusion of electroactive species to a spherical electrode:

$$\frac{\partial C(r,t)}{\partial t} = D\left[\frac{\partial^2 C(r,t)}{\partial r^2} + \frac{2}{r}\frac{\partial C(r,t)}{\partial r}\right] \tag{1}$$

The boundary conditions for the equation above are,

$$\lim_{r\to\infty} C(r,t) = C^{\infty}$$

$$C(r,0) = C^{\infty}$$

$$C(r, t) = 0 \text{ for } t > 0$$

where r is the distance from the center of the sphere, C is the concentration as a function of distance r and time t, and D is the diffusion coefficient for the redox active species. The solution to this set of equations may be found by Laplace transform techniques where the time evolution of the current, i(t) is described as;

$$i(t) = \frac{nFADC^{\infty}}{r_s} + \frac{nFAD^{1/2}C^{\infty}}{\pi^{1/2}t^{1/2}} \tag{2}$$

where n is the number of electrons transferred in the redox reaction, F is Faraday's constant, and A is the geometric electrode area. The current response following a potential step contains both a time-independent and time-dependent term.

Short times

At short times, the second term in equation in Equation 2 is much larger than the first and the current density is given by the Cottrell equation,

$$i(t) = \frac{nFAD^{1/2}C^{\infty}}{\pi^{1/2}t^{1/2}} \tag{3}$$

In this case, a transient current with the same shape as that occurring with a macroelectrode is obtained, i e , a plot of i(t) vs $t^{1/2}$ is linear Figure 1 2 illustrates that at these sufficiently short times the diffusion field is small compared to the electrode radius, and linear flux of electrolyte species perpendicular to the layer on the electrode predominates

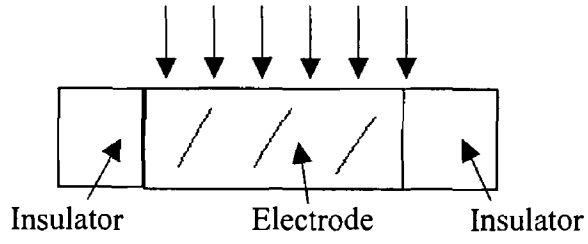

Figure 1 2 Linear diffusion at an electrode at short timescales where the diffusion field is small compared to the electrode radius

Long Times

As t increases, the transient second term of Equation 2 decays and the current is dominated by the first term of the equation The current attains a time-independent steady-state value given by

$$i_{ss} = \frac{nFADC^{\infty}}{r_e} \tag{4}$$

Carrying out long pulse experiments causes the diffusional layer to exceed the size of the electrode and this is shown in Figure 1 3 as radial (nonlinear) diffusion

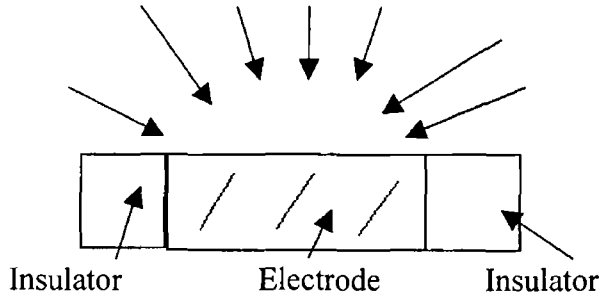

Figure 1 3 Radial diffusion at the electrode at long timescales where the diffusional layer exceeds the size of the electrode

The steady state response arises because the electrolysis rate is equal to the rate at which electrolyte ions can diffuse to the electrode surface

Equation 2 describes a spherical electrode but can be modified to describe the predominantly used microdisk electrode

$$r_s = \frac{\pi r_d}{4} \tag{5}$$

where r_d is the radius of the disk electrode

Therefore, the response to the potential step described in Equation 2 for a microdisk electrode is given by,

$$i(t) = \frac{4nFDC^{\infty}}{\pi r_d} + \frac{nFD^{1/2}C^{\infty}}{\pi^{1/2}t^{1/2}} \tag{6}$$

The steady state current is readily calculated by multiplying the steady state term by the disk area πr_d^2, giving the following equation,

$$i(t) = 4nFDC^{\infty}r_d \qquad (7)$$

Electrodes modified with the redox material offers a convenient means to both probe and control the properties of the material These electrode/material assemblies underpin technologies ranging from electrocatalysis[20] to redox-switchable non-linear optical materials [21]

1 3 Film Formation

While immobilising solid deposits and polymers on electrode surfaces is relatively straightforward a true three-dimensional molecular-scale organization cannot be easily obtained However, there are many reasons to investigate the capacity of macromolecules as assemblies The processes occurring in synthetic macromolecules can be compared to those of biological systems such as proteins The function of proteins is to regulate reactions of reactive centers and this regulation may be based on either kinetic or thermodynamic principles [22] Often, metal centers in enzymes are forced into particular coordination modes by steric confirmation of the protein In other cases, while the metal center in the co-enzyme might control the thermodynamics of a process (for example, by its redox potential or excited state energy), the protein controls the kinetics

1 3 1 Solids

Applying a solid state material to an electrode generally entails placing 1-3 mg of the powdered material on a coarse-grade filter paper [23 24] The electrode is gently rubbed into the powder until it is visibly thoroughly coated Another approach involves adding a drop of Milli-Q water to the powdered material before transferring the material onto the electrode surface as a paste [25] Prior to electrochemical measurements, the coating is allowed to dry

1 3 2 Polymers

A wide range of deposition techniques can be employed to obtain relatively well-defined polymer thin films with thickness of the order of microns and less The methods that have been used include the following

- Solvent evaporation
- Dip coating
- Spin coating

- Langmuir-Blodgett techniques
- Electrostatic self-assembly
- Electrochemical polymerisation and deposition
- Chemical bonding and grafting

In the solvent evaporation technique, a known amount of polymer material is mixed with solvent and is placed on the surface. The solvent is then slowly evaporated under controlled conditions.[26] In this way, the amount of material deposited can be controlled. However, factors such as the composition of the coating solution (concentration of polymer and solvent), drying time, environment and temperature need to be controlled carefully so as to achieve a reproducible and strongly adhering film. Spin-coating is generally regarded as the best way to deposit a uniform coating. For this technique, the rotation speed used is important. while for dip coating the rate of withdrawal of the substrate affects the properties of the layer obtained.[27] Dip coating is an easier, faster, and less expensive alternative to spin-coating. However, it cannot achieve the high level of uniformity and extremely thin layers that can be achieved with spin-coating.

In the Langmuir-Blodgett technique, amphilic polymers that are formed at a liquid-air interface are transferred to a solid substrate by horizontal or vertical transfer.[28] The thickness of such polymers is of the order of a few nanometers depending on the material being used. With this method, multilayer structures can be produced usually by repeated deposition of the same layer. With electrostatic self-assembly,[29] alternating positively and negatively charged layers can be deposited. This method leads to well-ordered multilayer systems with molecular level control over the architecture.

Electrochemical methods have also been widely used to produce surface immobilized layers.[30,31] A prerequisite for the application of these techniques is the presence of an electroactive group in the precursor material. Materials that have been widely studied include polyanilines, polypyrroles and polythiophenes.[32] With these compounds, thin conducting layers can be obtained for which the structure and layer thickness can, to a certain extent, be controlled by the electrochemical methods used to produce them. Self-assembly and grafting techniques have been used to attach both polymeric and

monomeric materials to surfaces [33] Polymers with active end groups have been immobilized using this technique e g silanes on silicon [34]

1 4 'Break In'

Due to the close packing of electrocrystallised compounds in the solid state the internal free volume is low and solvent/counterion uptake can be slow One approach to creating solids that facilitate more rapid ion transport is to encourage a higher free volume in the solid deposit using complexes with bulkier side groups that would increase the inter redox site separation On the other hand, polymeric materials are rapidly swollen in the supporting electrolyte and uptake of solvent/counterions can be fast

1 4 1 Solids

An interesting model postulated to explain charge propagation across the solid Dawson molybdate anion salts is illustrated in Figure 1 4, with steps I to III [35] It is proposed in step I that a surface charge transport reaction occurs which allows charge propagation across the particle surface from the three-phase boundary (electrode/solid deposit/electrolyte) This is believed to take place via electron hopping The 'breaking-in' process describes the process that occurs at step II When the surface potential reaches a sufficiently negative value, reduction and transfer (insertion) of ions from the solution into the solid becomes possible The surface of the solid is suggested to most likely become broken (fractured) and increases in volume, which enables both ions and solvent to penetrate the solid In the case of Dawson molybdate anion salts, protons efficiently neutralize charges and thus the 'breaking-in' potential occurs when conditions of both a negative potential and a low proton concentration exist The reduction may follow step III, with charge neutralization being achieved by protons because at least part of the newly exposed bulk is similar to the surface

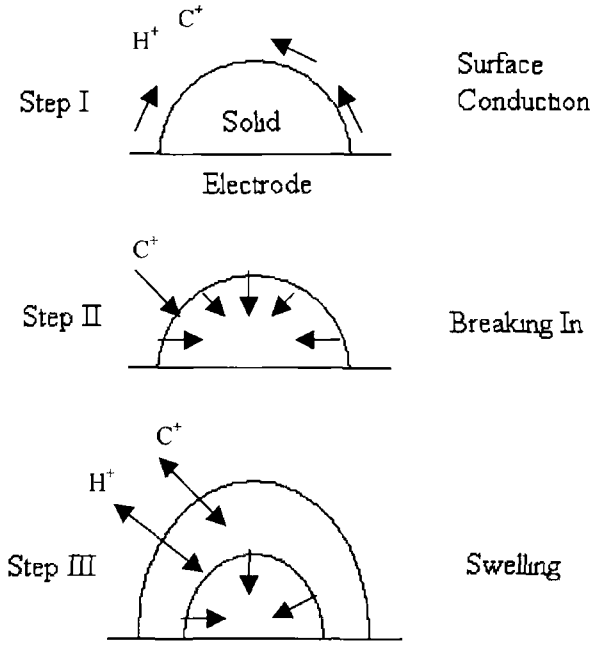

Figure 1 4 Schematic representation of the reduction processes of solid microcrystalline particles mechanically attached to a graphite surface C^+ denotes cations such as Cs^+ or Ba^+ and H^+ represent protons Altered from Reference (35) Step I represents charge propagation across the particle surface upon a surface charge transport reaction Step II illustrates the 'breaking-in' process and Step III shows subsequent charge neutralization by cations and protons

The observation of 'break-in' in solid-state voltammetry for ferrocene, cobaltocene and mercurous chloride was first reported by Sholtz and co-workers and explained in terms of dissolution of species from the electrode [36] However, the description of 'break-in' in the literature is the compound having to be converted into its equilibrium form during the first cycle, i e , the form of the compound that has intercalated the equilibrium amount of

equilibrium is reached after several scans is usually taken as evidence of a 'break in' effect For example, a decrease in the anodic peak current during repetitive scanning was observed for a solid deposit of osmium bis(bipyridyl)tetrazine chloride, $[Os(bpy)_2\text{-}4\text{-}tet\text{-}Cl]ClO_4$ and is illustrated in Figure 1 5 [25]

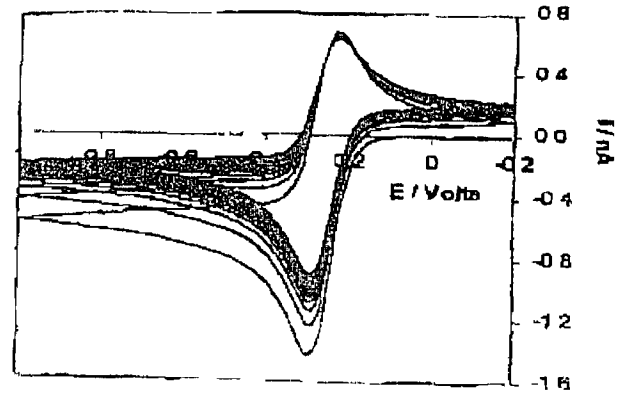

Figure 1 5 Effect of initial scanning on the voltammetric responses of an $[Os(bpy)_2\text{-}4\text{-}tet\text{-}Cl]ClO_4$ film that is mechanically attached to a 5 μm radius platinum microelectrode The supporting electrolyte is 1 0 M $NaClO_4$ at scan rate is 50 mV s^{-1} From Reference (25)

1 4 2 Polymers

Because of structural and compositional differences, the uptake of solvent/counterions in polymer films is fast when compared to solid deposits and therefore 'break in' effects are expected to be less pronounced Solvent transport in thin films of $[Os(bpy)_2\ (PVP)_{10}\ Cl]Cl$ (bpy = 2,2'-bipyridyl, PVP = poly-4-vinylpyridine) using a quartz crystal microbalance reveals that water accompanies anion movement into or out of the film during oxidation and reduction corresponding to a 30 % swelling due to water uptake at 1 mVs^{-1} [38] The chemical properties of the polymer backbone are important on the overall polymer properties as increasing the styrene content of the polymer backbone seems to slightly increase the hydrophobicity of $[Os(bpy)_2\ (PVP_x)_{10}\ Cl]Cl$ which is

reflected in a reduced ion and solvent content [39] With electrochemical quartz crystal microbalance, 'break-in' effect is proposed to be the film resistance to counterion transport[40] and was identified for [Os(bpy)$_2$ PVP$_{10}$ Cl]Cl by the broadening of the resonance and the change in resonant frequency below 0 01 mol dm^{-3} $HClO_4$ [41] The authors describe the 'break-in' effect as the inner polymer layer accomplishing equilibrium levels of solvation, which can be facilitated only by the extensive counterion and solvent transfer occurring during electrochemical cycling Conversely, quaternization of polymers can increase film swelling as scanning electron microscopy imaging of quaternized redox polymers of poly(4-vinylpyridine) complexed with $Os[(bpy)_2Cl]^{+/2+}$ showed swelling when immersed in poly(ethylene glycol)diglycidyl ether (PEGDGE) solution [42]

Figure 1 6 depicts the structure of [Os(II)(bpy)$_2$((2EH-PVP)Br)Cl]Cl where EH is ethylhexyl The cyclic voltammogram of Figure 1 7 illustrates that in nitrophenyl-based solvents this osmium-containing redox polymer demonstrated poor solvation [43] Although not called 'break-in' effect, voltammetric distortions are evident with repeated potential cycling of the osmium-containing redox polymer in 3-nitro-*o*-xylene The inset of Figure 1 7 shows the fifth voltammogram scan after an identical dry osmium-containing polymer-coated electrode had been soaked in 3-nitro-*o*-xylene/0 1 M tetrabutylammomum perchlorate for 2 hours The peak current of the voltammogram waves in the inset is small Thus, the authors report that it is repeated potential cycling and not the exposure to the supporting electrolyte that helped the solvation of the polymer A large peak-to-peak separation, ΔE_p, of 415 mV is evident in Figure 1 7, which may be due to ohmic effects arising from the macroelectrode Microelectrodes exhibit higher resistances than macroelectrodes but because the current observed at microelectrodes are typically of smaller magnitude, they often eliminate ohmic drop effects

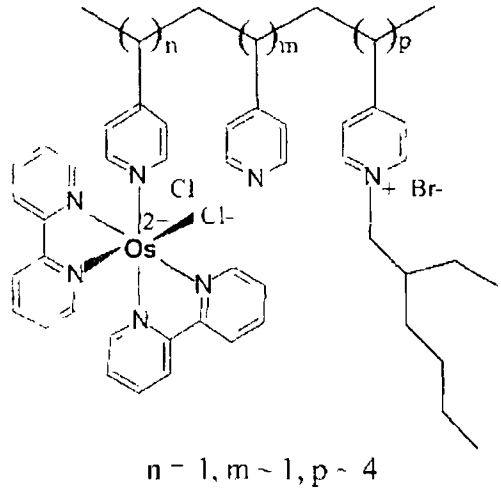

Figure 1 6 Structure of the osmium-containing redox polymer $[Os(II)(bpy)_2((2EH\text{-}PVP)Br)Cl]Cl$ From Reference (43)

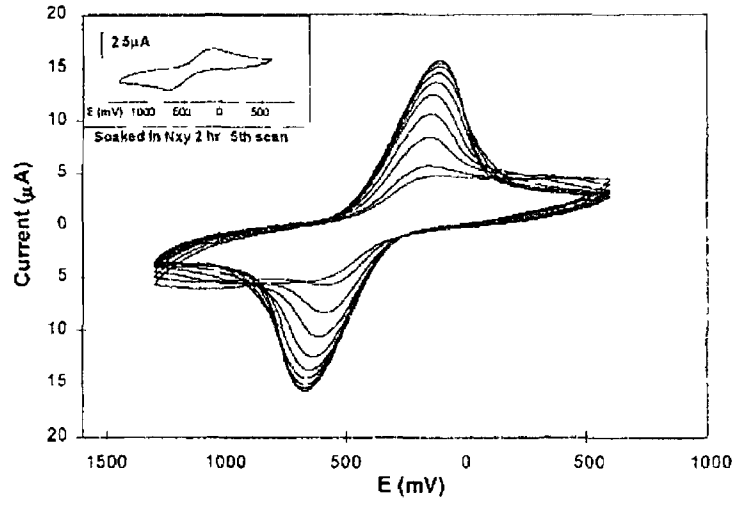

Figure 1 7 Continuous potential cycling of an osmium-containing redox polymer, $[Os(II)(bpy)_2((2EH\text{-}PVP)Br)Cl]Cl$ -coated glassy carbon electrode (3 mm diamter) in 3-nitro-*o*-xylene The smallest wave corresponds to the third scan, and the largest wave corresponds to the 45^{th} scan The sweep rate was 100 mVs^{-1}, and the supporting electrolyte was 0 1 M tetrabutylammonium perchlorate A silver wire was used as the reference electrode The inset shows the fifth CV scan after the identical dry electrode being soaked in 3-nitro-*o*-xylene for 2 h From Reference (43)

The anodic peak height response did not change significantly when films of tetracyanoquinodimethane (TCNQ) polymer-modified electrodes were repeatedly cycled, which indicated that they were rapidly swollen in the electrolyte [26] Conversely, the 'break-in' effect observed for dilute blends of TCNQ with polyester material was described as phase separation and composite formation since upon redox cycling of the TCNQ sites as the cathodic peak current on the first potential sweep was considerably less than on subsequent cycles Interchain interactions representing a crosslinking process of the TCNQ radical polymer was also concluded by the authors Even though not mentioned, the polymer crosslinking probably reduced the internal free volume thus making the layer less permeable to counterions/solvent

1 5 Homogeneous Charge Transport

To maintain electroneutrality upon the application of an oxidative potential to a redox film, electrolyte ions diffuse to the modified electrode surface and counteract the charge Likewise, when a reductive charge is applied the counterions are no longer required and are excluded from the film Electrochemical charge transport occurs by electron self-exchange reactions between neighbouring oxidised and reduced sites The movement of charge-compensating counterions that are mobile within the layers accompanies this electron hopping process Provided that the depletion layer remains well within the deposit, and ohmic and migration effects are absent, the voltammetric response is similar to a solution-phase reactant The effective diffusion coefficient, D_{CT}, corresponding to 'diffusion' of either electrons or charge compensating counterions can be estimated This process can be viewed schematically in Figure 1 3

1 5 1 Solids

Steady state voltammograms of solid state osmium bis(bipyridyl)tetrazine chloride films, $[Os(bpy)_2\text{-}4\text{-}tet\text{-}Cl]^+$, are shown in Figure 1 8 [25] A steady state plateau is observed which is independent of scan rate for $0\ 1 < \upsilon < 5$ mV s^{-1} and the currents in the forward and in the reverse scans are similar This steady state process is schematically represented in Figure 1 2 where radial diffusion is dominant

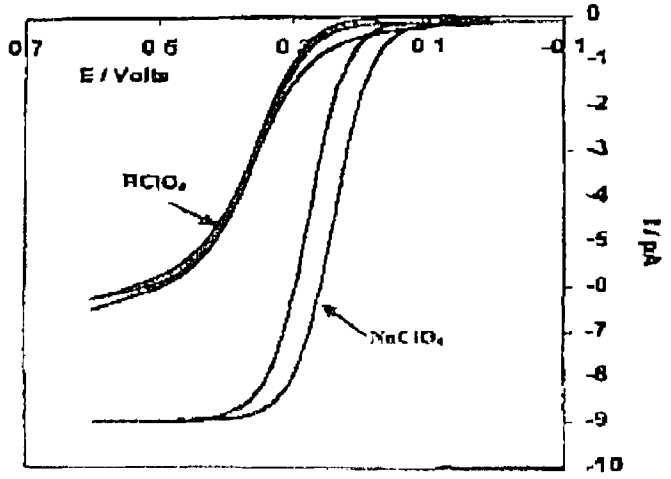

Figure 1 8 Steady state voltammograms at 1 mV s^{-1} using a 2 μm radius microelectrode The supporting electrolyte is 1 M $HClO_4$ and 1 M $NaClO_4$ for the smaller and larger limiting currents, respectively From Reference (25)

The limiting currents of $[Os(bpy)_2\text{-}4\text{-}tet\text{-}Cl]^+$ are larger in the $NaClO_4$ than in the $HClO_4$ electrolyte, which suggests that the diffusion coefficients and/or fixed site concentrations are not identical in the two circumstances Figure 1 9 depicts the peak shaped voltammetry that is observed for $[Os(bpy)_2\text{-}4\text{-}tet\text{-}Cl]^+$ when the scan rate was increased to 100 mVs^{-1} Figure 1 1 shows a schematic illustration of this linear diffusion response When ohmic loss is less than 1 mV and the peak currents are proportional to square root scan rate at short timescales, the peak currents can be described in terms of the Randles-Sevçik equation

$$i_p = 2\,69 \times 10^5 n^{3/2} A D_{app}^{1/2} C_{eff} \upsilon^{1/2} \qquad (8)$$

where n is the number of electrons involved in the oxidation/reduction reaction, A is the area of the electrode, D_{app} is the apparent charge transport coefficient and C_{eff} is the effective fixed site concentration Concentrations of 1 8 ± 0 05 and 1 6 ± 0 06 M and apparent diffusion coefficients of 6 4 ± 0 3 x 10^{-11} and 5 0 ± 0 4 x 10^{-11} cm^2s^{-1} are

calculated for the $NaClO_4$ and $HClO_4$ electrolytes, respectively, suggesting that the current response is dominated by anion diffusion

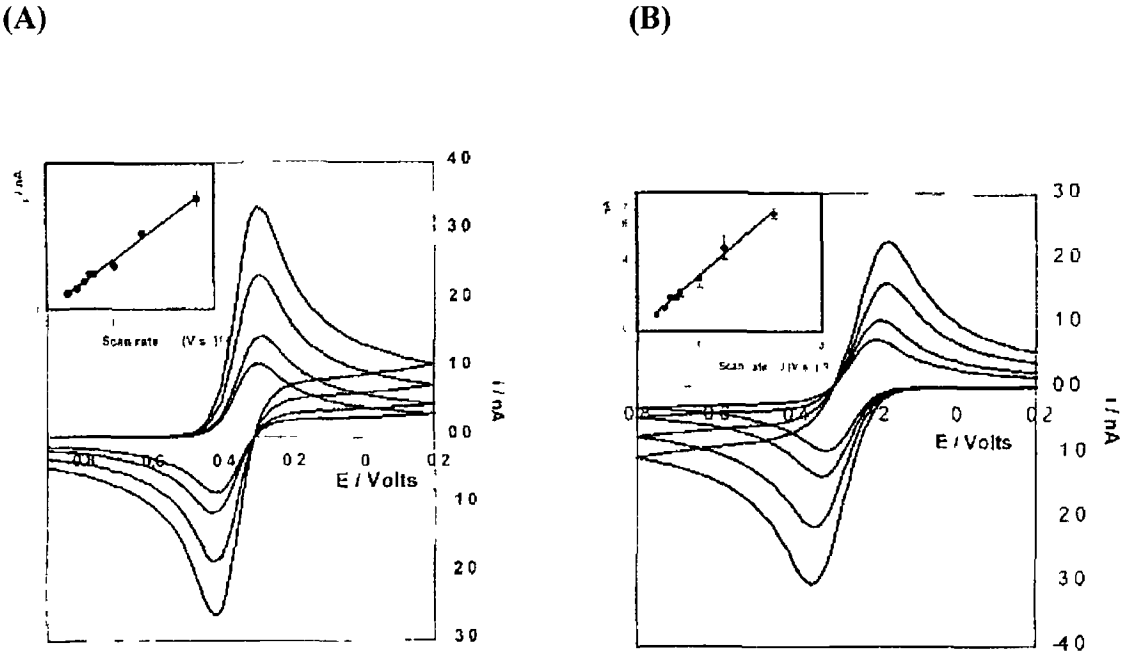

Figure 1 9 Voltammetric response of solid $[Os(bpy)_2\text{-}4\text{-}tet\text{-}Cl]ClO_4$ mechanically attached to a platinum microelectrode The supporting electrolyte is (a) 1 M $NaClO_4$ and (b) 1 M $HClO_4$ The scan rates are the same in both experiments From top to bottom the scan rates are 1000, 500, 200 and 100 mV s^{-1} The insets show i_p vs $\upsilon^{1/2}$ for films under these conditions From Reference (25)

1 5 2 Polymers

When redox centers are essentially immobile and separated by an insulating medium (polymer backbone), electron tunneling between redox centers is an important pathway for charge transport Electron transfer over large distances is governed by the ability of the electron to quantum mechanically tunnel through energy barriers over which the electron has insufficient energy to cross classically Saveant et al have provided the theoretical framework for electron transfer between nonadjacent redox sites [44]

Redox polymer layers display finite or semi-infinite diffusional behaviour depending on the scan rate Figure 1 10 illustrates the structure of $[Os(bpy)_2(PVI)_nCl]^+$ where bpy is 2,2 -dipyridyl and PVI is poly(N-vinylimidazole) Figure 1 11 shows the respective cyclic voltammetry of the polymer where radial diffusion predominates The peak shape is independent of scan rate up to 50 mV/s, and the peak height scales linearly with scan rate [45] Under semi-infinite conditions for sweep rate between 100 and 2000 mV/s, the peak current of $[Os(bpy)_2(PVI)_nCl]^+$ increases linearly with square root of scan rate

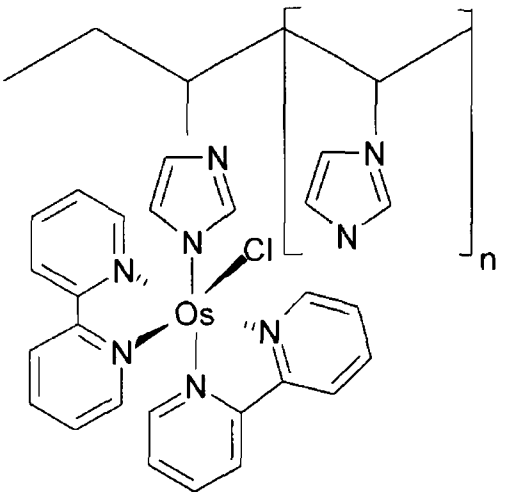

Figure 1 10 Schematic illustration of $[Os(bpy)_2(PVI)_nCl]^+$ From Reference (45)

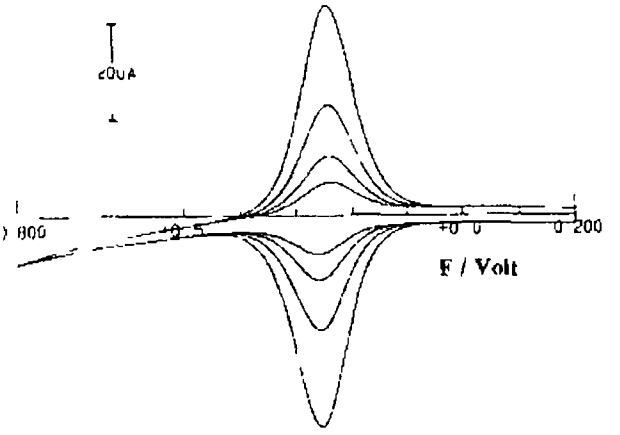

Figure 1 11 Sweep rate dependence of the cyclic voltammograms under finite conditions for an $[Os(bpy)_2(PVI)_{10}Cl]^+$ film on a 3 mm glassy carbon electrode Sweep rates (top to bottom) are 40, 20, 10 and 5 mV/s Surface coverage Γ is $1\ 8 \times 10^{-8}$ mol cm^{-2} Supporting electrolyte is aqueous 0 1 M p-tolunesulfonic acid From Reference (45)

1 6 Rate Determining Step for Homogeneous Charge Transport

The following section describes the three processes that can control the rate of homogenous charge transport through a redox active layer, i e electron self-exchange between the redox-active centers, ion movement to maintain electroneutrality or the polymer movement required to bring together redox-active centers so that electron self-exchange can occur The measurement conditions involve studies on the dependence of the charge transport rate on the concentration of the electrolyte The fastest charge transport rates are expected when the process is controlled by electron hopping In this case, the counterions do not play a part in the charge transport and the self-exchange between the redox centers is rate limiting Sometimes, for redox polymers the nature of the polymer film is rate limiting Important factors such as the permeability of the polymer matrix, the amount of swelling, and the distance between the redox centers are considered

1 6 1 Solids

Upon investigation of the diffusion coefficient of co-crystals of Hydroquinone and Bipyridyl Triazole, HQBpt, cycled in 0 1 M $HClO_4$, D_{CT} was insensitive to $NaClO_4$ and $HClO_4$ electrolyte concentration 0 1 ≤ [electrolyte] ≤ 1 0 M [46] This insensitivity infers that counterion or proton motion does not limit the rate of charge transport through these deposits and that ion transport is facile Electron self-exchange between adjacent H_2Q/Q moities was calculated to be the rate-limiting step by means of the Dahms Ruff expression [47 48]

$$D_{CT} = D_{phys} + \frac{1}{6} k_{SE} \delta^2 C_{H_2Q} \qquad (9)$$

where D_{Phys} is the physical diffusion in the absence of electron hopping, C_{H2Q} describes the fixed site concentration of hydroquinone in a fully reduced co-crystal and δ is the inter-site separation between adjacent hydroquinone moieties D_{Phys} is assumed to be zero as the hydroquinones are bound within a solid crystal δ is determined from the x-ray crystal structure The very large electron self-exchange rate constant of $2\,84 \times 10^9$ $M^{-1}s^{-1}$ is two orders of magnitude larger when compared to benzoquinone in aqueous media [49] The Q/H_2Q moieties are linked through π-stacking and hydrogen bonding interactions It has been demonstrated previously that π-stacked, H-bonded network can efficiently facilitate electron transfer[50] thus, a large k_{SE} for Q/H_2Q supports the assertion that electron self exchange represents the rate determining step

$[Os(bpy)_2$ bpt $Cl]^+$ films exhibit a different dependence of D_{CT} on the concentration in supporting electrolyte of varying concentration [51] In both $NaClO_4$ and $HClO_4$, D_{CT} increases by more than an order of magnitude on going from 0 1 to 1 0 M electrolyte This observation implies that counterion movement limits the rate of charge transport The k_{SE} constant was also much less than other osmium poly-pyridyl complexes in solution[52] or within monolayers[53 54] which supports this assertion The authors infer that the negative charge on the triazole ligand, Figure 1 12, impedes ion diffusion through the solid as the maximum D_{CT} value ($8\,3 \pm 0\,5 \times 10^{-12}$ cm^2s^{-1}) observed is an order of magnitude smaller than that found for $[Os(bpy)_2$ 4-tet $Cl]^+$ films[25]

(D_{CT} = 6 4 x 10^{-11} cm^2s^{-1}) However, there could also be closer packing of the material on the electrode surface, which could affect D_{CT} Even though solid deposits can be structurally similar, their charge transport properties can be different which could have implications in development of electrochemical sensors and biosensors [55]

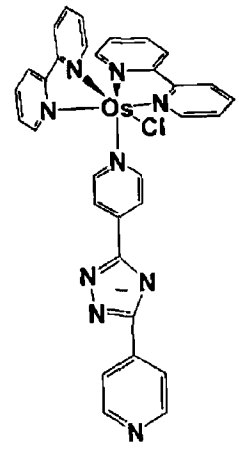

Figure 1 12 Schematic illustration of $[Os(bpy)_2 bpt Cl]^+$ From Reference (51)

To understand the electron self exchange mechanism of solid deposits, Bond et al postulated a model for the mechanism of Dawson molybdate anion $[S_2Mo_{18}O_{62}]^4$ salts at low pH electrolyte [35] Figure 1 13 illustrates the model that could also be used for other solid deposits in low pH electrolyte

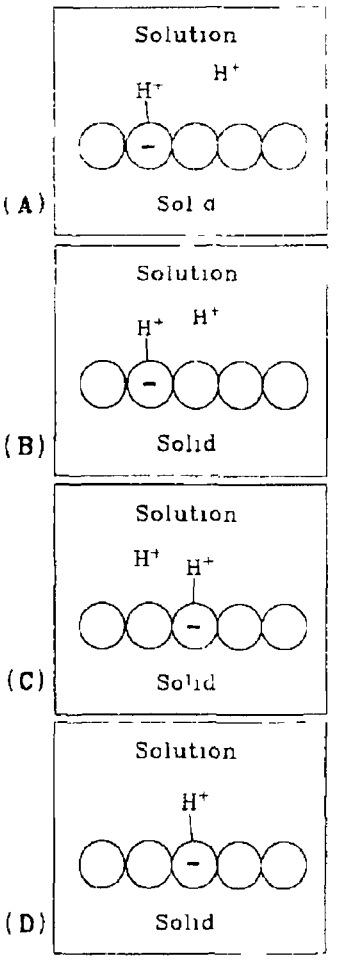

Figure 1 13 Schematic representation of the postulated electron hopping mechanism in the solid coupled to proton exchange with the aqueous solution phase From Reference (35)

Figure 1 13 (A) shows a proton bound to the molecule balances the negative charge created on the surface by reduction For this negative charge to become mobile either the proton has to dissociate or a neighbouring molecule has to become protonated An 'associative' mechanism may be operative and a high proton concentration in solution increases the rate of conduction To a first approximation the theory for conduction can be formulated in an analogous manner to Fick's first law of diffusion

$$j' = D_{CT}(dc'/dx) \qquad (10)$$

where j^s and c^s denote the surface current density and surface concentration, respectively Thus, a surface concentration gradient drives the process, which is determined by an apparent diffusion constant D_{CT} D_{CT} can be correlated with the jump length δ and the rate of electron hopping k_{ex}

$$D_{CT} = 0.25 k_{ex} \delta^2 c \tag{11}$$

where c is the overall concentration of the redox species and 0 25 accounts for an approximately 2-D transport problem The rate constant k_{ex} may include factors such as the adsorption kinetics of counter-ions and is of importance in conduction processes in which the chemical step competes with electron hopping [56]

1 6 2 Polymers

Polymer chain motion can limit charge transport through bulk material as was reported for $[Os(bpy)_2(PVI)_nCl]Cl$ where bpy is 2,2'bipyridyl, PVI is poly(N-vinylimidazole), $25 \geq n \geq 5$ [57] Depending on the distance separating the active sites, polymer chain motion may be required to bridge the intersite separation in order to allow electron self-exchange to occur The charge transport rate for $[Os(bpy)_2(PVI)_nCl]Cl$, D_{CT}, of 10^{-10} cm^2s^{-1} was lower than that for similar osmium containing polymer system with rates of $10^{-6} - 10^{-8}$ cm^2s^{-1} [58] When the H_2SO_4 concentration was increased from 0 1 M to 1 0 M, D_{CT} increased from 3.9×10^{-10} cm^2s^{-1} to 4.5×10^{-10} cm^2s^{-1} An increased electrolyte concentration is likely to swell the immobilized layers, thus increasing the osmium-osmium separation If electron self exchange was rate limiting, then an increased intersite separation at high electrolyte concentration would be expected to reduce, rather than increase, the charge transport rate D_{CT} was also reported to be independent of redox site loading in 0 1 M H_2SO_4 despite the intersite separation being changed from over 60 Å to approximately 10 Å suggesting that electron-self-exchange was not rate limiting

For tris (2,2'-bipyridine)ruthenium complexes in films of poly(styrenesulfonate) the charge transport rate of was found to be limited by the insertion into, and diffusion of counterions through the polymer matrix [27]

1 7 Counterion Effects

1 7 1 Solids

Frequently the effects of the counterion that diffuses through the redox active material during electrochemical cycling can be observed through cyclic voltammetry and scanning electron microscopy Figure 1 14 shows the effect of deposited N, N, N', N'-tetrahexylphenylene diamine, THPD, exposed to a number of different electrolyte salts [59] In 0 1 M aqueous perchlorate, a well-defined and stable response is observed However, in 0 1 M aqueous chloride, the voltammogram for the first one-electron oxidation of THPD splits into several waves depending on the potential scan rate Even though anion sensitivity is evident here, cation uptake by THPD was not considered

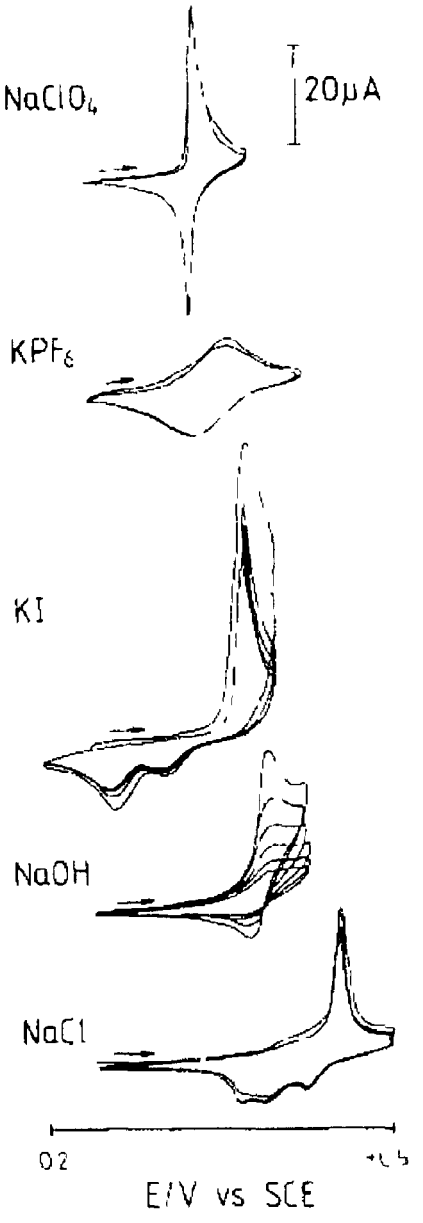

Figure 1 14 Cyclic voltammograms of the oxidation of THPD deposited on a basal plane pyrolytic electrode and immersed in aqueous (a) 0 1 M $NaClO_4$, (b) 0 1 M KPF_6, (c) 0 1 M KI, (d) 0 1 M NaOH, and (e) 0 1 M NaCl Scan rate is 0 01 Vs^{-1} From Reference (59)

Counterion diffusion and solvent ingress/egress can cause physical changes to the solid deposit during electrochemical cycling Changes in film morphology to the solid deposit osmium bis(bipyridyl) tetrazine chloride were reported through scanning electron microscopy [25] SEM revealed that the size and range of particle size changed with evidence of microcrystalline plates on the electrode surface cycling in $NaClO_4$ and was due to cation effects Even though not mentioned by the authors, the slight increase in D_{CT} for the solid in $NaClO_4$ compared to $HClO_4$ may arise from increased diffusion of counterions upon layer structural changes The D_{CT} values are 6 4±0 3 x 10^{-11} cm^2s^{-1} and 5 0±0 4 x 10^{-11} cm^2s^{-1} for 1 0 M $NaClO_4$ and $HClO_4$ electrolytes, respectively

The perchlorate anion movement changed the morphology of hydroquinone and bipyridyl Triazole (HQBpt) during cycling in 0 1 M $HClO_4$ [46] Needle-like crystals about 50 μm long assembled in rosette formation developed and Figure 1 15 shows pronounced differences between with this image to the deposit before voltammetric exposure in acid and near neutral electrolyte Significantly, the proton induced changes in the HQBpt structure in acid electrolyte leads to increased D_{CT} in electrolyte concentrations between electrolyte pH 0 7 and –0 2 whereas, D_{CT} is independent of the electrolyte pH for 1 1≤pH≤6 6 Furthermore, bulk electrolysis reveals no change in material morphology and this suggests that ion ingress and egress are responsible for the changes in deposit morphology when cyclic voltammetry is performed

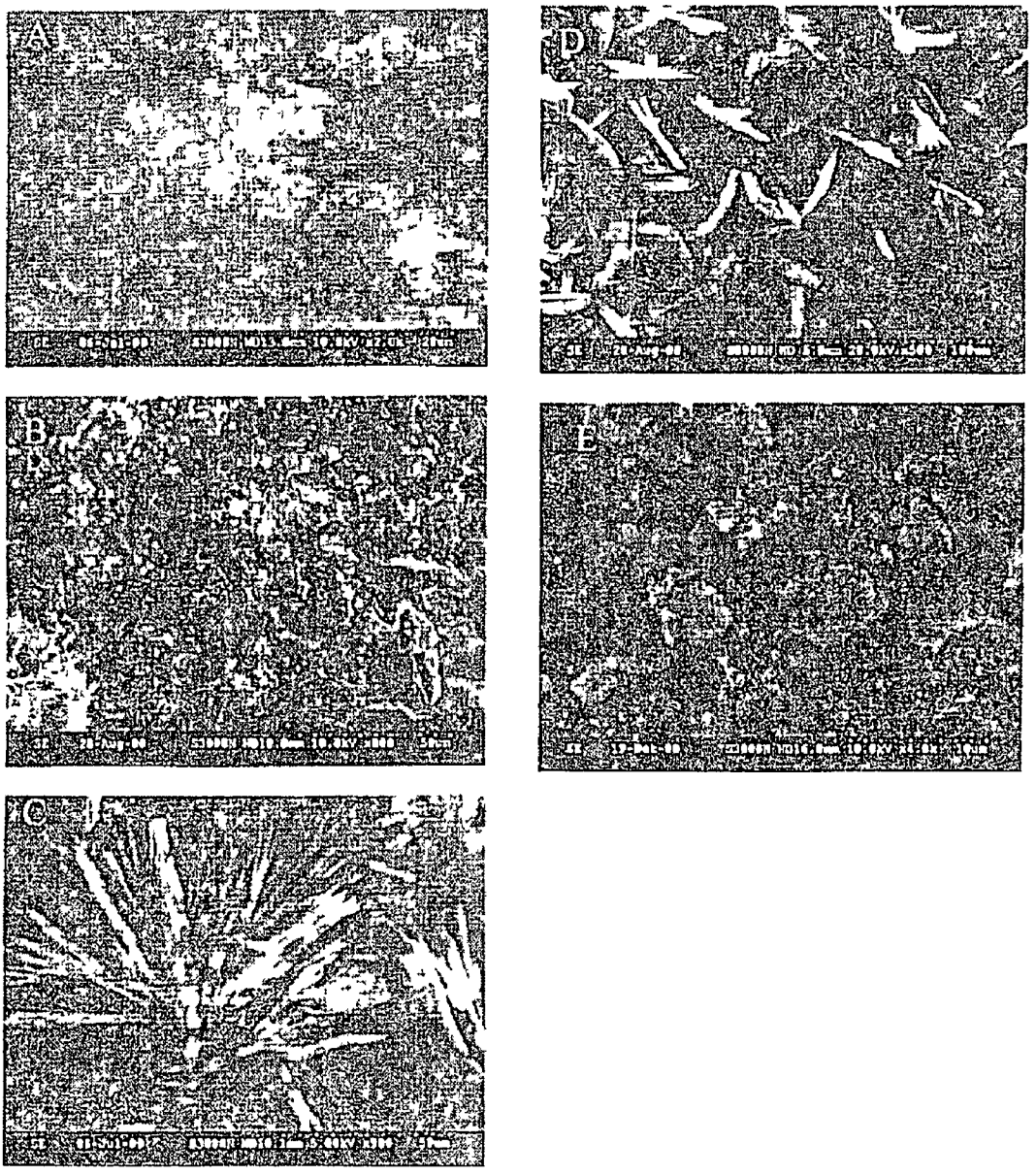

Figure 1 15 SEM images of HQBpt deposits on a 3 mm radius carbon disk (A) As deposited, prior to voltmmetric cycling (B) After exhaustive bulk electrolysis at 0 900 V in 0 1 M $LiClO_4$ (C) After 30 voltammetric cycles between –0 500 and +0 900 V in 0 1 M $NaClO_4$ at scan rate 0 1 V s^{-1} (D) After 30 voltammetric cycles between –0 500 and +0 900 V in 0 1 M $HClO_4$ at scan rate 0 1 V s^{-1} (E) After 30 voltammetric cycles between –0 500 and +0 900 V in 3 0 M $HClO_4$ at scan rate 0 1 V s^{-1} From Reference (46)

The mechanism by which these electrocrystallisation reactions proceed has been considered in the literature For example, Fletcher and co-workers represented the model for the nucleation process in Figure 1 16 for the solid TCNQ crystal that could represent the nucleation process of other solid deposits [60]

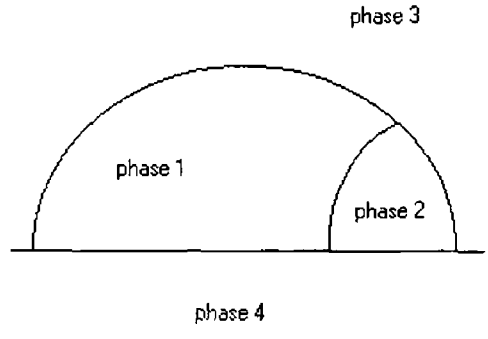

Figure 1 16 Schematic representation of nucleation in the four-phase system electrode (phase 4)/ solids (phase 1 and phase 2)/ solution (phase 3) From Reference (60)

In this model a TCNQ crystal (phase 1) is treated as a hemispherical volume that does not change on its tranformation to its cation salt (phase 2) Phase 3 and 4 represent the electrolyte and electrode respectively The reversible work of formation of unit area of interface between two phases p and q is called the specific interfacial free energy γ_{pq} This parameter plays a controlling role in the solid-solid transformation The first nucleus of the new phase 2 arising from reduction of phase 1 could appear at four different locations inside phase 1, at the two-phase boundaries (1,3) or (1,4), or at the three-phase boundary (1,3,4) It is shown that nucleation is most likely to occur at the (1,3,4) phase boundary since this is the location that minimizes the emergent area of the high-energy (1,2) interface in the nucleus and the region in which electrochemical reactions is most likely to occur Jiang and co-workers postulated a similar model for solid-solid phase transformations of platinum phthalocyanine [61]

Electrochemical evidence of crystal formation was first identified by Fletcher and co-workers in the study of solid state TCNQ (7,7,8,8-tetracyanoquinodimethane) [62] Figure 1 17 illustrates an 'inert zone' in the cyclic voltammetry that was absent in the cyclic voltammetry of dissolved TCNQ In this zone no faradaic reaction occurs and arises because nucleation overpotentials are needed to trigger the solid-solid transformations, i e , to begin the phase transformation process on each subsequent scan SEM imaging of the solid compound further proved the evidence for formation of crystals

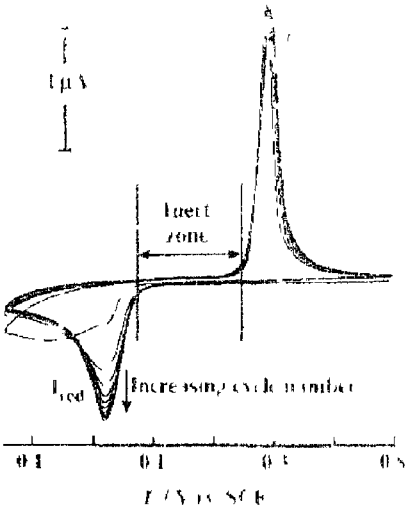

Figure 1 17 Voltammetric response of solid microcrystals of TCNQ (7,7,8,8-tetracyanoquinodimethane) beneath a coating of Nafion on a RAM™ (specially prepared carbon-fibre based random assemblies of microdisks) electrode immersed in 1 M KCl The scan rate is 100mV s^{-1} From Reference (62)

A similar 'inert zone' in voltammetry was observed for C_{60}/NBu_4C_{60} and associated with the process of cation ingress and egress into/from the solid [63] Along with the unusual peak-to-peak potential difference, the presence of sharp peaks in voltammtery was indication of a nucleation-growth controlled solid-solid phase transformation [64] Figure 1 18 depicts another tell-tale sign of nucleation and growth in the voltammetry of TCNQ microcrystals i e , the emergence of peaks at lower scan rates from the rising portions of

the voltammograms at higher scan rates [62] Indications of nucleation and crystal growth kinetics can also be observed where the scan directions are reversed in the foot of each voltammogram and current maxima occur on the reverse scans, Figure 1 19 Nafion is utilised to stabilise the microcrystals on the electrode surface as some TCNQ salts have a small solubility in water and would therefore dissolve in the electrolyte Nucleation at high overpotentials results in an enhanced current at low overpotentials This is in contrast to diffusion-controlled processes, which show lower currents on reverse scans due to the depletion of reactant The authors also state that the absense of a tail in the voltammograms means that diffusion also is not responsible for the patterns seen here

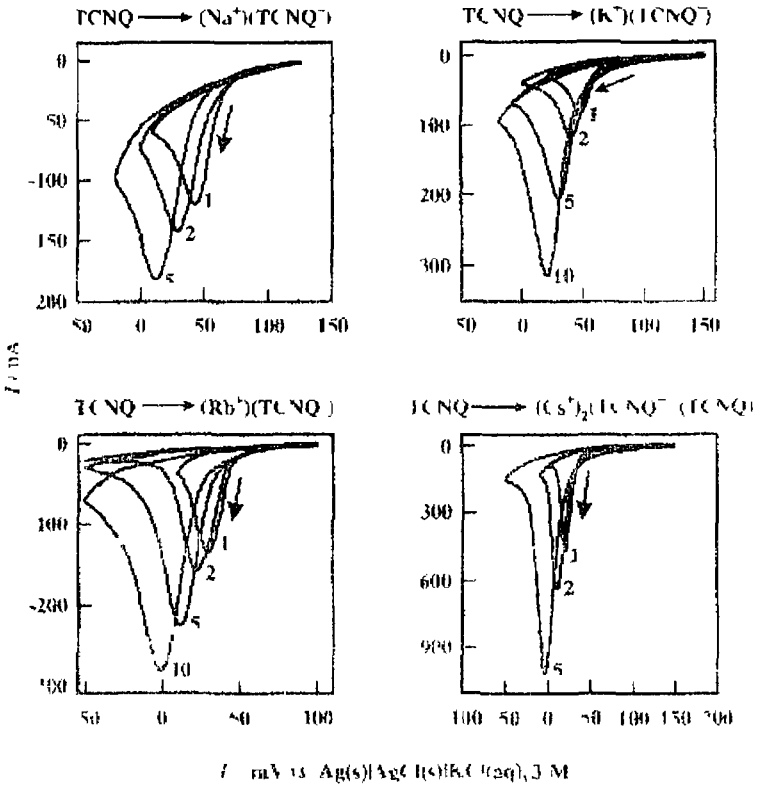

Figure 1 18 Effect of scan rate on the reduction of TCNQ microcrystals on Nafion coated RAM (carbon-fibre based random assemblies of microdisks) electrode in solutions of 0 1 M NaCl, 0 1 M KCl, 0 1 M $RbNO_3$ and 0 1 M CsCl From Reference (62)

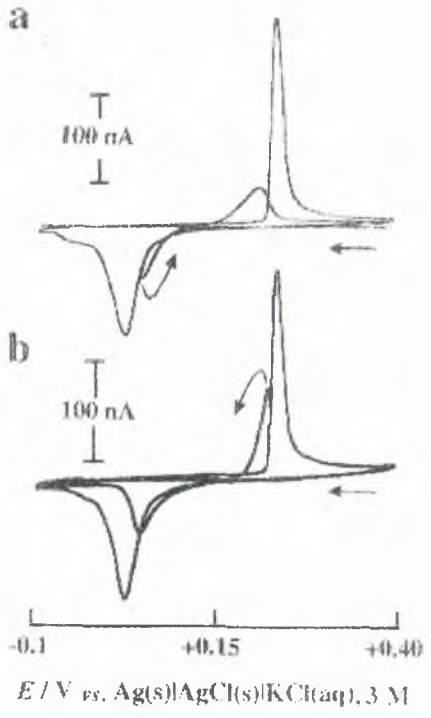

Figure 1.19. Cyclic voltammograms of TCNQ microcrystals on a Nafion coated RAM electrode in aq. 0.01 M NaCl. Scan rate is 100 mV s^{-1}. The scan directions are reversed at potentials corresponding to the foot of (a) the reduction and (b) the re-oxidation. From Reference (62)

Chronoamperometric (double potential step) measurements of TCNQ microcrystals and C_{60} exhibit characteristics for solid-state processes associated with nucleation-growth kinetics.[62,63] The reduction and the reoxidation current-time profile exhibit 'rising' current transients which contrasts to monotonic current decay ususally observed with diffusion or electron transfer controlled systems. Figure 1.20 illustrates the chronoamperogram for the reduction and reoxidation of solid C_{60} in acetonitrile/0.1 M NBu_4PF_6.[63] The authors state that the existence of peaks in response to potential steps is highly characteristic for solid-state processes associated with nucleation-growth kinetics. Microscopic imaging of the C_{60} subsequent to the voltammetric step further proved this theory by the formation of a crystal product.

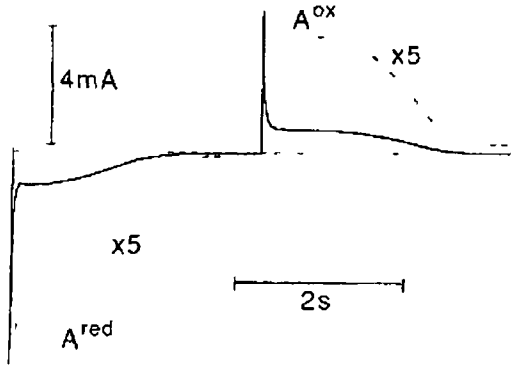

Figure 1 20 Chronoamperogram for the reduction and reoxidation of solid C_{60} mechanically attached to a basal plane pyrolytic graphite electrode From Reference (63)

1 7 2 Polymers

Like redox active solid state material, counterions can also affect redox polymers Faulkner et al have demonstrated the cyclic voltammetry effect of exposing [(QPVP)Ru(bpy)$_2$Cl]Cl, where QPVP is quaternized poly(4-vinylpyridine) in three different electrolytes and the voltammetry is illustrated in Figure 1 21 [65] In 0 1 M KNO_3, the voltammogram is well developed, yet the peaks are almost invisible in 0 1 M $NaClO_4$ The well-developed voltammograms can be reproduced when the electrode is moved back to KNO_3 solution This illustrates that the Ru(II) complex is not decomposed or leached out from the polymer film upon exposure to perchlorate The anion dependence of electron diffusion arises from anion-induced changes in the film structure

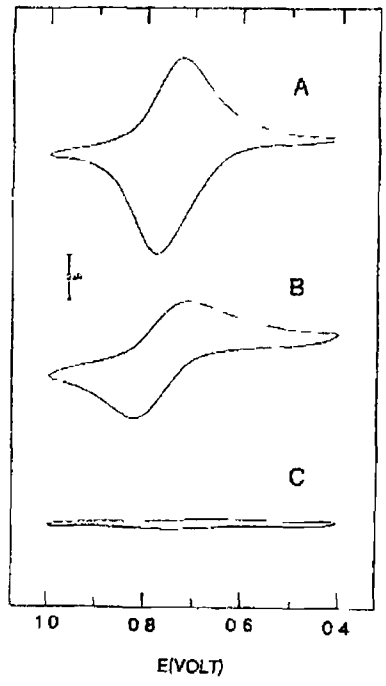

Figure 1 21 Cyclic voltammograms of QPVP-$Ru(bpy)_2Cl^{2+/1+}$ deposited on glassy carbon electrodes in different background electrolytes The concentration of $Ru(bpy)_2Cl^{1+}$ moieties was ~ 5 x 10^{-4} mol/cm^3 based on the dry film thickness (6500 Å) (A) in 0 1 M KNO_3, (B) in 0 1 M KOTs, (C) in 0 1 M $NaClO_4$ Scan rate = 50 mV/s, T = 23 °C Reference electrode was Ag/AgCl/KCl (3 5 M) From Reference (65)

Anion effects were observed in the cyclic voltammetry for the osmium polymer complex $[Os(bpy)_2(PVP)Cl]^{+}$ [66] The anions NO_3^-, Cl^- and SO_4^{2-} were responsible for polymer mass changes of 20%, 43% and 54%, respectively when the polymer was cycled in supporting electrolytes of $NaNO_3$, NaCl and Na_2SO_4 Replacing the cation K^+ for Na^+ in the nitrate form showed no polymer mass changes In another report on $[Os(bpy)_2(PVP)Cl]^{+}$, the anions of the acid electrolytes, hydrochloric, perchloric, trifluoroacetic and 4-toluenesulfonic, indirectly effect the overall polymer transport dynamics by modifying the film structure [67]

QCM measurements of ion and solvent populations in thin films of polyvinyl ferrocene, PVF, revealed that during oxidation no solvent accompanied anion PF_6^- insertion into the film whereas small amounts of water entered the film with ClO_4^- [40] The authors propose that large anions such as PF_6^-, ClO_4^- and BF_4^- are weakly hydrated in aqueous solutions

because of relative insolubility of their salts with organic cations in water Nonetheless, polymers already contain large amounts of water prior to any electrochemical cycling and this is not addressed here When the anion is Cl , the situation is quite different compared to the other two anions, as after Cl^- insertion into the film, there is dissolution of the oxidised PVF from the electrode surface Figure 1 22 illustrates the voltammetry of the PVF in 0 1 M KPF_4, 0 1 M $NaClO_4$ and 1 0 M NaCl

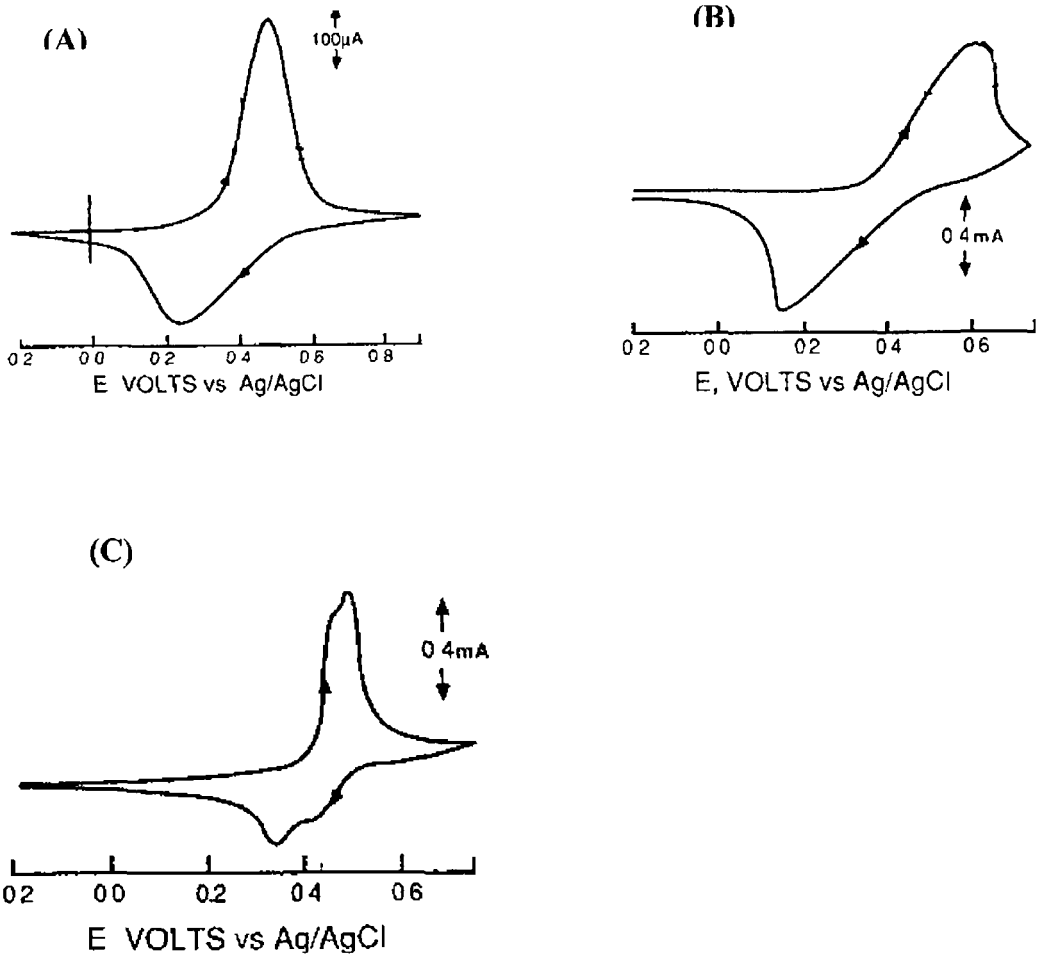

Figure 1 22 Cyclic voltammogram of PVF on a gold electrode in (A) 0 1 M KPF_4 at 10 mV/s, (B) 0 1 M $NaClO_4$ at 25 mV/s and (C) 1 0 M NaCl at 50 mV/s From Reference (40)

It is interesting to point out that the scan rate varies in each of the voltammograms of Figure 1 22 which can influence the type of diffusion, finite or semi infinite (section 1 2)

The authors suggest that the double peaks of PVF in 1 0 M NaCl in Figure 1 22 arise from a large change in polymer film density, in concentration of the sites and distribution of site to site differences

1 8 Heterogeneous Electron Transfer

Understanding the effects of distance, molecular structure and microenvironment on the dynamics of heterogeneous electron transfer across the electrode / material interface plays an important role in dictating the success of solid deposits and polymeric chemistry in the development of useful devices

Driving the working electrode to more negative potentials raises the energy of the electrons within the electrode They can become sufficiently energetic to transfer into vacant electronic states within molecules close to the interface In this case, a flow of electrons from electrode to deposit occurs Similarly, imposing a more positive potential can lower the energy of the electrons, and at some point electrons within the film will find a more favourable energy on the electrode and will transfer there Their flow, from solution to electrode, is an oxidation current

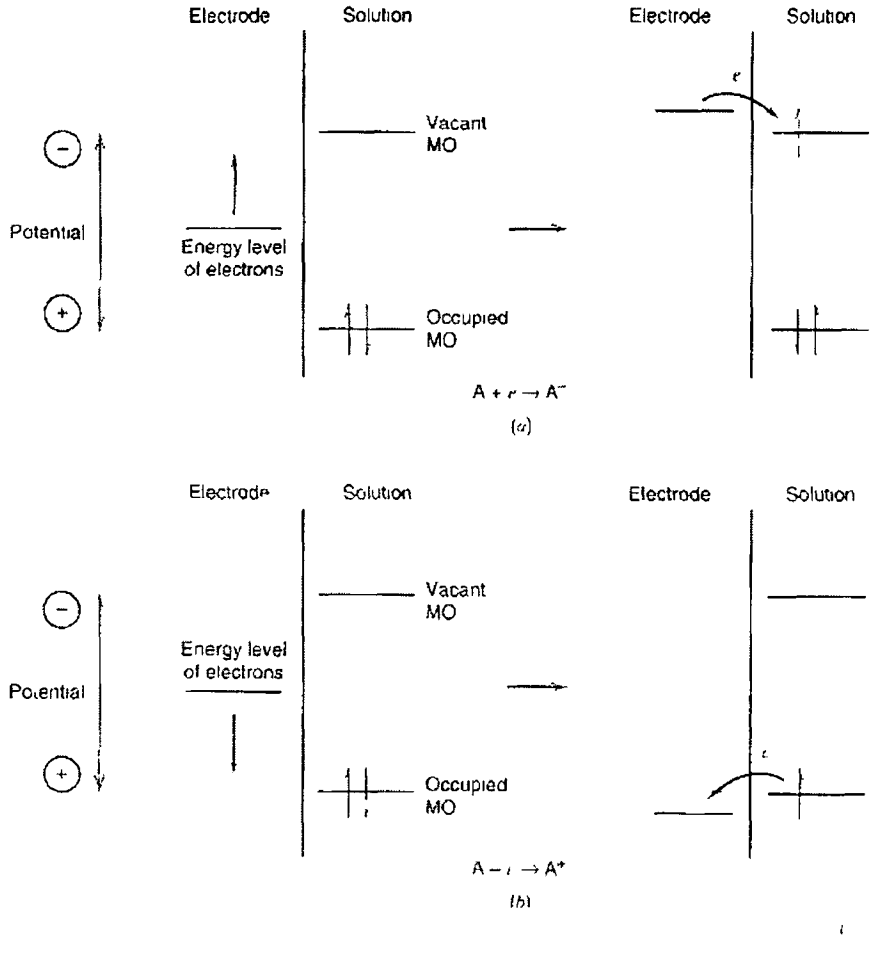

Figure 1 23 Representation of (a) reduction and (b) oxidation process of species, A, immobilized on the electrode The molecular orbitals (MO) of species A shown are the highest occupied MO and the lowest vacant MO These correspond in an approximate way to the E^0s of the A/A and A^+/A couples, respectively Altered from Reference (69)

The ability to resolve electron transfer dynamics allows the reactivity of the redox material to be determined Cyclic voltammetry can be used to estimate the heterogeneous rate constant of the immobilised material[51 68] by determining the separation between the cathodic and anodic peak potentials as a function of the scan rate Sufficiently fast scan

rates must be applied to make reversible, diffusion-controlled reactions show some kinetic irreversibility Under these circumstances for an immobilised reactant on an electrode, the peak-to-peak separation, ΔE_p, will increase and the peak current no longer increases proportionally to the square root scan rate Such behaviour and is due to the finite rates of electron transfer However, it is important that the uncompensated resistance (iR) be small enough to ensure that the peak-to-peak separation is due to electron transfer and not to uncompensated resistance IR is an undesirable process that distorts voltammetric responses Microelectrodes exhibit higher resistances than macroelectrodes but because the current observed at microelectrodes are of smaller magnitude, they often eliminate ohmic drop effects In most circumstances when microelectrodes are utilised this iR drop is nearly negligible accounting for approx 5% of ΔE_p at high scan rates

Butler Volmer Model

One of the oldest theories that describe heterogeneous electron transfer is the Butler-Volmer model [69] However, it does not address the individual steps in the electron-transfer event, but it is one of the least complicated models Consider the following reaction in which as oxidised species, Ox, is converted to the reduced form, Red by adding a single electron

$$Ox + e^- \xrightarrow{k_f} Red$$

The situation for a chemical, as opposed to an electrochemical reaction is considered first The forward rate constant k_f, according to simplified activated complex theory assumes an Arrhenius dependence on the chemical free energy of activation, $\Delta G^{\neq}$

$$k_f = \frac{k_B T}{h} \exp\left(\frac{-\Delta G^{\neq}}{RT}\right) \qquad (12)$$

where k_B, h and R are the Boltzmann, Planck and gas constants, respectively, and T is the absolute temperature Electrochemistry has significant advantage that the driving force for the reaction can be controlled instrumentally For a heterogeneous electron transfer reaction, the free energy of the reaction depends on the electrical driving force,

i e the applied potential relative to the formal potential, E^0, and $\Delta G^{\neq}$ must be replaced by the electrochemical free energy of activation, $\Delta\overline{G}^{\neq}$ The electrochemical rate constant for the forward reaction, i e reduction, is given by the following equation

$$k_f = \frac{kT}{h}\exp\left(\frac{-\Delta\overline{G}_f^{\neq}}{RT}\right) \tag{13}$$

Figure 1 24 illustrates both the 'chemical' and 'electrical' components where they contribute to the electrochemical free energies of activation The dashed line shows that a shift in the potential of the electrode to a value E, changes the energy of the electrons within the electrode by –nFE

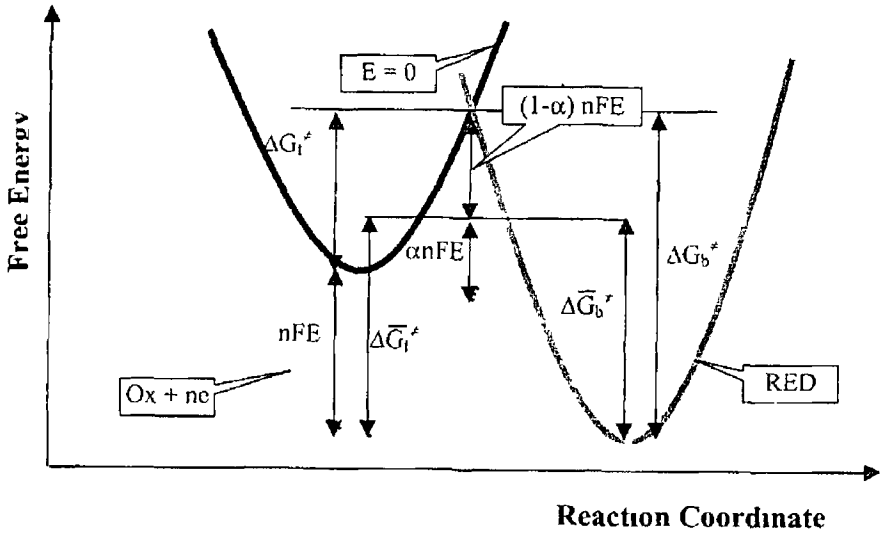

Figure 1 24 Illustration of the effects of potential on the free energies of activation for oxidation and reduction according to the Butler-Volmer formulation of electrode kinetics From Reference (70)

Under these circumstances, the barrier for the oxidation process, $\Delta\bar{G}_b^{\neq}$, is now less than $\Delta G_b^{\neq}$ by a fraction of the total energy change This fraction is designated as (1-α) where α is the transfer coefficient It takes on values between zero and unity depending on the shape of the free energy curves in the intersection region Thus, the free energies of activation can be separated as described by Equations 14 and 15

$$\Delta\bar{G}_f^{\neq} = \Delta G_f^{\neq} + \alpha nFE \tag{14}$$

$$\Delta\bar{G}_b^{\neq} = \Delta G_b^{\neq} - (1-\alpha)nFE \tag{15}$$

Substitution into Equation 13 yields the following expressions describing the potential dependence of the reduction and oxidation reactions, respectively

$$k_f = \frac{kT}{h}\exp\left(\frac{-\Delta G_f^{\neq}}{RT}\right)\exp\left(\frac{-\alpha nFE}{RT}\right) \tag{16}$$

$$k_b = \frac{kT}{h}\exp\left(\frac{-\Delta G_b^{\neq}}{RT}\right)\exp\left(\frac{(1-\alpha)nFE}{RT}\right) \tag{17}$$

The first exponential terms in both equations are independent of the applied potential and are designated as k_f^o and k_b^o for the forward and backward processes, respectively They represent the rate constants for the reaction at equilibrium, i e , for a solution containing equal concentrations of both oxidised and reduced forms However, the system is at equilibrium at E^o and the product of the rate constant and the bulk concentration are equal for the forward and backward reactions, i e k_f^o must equal k_b^o Therefore, the standard heterogenous electron transfer rate constant is designated simply as k^o Substitution into Equations 16 and 17 yields the Butler Volmer equations

$$k_f = k^o \exp\left(\frac{-\alpha nF(E-E^o)}{RT}\right) \tag{18}$$

$$k_b = k^o \exp\left(\frac{(1-\alpha)nF(E-E^o)}{RT}\right) \tag{19}$$

The dynamics of the system are described by k^o and its units are cms^{-1} and s^{-1} for solution and adsorbed reactants, respectively A redox couple with a large k^o will establish the equilibrium concentrations given by the Nernst equation on a short timescale Kinetically facile systems of this type require high speed electrochemical techniques to successfully probe the electrode dynamics The Butler-Volmer formulation is deficient in a number of respects First, the prediction that the rate constants for simple outer sphere electron transfer reactions will increase exponentially with increasing electrical driving force agrees with experiment only over a limited range of overpotentials The advent of microelectrodes allows heterogeneous electron transfer rates to be measured over very wide ranges of overpotentials, η Experimentally, k initially depends exponentially on η but then becomes independent of the driving force for sufficiently large values Second, the Butler-Volmer formulation fails to account for the known distance dependence of heterogenous electron transfer rate constants Third, it cannot predict how changes in the redox centre's structure or the solvent affect k^o

Electrodes modified with solid deposits and polymeric materials offer a facile means of controlling the chemical composition and physical structure of a surface These materials are strongly influenced by external factors including contacting solvent and ionic strength However, these materials are poorly ordered structurally on the electrode surface and the differences in k^o for solids and polymers are expected to be minimal

1 8 1 Solids

The apparent heterogeneous rate constant has been determined for solid state $[Os(bpy)_2$ bpt $Cl]^{+}$ [51] k^o increased with increasing concentrations of $HClO_4$ and $NaClO_4$ up to 0 5 M before becoming independent of the electrolyte concentration This result suggests that at high electrolyte concentration, heterogeneous electron transfer is not coupled to ion movement Also, k^o did not depend on the identity of the supporting electrolyte, indicating that k^o values obtained in 1 0 M electrolyte reflects the dynamics of the basic electron transfer event

1 8 2 Polymers

Previous investigations of the polymer film in p-tolunenesulfonic acid revealed a dependence of the formal potential on pTSA concentration indicating that ion-pairing is important for these systems and could be responsible for the larger D_{CT} values observed at higher pTSA concentrations Alternatively, the authors report that when the reaction site is located within the diffuse double-layer region, the measured apparent rate constant may need to be corrected for double layer effects The heterogeneous electron transfer rate depends exponentially on overpotential, and any difference between the applied potential and that at the outer Helmholtz plane (OHP) will significantly affect the observed electrode kinetics The authors corrected the observed standard rate constants for double-layer effects according to the Frumkin equation

$$k^{o} = k_{t}^{o} \exp(\alpha n - z) F\varphi_{2} / RT \qquad (20)$$

where k_t^0 is the 'true' standard rate constant, α is the transfer coefficient, z is the charge on the reactant, and φ_2 is the potential at the outer Helmholtz plane (OHP) The potential at the OHP decreased (calculated using the Gouy-Chapman-Stern model) as the electrolyte concentration increased, and k_t^0 became similar to k^0 for the highest pTSA concentrations investigated The fact that this correction factor depends on the electrolyte concentration means that k_t^0 is independent of the pTSA concentration For example, where n = 25, k^0 apparently increases from 2 6 to 7 5 x 10^{-4} cms $^{-1}$as the pTSA concentration is increased from 0 1 to 1 0 M In contrast, k_t^0 remains constant at a value of (2 1 ± 0 2) x 10^{-3} cms $^{-1}$ over this electrolyte concentration range

1 9 Comparisons between Redox Films and Solution Phase

Heterogeneous kinetics is affected by the nature and structure of the reacting species, the solvent system, the electrode material and adsorbed layers on the electrode The approach taken in the following section is based on the Marcus Model [69] In an *outer-sphere electrode reaction*, the reactant and product do not interact strongly with the electrode surface, and they are generally at a distance of at least a solvent layer from the electrode In an *inner-sphere electrode* reaction, there is a strong interaction of the reactant, intermediates, or products with the electrode, that is such reactions involve specific adsorption of species involved in the electrode reaction In general, solids/polymer materials and solution phase species involve outer-sphere electrode reactions

1 9 1 Solids

The cyclic voltammograms for Vanadium (IV) has been investigated in both solid and solution phase [71] When the formal potential results for both immobilized and solution phase were compared it was found that the dichloromethane solutions showed more negative values by approximately 100 mV The authors gave no explanation for the formal potential difference for the two phases but it is stated that the formal potentials can be used as a criterion of stability Further investigations of the Vanadium (IV) complexes would need to be explored, as the microenvironment of the complex in the two phases is dissimilar as indicated by the formal potential

Solution and microcrystalline solid phase voltammetry of $[Co(mtas)_2](X)_n$ (mtas=Bis(2-(dimethylarsino)phenyl)methylarsine, X=BF_4, n=3, X=ClO_4, n=2, 3, X=BPh_4, n=2) have been compared [72] The structure of the ligand is illustrated in Figure 1 25 The solution and the solid phase samples exhibit the same spectroscopic features and suggests that the molecular structure of the primary coordination sphere that accompanys the Co(III)/Co(II) redox reaction is indistinguishable in both cases However, the shape and scan rate dependence of the voltammetric responses are different for the solid and dissolved complex The authors propose that the stabilization of $[Co(mtas)_2]^{3+}$ relative

to $[Co(mtas)_2]^{2+}$ in aqueous solution is significantly greater than in the solid, due to the effects of hydration and ion-dipole interactions in the solution phase

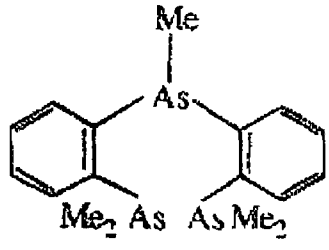

Figure 1 25 Structure of bis(2-(dimethylarsino)phenyl)methylarsine), mtas From Reference (72)

1 9 2 Polymers

A similarity in formal potentials between solution phase $[Os(bpy)_2(N\text{-methylimidazole})Cl]^+$ and the redox couple coordinatively bound within polymer films suggested that the local microenvironment of the redox center is similar in both cases [45] The formal potential is sensitive to the effective dielectric constant[73] and the similarity in formal potentials suggests that the water content of the films is high

1.10 Nanoparticles

1.10.1 Enhanced Electron Transfer Pathways within Polymers

Studies of electron transport in conjugated metallopolymers in which metal sites are in direct electronic communication with a conjugated backbone provide insight into long-range electron-transfer mechanisms that will likely be important in the development of viable molecular electronic devices[74] and electrocatalytic polymers.[75] Electron exchange between redox active centres of polymers may be further enhanced with the introduction of metal nanoparticles to the polymeric matrix and for this reason they are being applied to technology for electrical and optical devices.[76]

Previous conductivity experiments with monolayer protected nanoparticles have shown that these materials do not possess metallic conductivity but resemble the behaviour associated with electron hopping in discontinuous metal island films.[77,78]

The mechanism for redox conduction in polymers is represented in Figure 1.1 and involves electron self-exchange reactions between adjacent oxidized (acceptor) and reduced (donor) sites.[79,80] By the self-exchange reaction, the electron moves (hops) from one physical site to another and is thereby moved toward or away from the electrode. Conductivity occurs by charge carriers hopping from one nanoparticle to another through the thin dielectric layer of polymer. The properties of the composite are mostly dominated by the nature of the nanoparticle filler, whereas the polymer matrix determines the environmental characteristics of the composite. The electrical properties of polymer nanoparticle structures can be adjusted by changing the content of nanoparticles in the composite.[81] Therefore, the overall composite properties can be tailored to fit the desired application through proper choice of filler and matrix.

The transition to composite conductivity is attributed to the percolation phenomenon, which is based on the fact that the conductive filler loading is sufficiently high so that the particles can come into contact with one another as the filler loading exceeds the threshold concentration.[82,83] The main question concerning mixtures of electrically conducting particles incorporated in an insulating / conductive matrix is how the

conductivity changes with the content of the conductive filler. Figure 1.26 illustrates a typical conductivity / filler concentration curve.[84]

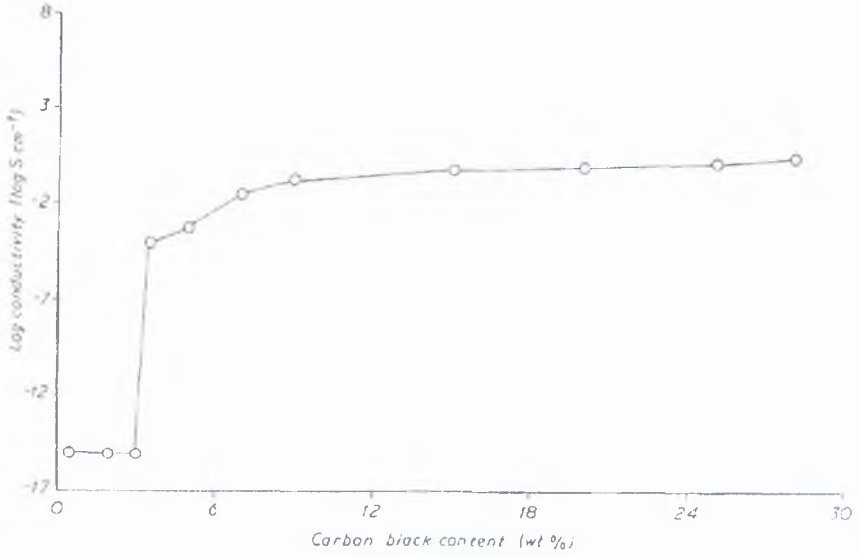

Figure 1.26. Conductivity of a binary mixture, made of an insulating matrix (polyethylene) and a conductive filler (carbon black); dependence of the conductivity of the mixture on the filler content. From Reference (84).

In the region of low filler concentrations, the filler (carbon black), incorporated in the form of small particles with a different shape, is distributed homogeneously in the volume of the insulating host (polyethylene). There is no contact between adjacent filler particles and with increasing filler concentration; agglomerates of the filler particles begin to form. In these agglomerates the filler particles are in contact with each other. At a certain filler content, the growing agglomerates reach a size which makes it possible for them to touch each other; a compact one-, two-, or three-dimensional network of the conducting phase within the insulating one is formed. As a consequence of the appearance of the network, the conductivity of the mixture shows a dramatic increase.

After the first conductive network is formed, the conductivity of the mixture again shows a slow increase with growing filler content This can be explained as a slightly improved quality of the conductive network

The electrical conductivity of composites can be expressed by the equation [85]

$$\sigma = \sigma_c + (\sigma_m - \sigma_c)[(\varphi - \varphi_c)/(F - \varphi_c)]^t \quad (21)$$

where σ is the composite conductivity, σ_c the conductivity at percolation threshold, σ_m the maximum conductivity, φ the volume filler fraction and φ_c is the volume filler fraction at the percolation threshold The value of F characterizes the filler phase topology taking into account the particle shape, fractional size and spatial distribution of particles and has a value smaller than 0 64 [86] t is a critical exponent and lies between 1 6 and 1 9 [87] However, this equation does not take particle shape, polymer-filler interaction, and existence of contact phenomena on the particle-particle boundary, influence of preparation conditions on the volume distribution of conductive particles

Polymer filled composites exhibit several interesting features Above room temperature a sharp, reversible drop in conductivity is sometimes observed [88] This effect depends on the composition of the material (filling factor, polymer, filler nature) but the authors state its origin is still not understood This drop in conductivity may be explained as the composite becoming less stable due to break down of polymer nanoparticle bonds Below room temperature, various behaviours may be observed and the temperature dependence of the resistivity provides a good means for investigating the conduction process in such heterogeneous materials Two approaches 'local' and 'global' have been described to interpret the experimental temperature dependences of the conductivites The 'local' approach in which hopping of carriers is dominated by thermal fluctuations is expressed by

$$\rho = \rho_0 \exp \frac{T_1}{T + T_0} \quad (22)$$

where ρ_0, T_1 and T_0 are constants which depend on the characteristics of the tunnel junctions, which are supposed to be functions of various parameters (filling factor, particle size and shape) The 'global' approach is represented as follow

$$\rho = \rho_1 \exp \frac{T_2}{T^{\alpha}} \qquad (23)$$

where ρ_1, T_2 and α are constants, the latter being supposed to depend on the particle-size distribution Such behaviours are expected when conducting particles belonging to the infinite conducting cluster of percolation theory remain separated by thin layers of polymer Equations 23 and 24 have been utilised in three distinct series of carbon polymer composites with the carbon black filler varying in nature, shape and size [89] They report that Equation 22 seems to be appropriate to one of the series of materials, whereas neither of the proposed Equations 22 or 23 holds for the other two series Instead the authors propose a new mechanism for the temperature dependence and demonstrate that the observed differences in temperature dependence are correlated to differences in the particle aggregation process In conclusion carbon particle-filled polymers may exhibit two distinct conductivity temperature dependences The first due to tunnelling of electrons among particles, is generally found in carbon-black-filled polymers The second is found when carbon particles are large and comes from differential thermal expansions of the matrix and the filler In the study undertaken on other carbon-polymer, non-semiconducting materials the results were not consistent with tunnelling conduction, but rather direct contact of particles This temperature study underlines the importance of the processing conditions of the composites on their electrical properties

1 10 2 Nanoparticle Polymer Composite Size Distribution

The formation of polymer nanoparticle assemblies is often accomplished by chemical reduction of a metal salt with in the polymer [90 91 92 93] Incorporating a metal particle in a polymer matrix can change the properties of the polymer as the polymer concentration influences the size and absorption spectra of the metal particles [94 95] Polyethylene glycol (PEG) acted as not only a protective agent but also a reducing agent for silver nanoparticles [96] With increasing $AgNO_3$ concentration (decreasing PEG concentration), the mean diameters of the Ag nanoparticles were 3 8-9 0 nm Similarly, Walker and co-workers demonstrated that increasing the amount of stabilizing poly(methylphenylphosphazine), PMPP, decreased the average size of the nanoparticles [97] In the synthesis of cobalt disulfide nanoparticles, the polymer matrix played an important role in shaping rod- or needle-like nanoparticles [98] TEM images of uncoated and polymer-coated gold nanoparticles with poly(methyl methylacrylate) (PMMA) are shown in Figure 1 27 [99] The average sizes of the nanoparticles are in the range 50-70 nm A thin polymer layer surrounds the gold core, which is not imaged in the TEM pictures because the polymer layer contains less electron density relative to the gold nanoparticle cores However, FTIR characterization confirmed that the nanoparticles were coated with polymer

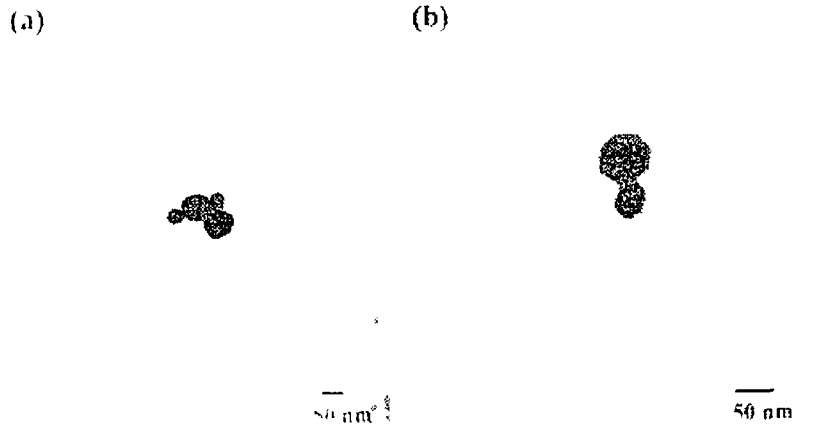

Figure 1 27 Transmission electron micrographs of (a) uncoated, and (b) PMMA-coated gold nanoparticles From Reference (99)

1 10 3 Composite Electrochemical Properties

There have been few reports in the literature on the electrochemical properties of nanoparticle polymer composites However, there are some reports of monolayer protected clusters [100 101] Figure 1 28 shows the dependence of the electrochemical response on the number of Au colloidal layers has been investigated for $[Ru(NH_3)_6]^{3+}$ in aqueous 0 1 M Na_2SO_4 at colloidal Au working electrodes ranging from 3 to 15 layers [102]

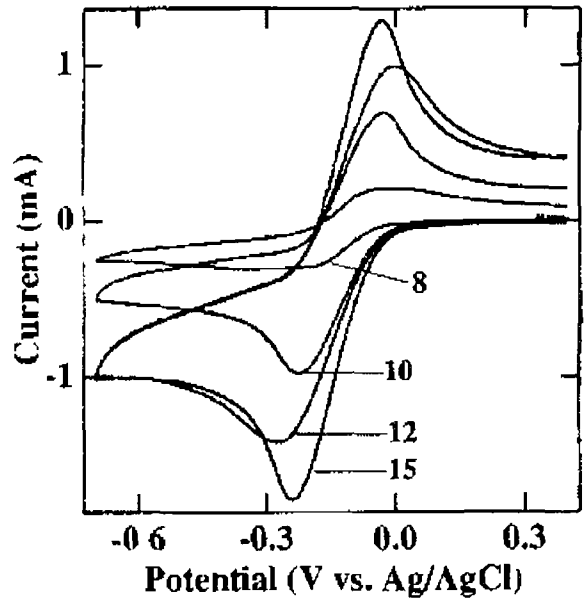

Figure 1 28 Cyclic voltammograms of colloidal Au multilayers in 5mM $[Ru(NH_3)_6]^{3+}$ with 0 1 M Na_2SO_4 supporting electrolyte recorded at 100 mVs ^{1} as a function of number of colloidal Au layers (number of colloidal layers indicated on graph) From Reference (102)

The chronoamperometry transients of electrodes with greater than seven layers exhibit linear diffusion, characteristic of a planar macroelectrode The electrode may be modelled as either a continuous metal surface or a microelectrode array whose component diffusion layers overlap over the time frame of the experiment due to the

high density of gold on the electrode surface The 12-layer voltammogram yields a peak potential difference (ΔE_{peak}) at 100 mVs^{-1} of 92 mV using positive feedback IR compersation, compared to 238 mV without IR compensation This observation leads to two important conclusions (1) voltammetry at these electrodes can approach the nearly reversible behaviour observed for $[Ru(NH_3)_6]^{3+}$ at a bulk Au electrode (ΔE_{peak} = 78 mV), and (2) colloid multilayer electrodes are resistive enough that IR compensation is required to achieve this approximate reversibility The fact that IR compensation is successful in lowering ΔE_{peak} indicated that intrinsic barriers to electron transfer are not the major contributor to peak separations Two possible sources of the resistivity are poor electrical contact to the Au surface and/or poor conductivity through the cross-linker that binds the colloidal particles together Estimated values of k^o, the heterogeneous electron transfer rate constant, for Au colloid multilayer electrodes were obtained and the resulting values were reasonably close to values obtained at bulk Au electrodes i e 7 9 x 10^{-3} cms^{-1} for $[Fe(CN)_6]^{3}$ at a bulk Au electrode and 7 6 x 10^{-3} cms^{-1} at a 10-layer colloidal Au film

The area of the modified electrodes was determined using the Cottrell equation and the active electrochemical areas were typically 40-60% larger than the geometric areas The magnitude of current was larger than the geometric area suggested The Cottrell model assumes a planar macroscopic electrode and does not consider microscopic roughness or the possibility of complex diffusion patterns that accompany the presence of passivated and highly conducting regimes on the electrode Colloid multilayers have been reported to display fractal properties due to surface roughness or passivation The actual electrode surface area being larger than the geometric area is consistent with supporting AFM data, which shows a complex morphology

1.10.4 Optical Effects

When external electric fields are applied to a nanometre-size metal, electrons move so as to screen perturbed charge distribution, further move beyond the neutral states, and again return to the neutral states and so on. The collection motion of electrons is called a 'plasma oscillation'. The surface plasmon resonance is a collective excitation mode of the plasma localized near the surface and electrons confined in a nanoparticle conform the surface plasmon mode. The surface plasmon band arises from oscillation of the electron density where there are interband transitions between the highly polarizable Au $5d^{10}$ band and the unoccupied states of the conduction band. Figure 1.29 represents the energy level diagram of a nanocrystal.[103]

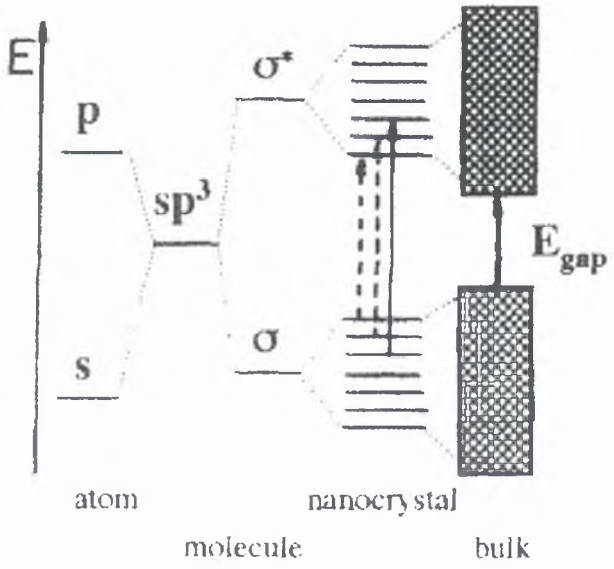

Figure 1.29. Size evolution of the density of electronic states in nanocrystals. From Reference (103)

Figure 1.30 illustrates the visible spectra of a gold sol prepared with and without dodecanethiol.[77] The plasmon resonance absorption characteristic of the bulk metal is evident at 520 nm in the solutions from the larger thiol-free preparations, but is almost

totally absent when the thiol is present When the thiol is present the particles are accordingly much smaller as observed in TEM images and the surface plasmon resonance is not evident The loss of the surface plasmon band has been interpreted as an indication of the loss of bulk character for the smallest gold nanoparticle core [104] However, the absorbance scales of the spectra are dissimilar and the surface plasmon band may only be masked by the dodecanthiol spectra

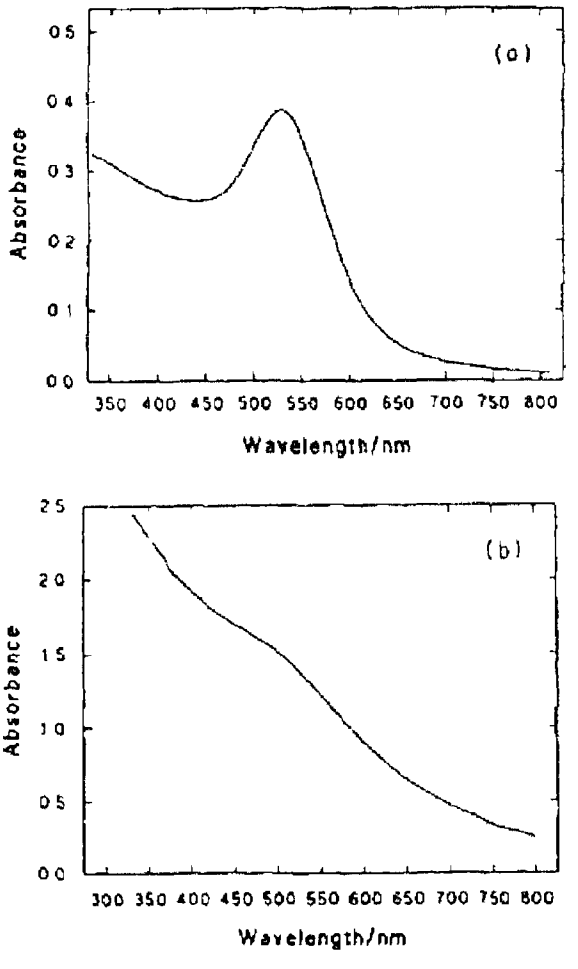

Figure 1 30 Visible absorption spectra of solutions of gold nanoparticles in toluene solution (a) no thiol present during the preparation, (b) nanoparticles generated in the presence of dodecanethiol From Reference (77)

1 11 Photoinduced Processes

In this literature review so far it has been demonstrated that redox active solid deposits and polymeric species have the ability under certain conditions to become modified in order to enhance charge transport through the materials Redox active solid deposits and polymer species have the potential to exhibit interesting examples of light and electrically stimulated functions and may represent the precursors for molecular based machines [74] To demonstrate real world applications of these materials as optical devices it is necessary to perform photoinduced processes for integration into circuitary or devices

Fluorescence quenching refers to any process which decreases the fluorescence intensity of a material, has been widely studied both as a fundamental phenomenon and as a source of information about biochemical systems [105] The biochemical applications of quenching are due to the intrinsic role of molecular interactions in quenching phenomena [106] Fluorescence quenching has been incorporated into the development of an optical water sensor [107] The sensor contains a fluorescent metal-ligand compound, dipyridol[3,2-a 2",3"-c]phenazine, di[cis-1,2-bis(diphenylphosphino)-ethylene] osmium(II) hexafluorophosphate, $[Os(dppz)(dppe)_2](PF_6)_2$ and is illustrated in Figure 1 31 The dppz ligand is not fluorescent in water and suggests that quenching occurs when water interacts with the exposed heterocyclic nitrogen in the dppz ligand Figure 1 32 shows the change in emission spectra with the change in water content of an acetone solution Though the emission peak at 610 nm remains constant, the peak intensity drops dramatically with increasing water content, i e the fluorescence intensity from the solution containing 45 % water was only 4 % of that from water-free solution These results are an indication that the compound is a very good water-sensitive indicator, and suitable for constructing a water sensor

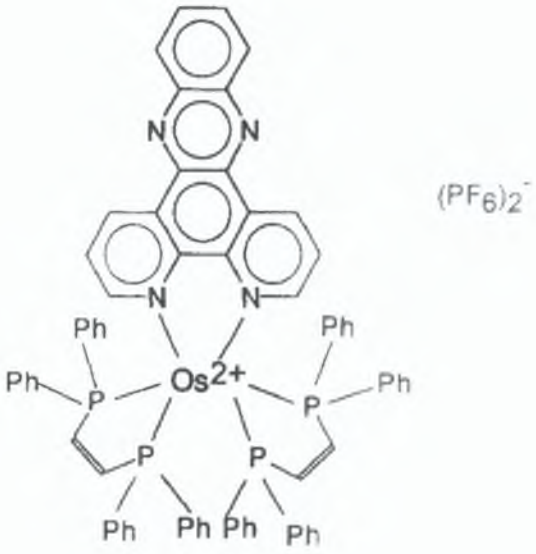

Figure 1.31. Structure of $[Os(dppz)(dppe)_2](PF_6)_2$. From Reference (107)

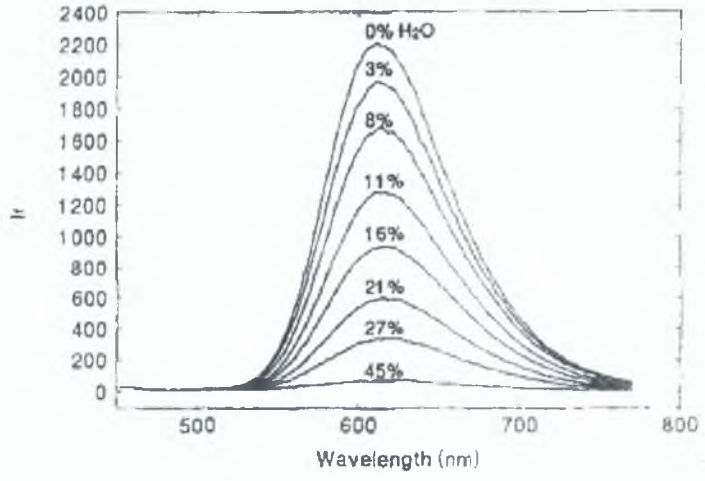

Figure 1.32. Water-dependent emission spectra of 1.1×10^{-5} M $\{Os(dppz)(dppe)_2](PF_6)_2$ in acetone with various amount of water. From Reference (107)

To describe the likely future developments in the area of fluorescence quenching, it is important to outline the main photoinduced events that can occur in redox active systems and how these photochemical processes may be influenced by the presence of solid state and polymeric materials. Even though these materials tend to exhibit poorly defined primary structures their secondary structure is strongly influenced by external factors

such as photexcitation, ionic strength etc The possibility of controlling their secondary structure to achieve a specific function is one of the most attractive features of these materials

1 11 1 Excited State processes

Photoexcitation of a ground state molecule leads to the formation of an excited state species whose lifetime will depend on the efficiency with which this species can dissipate its excess energy The most common radiative decay pathways are fluorescence and phosphorescence, which are distinguished on the basis of whether the transition involves a change in spin multiplicity In fluorescence, the spin is conserved and this allowed process tends to be short lived with lifetimes typically between 10^{12} and 10^{6} s In phosphorescence, spin is not conserved and yields relatively weak emissions that tend to be strongly Stokes shifted with respect to the associated exciting absorbance Phosphorescence, as a result of its forbidden nature, tends to be long-lived, 10^{-6} to 1 s

The fluorescence lifetime and quantum yield are perhaps the most important characteristics of a fluorophore The quantum yield is the number of emitted photons relative to the number of absorbed photons The lifetime determines the time available for the fluorophore to interact with or diffuse in its environment by way of emission The Jabłonski diagram, Figure 1 33, represents best the meaning of the quantum yield and lifetime In this diagram the individual relaxation processes leading to the relaxed S_1 state are not illustrated but the processes responsible for return to the ground state

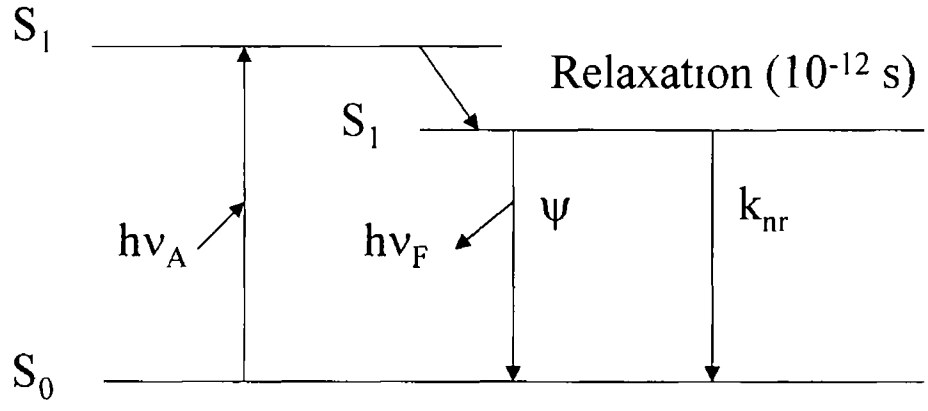

Figure 1 33 A simplified Jabłonski diagram From Reference (110)

The fluorescence quantum yield is the ratio of the number of photons emitted to the absorbed The processes governed by the rate constants Ψ and k_{nr} both depopulate the excited state The fraction of fluorophores which decay through emission, and hence the quantum yield is given by

$$Q = \frac{\Psi}{\Psi + k_{nr}} \tag{24}$$

The quantum yield can be close to unity if the radiationless decay rate is much smaller than the rate of radiative decay, that is, $k_{nr} << \Psi$ The energy yield of fluorescence is always less than unity because of Stokes' loss and all possible nonradiative decay processes can be represented with the single rate constant k_{nr}

The lifetime of the excited state is defined by the average time the molecule spends in the excited prior to return to the ground state Generally, fluorescence lifetimes are near 10 ns For the flurophore illustrated in Figure 34 the lifetime is

$$\tau = \frac{1}{\Psi + k_{nr}} \tag{25}$$

where Ψ is the emissive rate of the fluorophore and k_{nr} is the rate of nonradiative decay The lifetime of the fluorophore in the absence of nonradiative processes is called the intrinsic or natural lifetime and is given by

$$\tau_n = 1/\Psi \tag{26}$$

The natural lifetime τ_n can be calculated from the measured lifetime (τ) and quantum yield

$$\tau_n = \tau/Q \tag{27}$$

The quantum yield and the lifetime can be modified by factors, which affect either of the rate constants (Ψ or k_{nr}) For example, a molecule may be nonfluorescent as a result of a fast rate of internal conversion or a slow rate of emission

1 11 2 Quenching Process

Fluorescence quenching is a process, which decreases the intensity of the fluorescence emission Quenching may occur by several mechanisms

- collisional or dynamic quenching
- static quenching
- quenching by energy transfer
- charge transfer reactions

In the case of redox active material such as $Os(bpy)_3^{2+}$, quenchers including $Co(CN)_6^{3}$ and $Co(NH_3)_5Br^{2+}$ have been reported [108 109] In this section dynamic quenching resulting from collisional encounters between the fluorophore and quencher is mainly discussed

Both dynamic and static quenching require molecular contact between the fluorophore and quencher In the case of collisional quenching, the quencher must diffuse to the fluorophore during the lifetime of the excited state Upon contact, the flurophore returns to the ground state, without emission of a photon In the case of static quenching, a complex is formed between the fluorophore and the quencher, and this complex is nonfluoroescent For either static or dynamic quenching to occur, the fluorophore and quencher must be in contact

Depending upon the sample under investigation, it is frequently necessary to remove dissolved oxygen to obtain reliable measurements of the intrinsic fluorescence yields or lifetimes The mechanism by which oxygen quenches fluorescence occurs by the paramagnetic oxygen causing the fluorophore to undergo intersystem crossing to the triplet state Since emission from the triplet state is slow, the triplet emission is highly quenched by processes of this kind

Collisional quenching of fluorescence is the dependence of the emission intensity, F on quencher concentation [Q] and is given by the Stern-Volmer equation

$$F_o/F = \tau_o/\tau = 1 + k_q \tau_o [Q] \qquad (28)$$

where τ and τ_0 is the lifetime in the presence and absence of quencher, respectively, k_q is the bimolecular rate constant for the dynamic reaction of the quencher with the fluorophore The product of $k_q\tau_o$ is referred to as the Stern-Volmer constant or K_{SV} If the quenching is known to be dynamic, the Stern-Volmer constant is represented by K_D or dynamic constant Observation of a linear Stern-Volmer plot does not prove that collisional quenching of fluorescence has occurred as static quenching also results in linear Stern-Volmer plots Static and dynamic quenching can be distinguished by their differing dependence on temperature and viscosity, or preferably by lifetime measurements Higher temperatures result m faster diffusion and hence larger amounts of collisional quenching Higher temperatures will typically result in the dissociation of weakly bound complexes, and hence smaller amounts of static quenching Figure 1 34 illustrates the comparison of dynamic and static quenching

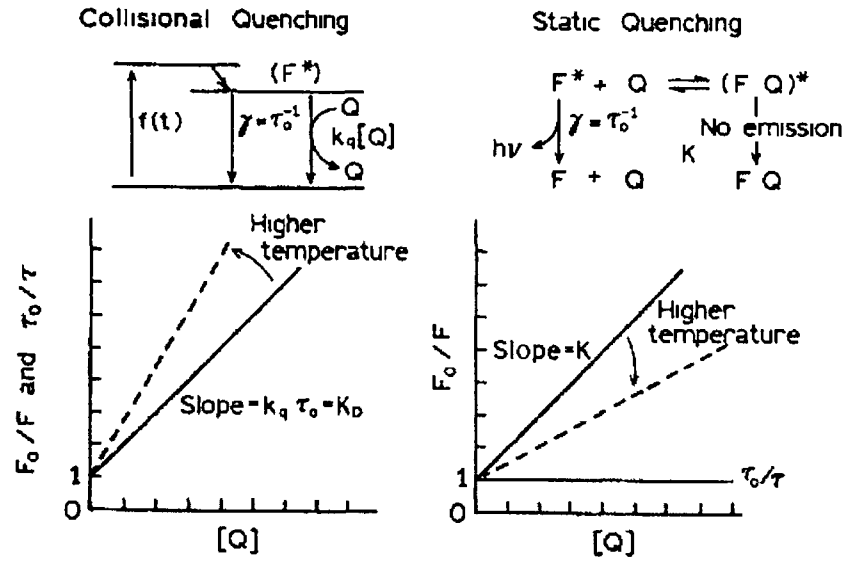

Figure 1 34 Comparison of dynamic (collisional) and static quenching From Reference (110)

The bimolecular quenching constant (k_q) reflects the efficiency of quenching or the accessibility of the fluorophores to the quencher Diffusion-controlled quenching typically results in values of k_q near 1 x 10^{10} $M^{-1}s^{-1}$ Smaller values of k_q can result from steric shielding of the fluorophore, and larger values of k_q usually indicate some type of binding interaction The significance of the bimolecular quenching constant can be understood in terms of the frequency of collisions between freely diffusing molecules

The measurement of fluorescence lifetimes is the most definitive method to distinguish static and dynamic quenching Static quenching removes a fraction of the fluorophores from the observation The complexed fluorophores are nonfluorescent, and the only observed fluorescence is from the uncomplexed fluorophores The uncomplexed fraction is unperturbed, and hence the lifetime is τ_0 Therefore, for static quenching $\tau_0/\tau = 1$ (Figure 1 34 above) In contrast, for dynamic quenching, $\tau_0/\tau = F_0/F$ Static and dynamic quenching can often be distinguished on the basis of other considerations Higher temperatures result in larger diffusion coefficients and the bimolecular quenching constants are expected to increase with increasing temperature In contrast, increased temperature is likely to result in decreased stability of complexes, and thus lower values

of the steric quenching constants One additional method to distinguish static and dynamic quenching is by careful examination of the absorption spectra of the fluorophore Collisional quenching only affects the excited states of the fluorophores, and thus no changes in the absorption spectra are expected In contrast, ground-state complex formation will frequently result in perturbation of the absorption spectra of the fluorophore

1 11 3 Combined Dynamic and Static Quenching

In many instances the fluorophore can be quenched both by collisions and by complex formation with the same quencher Figure 1 35 shows the characteristic feature of the Stern-Volmer plots in such circumstances is an upward curvature, concave towards the *y*-axis Hence,

$$\frac{F_0}{F} = (1 + K_D[Q])(1 + K_S[Q]) \tag{29}$$

This modified form of the Stern-Volmer equation is second-order in [Q], which accounts for the upward curvature observed when both static and dynamic quenching occur for the same fluorophore

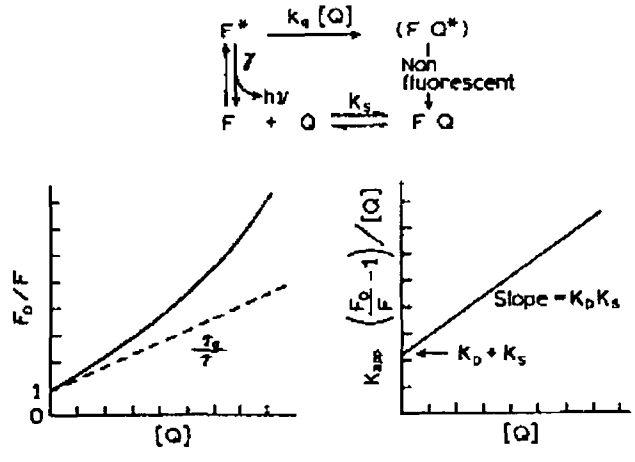

Figure 1 35 Dynamic and static quenching of the same population of fluorophores From Reference (110)

1 11 4 Quenching of $[Os(bpy)_3]^{2+}$

One of the earliest reports on the quenching effects of $Os(bpy)_3^{2+}$ by Cu^{2+} have detailed that the quenching proceeds by oxidation i e electron transfer of the complex rather than the energy transfer [111] It was stated that static quenching was not present when $Os(bpy)_3^{2+}$ was quenched with $Fe(CN)_6^{3}$ [112] Though the Stern-Volmer plots were not presented, the authors ascertain that a non-linear Stern-Volmer plot was obtained from steady state emission intensity measurements but a linear plot was obtained with lifetime measurements with a bimolecular quenching constant, k_q, of 9 4 x 10^9 $M^{-1}s^{-1}$ reported However, according to Figure 1 34 linear dependences of intensity / lifetime versus quencher concentration and are expected for dynamic quenching and a linear dependence of lifetime with quencher concentration static quenching with lifetime measurements being non dependent on quencher concentration It is seems likely that combined dynamic and static quenching are present as the Stern-Volmer plots described for the quenching effect of $Fe(CN)_6^{3}$ on $Os(bpy)_3^{2+}$ are analogous to the Stern-Volmer plots of Figure 1 35

There has been considerable interest in elucidating the mechanism of electron transfer in biological molecules [113] To gain more insight into the nature of the protein/complex interactions, excited $Os(bpy)_3^{2+}$ was used as an oxidant and the transfer rate was determined by studying the luminescence quenching of the complex with cytochrome c (Cyt-c) [114] The bimolecular quenching constant was reported as 5 4 x 10^9 $M^{-1}s^{-1}$

1 12 Voltammetry and Microelectrodes

For solid deposits and polymeric materials immobilised on electrode surfaces, the rate of charge transport influences the voltammetric response In cyclic voltammetry, a triangular wave potential is applied to the cell so that the working electrode potential is swept linearly through the voltammetric wave and the back again On the forward scan, the current response in just the linear potential sweep voltammogram as R (reduced species) is oxidised to O (oxidised species) On the reverse scan, the O molecules near the electrode are rereduced to R and a cathodic peak, E_{pc}, results and this is represented in Figure 1 36

If the initial scan is carried far beyond the anodic peak, E_{pa} so that the diffusion layer is still very thick and the anodic current has decayed nearly to zero, then the concentration of O at the electrode surface is equal to C_R^* Thus, the amount of O available for reduction on the reverse scan is the same as the R available on the forward scan and the current peak has the same shape and magnitude as on the forward scan, but reflected at E = $E_{½}$ and changed in sign The anodic-to-cathodic peak current is exactly 1 for a reversible process uncomplicated by capacitive current and iR drop in solution The anodic peak occurs 28 5 / n mV more positive than the half wave potential and the cathodic peak is 28 5 / n mV more negative (at 25 °C) Therefore, $E_{½} = ½(E_{Pc} + E_{Pa})$ and the anodic and cathodic peaks are separated 57 0 / n mV A peak separation of 57 0/n mV is often used as a criterion for Nernstian behaviour

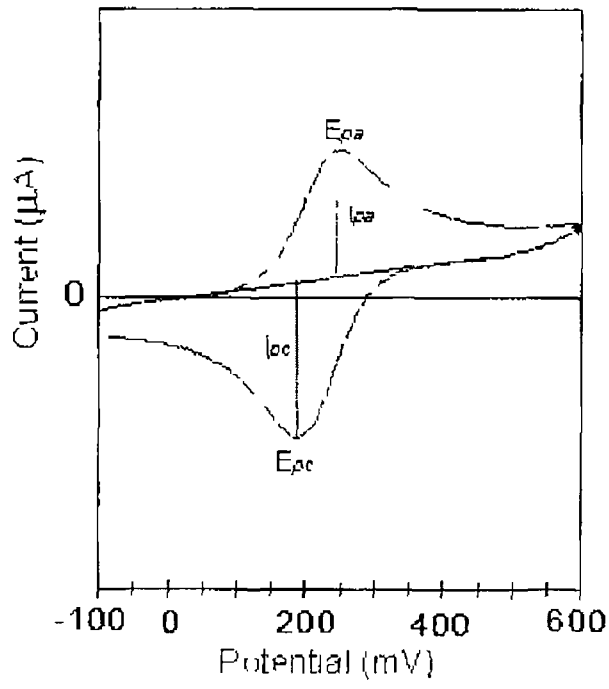

Figure 1 36 Cyclic Voltammogram

Microelectrodes have small currents, steady-state responses, and short response times and it is the reduced currents that are important for their successful application In a voltammetric experiment microelectrodes can often eliminate the problem of iR drop as decreasing the electrode area decreases the size of the current Several different types of microelectrode exist including disc, cylinders, arrays, bands and rings Microdisk electrodes predominate because of their ease of construction, and because the sensing surface of the electrode can be mechanically polished

Charging Currents

When an electrode comes into contact with an electrolytic solution, a double layer is formed at the interface, in which the charge present on the metal electrode is compensated for by a layer of oppositely charged ions in solution, Figure 1 37

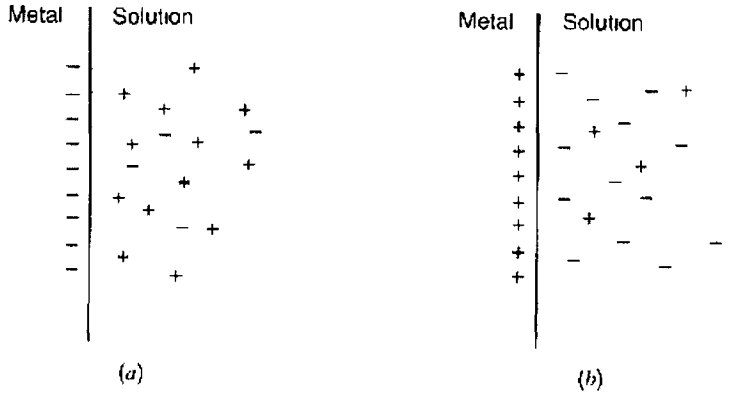

Figure 1 37 The metal-solution interface as a capacitor with a charge on the metal, q^M, (a) negative and (b) positive From Reference (69)

This electrochemical double layer behaves like an electrolytic capacitor and when the applied potential is changed, a current flows to charge the double layer capacitance However, unlike real capacitors, whose capacitances are independent of the voltage across them, the double layer capacitance is often a function of potential The charging process complicates the electrochemical measurement, as the interface does not attain the applied potential until the charging process is complete This charging current adds to the Faradaic response and distorts the experimental data Since the charging current may be similar or even greater magnitude than the Faradaic current under certain conditions, e g at short times or with low concentrations of electroactive species, it is desirable to increase the ratio of the Faradaic to charging current and reduce this distortion Microelectrodes facilitate this discrimination against charging currents

Considering a spherical microelectrode under pseudo – steady state conditions, the diffusion controlled or Faradaic current, i_f is proportional to the radius of the sphere, r_o, whereas the charging current, i_c, is an extensive property and is proportional to the area Hence,

$$\frac{i_f}{i_c} \propto \frac{r_0}{r_0^2} \propto \frac{1}{r_0} \tag{30}$$

Equation 30 shows that the ratio (i_f / i_c) improves as the electrode size decreases whichexplains how microelectrodes discriminate against charging currents The same conclusion can be drawn for microdisks

RC Cell Time Constants

The current required to charge the double layer of capacitance C, must flow through a resistance R corresponding to the total cell resistance Electrochemical measurements have a lower timescale limit that is imposed by the RC cell time constant, i e , the product of the solution resistance, R, and the double layer capacitance, C, of the working electrode The RC cell time constant dictates the lower timescale limit for every electrochemical measurement and determines the shortest time at which electrochemical measurements are not distorted Electrochemical data can only be extracted at timescales that are longer than the cell time constant, typically five to ten times the RC time constant Obviously the RC cell time constant is of fundamental importance when measuring fast electrochemical processes

The solution resistance for a disc-shaped microelectrode is inversely proportional to the electrode radius,

$$R = \frac{1}{4\kappa r} \tag{31}$$

where κ is the conductivity of the solution and r is the radius of the microdisk electrode Accordingly, R increases as the electrode radius decreases The double layer capacitance for a disc-shaped microelectrode is proportional to the area of the electrode surface and is given by

$$C = \pi r^2 C_O \tag{32}$$

where C_O is the specific double layer capacitance of the electrode The time constant for this charging process is given by,

$$RC = \frac{\pi r C_O}{4\kappa} \tag{33}$$

Decreasing the resistance of the solution (achieved by increasing its concentration), through which the Faradaic and charging currents must flow, will decrease the cell time constant The smaller RC cell time constants of microelectrodes mean that they respond more rapidly to changes in the applied potential compared to their macroscopic counterparts This ability to respond to changes in the applied potential at short timescales makes microelectrodes very attractive for investigating high-speed electron-transfer reactions

iR Drop

When faradaic and charging currents flow through a cell, they generate a potential that acts to weaken the applied by an amount iR, where i is the total current and R is the resistance This is an undesirable process that leads to distorted voltammetric responses Due to their smaller size, microelectrodes exhibit higher resistances than macorelectrodes but because the current observed at microelectrodes are typically of smaller magnitude, they often eliminate ohmic drop effects For microelectrodes, the iR drop is usually of the order of 5 to 10 mV Under these circumstances, distorted current responses and shifted peak potentials would be observed in the cyclic voltammetry At short times, the dominant mass transport mechanism is linear diffusion and the current decreases with decreasing electrode area Since the resistance increases with decreasing electrode radius rather than electrode area, the product iR decreases with decreasing electrode in short timescales experiments In contrast, at long experimental timescales the Faradaic current depends directly on the radius making the product iR independent of the electrode radius

1 13 Conclusion

Charge transport studies have lead to some interesting aspects of solids, polymers and nanoparticle composite materials being discussed in this chapter Mass transport of counterions into materials has major significance particularly in the area of 'break in' 'Break in' has been found to more significant in solids than polymers This is expected as solids contain less solvent than polymers and counterion ingress/egress during the electrochemical cycling of solids also involves solvent uptake 'Break in' effect has been identified as voltammetric distortions in either the anidic/cathiodic region in the initial stages of cycling The rate at which counterions diffuse in solid state and polymeric materials indicates how quickly and efficiently the redox centre is oxidised/reduced It has been shown that several factors can influence the homogeneous charge transport including electron self exchange between the redox centres, by counterion diffusion or by chain movement in the case of polymeric species

The electro-inserted counterion can affect the voltammetric wave shape and size depending how it interacts with the redox centre Evidence of nucleation and crystal growth induced by counterion movement has been identified in solid state materials through scanning electron microscopy and by particular features in voltammetry Heterogeneous charge transfer investigations in both solid and polymeric materials have been limited which is surprising considering the information it can give regarding electrode-reactant separation, the chemical composition, and the effective dielectric constant of the film

Some insight has been presented to the effects of introducing metal nanoparticles to polymeric materials The electrochemistry regarding the homogenous and heterogeneous studies of these composites have not been reported in the literature thus far and exploring these issues in Chapter 4 have been very inciteful Through conductivity investigations, nanoparticles have been shown to enhance the electron transfer pathways of polymeric materials Redox active materials have the possibility to be applied in the areas of optical and molecular device research Performing photoinduced and quenching experiments allows for a better understanding of the type of electron transfer quenching dynamics

Stemming from this literature review, the experimental chapters of this thesis will make use of, and investigate the charge transport effects presented here Chapter 2 details the synthesis and characterisation of the redox-active solid state, metallopolymer and nanoparticle metallopolymer materials In Chapter 3, the charge transport dynamics of $[Os(OMe\text{-}bpy)_3]^{2+}$ is presented detailing enhanced electron transfer pathways leading to increased charge transport Chapter 4 details the investigation on the effect of introducing a gold nanoparticle core to the metallopolymer $[Os(bpy)_2(PVP)_{10}Cl]^+$ and how an enhance electron network can increase charge transport Finally, in Chapter 5 the results of the experiments which probe the fluorescence quenching of $[Os(bpy)_3]^{2+}$

1 14 References

(1) Moulzolf, S C , LeGore, L J , Lad, R J *Thin Solid Films*, **2001**, 400, 56

(2) Inoue, M , Cruz-Vazquez, C , Inoue, M B *Syn Metals*, **1993**, 57, 3748

(3) Shubba Reddy, Ch V , Sharma, A K , Narasimha Rao, V V R *J Power Sources*, **2003**, 114, 338

(4) Sun Ryu, K , Man Kim, K , Kang, S-G , Joong Lee, G , Joo, J , HoChang, S *Syn Metals*, **2000**, 110, 213

(5) Nešpůrek, S , Toman, P , Sworakowski, J , Lipinski, J *Current Applied Physics*, **2002**, 2, 299

(6) Kaneko, M *Prog Polymer Science*, **2001**, 26, 1101

(7) Bantikassegn, W , Darretun, P , Inganas, O , Saleneck, W R *Syn Metals*, **1993**, 55, 36

(8) Murray, R W *Acc Chem Res* , **1980**, 13, 135

(9) Murray, R W *Electroanal Chem* , **1984**, 13, 191

(10) Scholz, F, Nitchke, L, Henrion, G *Electroanalysis*, **1990**, 2, 85

(11) Scholz, F, Lange, B *T Anal Chem* **1992**, 11, 359

(12) De Guzman, R N , Shen, Y-F , Shaw, B R , Suib, S L , O'Young, C-L *Chem Mater* , **1993**, 5, 1395

(13) Abruña, H D *Coord Chem Rev* , **1988**, 86, 135

(14) Kaneko, M , Wohrle, D *Adv Polym Sci* , **1988**, 84, 141

(15) Nowak, R J , Mark, Jr , H B , MacDiarmid, A G , Weber, D *J Chem Soc Comm* , **1977**, 9

(16) Voulgaropoulos, A N , Nowak, R J , Kutner, W , Mark, Jr , H B *J Chem Soc Chem Comm* , **1978**, 244

(17) Efimov, O N , Belov, D G , Kozub, G I , Tkachenko, L I , Krinichnaya, L P , Petrova, G N *Syn Metals*, **1996**, 79 193

(18) Dautartas, M F , Evans, J F *J Electroanal Chem* , **1980**, 109, 301

(19) Balzani, V , Juris, A , Venturi, M *Chem Rev* **1996**, 96, 759

(20) Chen, S-M , Peng, K-T *J Electroanal Chem* , **2003**, 547, 179

(21) Bildstein, B *Coord Chem Rev* , **2000**, 206-207, 369

(22) *Methods in Enzymology*, **1970**, 19, Perkman, G E , Corand, C , (Eds), Academic Press

(23) Marken, F , Leslie, W M , Compton, R G , Moloney, M G , Sanders, E , Davies, S G , Bull, S D *J Electroanal Chem* , **1997**, 424, 25

(24) Bond, A M , Lamprecht, A , Tedesco, V , Marken, F *Inorg Chim Acta* , **1999**, 291, 21

(25) Forster, R J , Keyes, T E , Bond, A M *J Phys Chem B*, **2000**, 104, 6389

(26) Karimi, H , Chambers, J Q , *J Electroanal Chem* , **1987**, 217, 313

(27) Majda, M , Faulkner, L R *J Electroanal Chem* , **1984**, 169, 77

(28) Yazuzawa, M , Hashimoto, M , Fujii, S , Kunugi, A , Nakaya, T *Sensors and Actuators B Chemical*, **2000**, 65, 241

(29) Durstock, M F , Taylor, B , Spry, R J , Chiang, L , Reulbach, S , Heitfeld, K , Baur, J W *Syn Metals*, **2001**, 116, 373

(30) Peerce, P J , Bard, A J *J Electroanal Chem* , **1980**, 114, 89

(31) Clarke, A P , Vos, J G , Hillman, A R , Glidle, A *J Electroanal Chem* , **1995**, 389, 129

(32) Chiang, C K , Park, Y W , Heeger, A J , Shirakawa, H , Louis, E J , MacDiarmid, A J *Chem Phys Lett* , **1977**, 39, 1098

(33) Zhang, M Q , Rong, M Z , Yu, S L , Wetzel, B , Friedrich, K *Wear*, **2002**, 253, 1086

(34) Losche, M , Smitt, J , Decher, G , Bouwman, W G , Kjaer, K , *Macromolecules*, **1998**, 31, 8893

(35) Bond, A M , Cooper, J B , Marken, F , Way, D M *J Electroanal Chem* , **1995**, 396, 407

(36) Bond, A M , Scholz, F *Langmuir*, **1991**, 7, 3197

(37) Dostal A , Schroder, U , Scholz, F *Inorg Chem* , **1995**, 34, 1711

(38) Kelly, A J , Ohsaka, T , Oyama, N , Forster, R J , Vos, J G *J Electroanal Chem* , **1990**, 287, 185

(39) Kelly, D M , Vos, J G , Hillman, A R *J Mater Chem* , **1997**, 7, 913

(40) Varineau, P T , Buttry, D A *J Phys Chem* **1987**, 91, 1292

(41) Clarke, A P , Vos, J G , Glidle, A , Hillman, A R *J Chem Soc Faraday Trans* , **1993**, 89, 1695

(42) Aoki, A , Rajagopalan, R , Heller, A *J Phys Chem* **1995**, 99, 5102

(43) Sun, L , Jiao, K , Weber, S G *J Phys Chem B*, **1998**, 102, 1945

(44) Blauch, D N , Saveant, J-M *J Phys Chem* **1993**, 97, 6444

(45) Forster, R J , Vos, J G *Langmuir*, **1994**, 10, 4330

(46) Keyes, T E , Forster, R J , Bond, A M , Miao, W *J Am Chem Soc* , **2001**, 123, 2877

(47) Dahms, H *J Phys Chem* **1968**, 72, 362

(48) Ruff, I , Friedrich, V J , Demeter, K , Csillag, K *J Phys Chem* **1971**, 75, 3303

(49) Wang, Y N , Zhang, X D , Liu, Y , Zhang, Q Y *Acta Chimica Sinica*, **1999**, 57, 1114

(50) Wuttke, D S , Bjerrum, M J , Winkler, J, R , Gray, H B *Science*, **1992**, 256, 1007

(51) Forster, R J , Keyes, T E *Phys Chem Chem Phys* **2001**, 7, 1336

(52) Chan, M S , Wahl, A C *J Phys Chem* , **1978**, 82, 2542

(53) Forster, R J , Keyes, T E , Majda, M *J Phys Chem B* **2000**, 104, 4425

(54) Lee, W -Y , Majda, M , Brezesmski, G , Wittek, M , Mobius, *J Phys Chem B* **1999**, 103, 6950

(55) Bak, T , Nowotry, J , Rekas, M , Sorrell, C C *Solid State Ionics*, **2002**, 823, 152

(56) Majda, M and Murray, R W (eds), Molecular Design of Electrode Surfaces, Wiley, New York, 1992, p 159

(57) Forster, R J , Vos, J G *J Electrochem Soc* , **1992**, 139, 1503

(58) Chidsey, C E D *Science,* **1986**, 231, 25

(59) Marken, F , Webster, R D , Bull, S D , Davies, S G *J Electroanal Chem* , **1997**, 437, 209

(60) Bond, A M , Fletcher, S , Marken, F , Shaw, S J , Symons, P G *J Chem Soc , Faraday Trans* , **1996**, **92**, 3925

(61) Jiang, J , Kucarnak, A *Electrochim Acta*, **2001**, 46, 1223

(62) Bond, A M , Fletcher, S , Symons, P G *Analyst*, **1998**, 123, 1891

(63) Suarez, M F , Marken, F , Compton, R G , Bond, A M Miao, W , Raston, C L *J Phys Chem B* **1999**, 103, 5637

(64) Jiang, J , Kucarnak, A *Electrochimica Acta*, **2001**, 46, 1223

(65) Oh, S-M , Faulkner, L R *J Am Chem Soc* **1989**, 111, 5613

(66) Kelly, A J , Oyama, N *J Phys Chem* , **1991**, 95, 9579

(67) Mathias, M F , Haas, O *J Phys Chem* **1993**, 97, 9217

(68) Kulesza, P J , Faulkner, L R *J Am Chem Soc* **1993**, 115, 11878

(69) Bard, A J , Faulkner, L R Electrochemical Methods Fundamentals and Applications, Wiley, New York, 1980

(70) Interfacial Supramolecular Assemblies, **2003**, Johannes G Vos, Robert J Forster, Tia E Keyes, Ed Wiley & Sons, LTD

(71) Friedrich, A , Hefele, H , Mickler, W , Monner, A , Uhlemann, E , Scholz, F *Electroanal* , **1998**, 10, 244

(72) Downard, A J , Bond, A M , Hanton, L R , Heath, G A *Inorg Chem* **1995**, 34, 6387

(73) Creager, S E , Rowe, G K *Anal Chim Acta*, **1991**, 246, 233

(74) Saxena, V , Malhotra, B D *Current Applied Physics*, **2003**, 3, 293

(75) Antolini, E , Passos, R R , Ticianelli, E A *Electrochim Acta*, **2002**, 48, 263

(76) Fukumi, K , Chayahara, A , Kadono, K , Sakaguchi, T , Horino, Y , Miya, M , Fujii, K , Hayakawa, J , Satou, M *J App Physics*, **1994**, 75, 3075

(77) Bethell, D , Brust, M , Schiffrin, D J , Kiely, C *J Electroanal Chem* **1996**, 409, 137

(78) Brust, M , Bethell, D , Kiely, C J , Schiffrin, D J *Langmuir*, **1998**, 14, 5425

(79) Pickup, P G , Murray, R W *J Am Chem Soc* , **1983**, 105, 4510

(80) Mamunya, Ye P , Davydenko, V V , Pissis, P , Lebedev, E V *Eur Poly Jour* **2002**, 38, 1887

(81) Zhang, Z , Wan, M *Syn Metals*, **2003**, 132, 205

(82) Zhang, M Q , Xu, J R , Zeng, H M , Huo, Q , Zhang, Z Z , Yun, F C , Friedrich, K *J Mat Science*, **1995**, 30, 4226

(83) Stauffer D Introduction to percolation theory London Taylor and Francis, 1985

(84) Lux, F *J Mat Science* , **1993**, 28, 285

(85) Mamunya, E P , Davydenko, V V , Lebedev, E V *Polym Compos*, **1995**, 16, 318

(86) Mamunya, E P , Davydenko, V V , Lebedev, E V , Konpoz, *Polym Mater* **1991**, 50, 37

(87) Wu, J , McLachlan, D S *Phys Rev B* **1997**, 56, 1236

(88) Mehbod, M , Wyder, P , Deltour, R , Pierre, C , Geuskens, G *Phys Rev B*, **1987**, 36, 7627

(89) Carmona, F , Mouney, C *J Mat Science*, **1992**, 27, 1322

(90) Bonet, F , Delmas, V , Grugeon, S , Herrara Urbina, R , Silvert, P-Y , Tekaia-Elhissen, K *Nanostruc Mat* , **1999**, 11, 1277

(91) Zagorskii, V V , Ivashko, S V , Bochenkov, V E , Sergeev, G B *Nanostruc Mat* , **1999**, 12, 863

(92) Pomogailo, A D *NanoStruc Mat* , **1999**, 12, 291

(93) Peng, Z , Wang, E , Dong, S *Electrochem Comm* , **2002**, 4, 210

(94) Akamatsu, K , Deki, S *NanoStruc Mat* , **1997**, 8, 1121

(95) Pastoriza-Santos, I , Liz-Marzan, L M *Langmuir*, **2002**, 18, 2888

(96) Chen, D-H , Huang, Y-W *J Colloids and Interfaces Science*, **2002**, 255, 299

(97) Walker, C H , St John, J V , Wisian-Neilson, P *J Am Chem Soc* , **2001**, 123, 3846

(98) Bi, H , Jiang, X , Yang, C , Hong, *J Mat Lett*

(99) Mandal, T K , Fleming, M S , Walt, D R *Nano Letters*, **2002**, 2, 3

(100) Zamborini, F P , Gross, S M , Murray, R W *Langmuir*, **2001**, 17, 481

(101) Miles, D T , Murray, R W *Anal Chem* **2001**, 73, 921

(102) Musick, M D , Peña, D J , Botsko, S J , McEvoy, T M , Richardson, J N , Natan, M J *Langmuir*, **1999**, 15, 844

(103) Alivistos, A P *Endeavour*, **1997**, 21, 56

(104) Hostetler, M J , Wingate, J E , Zhong, C-J , Harris, J E , Vachet, R W , Clark, M R , Londono, J D , Green, S J , Stokes, J J , Wignall, G D , Glish, G L , Porter, M D , Evans, N D , Murray, R W *Langmuir*, **1998**, 14, 17

(105) Eftink, M R , Ghiron, C *Anal Biochem* **1981**, 114, 199

(106) Eftink, M R *Biophysical and Biochemical Aspects of Fluorescence Spectroscopy*, **1991**, T G Dewey (ed), Plenum Press, New York, pp 1 - 41

(107) Chang, Q , Murtaza, Z , Lakowicz, J R , Rao, G *Anal Chim Acta* , **1997**, 350, 97

(108) Juris, A , Manfrin, M F , Maestri, M , Serpone, N *Inorg Chem* , **1978**, 17, 2258

(109) Finkenberg, E , Fischer, P , Huang, S - M Y , Gaffney, H D *J Phys Chem* **1978**, 82, 526

(110) Principles of Fluorescence Spectroscopy, Second Edition, Joseph R Lakowicz

(111) Hoselton, M A , Lin, C – T , Schwarz, H A , Sutin, N *J Am Chem Soc* **1978**, 100, 2383

(112) Juris, A , Manfrin, M F , Maestri, M , Serpone, N *Inorg Chem* **1978**, 17, 2258

(113) Sisley, M J , Segal, M G , Stanley, C S , Adzamli, I K , Sykes, A G *J Am Chem Soc* , **1983**, 105, 225

(114) Cho, K C , Che, C M , Cheng, F C , Choy, C L *J Am Chem Soc* , **1984**, 106, 6843

Chapter 2

Synthesis and Characterisation of Osmium Polypyridyl and Nanoparticle Complexes

2 1 Introduction

Osmium polypyridyl complexes have many attractive properties such as chemical stability in a range of oxidation states and fast electron transfer dynamics [1 2] In this work, two osmium polypyridyl complexes were characterised, $[Os(OMe\text{-}bpy)_3)](PF_6)_2$ and $[Os(bpy)_2(PVP)_{10}Cl]Cl$ $[Os(OMe\text{-}bpy)_3)](PF_6)_2$, was produced elsewhere but the chromatographic and spectroscopic studies were undertaken during this research (OMe-bpy is 4,4′-dimethoxy and 2-2′-dipyridyl) The electrochemical properties of this compound are considered as solid deposits in Chapter 3 In contrast to solution state investigations, solid state studies have only been undertaken relatively recently [3 4] This situation is surprising given the pivotal roles that solid-state redox active materials play in devices ranging from optical detectors,[5] batteries,[6] redox supercapacitors and sensors [7 8 9]

The metallopolymer, $[Os(bpy)(PVP)_{10}Cl]Cl$, where PVP is poly(4-vinylpyridine) was synthesised and characterised spectroscopically and voltammetrically The advantages of preparing metallopolymers through covalent attachment to the metal centre have been discussed previously and include synthetic flexibility and a high level of structural control [10] This field has achieved a significant level of sophistication in terms of polymer structural characterisation as well as their rational design for specific functions, e g molecular electronics [11]

Another area that exploits the unique properties of polymers is polymer-protected nanoparticles In this chapter $[Os(bpy)_2(PVP)_{10}Cl]^+$ - nanoparticle assemblies have been formed through chemical reduction and their electrochemical properties probed in Chapter 4 Synthetic polymers have lead to considerable revelations of the detailed mechanism of stabilisation of colloidal dispersions Metal nanoparticles encompass such properties as the ability to be chemically manipulated, including their particle size, molecular arrangement and surface activity [12 13] These protected nanoparticles open up the possibility of size-function studies which exploit the chemical properties of these structures

Another approach explored where nanoparticles could act as charge compensators was attempted through the formation of citrate based nanoparticles metallopolymer composites An aqueous, citrate protected gold nanoparticle sol was synthesised and characterised using spectroscopy, cyclic voltammetry and microscopy Though aqueous based monolayer protected clusters have only been recently explored,[14 15] thiol Monolayer Protected Clusters (MPCs) have been extensively investigated since first reported by Brust et al in 1994 [16] The conditions for ligand place exchange reaction between the $[Os(bpy)(PVP)_{10}Cl]Cl$ and the citrate of the gold nanoparticles have been explored in Chapter 4

To show the application of these solid state and polymeric osmium polypyridyl complexes as optical devices, it is necessary to understand their photophysical properties Chapter 5 details the quenching properties of excited state Os^{2+} species by Os^{3+} using $[Os(bpy)_3](PF_6)_2$ as a model

2 2 Apparatus and Reagents

High Performance Liquid Chromatography

HPLC was performed using a Varian Star #1 Instrument Elution of components was detected using a UV detector at 280 nm Preparation of the compound involved dissolving 1-3 mg of the compound in 10 ml acetomtrile water, 80 20 v/v and 0 08 M $LiClO_4$ employed as an ion-pairing reagent An injection of 20 µl of 1 mM of the sample was made on to the column for a run time of 12 min A flow rate of 2 0 ml/min was utilised

Spectroscopy

The H^1 NMR spectroscopy was carried out using a Bruker 400 NMR spectrometer The sample for analysis was prepared in deuterated acetonitrile

UV-Vis Spectroscopy was performed using a Shimadzu UV-3100 diode array spectrometer Spectroscopic grade acetonitrile was used as the solvent for all complexes investigated Quartz cells of 1 cm path length were used and a slit width of 2 nm

IR Spectra were obtained using a Perkin Elmer System 2000 FT-IR with resolution of 4 cm^{-1} The sample for analysis was prepared as a KBr disk

Luminescent lifetimes and emission spectra were measured using the third harmonic (355 nm) of a Spectron Q-switched Nd-YAG laser for excitation Emission was detected in a right-angled configuration to the laser using an Oriel model IS520 gated intensified CCD coupled to an Oriel model MS125 spectrograph With suitable signal averaging, this configuration allows a complete emission spectrum (spectral range 250 nm) to be obtained within times as short as 10 ns The emission spectra were typically recorded using the average of twenty laser shots The gatewidth, i e , the exposure time of the CCD, was never more than 5% of the excited state lifetime The step size, i e , the time

between the acquisition of discrete spectra, was typically 5% of the excited state half-life

For shorter lived species of lifetimes < 10 ns, the excited state lifetime was determined using an Edinburgh Analytical Instruments Single Photon Counter in a T setting using J – ya monochromators The light source in this system is an nF 900 Nanosecond Flashlamp filled with nitrogen, with a profile of 1 ns The detector is a Single Photon Photomultiplier Detection system The program uses for the data correlation and manipulation is an F900 program The excitation wavelength was 337 nm and the lifetimes were collected and determined by analysing the emission decay at λ_{max}

Electrochemistry

For short timescale experiments (< 250 μs), that were designed to probe the cell resistance and the interfacial capacitance, a custom built programmable function generator-potentiostat was used [17] This instrument had a rise time of less than 10 ns and was used to apply potential steps of variable pulsewidth and amplitude directly to a two-electrode cell A large area Pt foil and an SSCE reference electrode were combined to form a counter electrode The current to voltage converter was based on a Comlinear CLC 203 AI operational amplifier with a 1500 Ω feedback resistance and a response time of less than 10 ns The chronoamperograms were recorded using a HP54201A digital oscilloscope in 64X time-average mode Cell time constants were extracted from the slope of ln i(t) vs t plots using software routines written in Microsoft EXCEL

Cyclic voltammetry was performed using a CH Instrument Model 660 Electrochemical Workstation and a conventional three-electrode cell The platinum working electrodes used in these experiments ranged in radii dimensions of 25 μm to 3 mm The working electrodes were polished successively with 1 0, 0 3 and 0 05 μm aqueous alumina slurries and sonicated in distilled water and rinsed with acetone after each polishing step After each mechanical polishing, electrochemical cleaning by cycling in 0 1 M H_2SO_4 was performed on the electrode Potentials were measured versus Ag/AgCl, or Ag wire The counter electrode was a 1 cm^2 platinum flag All electrochemical measurements

were carried out at 22 ± 3 ^{0}C The solvents utilised for solution phase cyclic voltammetry was HPLC grade acetonitrile All electrolyte solutions were thoroughly deoxygenated under a blanket of nitrogen for 15 minutes prior to measurement

Fabrication of platinum disk and cylinder microelectrodes

A method similar to that described by Wightman[18] was used in the construction of the microelectrodes The glass used to accommodate the electrodes was cut into lengths of 8 cm and soaked overnight in dilute nitric acid (HNO_3) Acid cleaning removes any dirt and grease, which may adhere to the inner surface of the glass After soaking, the glass was removed and washed copiously with Milli-Q water, acetone and finally rinsed with Milli-Q water before being dried in an oven

Copper wire of approximate length 4 cm was connected to a "hook up" wire by wrapping the hook up wire around the copper wire and soldering the two together The hook up wire, made from aluminium, was then bent in a zig-zag pattern in order to fit the internal diameter of the insulator Bending of the transition wire gives rigidity to the overall electrode and it reduces the risk of breakage while polishing For cylinder microelectrodes, the platinum micro wire of approximate length 4 cm and diameter 25 μm was carefully wound around the 'free' end of the hook up wire and soldered at the joint for electrical connection Shorter lengths of wire were used for the disk electrodes

The copper wire assembly for the cylinder micorelectrode was then placed into the glass length with 1 cm copper protruding from one open end and 2 cm of the platinum micro wire protruding out the other end A butane flame was used to seal the glass tip around the base of the platinum micro wire For the disk microelectrodes, 1 mm of the platinum microwire was left protruding from the glass tip after sealing with the butane flame The excess microwire was removed using emery paper followed by successive polishing with 5, 1, 0 3 and 0 05 μm alumina

A plastic cap was pierced so as to fit down over the protruding copper wire and to cover the open electrode The cap was sealed into place using a small volume of araldite epoxy resin Figure 1 depicts a schematic cross section through a platinum cylinder microelectrode

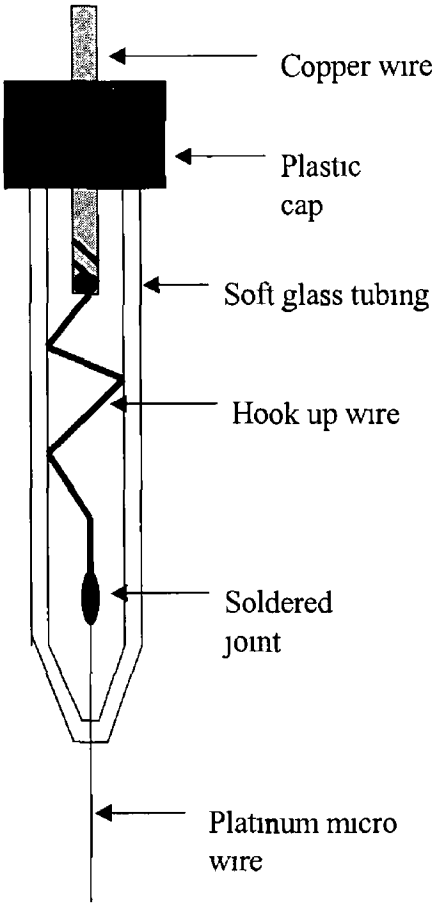

Figure 1 Cross section of the structure of a 25 μm platinum cylinder microelectrode

Electrode Modification

For solid state voltammetric measurements, two methods were used to transfer the solid onto the surface of the working electrode [19] In the first approach, the solid was transferred from a filter paper onto the surface of the working electrode by mechanical

abrasion This process caused some of the complex to adhere to the electrode surface as a random array of particles In the second approach that was used to achieve surface coverages greater than approximately 10^{-7} mol cm^{-2}, a drop of Milli-Q water was first added to the complex before transferring the material onto the electrode surface as a paste Prior to electrochemical measurements, the coating was allowed to dry Beyond minor differences in the initial scans, films prepared by both methods give indistinguishable voltammetric responses Films prepared using either approach show comparable stability toward dissolution After use, the electrode surface was renewed by polishing using aqueous slurry of 0 05 μm alumina

Electrochemical studies of the metallopolymer were performed using platinum cylinder and disk microelectrodes A known length of cylinder electrode was dipped in 1 5 M polymer ethanol solution to create a thick layer around the wire Flaming with a butane torch renewed the electrode wire and confirmed by electrochemical cycling in 0 1 M $HClO_4$ The polymer was also applied as a paste to the surface of a 25 μm disk platinum electrode by adding a drop of ethanol to the polymer The electrode surface was renewed by polishing using aqueous slurry of 0 05 μm alumina All electrochemical measurements were carried out in $HClO_4$ after the layers were left to dry Voltammetric responses of layers prepared by both methods showed minor differences

Electrical Conductivity

The specimens for measurements of electrical conductivity were prepared in the form of disks with 10 mm diameter and 1 mm thickness For high resistive samples (σ values less than 10^{-2} – 10^{-4}), the DC conductivity were measured using a Guideline Programmable Digital Teraohmmeter 6500A For more highly conducting samples, specimens in the form of plates were used and, in order to reduce the complications arising from the electrode-specimen contact resistance, the four-electrode method was used

Scanning Electron Microscopy

SEM was performed using a Hitachi S-3000N system A vacuum voltage of 20-30 kV was utilised For the solid state SEM investigations, films were formed on 3 mm radius carbon disks To probe counterion effects of the materials, the modified disks were electrochemically cycled and then the layers were copiously washed in electrolyte free Milli-Q water then dried in a vacuum dessicator for several hours Control experiments consisted of exposing the samples to electrolyte or Milli-Q water without electrochemical cycling

Transmission Electron Microscopy

TEM imaging of the gold nanoparticles was performed by Goran Karlsson at Uppsala University, Sweden and is greatly appreciated Transmission electron micrographs were taken with a JEOL-100 CX II transmission electron microscope in order to obtain the particle sizes, morphologies, and particle-size distributions of the gold nanoparticles Cryo-TEM was utilized for imaging the citrate protected nanoparticles as it enabled direct imaging of liquid specimens Preparation involved blotting 5 ml of the gold sol into a holey-carbon grid, which was subsequently immersed in liquid ethane (-183°C) In the microscope the images were recorded under cryogenic conditions The more traditional TEM procedure for solid state samples was carried out for the nanoparticle-polymer assemblies A drop of the colloid samples were placed on the carbon-coated copper grid and allowing solvent to evaporate The particle sizes of at least 200 individual particles were measured to obtain information about the size distribution

2 3 Synthesis of Osmium and Nanoparticle Complexes

2 3 1 $[Os(OMe\text{-}bpy)_3](PF_6)_2$

The complex $[Os(OMe\text{-}bpy)_3](PF_6)_2$, was prepared from $[Os(OMe\text{-}bpy)_2\ Cl_2]$ which was synthesized as described by Heller and co-workers [20] 208 mg (0 3 mmol) of $[Os(OMe\text{-}bpy)_2\ Cl_2]$ was placed in 40 cm^3 of methanol and refluxed for 10 minutes to ensure complete dissolution A solution of 65 mg (0 3 mmol) of 4,4′-dimethoxy, 2-2′-dipyridyl dissolved in 10 cm^3 of methanol was added, and the solution was refluxed for 15 hr The progress of the reaction was monitored using HPLC and cyclic voltammetry After the reaction was complete, the volume was reduced to 5 cm^3 by rotary evaporation Ammonium hexafluorophosphate (95+%, Aldrich) was then added, and the dark green / black product was collected by filtration and washed with diethylether The product was recrystallised from aqueous methanol to give dark green-black crystals, yield 295 mg, 88%

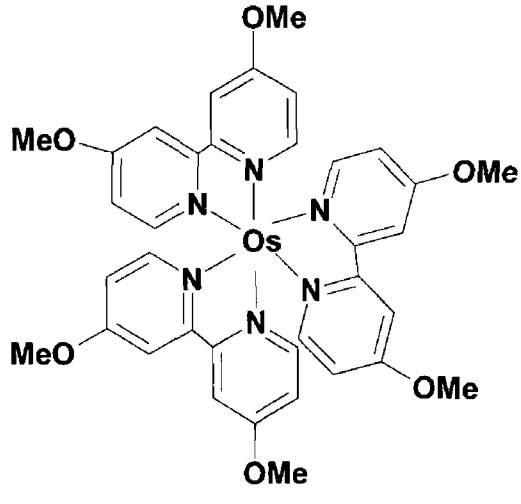

Figure 2 2 Schematic representation of $[Os(OMe\text{-}byp)_3]^{2+}$

2 3 2 $[Os(bpy)_2(PVP)_{10}Cl]^+$

The mono substituted metallopolymer was prepared by refluxing *cis* $Os(bpy)_2Cl_2$ with a ten fold molar excess of PVP (i e one osmium moiety per ten pyridine units) [21] The reflux was performed in 80 20 ethanol H_2O for 60 hours The reaction was monitored constantly by UV-visible spectroscopy and cyclic voltammetry using the conditions in the experimental section

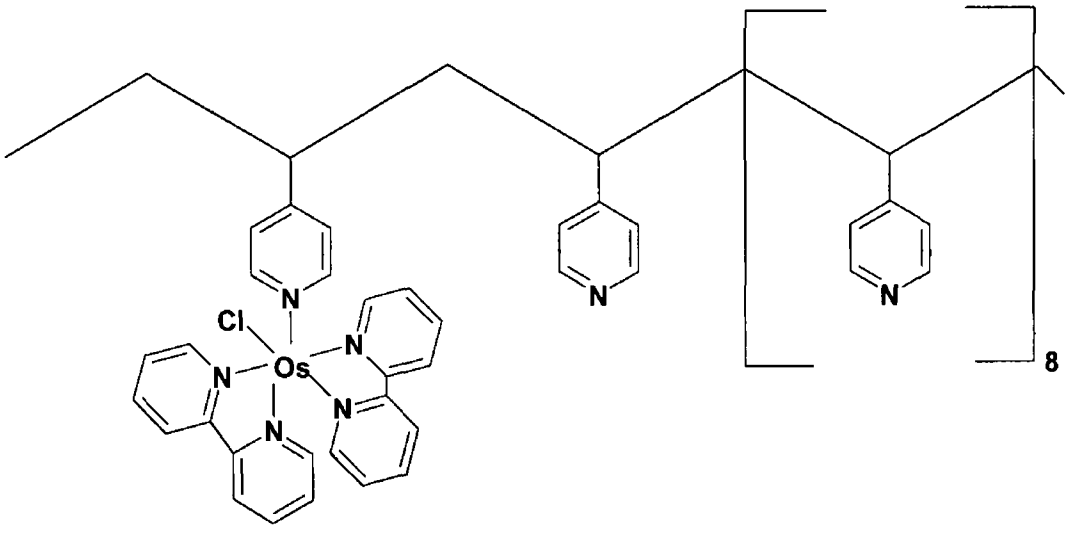

Figure 2 3 Structural representation of $[Os(bpy)Cl(PVP)_{10}]Cl$

2 3 3 Metallopymer Nanoparticle Assemblies

An aqueous solution of the reducing agent potassium borohydride, KBH_4, was prepared just before use It was then rapidly added to the stirred solutions containing the gold precursor tetrachloroauric acid, $HAuCl_4$ and either PVP or the metallopolymer in the desired mole ratio of polymer gold

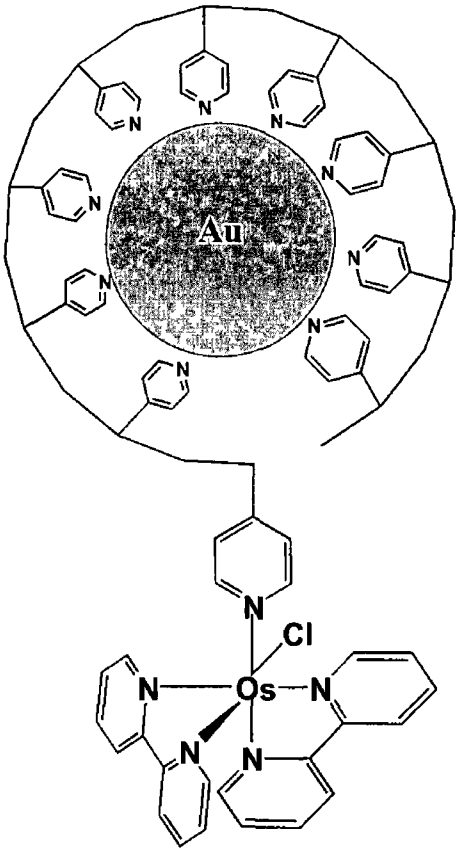

Figure 2 4 Schematic representation of the proposed gold nanoparticle loading within the $[Os(bpy)_2\ Cl\ (PVP)_{10}]^+$ polymer

2 3 4 Gold Sol

A citrate protected gold sol was prepared according to a method reported elsewhere [22] All glassware was initially acid washed prior to any synthesis 1 cm^3 solution of a 1% v/v gold chloride ($HAuCl_4$ $3H_2O$) was added to 100 cm^3 of distilled water The mixture was brought to the boil and 2 5 cm^3 of 1% sodium citrate solution was added After a few minutes a blue colour appeared followed shortly by a ruby-red gold sol

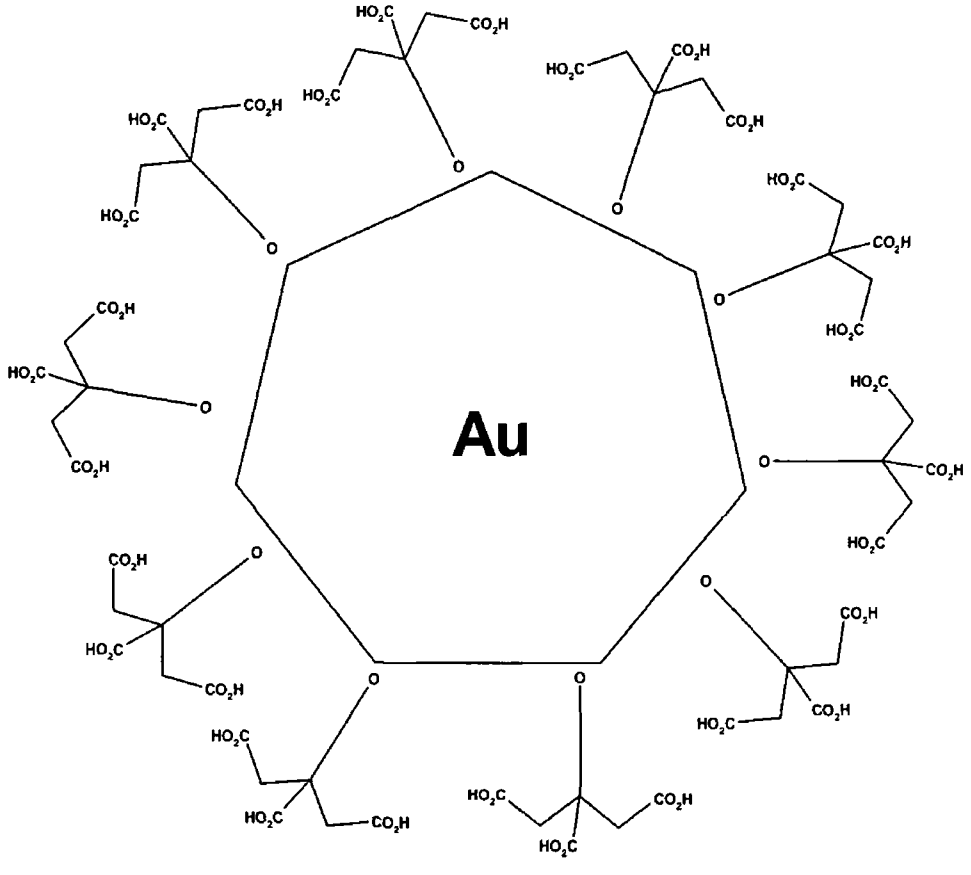

Figure 2 5 Schematic representation of a citrate protected gold nanoparticle Arrangement of citrates around the gold particle are for illustration purposes only

2 4 Characterisation and Results

Characterisation techniques including HPLC, H^1 NMR, elemental analysis, UV-Vis and IR spectroscopy have been performed on the osmium polypyridyl compounds to determine purity H^1 NMR, UV-Vis and IR spectroscopy also aid in the structural analysis of the materials

2 4 1 High Performance Liquid Chromatography

$[Os(OMe)\text{-}bpy)_3]^{2+}$

Figure 2 6 (A) and (B) illustrate the high performance liquid chromatograms of 1 mM $[Os(OMe\text{-}bpy)_3]^{2+}$ in acetonitrile water, 80 20 v/v, 0 08 M $LiClO_4$ The major peak at 2 2 minutes suggests that the synthesis predominately yields a single product The peaks at 1 9 minutes and 2 8 minutes may correspond to excess ligand and osmium starting material and account for less than 5% of the total yield No other visible peaks were reported during the course of the 12 minutes run

(A)

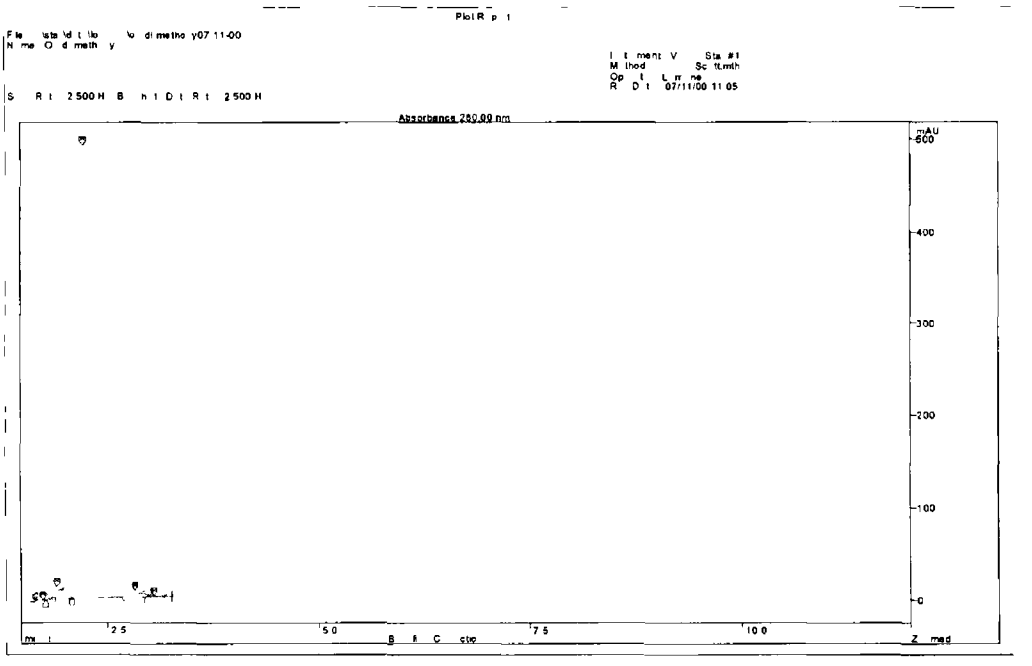

(B)

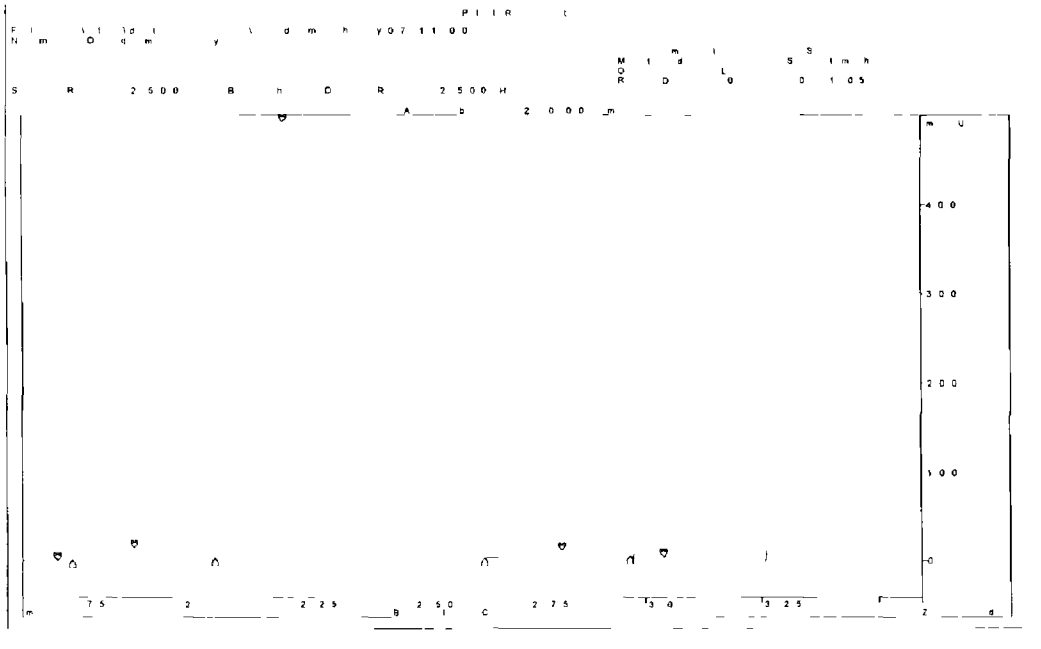

Figure 6 (A) & (B) High Performance Liquid Chromatograms of $[Os(OMe\text{-}bpy)_3]^{2+}$ in Acetonitrile Water, 80 20 v/v, 0 08 M $LiClO_4$ Flow rate is 2 0 ml/min and detector wavelength is 280 nm

2 4 2 NMR Analysis

$[Os(OMe)\text{-}bpy)_3]^{2+}$

The H^1 NMR spectrum of $[Os(OMe\text{-}bpy)_3]^{2+}$ in d-Acetonitrile is shown in Figure 2 7 Chemical shifts were assigned and the peaks with proton shifts at 7 4 ppm to 8 2 ppm revealed a doublet of peaks at each The shift at 6 9 ppm corresponds to a doublet of doublets These proton shifts were attributed to the protons of the pyridme rings The peak at 4 05 ppm was assigned to the methoxy group The integration of protons on the pyridme rings indicated that the methoxy group was in the para position of each ring

2 4 3 Elemental Analysis

$[Os(OMe)\text{-}bpy)_3]^{2+}$

The following results were calculated for $C_{36}H_{36}O_6N_6OsP_2F_{12}$, C 38 29%, H 3 19%, N 7 44% The experimental results were, C 38 7%, H 3 3%, N 7 2% The somewhat higher carbon and hydrogen content in the actual results may suggest that the solid produced during synthesis contains solvent of crystallisation, e g , diethyl ether or methanol

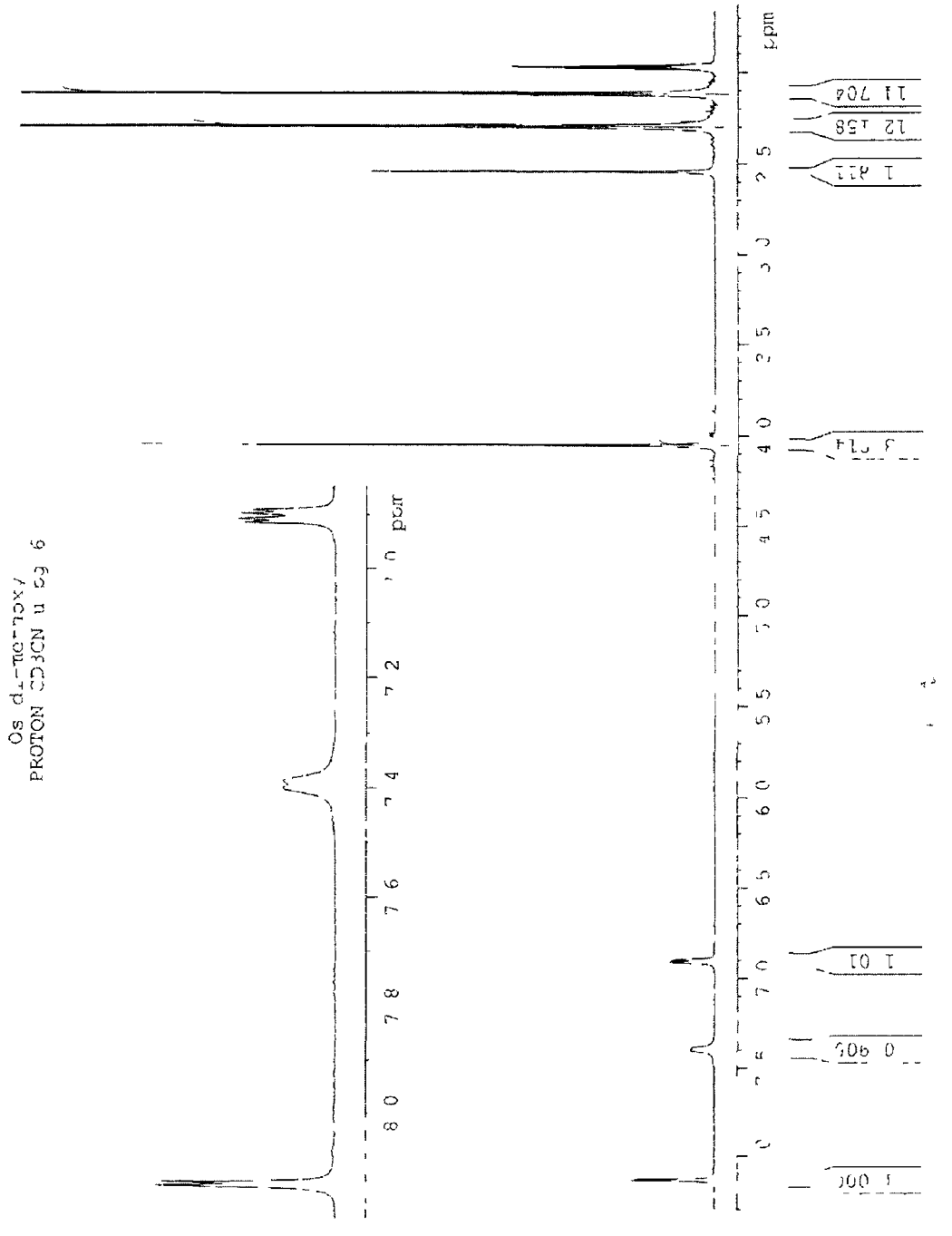

Figure 2 7 ^{1}H NMR of $[Os(OMe\text{-}bpy)_3]^{2+}$ in d-Acetonitrile

2 4 4 UV-Vis Spectroscopy

$[Os(OMe\text{-}bpy)_3]^{2+}$

In Figure 2 8 the spectrum of $[Os(OMe\text{-}bpy)_3]^{2+}$ of the strong bands below 300 nm correspond to ligand π-π^* transitions in the complex [23] The bands that occur at 340 nm and 380 nm correspond to metal centre d-d transitions found in the osmium centre Finally, the metal to ligand charge transfer (MLCT) produce the peaks at 465 mn and 500 nm In this case the transition involves transfer of charge from the osmium to the polypyridyl ligands The absorptions are too intense and too low in energy to be of ligand field (LF or MC) type The band in the visible region of 700 nm corresponds to the osmium centre The MLCT bands of $Os(bpy)_3^{2+}$ are found at 430 nm and 480 nm [24] The spectrum of $[Os(Me\text{-}bpy)_3]^{2+}$, where Me-bpy is 4,4′-dimethyl, 2-2′-dipyridyl, has similar MLCT bands compared to that of $Os(bpy)_3^{2+}$ [23] The methyl substituent has weaker electron donating ability compared to that of the methoxy substituent Therefore, the MLCT shifts to longer wavelengths in $[Os(OMe\text{-}bpy)_3]^{2+}$ are due to the electron donating properties of the methoxy moieties of the pyridine rings Charge transfer energy is decreased m the transition between the osmium 5d state and the ligand π^* due to the increase in electron density on the metal center

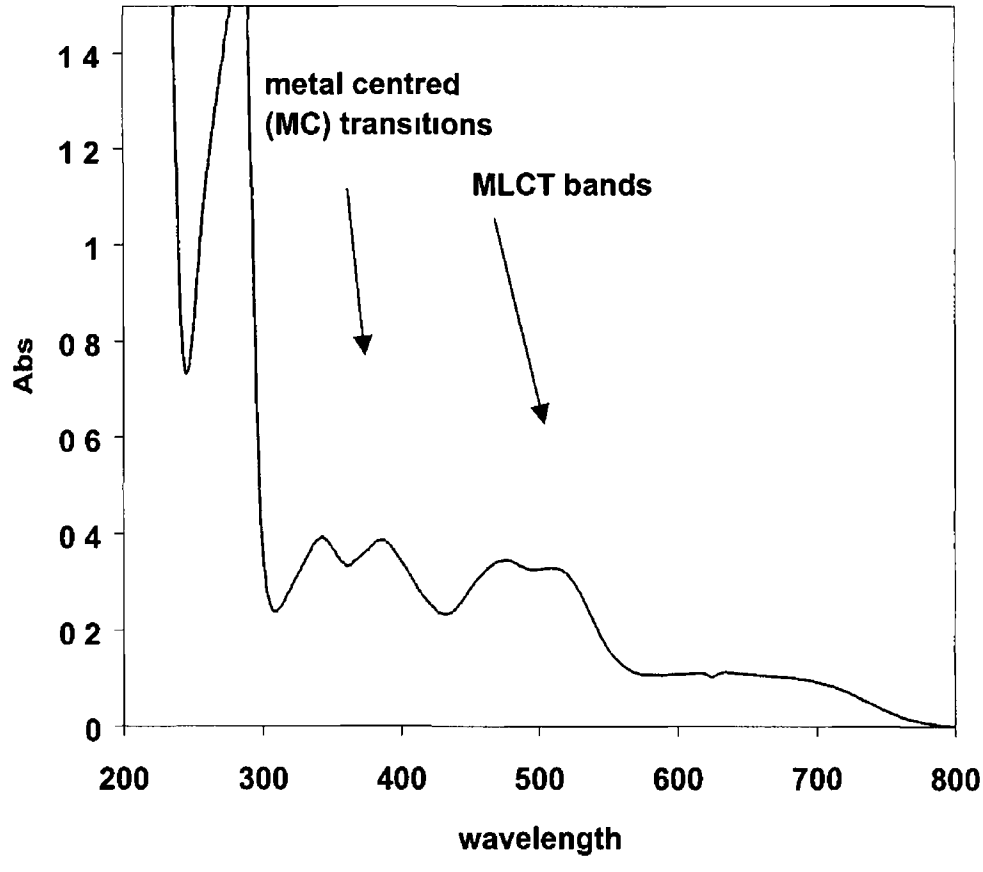

Figure 2 8 UV-Vis spectrum of $[Os(OMe\text{-}bpy)_3]^{2+}$ in acetonitrile Concentration is 4 nM Extinction coefficient is approximately 100,000 cm^2 mol^{-1} at 400 nm and 1 cm pathlength

$[Os(bpy)_2(PVP)_{10}Cl]^+$

Figure 2 9 illustrates the spectrum of $[Os(bpy)_2(PVP)_{10}Cl]^+$ where the metal centre (MC) transition is evident at 355 nm The broad peak on the shoulder of the MC transition in all spectra at 474 nm, corresponds to the MLCT $d\pi(Os)\rightarrow\pi^*(bpy)$ transition The band in the visible region of 700 nm is characteristic of the osmium centre Absorption in osmium involves transitions between filled and unfilled d-orbitals with energies that depend on the ligands bound to the metal ion In this case osmium is bonded to a chloride ligand (strong electron donor) that increases the electron density on the osmium centre The spectral detail is similar to that reported where it is also mentioned that the energy of the absorption maxima is unaffected by metal loading and generally rather a poor indicator of the coordination sphere [25] Consequently, if the bis-substituted polymer, $[Os(bpy)_2(PVP)_{10}]^{2+}$, were synthesised with the displacement of the chloride ion, the electron density around the central atom would decrease as PVP has poorer electron donating properties This leads to a shift in the absorption bands to shorter wavelengths (higher energy)

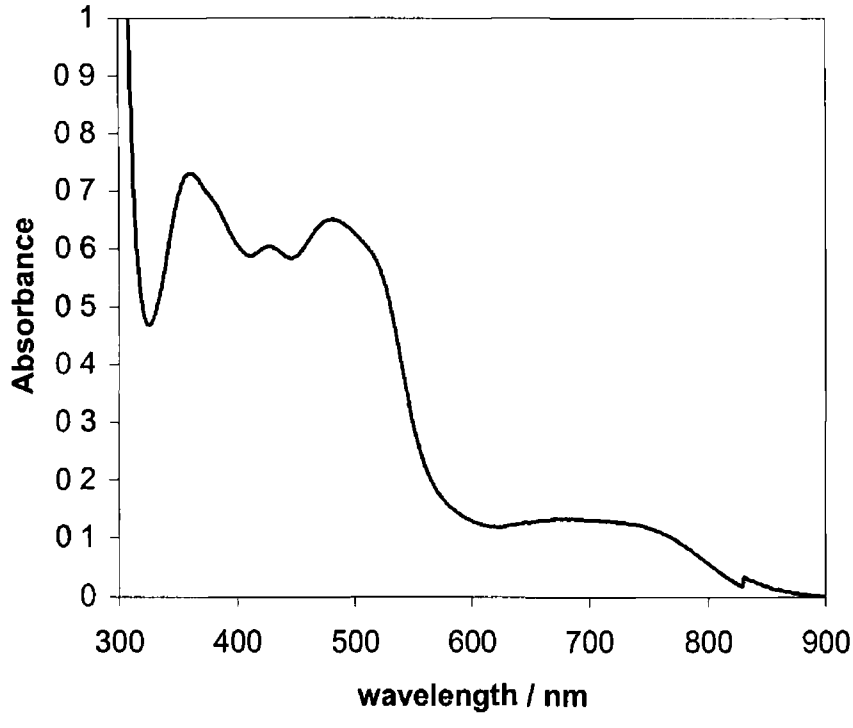

Figure 2 9 UV-Vis spectrum of $[Os(bpy)_2(PVP)_{10}Cl)]^+$ in ethanol Concentration is 7 nM Extinction coefficent is approximately 100,000 cm^2 mol^{-1} at 400 nm and 1 cm pathlength

Gold sol

From the UV-Vis spectroscopy, information regarding the surface plasmon resonance and the size of the gold nanoparticles can be revealed In Figure 2 10, the peak at 520 nm corresponds to the metal surface plasmon resonance (oscillation of the electron density) [26] Surface plasmon resonance is a phenomenon that occurs when the light is reflected off the nanoparticles A fraction of the incident light energy can interact with the delocalised electrons in the metal plasmon thus reducing the reflected light intensity The surface plasmon band arises from interband transitions between the highly polarizable Au $5d^{10}$ band and the unoccupied states of the conduction band [27]

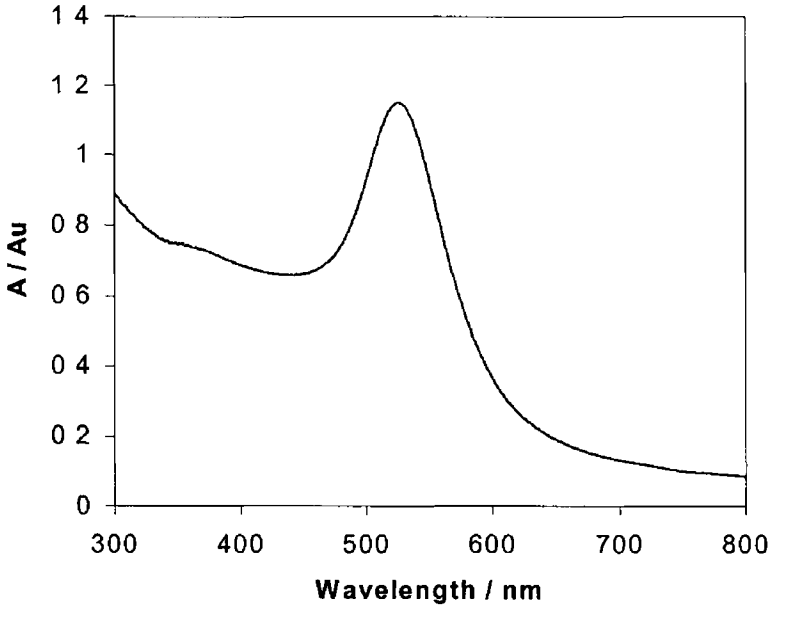

Figure 2 10 UV-Vis spectrum of citrate protected gold nanoparticles Concentration is approx 3 17 x 10^{20} nanoparticles / 1000 cm^3

2 4 5 Infrared Spectroscopy

$[Os(OMe\text{-}bpy)_3]^{2+}$

Figure 2 11 illustrates the spectrum of $[Os(OMe\text{-}bpy)_3]^{2+}$ The peaks are assigned according to IR data in McMurry [28] The $-CH_3$ groups of the methoxy substituents give rise to a symmetric C-H deformation at about 1375 cm^{-1}, and an asymmetric deformation at about 1489 cm^{-1} The broad band that occurs at approximately 3000 cm^{-1} arises from aromaticity in the compound The broad band at 3400 cm^{-1} is suggestive of an –OH moiety From the elemental analysis (section 2 3 4), the -OH may stem from the methanol during recrystallisation The sharp peaks that occur between 1200 cm^{-1} and 1000 cm^{-1} are due to –C-C-, -C-N- and –C-O- stretches that are associated with vibrations within the polypyridyl rings of the compound This analysis may confirm the presence of the methyl groups and methanol from the crytsallization of the product

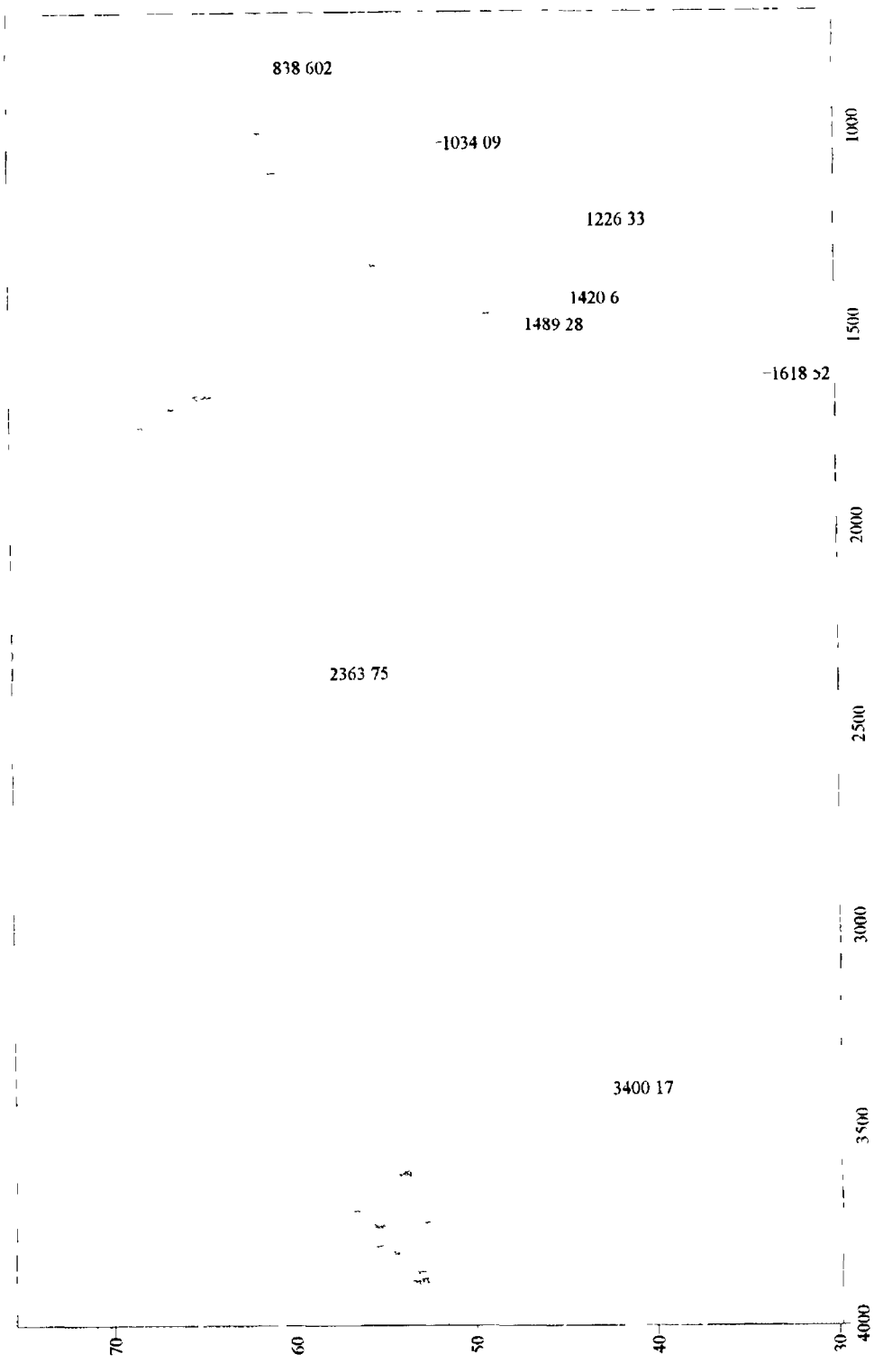

Figure 2 11 Infrared spectrum of $[Os(OMe\text{-}bpy)_3]^{2+}$ in KBr between 4000 cm^{-1} and 800 cm^{-1}

2 5 Conclusions

The osmium complexes $[Os(OMe\text{-}bpy)_3]^{2+}$ and $[Os(bpy)_2(PVP)_{10}Cl]^{+}$ were successfully synthesised and characterised by chromatography and spectroscopy The purity of $[Os(OMe\text{-}bpy)_3]^{2+}$ was confirmed from the HPLC and IR chromatograms and NMR spectrum which allows for further analysis by voltammetry in chapter 3 Elemental analysis of $[Os(OMe\text{-}bpy)_3]^{2+}$ was employed to confirm the % content of carbon, nitrogen and hydrogen The UV-Vis spectra of both osmium complexes (section 2 4 4) allow the coordination of the osmium redox center to be explored The spectra show well-defined MLCT and MC transition peaks along with the characteristic coordination mode of osmium in the visible region The metallopolymer gold nanoparticle composites were prepared and characterised by UV-Vis spectroscopy Cyclic voltammetry and transmission electron microscopy are performed in chapter 4

2 6 References

(1) Quaranta, F , Rella, R , Sicilıano, P , Capone, S , Epıfanı, M , Vasanellı, L , Lıcciullı, A , Zocco, A *Sensors and Actuators B* **1999**, 350

(2) Nı, J , Ju, H , Chen, H , Leech, D *Anal Chım, Acta* **1999**, *378*, 151

(3) Scholz, F , Nıtschke, L , Henrıon, G *Electroanalysıs* **1990**, *2*, 85

(4) Scholz, F , Lange, B *Trends Anal Chem* **1992**, *11*, 359

(5) Yang, C , He, G , Wang, R , Lı, Y *J Electroanal Chem* **1999**, *471*, 32

(6) Nazar, L F , Goward, G , Leroux, M , Duncan, H , Kerr, T , Gaubıcher, J *Internat J Inorg Mat* **2001**, *3*, 191

(7) Wrighton, M S *Scıence* **1986**, *231*, 32

(8) Chıdsey, C E D , Murray, R W *Scıence* **1986**, *231*, 25

(9) Tredıcucci, A , Gmachı, C , Capasso, F , Sıvco D L , Hutchınson, A L , Cho, A Y *Nature* **1998**, *396*, 350

(10) Hogan, C Ph D Thesıs, Dublın Cıty Unıversity, 1999

(11) Nešpůrek, S , Toman, P , Sworakowskı, J , Lıpmskı, J *Current Applıed Physıcs*, **2002**, 2, 299

(12) Zamborını, F P , Gross, S M , Murray, R W *Langmuır*, **2001**, 17, 481

(13) Clıffel, D E , Zamborını, F P , Gross, S M , Murray, R W *Langmuır*, **2000**, 16, 9699

(14) Templeton, A C , Chen, S , Gross, S M , Murray, R W *Langmuır*, **1999**, 15, 66

(15) Templeton, A C , Clıffel, D E , Murray, R W *J Am Chem Soc* **1999**, 121, 7081

(16) Brust, M, Walker, M , Bethell, D , Schıffrın, D J , Whyman, R J *J Chem Soc ,Chem Commun* , **1994**, 801

(17) Xu, C Ph D Thesıs, Unıversıty of Illınoıs at Urbana-Champaıgn, 1992

(18) Wıghtman, R M , Wıpf, D O *Electroanal Chem* **1989**, 15, 267

(19) Bond, A M , Marken, F *J Electroanal Chem* **1994**, *372*, 125

(20) Taylor, C , Kenaussıs, G , Katakıs, I , Heller, A *J Electroanal Chem* **1995**, *396*, 511

(21) Forster, R J , Vos, J G *Macromolecules*, **1990**, 23, 4372

(22) Basıc Prıncıples of Colloıd Scıence, D H Everett, Royal Socıety of Chemıstry

(23) Kalyanasundaram, K *Photochemıstry of Polypyrıdıne and Porphyrın Complexes*, Chapter 5, 1992

(24) Rodrıguez, M , Bard, A J *Anal Chem* **1990**, 62, 2658

(25) Kelly, D M , Vos, J G *Electroactive Polymer Electrochemistry, Part 2 Methods and Applications*, Ed Michael E G Lyons, New York, 1996

(26) Chumanov, G , Sokolov, K, Gregory, B W , Cotton, T M *J Phys Chem* , **1995**, *99*, 9499

(27) Chen, S , Murray, R W *Langmuir*, **1999**, 15, 682

(28) McMurry, Organic Chemistry, 3rd Edition, Brooks/Cole Publishing Company

Chapter 3

Dynamics of Charge Transport of $[Os(OMe\text{-}bpy)_3]^{2+}$ in the Solid State

3.1 Introduction

Chapter 1 reviewed the charge transport properties of many redox active solid state materials and polymeric materials reported in the literature. From this review it is clear that there have been few investigations into the dynamics of charge transport within solid films[1,2] which is surprising when considering the potential applications solid state material could have in sensor[3] and electronic devices.[4] Osmium complexes are particularly attractive in this regard because of their stability of numerous oxidation states and very large self-exchange rate constants.[5,6] Electrochemical cycling of a redox active solid deposit causes it to become oxidised and reduced and to counteract this charge, ions from solution diffuse in to and out of the film structure. Hence, the effect of enhancing this counterion diffusional process is the main focus of the work presented.

In this chapter, the voltammetric properties of solid deposits of $[Os(OMe\text{-}bpy)_3](PF_6)$, where OMe-bpy is 4,4'-dimethoxy, 2-2'-dipyridyl (Figure 2.1) are reported. These solid deposits have been formed on platinum microelectrodes by mechanical abrasion of the solid onto the electrode surface. In the second approach, a drop of Milli-Q water was first added to the complex before transferring the material onto the electrode surface as a paste. Prior to electrochemical measurements, the coating was allowed to dry. Beyond minor differences in the initial scans, films prepared by both methods give indistinguishable voltammetric responses. The electrochemistry was investigated in aqueous electrolyte due to the lack of solubility of the film in this medium.

For electrocrytallised compounds in the solid state, there is probably close packing of the complexes thus decreasing the free internal volume. 'Break in' effect or the degree of solvation of $[Os(OMe\text{-}bpy)_3]^{2+}$ has been probed and can be identified when a solid deposit is initially electrochemically cycled in electrolyte.[7] 'Break in' effect indicates the slow uptake of counterions into the deposit. One approach to creating solids that facilitate more rapid ion transport is to encourage a higher free volume in the solid deposit by using complexes with bulkier side groups.

Electrochemically cycling the solid $[Os(OMe\text{-}bpy)_3]^{2+}$ can physically modify the solid layer structure and can be identified using scanning electron microscopy. Modifying the deposit structure can impact the rate of counterion movement within the layer thus

affecting the homogeneous charge transport coefficient, D_{CT} D_{CT} of a solid phase redox materials is an important parameter as it is an indication to the efficiency of the rate of counterion movement to the layer to maintain electoneutrality during redox cycling For technological purposes, it must be possible to quickly switch the redox composition of the solid and an increased D_{CT} is an indication of this

Cyclic voltammetry under semi-infinite linear diffusion conditions has been used to measure the rate of homogeneous charge transport through the deposits [8] Semi- infinite linear conditions are described in Chapter 1 and this diffusion regime describes the peak current where it varies linearly with square root scan rate The layer is subjected to a series of scan rates and peak current increases with increasing scan rate By systematically varying the concentration of the supporting electrolyte, an insight into whether electron transfer or counterion transport limits the rate at which the redox composition can be switched have been obtained [9] In the case of electron hopping, charge-compensating counterions are freely available within the structure Limitations due to counterion diffusion would reveal a dependency of D_{CT} with counterion concentration It has been demonstrated that for solid deposits of $[Os(bpy)_2$ bpt Cl] deposits where bpy is 2,2'-bipyridyl and bpt is 3,5-bis(pyridin-4-yl)-1,2,4,-triazole[10] that the rate of charge compensating counterions rather than electron hopping between the redox centres limits the overall rate of charge propagation This situation probably arises because close packing of the complexes in the electrocrystallized deposit limits the internal free volume causing slow counterion diffusion

For technological applications ranging from molecular electronics to sensors, it is important to understand those factors that control the rate of electron transfer across the interface between the metal substrate and molecular material Therefore, the rate of heterogeneous electron transfer has been probed for this complex as both solid deposit and as a solution phase reactant At high scan rates, the voltammetric peak-to-peak separation increases significantly and using this peak separation the heterogeneous rate constant can be measured A similarity in the heterogeneous rate constant for both solid and solution phase would indicate that the solvation of the compound at the electrode in both cases is similar

3 2 Electrochemistry of $[Os(OMe\text{-}bpy)_3]^{2+}$ in Solid and Solution Phase

When attempting to understand the electrochemical response that arises from the complex in the solid state, comparisons were made between the $[Os(OMe\text{-}bpy)_3]^{2+}$ in solid and in solution phase Figure 3 1 illustrates cyclic voltammograms for the complex dissolved in acetonitrile and for a solid deposit that has been repeatedly cycled until an equilibrium response is obtained It is clear that the electrochemical response of the osmium bypyridyl complex is similar in both cases with the formal potentials, $E^{o\prime}$, 0 240 V and 0 230 V for the solid deposit and solution phase reactants, respectively Applying the solid deposit to the electrode does not change the electron density on the redox centre as oxidation of the layer is thermodynamically unchanged when compared to the solution phase Therefore the local microenvironment of the redox centre within the solid is analogous to that found for the same species in solution For both cases, the electron transfer reaction at the electrode can be described as an outer-sphere reaction[11] and the oxidised and reduced species are at a distance of at least a solvent layer from the electrode The similarity in formal potential for both solid and solution phase suggest that the local solvation and dielectric constants are comparable

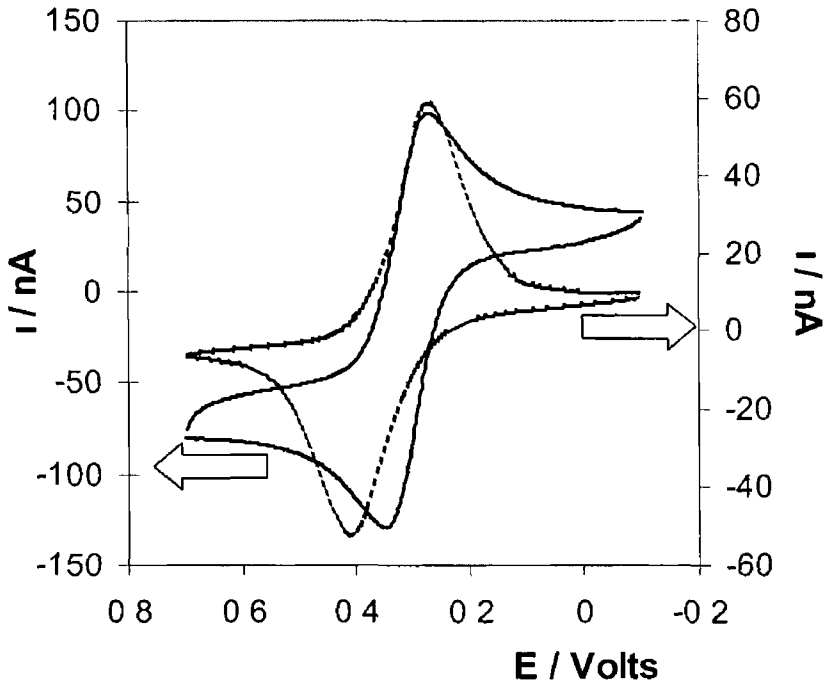

Figure 3 1 Cyclic voltammograms for a 0 8 mM solution of $[Os(OMe\text{-}bpy)_3]^{2+}$ dissolved in acetonitrile (solid line) and as a solid deposit (hashed line) In both cases the supporting electrolyte is 0 1 M $HClO_4$, the working electrode is a 25 μm platinum electrode and the scan rate is 0 1 Vs^{-1}

3 3 'Break In' Response

'Break-in' can be described as the material having to be converted to its equilibrium form with the intercalation of the equilibrium amount of the electrolyte ion [12] Applying a potential to the layer causes the ingress/egress of ions from the electrolyte into the layer to counteract charge The counterions are solvated and counterion uptake by the layer involves a significant increase in layer solvation Initial repetitive cycling of the solid layer in 0 1 M $HClO_4$ shows significant changes in anodic peak current, i_{pa}, over time In Figure 3 2, the anodic peak current is shown to decrease over the initial 50 scans The anodic peak decreases because the layer is equilibrating due to the close packing of the crystals with the result of slow solvent and ClO_4 uptake into the layer

However, Figure 3 3 shows that with further cycling of the layer in 0 1 M $HClO_4$ the i_{pa} approximately doubles over the later 50 cycles before becoming constant Furthermore, the anodic peak potential, E_{pa}, shifts in a positive potential direction by almost 75 mV during the first 25 cycles It becomes thermodynamically more difficult to oxidise the layer as the counterion may have become ion paired with the osmium centre In contrast, the peak currents and potentials associated with the reductive process remain virtually unchanged when the solid deposit is repeatedly cycled

Following the preliminary 100 cycles of the layer, the final cyclic voltammogram in Figure 3 4 of the Os^{2+}/Os^{3+} system is at equilibrium as there no further change in peak current height The voltammetry is now electrochemically reversible with $i_{pa}/i_{pc} \approx 1\ 0$ but the peak-to-peak, ΔE_p, of 100 mV, is larger than ΔE_p of 57 mV expected for an ideal one electron oxidation/reduction reaction Such a deviation may arise from ion pairing and double-layer effects

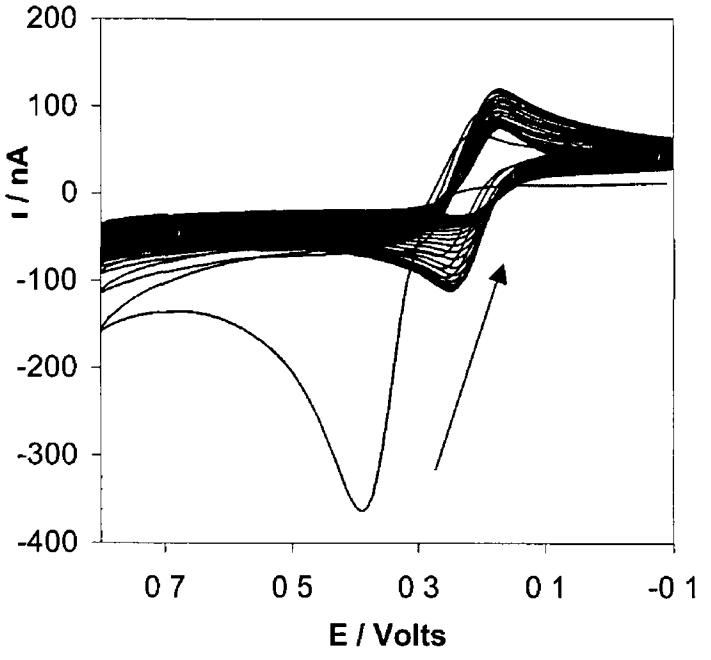

Figure 3 2 Initial cyclic voltammograms (50 scans) for an $[Os(OMe\text{-}bpy)_3]^{2+}$ solid deposit immobilized on a 25 μm platinum electrode The supporting electrolyte is 0 1 M $HClO_4$ and the scan rate is 0 1 Vs^{-1} The initial potential is –0 100 V, oxidation currents are negative

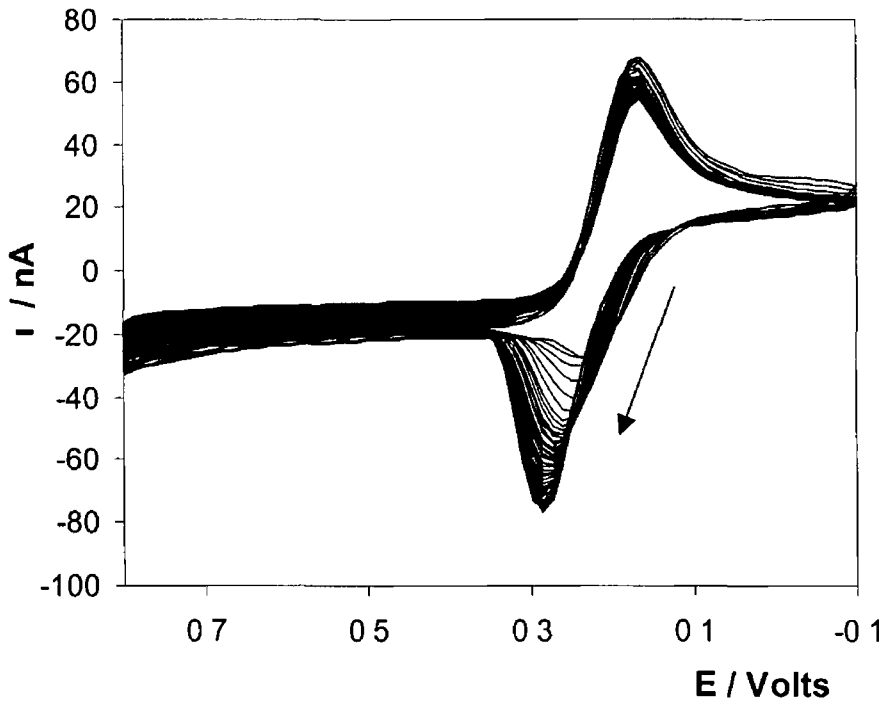

Figure 3 3 Cyclic voltammograms for an $[Os(OMe\text{-}bpy)_3]^{2+}$ solid deposit for the subsequent 50 scans immobilized on a 25 μm platinum electrode The supporting electrolyte is 0 1 M $HClO_4$ and the scan rate is 0 1 Vs^{-1}

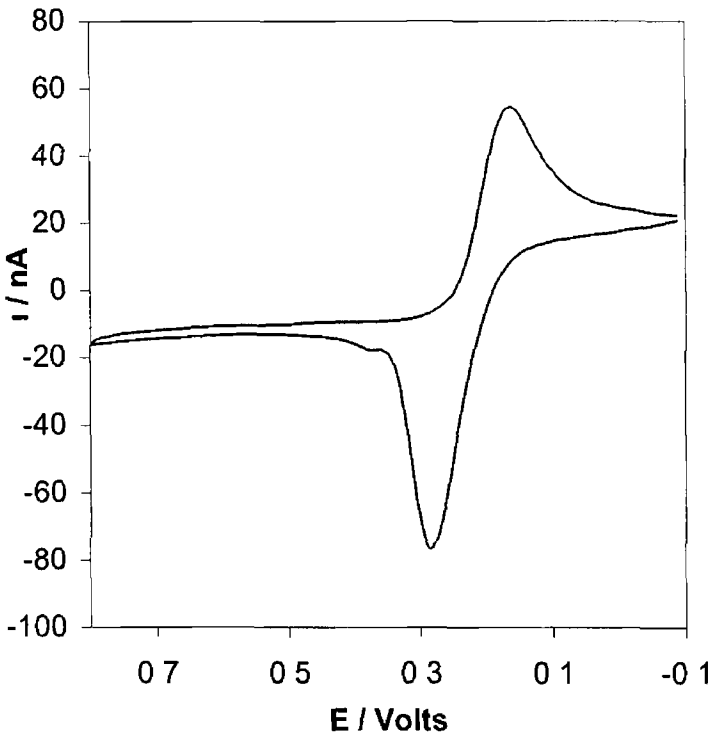

Figure 3 4 Cyclic Voltammogram of $[Os(OMe\text{-}bpy)_3]^{2+}$ on a 25 μm platinum electrode after break in is complete The supporting electrolyte is 0 1 M $HClO_4$ and the scan rate is 0 1 Vs^{-1} The initial potential is –0 100 V, oxidation currents are negative

3 4 Morphology Changes

Given that oxidation of the deposit is accompanied by the ingress of charge compensating counterions, changes observed in the voltammetry when the deposit is first cycled may be associated with structural or solvation changes [13 14 15] To address this issue, scanning electron microscopy was used to image the deposits before and after voltammetric cycling in perchloric acid

Figure 3 5 shows the SEM image of the complex before cycling with no washing or exposure to electrolyte and shows particles of between approximately 1 and 20 μm Figure 3 6 shows the image of the control experiment where the complex was not cycled but exposed to the electrolyte There were no signs of crystal growth as the structural morphology was similar to the dry layer Given that crystallographic studies have been successfully performed on this material by other investigators, it is likely that the material is microcrystalline [16]

Figure 3 7 illustrates the image of the solid deposit after cycling in 0 1 M perchloric acid for 100 cycles The morphology and size of the particles changes and the crystal structure formed is that of very thin platelets Figure 3 8 shows that electrochemical cycling of the solid deposit in 0 1 M $HClO_4$ for 250 cycles also shows the formation of crystals Figure 3 9 shows that increasing the electrolyte concentration to 1 0 M $HClO_4$ still induces crystal formation during electrochemical cycling

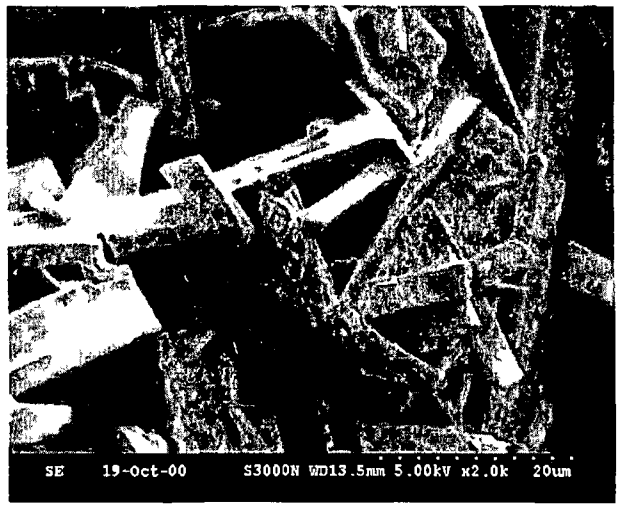

Figure 3 5 Scanning electron microscopy image of $[Os(OMe\text{-}bpy)_3]^{2+}$ solid deposits as deposited, before electrochemical cycling

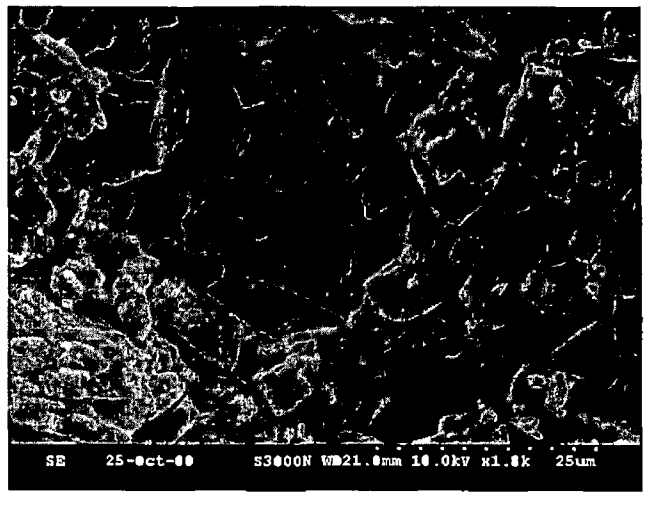

Figure 3 6 Scanning electron microscopy image of $[Os(OMe\text{-}bpy)_3]^{2+}$ solid deposits exposed to 0 1 M $HClO_4$, with no electrochemical cycling

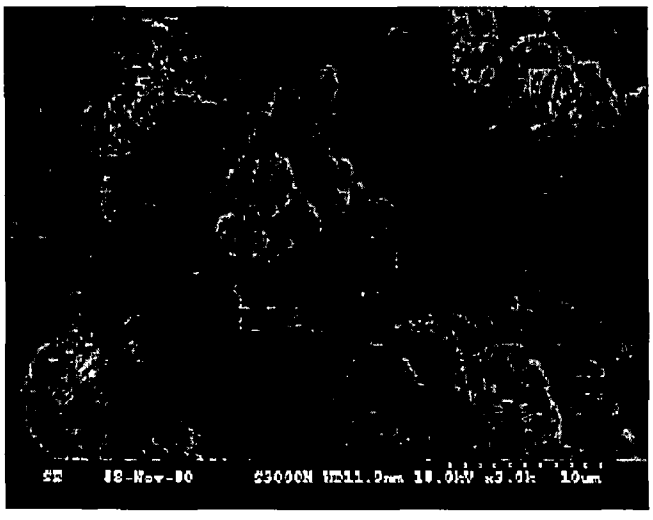

Figure 3 7 Scanning electron microscopy image of $[Os(OMe\text{-}bpy)_3]^{2+}$ solid deposits as deposited after 100 voltammetric cycles between –0 1 and 1 0 V in 0 1 M $HClO_4$ at a scan rate of 0 1 Vs^{-1}

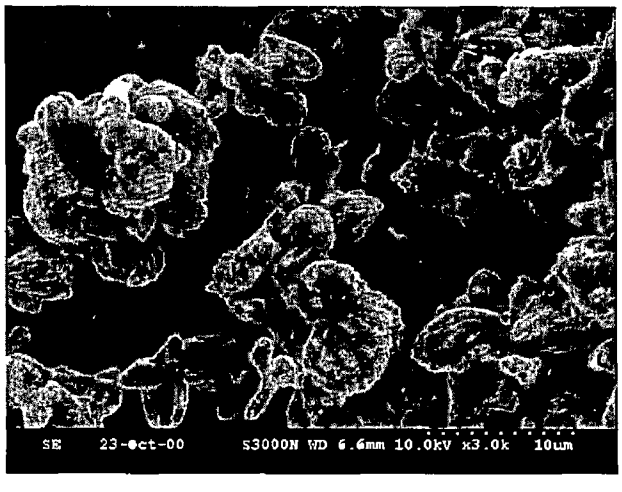

Figure 3 8 Scanning electron microscopy image of $[Os(OMe\text{-}bpy)_3]^{2+}$ solid deposits as deposited after 250 voltammetric cycles between –0 1 and 1 0 V in 0 1 M $HClO_4$ at a scan rate of 0 1 Vs^{-1}

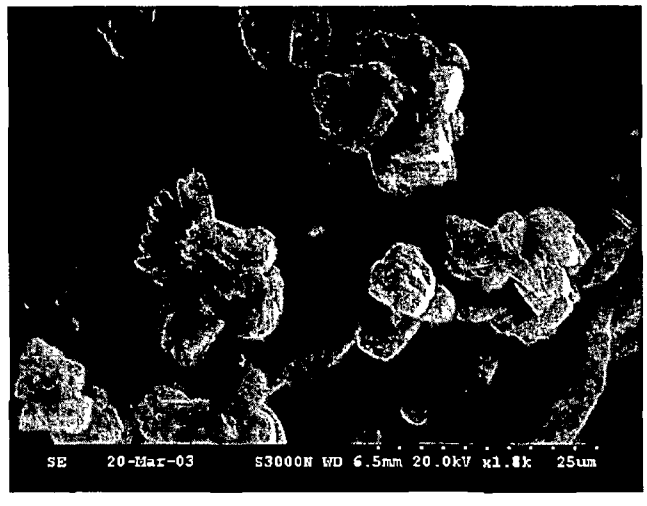

Figure 3 9 Scanning electron microscopy image of $[Os(OMe\text{-}bpy)_3]^{2+}$ solid deposits as deposited after 250 voltammetric cycles between –0 1 and 1 0 V in 1 0 M $HClO_4$ at a scan rate of 0 1 Vs^{-1}

3 5 Bulk Electrolysis

Bulk electrolysis experiments on the solid layer confirms the possibility that redox cycling of osmium and its associated ion ingress and egress encourages growth of crystals Figures 3 10 (A) & (B) show that bulk electrolysis of the material where +0 800 V bias is applied to one solid sample (osmium +3 state), and +0 250V bias is applied to the other (the +2 state of osmium) Bulk electrolysis does not trigger any detectable changes in the macroscopic structure of the material This implies the possibility that it is electrochemically cycling that facilitates the nucleation and growth of crystals and not oxidation and reduction of the layer alone

(A)

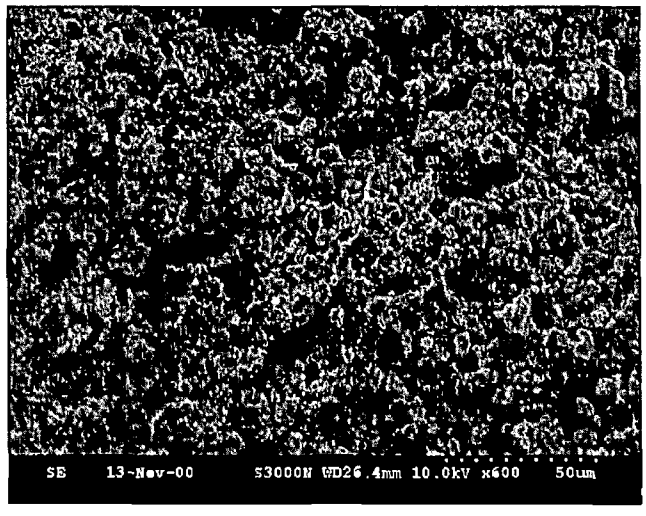

(B)

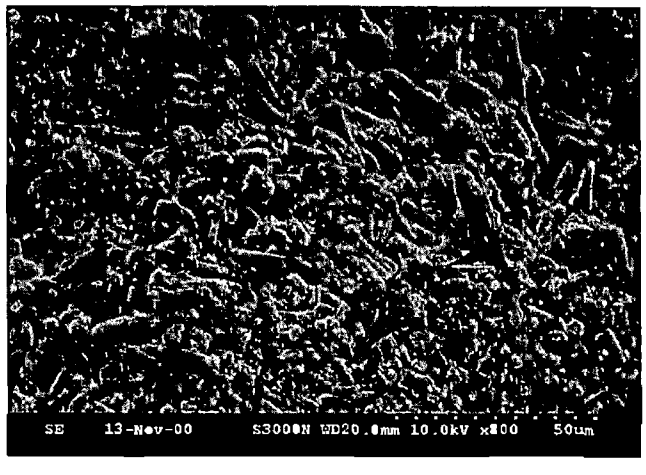

Figure 3 10 SEM image of $[Os(OMe\text{-}bpy)_3]^{2+}$ solid deposit after bulk electrolysis at (A) +0 800 V, (B) +0 250 V in 0 1 M $HClO_4$ for 15 minutes

3 6 pH Effects of Solid Deposit

When the layer is exposed to a neutral electrolyte, 0 1 M $NaClO_4$, the 'break in' effect observed for the layer in 0 1 M $HClO_4$ was not observed However, unlike the solid deposit in 0 1 M $HClO_4$, the layer is not as stable when exposed to 0 1 M $NaClO_4$ In Figure 3 11 the anodic and cathodic peak currents, i_p, decrease to zero over 50 voltammetric cycles

Scanning electron microscopy was performed on the layers to identify any structural changes associated with ion movement within the deposit during cyclic voltammetry Figures 3 12 shows the image of the layer cycled in 0 1 M $NaClO_4$ for 50 voltammetric cycles There were no signs of crystal growth when compared to the dry layer in Figure 3 5

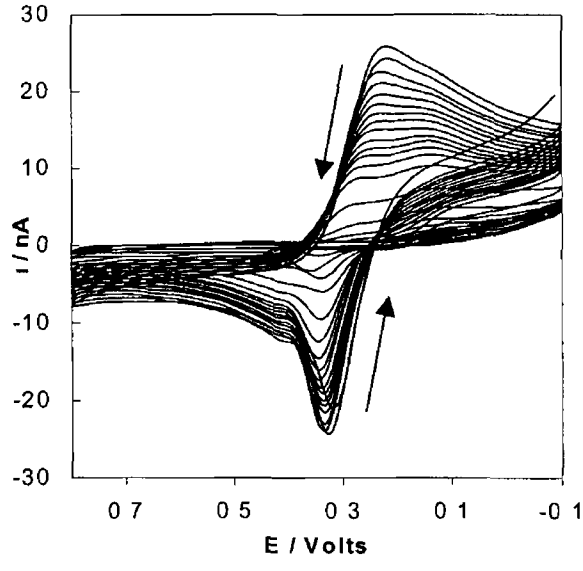

Figure 3 11 Cyclic voltammograms of the solid $[Os(OMe\text{-}bpy)_3]^{2+}$ deposit in 0 1 M $NaClO_4$ Scan rate is 0 05 Vs^{-1}

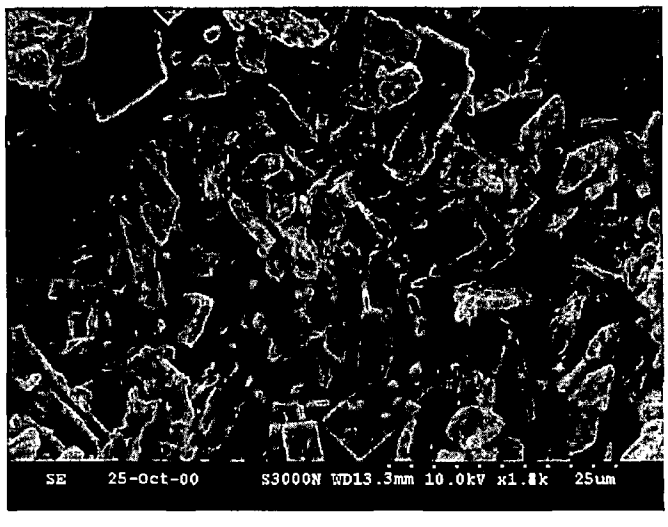

Figure 3 12 SEM image of $[Os(OMe\text{-}bpy)_3]^{2+}$ solid deposit after 50 voltammetric cycles between –0 1 and 1 0 V in 0 1 M $NaClO_4$ at a scan rate of 0 1 Vs^{-1}

3 7 Protonated Crystal

Electrocrystallisation of the solid in perchloric acid suggests that counterion ingress/egress are possibly responsible for crystal growth Investigations on solid state osmium bis(bipyridyl)tetrazine chloride reveal that cycling in sodium perchlorate electrolyte actually induces crystallisation in the material whereas cycling in $HClO_4$ does not [17] Cycling in $HClO_4$ probably causes the methoxy moieties of the bipyridyl ligands to become protonated This protonations may induce hydrogen-bonding interactions between the complexes thus promoting the formation of crystals, Figure 3 13

Significantly, protonation of all six of the methoxy groups yields a highly polycationic layer with the overall charge on the reduced and oxidized forms of the complex being be 8+ and 9+, respectively Under these circumstances, electroneutrality will be maintained by the ingress of perchlorate anions that are likely to be mobile within the deposit Anion incorporation is significant from the perspective of rapid charge transport since it will lead to a deposit that is porous on the molecular scale thus facilitating ion transport

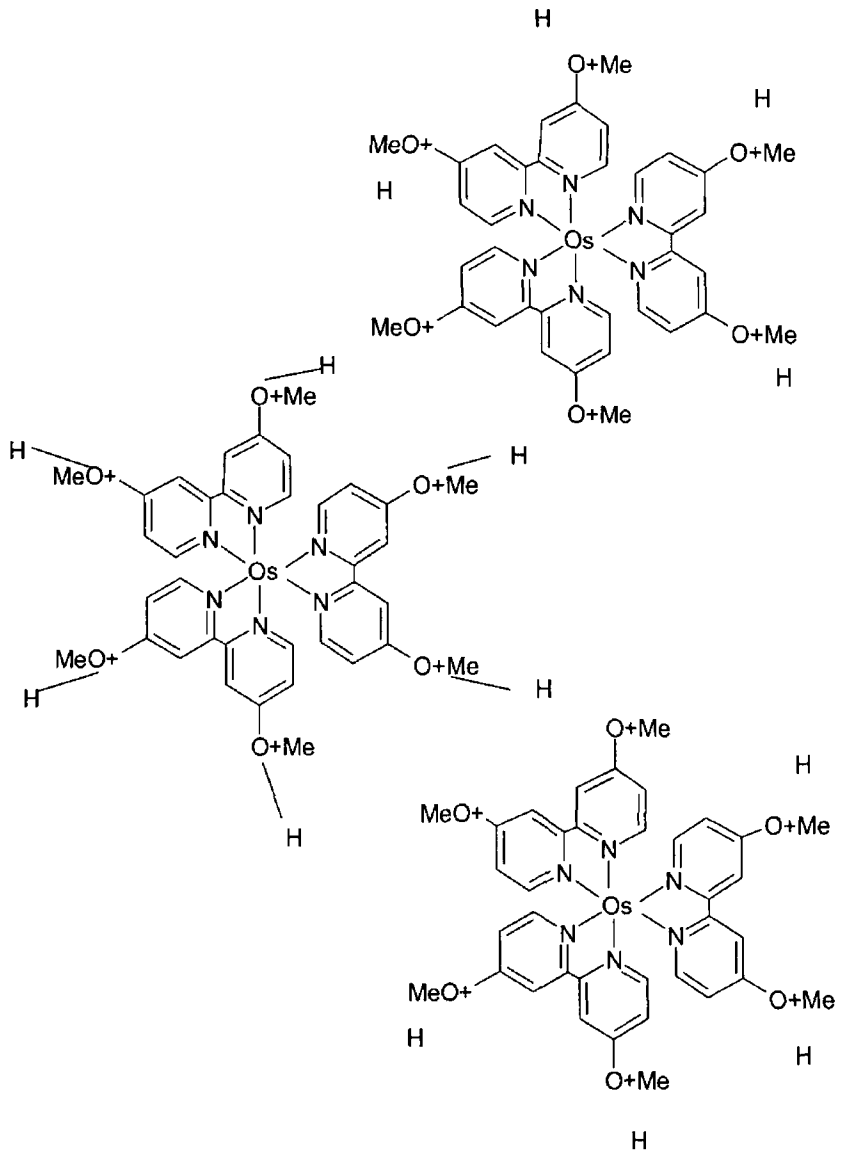

Figure 3 13 Proposed schematic representation of the protonated methoxy moieties that induce hydrogen-bonding interactions between complexes, promoting the formation of crystals

3 8 Resistance and Interfacial Capacitance

When a polycationic deposit is placed in a dilute solution of a strong electrolyte, the concentration of counterions (PF_6 in this case) within the deposit is typically considerably larger than that found in the contacting solution For the films considered here, the anion concentration initially present in the deposit is expected to be of the order of 3 M Thus, under the influence of the concentration gradient, counterions may diffuse from the deposit into the solution until the concentrations become equal in the two phases However, if diffusion of charged counterions occurs, then electroneutrality within the film would be violated, and an electrical potential would develop at the interface This "Donnan potential" would then increase until equilibrium was reached in which it completely opposed the tendency of the counterions to move down the concentration gradient Under these equilibrium conditions the net diffusion of counterions across the interface would be zero, and co-ions would be excluded from the solid deposit [11]

The existence of such a permselective response for these solid deposits has been probed by determining the contribution of the film resistance to the total cell resistance as the supporting electrolyte concentration is changed In the case of an ideally permselective response, ions would be effectively excluded from the membrane, and the film resistance would be independent of the supporting electrolyte concentration To determine the total cell resistance, we have performed short timescale, small amplitude, and potential step chronoamperometry, in a potential region where no Faradaic response is observed In a typical experiment, the potential was stepped from -50 mV to 0 mV at both bare and modified microelectrodes, and the resulting current was recorded over the following 20 μs This capacitive current vs time transient can be described by Equation (1) [8]

$$i_C(t) = (\Delta E / R_u) \exp(-t / R_u C_{dl}) \qquad (1)$$

where ΔE is the pulse amplitude, R_u is the total cell resistance, and C_{dl} is the integral double layer capacitance For both modified and bare electrodes, the current decays in time according to a single exponential, which is consistent with double layer charging

alone [11] Figure 3 14 illustrates ln $i_C(t)$ vs t plots for the solid deposits as the sodium perchlorate concentration is changed from 0 to 0 4 to 1 0 M in a fixed pH background of 0 1 M $HClO_4$

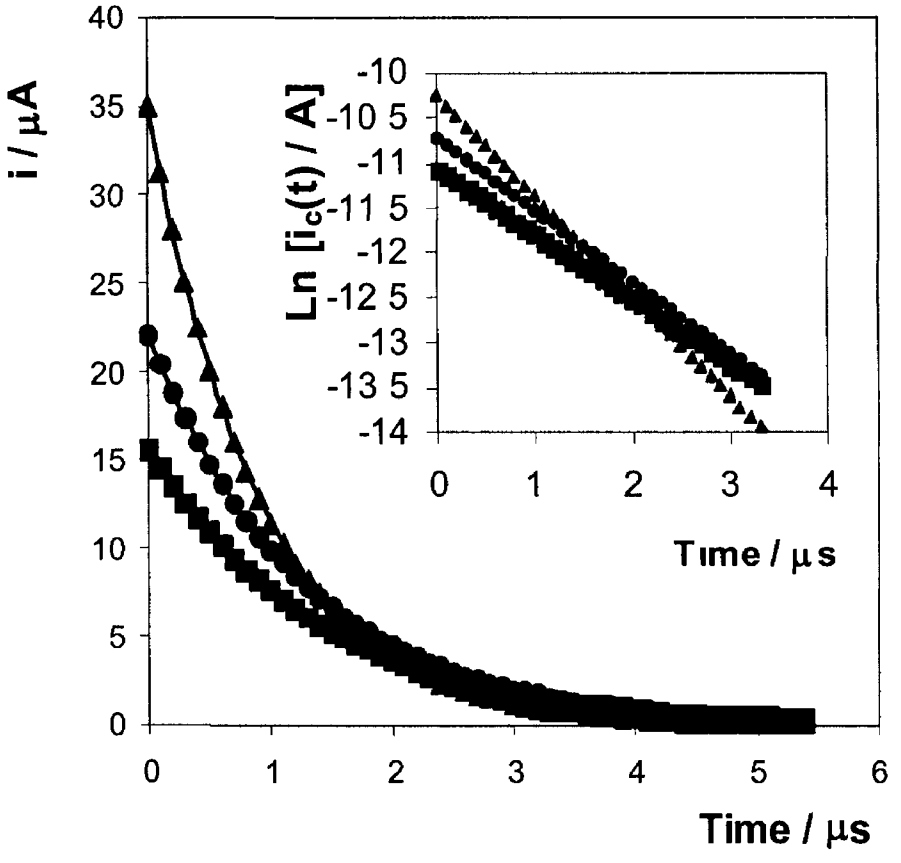

Figure 3 14 Current-time transients for a 25 μm radius platinum microelectrode modified with an $[Os(OMe\text{-}bpy)_3]^{2+}$ deposit following potential steps from –0 050 to 0 000 V From top to bottom, the data correspond to 0 0, 0 4 and 1 0 M $NaClO_4$ in a fixed background of 0 1 M $HClO_4$ as supporting electrolyte The inset illustrates the corresponding semi-log current vs time plots

The absolute slope of these plots represents the reciprocal of the cell time constant R_uC_{dl} Table 1 presents R_uC_{dl} values for an electrode before, and after modification with $[Os(OMe\text{-}bpy)_3]^{2+}$ as a function of the perchlorate concentration This table shows that both the bare and the modified electrode cell time constants decrease with increasing electrolyte concentration as expected [11] However, the response time is considerably more sensitive to the supporting electrolyte concentration for the microelectrode coated with the solid deposit

Table 1 Resistance, R_u, Double Layer Capacitance, C_{dl}, and Electrode Response Times, R_uC_{dl}, for 25 μm Radius Platinum Microelectrodes Before and After Modification with a Solid Deposit of $[Os(OMe\text{-}bpy)_3]^{2+}$ as the Concentration of $NaClO_4$ is Systematically Varied in a Background of 0 1 M $HClO_4$ *

	Bare			Modified		
[$NaClO_4$] /M	**R_u / Ω**	**10^{10} C_{dl} /F**	**R_uC_{dl} / μs**	**R_u / Ω**	**10^{10} C_{dl} /F**	**R_uC_{dl} / μs**
0 0	2400(192)	5 89(0 53)	1 41(0 25)	3200(256)	4 32(0 21)	1 38(0 18)
0 1	2200(188)	6 28(0 50)	1 38(0 23)	2900(203)	4 71(0 23)	1 36(0 16)
0 2	2056(132)	6 48(0 58)	1 33(0 21)	2620(209)	5 10(0 31)	1 33(0 19)
0 4	1877(140)	7 06(0 14)	1 32(0 12)	2268(181)	5 49(0 32)	1 24(0 18)
0 6	1700(119)	7 06(0 28)	1 20(0 13)	1955(195)	5 31(0 15)	1 03(0 13)
0 8	1550(15 5)	7 46(0 74)	1 15(0 12)	1711(136)	5 89(0 58)	1 04(0 18)
1 0	1400(70)	8 24(0 49)	1 15(0 13)	1430(28)	6 28(0 37)	0 89(0 07)

* The numbers in parentheses represent errors obtained by standard deviation from at 3 independent experiments

It is apparent from Equation (1) that R_u can be extracted from the intercepts of the insets shown in Figure 3 14 Figure 3 15 shows the total cell resistance for a bare and a coated electrode as the perchlorate concentration is changed from 0 1 to 1 0 M

It is clear that in both circumstances R_u is reduced at high electrolyte concentrations reflecting a reduced solution resistance Importantly, the cell resistance with the modified electrode is never more than 33% larger than that observed with a bare electrode over this range of electrolyte concentrations This observation suggests that the solution resistance rather than the resistance of the deposit dominates the cell resistance for the coated electrode These results suggest that these deposits do not contribute significantly to the overall cell resistance probably because electrolyte can permeate into the individual particles that exist on the microelectrode surface

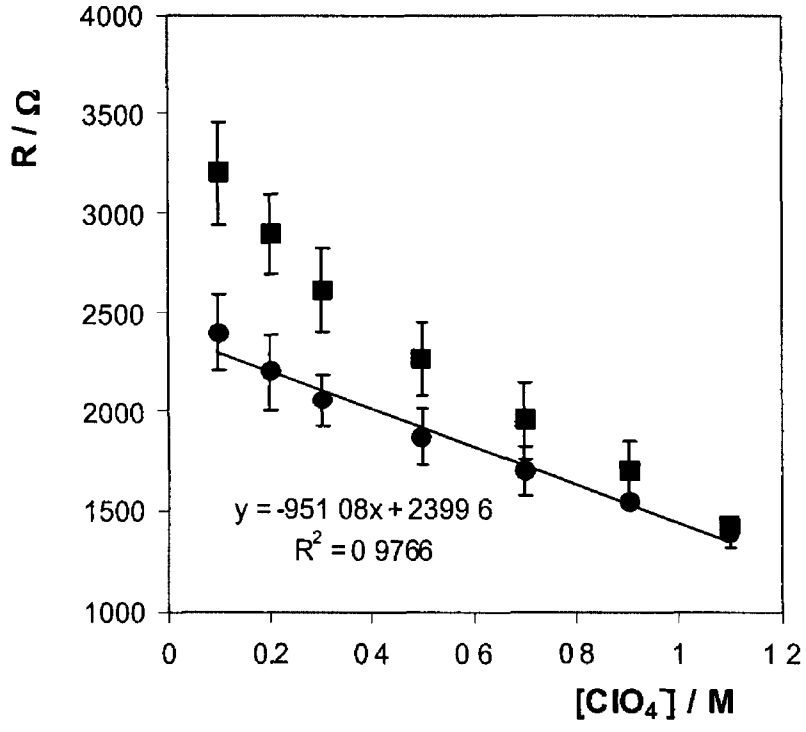

Figure 3 15 Dependence of the total cell resistance, R_u, on the concentration of $NaClO_4$ in a fixed background of 0 1 M $HClO_4$ as supporting electrolyte Data for a bare 25 μm radius platinum microelectrode are shown on the lower curve (●) while the upper curves are for the same microelectrode modified with an $[Os(OMe\text{-}bpy)_3]^{2+}$ solid deposit (■) Surface coverage is 7 x 10^{-8} mol cm^{-2}

3 9 Charge Transport through the Deposit

To understand the dynamics of charge transport that occurs in osmium polypyridyl compounds[18], the solid layer was exposed to a series of fast scan rates in order to determine the homogeneous charge transfer coefficient [19] Figure 3 16 illustrates the effect of increasing the scan rate from 50 to 500 mVs^{1} in 0 8 M $HClO_4$ For fast scan rates, only a small fraction of the total amount of material immobilized is electrolyzed and the depletion zone remains well within the deposit Under these conditions, linear diffusion predominates with peak shaped voltammograms being observed In common with solution phase reactants, the peak current varies as $\upsilon^{1/2}$, Figure 17 [8 20 21]

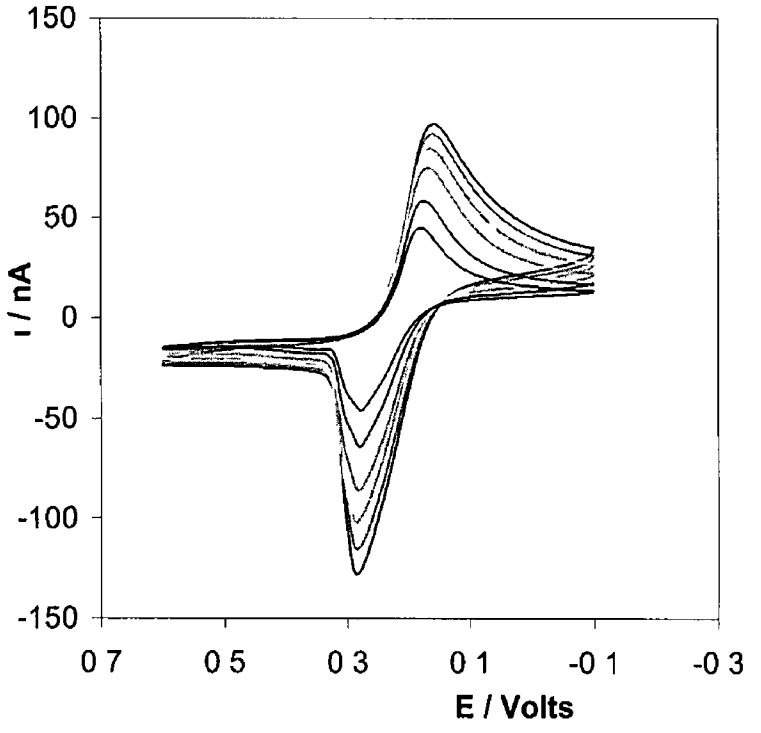

Figure 3 16 Cyclic voltammograms of $[Os(OMe\text{-}bpy)_3]^{2+}$ solid deposits on a 25 μm platinum electrode in 0 1 M $HClO_4$ From bottom to top, the scan rates are 50, 100, 200, 300, 400 and 500 mVs^{-1}

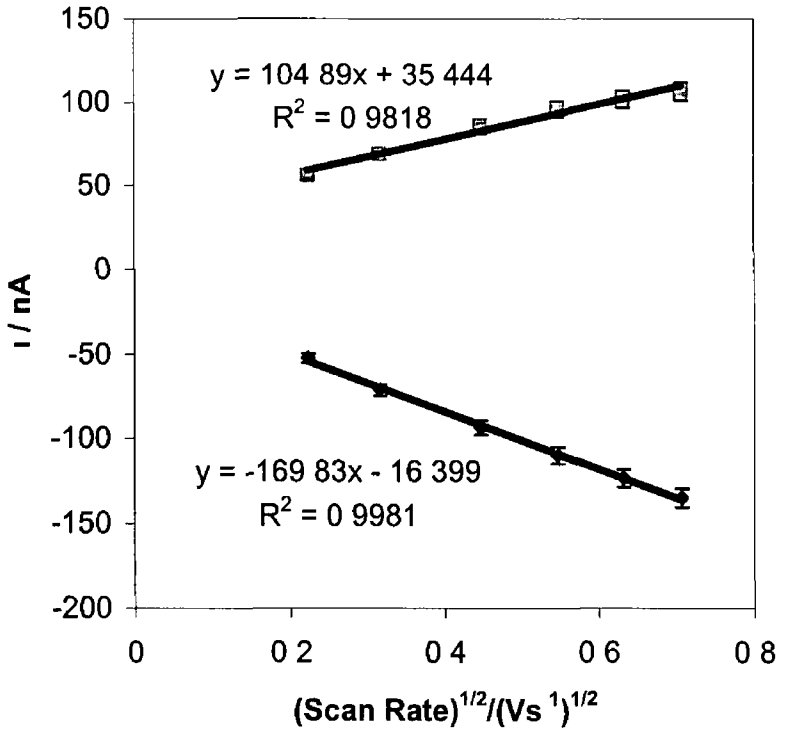

Figure 3 17 The dependence of the peak current on square root of scan rate for $[Os(OMe\text{-}bpy)_3]^{2+}$ solid deposits on a 25 μm platinum electrode in 0 1 M $HClO_4$

Figure 3 17 shows that the peak current, i_p, increases linearly with increasing $\upsilon^{1/2}$ indicating that semi-infinite linear diffusion dominates the observed response Electrochemical charge transport occurs by electron self-exchange reactions between the neighbouring oxidised and reduced sites This electron hopping process is accompanied by the movement of charge-compensating counterions that are mobile within the layer Under these circumstances, the peak current, i_p, can be described in terms of the Randles-Sevçik equation

$$i_p = 2\ 69x10^5\ n^{3/2}\ AD^{1/2}{}_{CT}\ C_{eff}\ \upsilon^{1/2} \qquad (2)$$

where n is the number of electrons transferred, A is the area of the electrode, D_{CT} is the apparent charge transport diffusion coefficient and C_{eff} is the effective fixed site concentration Previous investigations on related systems indicate that the fixed site concentration in systems is of the order of 1 5 M [10 22] and this concentration is consistent with x-ray crystallographic studies on osmium and ruthenium poly-pyridyl complexes [23,24] Using this fixed site concentration, the data illustrated in Figure 3 17 yields a D_{CT} value of $1\ 2\pm0\ 1x10^{-9}$ cm^2s^{-1} for both oxidation and reduction processes Schematic representations of both finite and semi-infinite diffusion response are covered in chapter 1

3 10 Perchloric Acid Concentration Effect on D_{CT}

The rate of homogeneous charge transport, D_{CT}, through these solid state deposits could be limited either by electron hopping between the sites or by counterion diffusion necessary to maintain electroneutrality[9] In the case of electron hopping, charge-compensating counterions are freely available within the structure and D_{CT} is expected to depend weakly on the electrolyte concentration In this case the electrolyte does not play a part in the charge transport and the self-exchange between the redox centers is rate limiting As illustrated in Figure 3 18, D_{CT} is approximately independent of the perchloric acid concentration maintaining a value of $1\ 5\pm0\ 4x10^{9}$ cm^2s^{1} for $0\ 1\leq[HClO_4]\leq0\ 6$ M Above 0 6 M electrolyte, D_{CT} increases significantly reaching a value of $13\ 1x10^{9}$ cm^2s^{1} in 1 0 M $HClO_4$

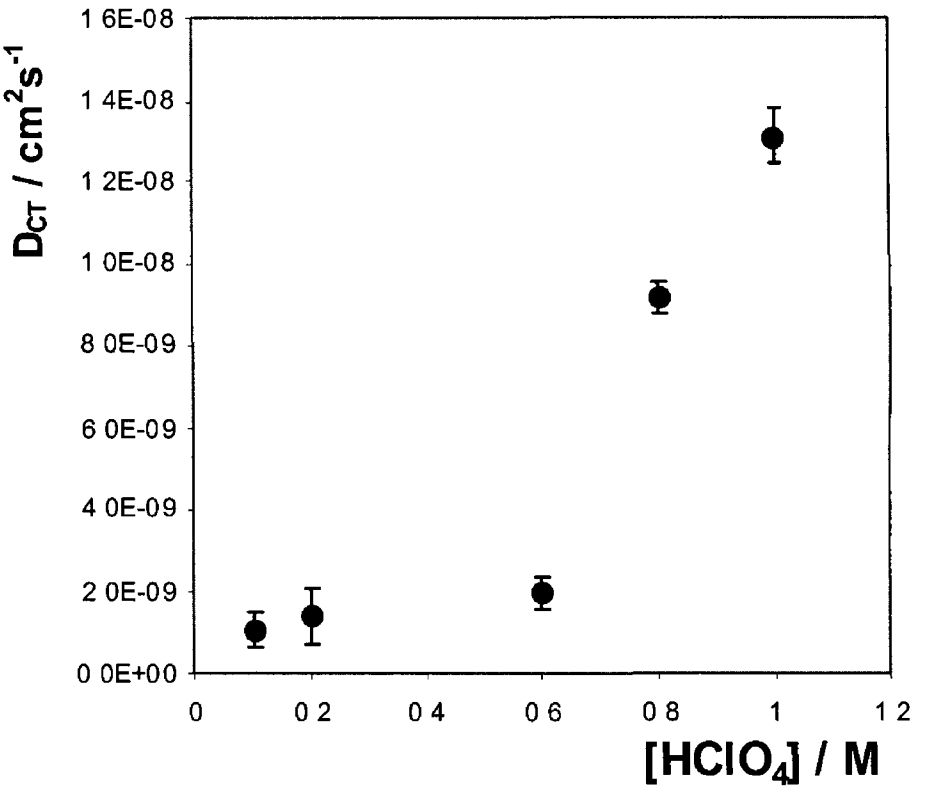

Figure 3 18 Dependence of the homogeneous charge transport diffusion coefficient of solid state $[Os(OMe\text{-}bpy)_3]^{2+}$ on the concentration of $HClO_4$ as supporting electrolyte

The Dahms-Ruff equation[25,26] can be used to calculate the electron self-exchange rate constant from the maximum D_{CT} value assuming that electron hopping represents the rate-determining step This equation is given by

$$D_{CT} = D_{Phys} + 1/6\ k_{SE}\delta^2 C \qquad (3)$$

where D_{Phys} describes physical diffusion in the absence of electron hopping, C is the fixed site concentration of the osmium complex and δ is the inter-site separation between adjacent Os^{2+} and Os^{3+} moieties Given that crystalline solid deposits are being considered, D_{Phys} is assumed to be zero On the basis of crystallographic data for $[Os(OMe\text{-}bpy)_3]^{2+}$, the intersite separation was taken to be 9 6 Å [16]

The maximum D_{CT} value, 13 1 x 10^{-9} cm^2s^{-1}, yields a self-exchange rate constant of 5 7x10^6 $M^{-1}s^{-1}$ This value is approximately an order of magnitude smaller than the values typically reported for osmium poly-pyridyl complexes in solution[27] or within monolayers [17,28,29,30] Given the assumptions made in the calculation of k_{SE}, the value obtained does not allow an unambiguous determination of whether counterion motion or electron transfer limits the overall rate of charge transport However, the data indicate that the rate of charge transport is significantly higher than that found in structurally related systems, e g , for solid deposits of $[Os(bpy)_2$ 3,5-bis(pyridin-4-yl)-1,2,4,-triazole Cl] where counterion movement limits the rate of charge transport [10] The D_{CT} is 6 3x10^{-12} cm^2s^{-1} in 1 0 M $HClO_4$, i e , more than three orders of magnitude smaller than those found here

The large k_{SE} most likely arises because the redox centers are immobilized within an ordered crystalline array in which individual sites are linked by hydrogen bonds between protonated and deprotonated methoxy groups The ability to rapidly switch the redox composition of these solid deposits in a highly reversible way makes them attractive for electrochromic and supercapacitor applications The D_{CT} sensitivity most likely arises because the methoxy groups are deprotonated for $[HClO_4] \leq 0\ 6$ M but tend to become protonated at higher concentrations This protonation reaction will create a hydrogen-bonded network that supports more rapid electron transfer between the sites Similar

findings for proton induced changes in Hydroquinone and Bipyridyl Triazole (HQBpt) leading to increased D_{CT} in acid electrolyte have been reported [2]

3 11 Ion Pairing Effects

The formal potential of the complex is sensitive to the concentration of the supporting electrolyte Shifts in formal potential with changes in electrolyte concentration is due to movement of charge compensating counterions into and out of the deposit as the redox composition is switched Therefore, the electrolyte concentration dependence of $E^{o\prime}$ was examined for reactants in solution and in the solid phase to obtain an insight into the effects of immobilization on the extent of ion pairing Figure 3 19 shows that $E^{o\prime}$ for the solid deposits shifts in a negative potential direction with increasing log $[ClO_4]$ where the pH of the supporting electrolyte is fixed at 1 0±0 1

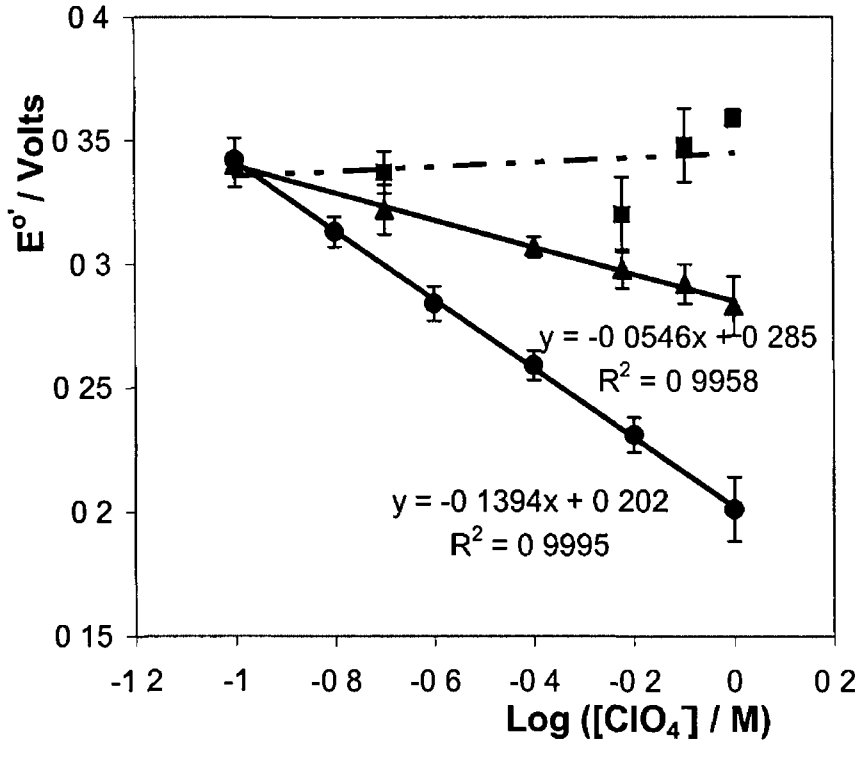

Figure 3 19 Dependence of the formal potential on the concentration of $HClO_4$ as supporting electrolyte for $[Os(OMe\text{-}bpy)_3]^{2+}$ solid deposits (■) and dissolved in acetonitrile (●) while (▲) denotes the effect of increasing the $NaClO_4$ concentration for the solid deposit in a fixed background of 0 1 M $HClO_4$

Consistent with ion pairing, it becomes progressively easier to oxidize the deposits with increasing perchlorate concentration This situation is summarized in the following reaction

$$[Os(OMe\text{-}bpy)_3]^{2+}(X^-)_q - e + n(X^-) \leftrightarrow [Os(OMe\text{-}bpy)_3]^{3+}(X^-)_{q+n}$$

where both redox forms are considered to participate in both the ion-pairing equilibria The formal potential, E^0, can be related thermodynamically to the electrode potential, E, through the Nernst equation

$$E^0 = E - (2.303RT/nF)\log [ClO_4^-] \quad (4)$$

R is the gas constant, K the Kelvin temperature, n the number of electrons transferred between the oxidised and reduced species and F the Faraday constant The equation can be simplified slightly by combining constants At 25°C, the term 2 303RT/F is equal to 0 0591 V, so

$$E^0 = E - (0.0591/n)\log [ClO_4^-] \quad (5)$$

From a plot of formal potential, E^0, versus logarithmic ClO_4^- concentration, the Nernst equation predicts a slope of –59/p mV per decade change in $[ClO_4^-]$ The experimentally observed slope, -55±4 mV dec^{-1} is consistent with the Os^{3+} form becoming ion-paired with a single extra anion However, as shown in the following reaction, the complexes used to form these deposits are also capable of undergoing acid/base reactions

$$[Os(OMe\text{-}bpy)_3]^{2+}(X^-)_q + H^+ + r(X^-) \leftrightarrow [Os(H\,OMe\text{-}bpy)_3]^{3+}(X^-)_{q+r}$$

where both redox forms are considered to participate in both the ion pairing and acid/base equilibria Therefore, if the oxidized form becomes ion-paired with two extra anions, one to compensate the charge on the electrochemically generated cation and a second to compensate for the protonated form, the Nernst equation predicts a shift of -118 mV per decade change in the perchloric acid concentration Figure 3 19 shows that

the slope observed for the complex dissolved in solution is -139±5 mV/decade, which is somewhat larger than that predicted by the Nernst equation for the situation where both ion pairing and protonation reactions occur In contrast, Figure 3 19 also shows that E°′ for the solid deposits remains constant as the perchloric acid concentration is increased from 0 1 to 1 0 M This observation suggests that in the solid state, the complex does not become protonated and that it exhibits little tendency to ion pair in either oxidation state

3 12 Heterogeneous Electron Transfer

The rate of heterogeneous electron transfer across the electrode/deposit interface influences the voltammetric response causing the voltammetric peak-to-peak separation to increase significantly [30] Figure 3 20 illustrates representative cyclic voltammograms at scan rates of 5 and 30 Vs^{1} which show that the ΔE_p values increase with increasing scan rate

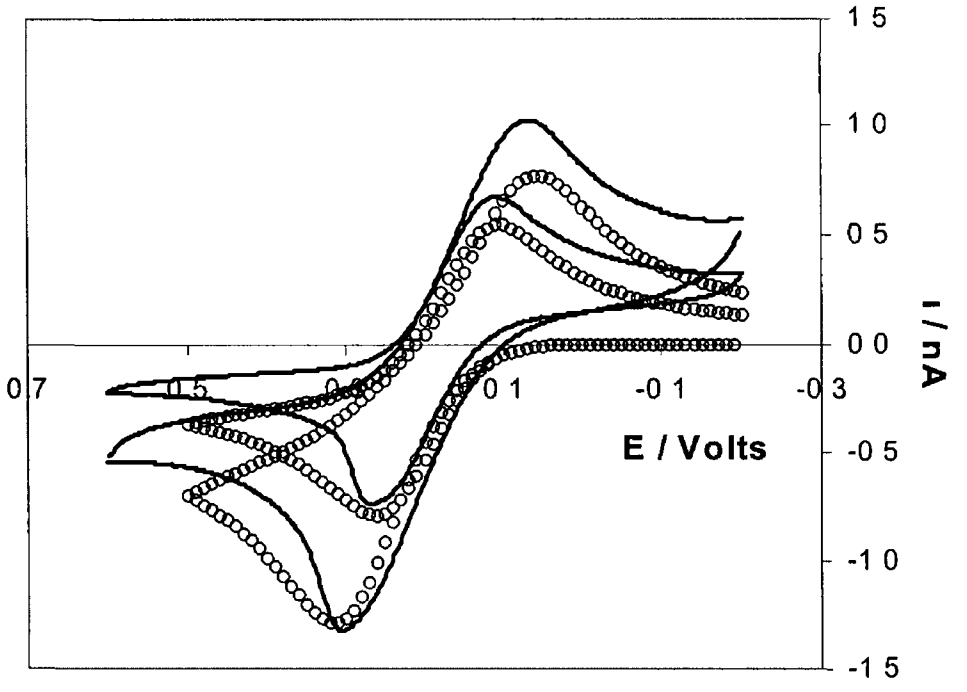

Figure 3 20 Cyclic voltammograms for a solid deposit of $[Os(OMe\text{-}bpy)_3]^{2+}$ on a 25 μm radius platinum microdisk electrode From top to bottom the scan rates are 30 and 5 Vs^{-1}, respectively Experimental data are denoted by the solid lines while the open circles represent theoretical fits generated according to the Butler-Volmer formalism of electrode kinetics where D_{CT} and k° are 1 1x10 $^{-9}$ cm^2s^{-1} and 1 0x10^{-4} cms^{-1}, respectively The supporting electrolyte is 1 0 M $HClO_4$

When measuring the heterogeneous electron transfer rate constant it is important to take into account factors that can also result in increasing peak-to-peak separation Ohmic effects represent a serious problem, not only because they will cause a significant ΔE_P to be observed even when heterogeneous electron transfer is fast, but also because the magnitude of the ohmic effect depends on the experimental timescale In the experiments reported here, microelectrodes and relatively high concentrations of supporting electrolyte have been used to avoid iR drop For example, as indicated in Table 1, the total resistance in this solution even with the modified electrode is 1430 Ω Therefore, even for the highest scan rate investigated, 100 Vs^{-1}, where the peak current is approximately 2 μA, the iR drop is less than 3 mV

Figure 3 20 illustrates theoretical fits to the experimental cyclic voltammograms generated according to the Butler-Volmer formalism of electrode kinetics [31] However, as a macroscopic model it does not consider a number of steps including mass transport, thermal fluctuations in electron donor and acceptor levels and timescale of electron transfer [32] However, this model does provide an experimentally accessible description of electrode kinetics The disadvantages of this formulation include the prediction that the rate constants increase exponentially with electrical driving force is only applicable experimentally over a limited range of overpotentials The Butler-Volmer model does not account for the known distance dependence of electrode electron transfer rates and the changes in either redox center structure or solvent that affect k^{o}

In fitting these voltammograms, the residual sum of squares between the experimental and theoretical oxidation currents were minimized and then the reduction branch of the voltammogram was predicted The satisfactory agreement observed between theory and experiment suggests that conventional solution phase models based on semi-infinite linear diffusion can adequately describe the voltammograms for the solid state films Moreover, the satisfactory fits suggest that the films are solvated and that electrochemical double layer sets up at the electrode/layer interface

This conclusion is consistent with the observation that the formal potentials of solution phase and solid deposits are similar For $5<\upsilon<100$ Vs^{-1}, the best fit simulated voltammogram is obtained where D_{CT} is 1.1×10^{-9} $cm^2 s^{-1}$ and a standard heterogeneous

electron transfer rate constant, k°, is $1.0 \pm 0.05 \times 10^{-4}$ cms^{-1}. The diffusion coefficient obtained by fitting the complete voltammogram is similar to that using the Randle-Sevçik analysis, $13.1 \times 10^{-9} \pm 0.5$ cm^{2}s^{-1}. Significantly, the standard heterogeneous electron transfer rate constant is independent of the scan rate indicating that the layers are kinetically homogeneous. The observation that the rate constants for all redox centers capable of undergoing heterogeneous electron transfer are experimentally indistinguishable suggests that the local microenvironments, electron transfer distances and reorganization energies are identical for individual redox centers.

Immobilizing the complex as a solid layer on an electrode surface could alter the microenvironment of the redox centers, e.g., by changing the dielectric constant, or the electron transfer distance. An insight into the importance of these effects for the $[Os(OMe\text{-}bpy)_3]^{2+}$ system can be obtained by comparing k° values obtained for solid and solution phase reactants. Figure 3.21 illustrates cyclic voltammograms for the complex dissolved in acetonitrile where the scan rate is sufficiently large so as to influence the voltammetry. Fitting these solution phase voltammograms reveals diffusion coefficients, D_{Soln}, and standard heterogeneous electron transfer rate constants, $k_{Soln}°$, of $5.0 \pm 0.3 \times 10^{-6}$ cm^{2}s^{-1} and $6.1 \pm 0.2 \times 10^{-5}$ cms^{-1}, respectively.

However, the k° values for the solid and solution phase reactants cannot be compared directly because of the different double layer structures and reactant mobilities under the two circumstances. However, it is striking that the k° values obtained for solution and solid phase reactants are very similar with $k_{Soln}°$ being only 30% smaller than that found for the solid layer. This means that electron transfer from the electrode to the redox active species is similar in solid and solution phase.

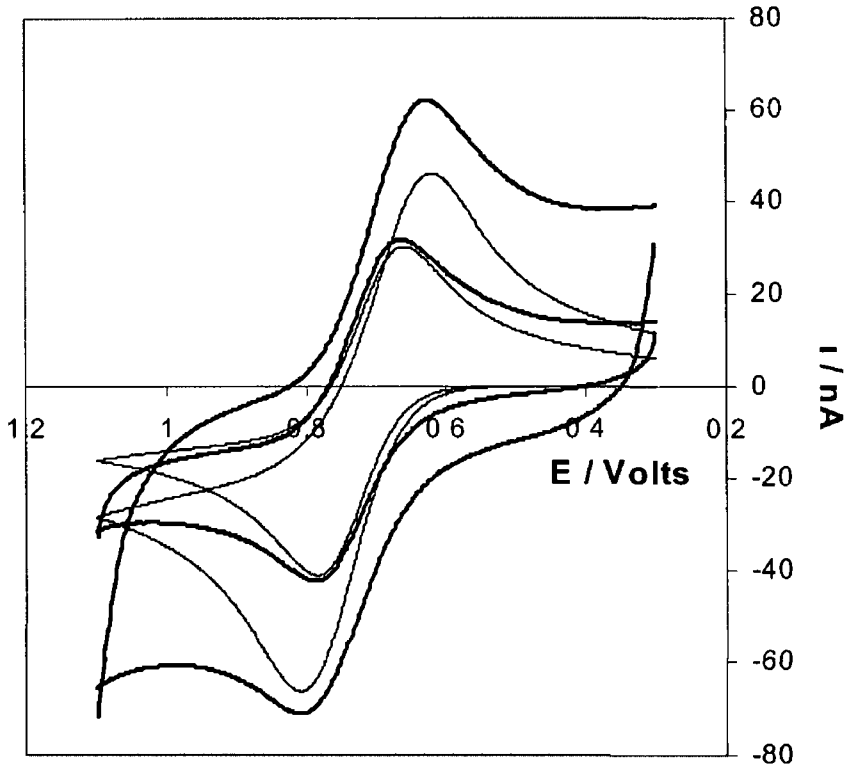

Figure 3 21 Cyclic voltammograms for a 5 mM solution of $[Os(OMe\text{-}bpy)_3]^{2+}$ m acetonitrile The working electrode is a 25 μm radius platinum microdisk From top to bottom the scan rates are 30 and 5 Vs^{-1}, respectively Experimental data are denoted by the thick solid lines while thin lines are theoretical fits generated using to the Butler-Volmer formalism of electrode kinetics D_{Soln}, and $k_{Soln}°$ are 5.0×10^{-6} $cm^2 s^{-1}$ and $6.1 \pm 0.2 \times 10^{-5}$ cms^{-1}, respectively

3 13 Conclusion

Mechanically attached, solid deposits of $[Os(OMe\text{-}bpy)_3](PF_6)$ where OMe-bpy is 4, 4'-dimethoxy, 2-2'-diptridyl have been formed on platinum microelectrodes Solid phase voltammetry is another means for examining this compound as it has a similar formal potential and cyclic voltammetry shape to that of its solution phase counterpart The formal potential similarity indicates that the local solvation and the dielectric constants are analagous Initial voltammograms of the layer in acidic electrolyte suggests that the layer undergoes a 'break in' step This 'break in' step is observed in voltammetry in the anodic direction during the initial 100 cycles

Counterion movement within the layer during electrochemical cycling brings about changes in the morphology of the deposit Scanning Electron Microscopy reveals that electrochemically cycling the deposits in $HClO_4$ triggers electrocrystallization forming a plate-like structure However, no noticeable changes were observed in the layer when cycled in neutral electrolyte It is probable that protonation of the methoxy groups encourages bonding between complexes thus promoting the formation of crystals The hydrogen-bonded network that forms within the layer may contribute to its increased stability in acidic electrolyte when compared to that of cycling in neutral electrolyte

For the solid deposit in $HClO_4$, the diffusion coefficient is $1\ 5\pm0\ 1x10^{-9}$ cm^2s^{-1} for $0\ 1\leq[HClO_4]\leq0\ 6$ M and above 0 6 M $HClO_4$ it increases to $13\pm1x10^{-9}$ cm^2s^{-1} in 1 0 M $HClO_4$ Given that D_{CT} is independent of electrolyte for $0\ 1\leq[HClO_4]\leq0\ 6$ M, and dependent on electrolyte concentration above 0 6 M, k_{SE} value obtained does not allow conclusions to be drawn on whether counterion motion or electron transfer limits the overall rate of charge transport The heterogeneous electron transfer rate constants are indistinguishable for solid and solution phase reactants being $1\ 0\pm0\ 05x10^{-4}$ cms^{-1} and $6\ 1\pm0\ 2x10^{5}$ cms^{-1} respectively For practical applications in areas such as electrochromic devices or energy storage devices, the charge transport activities of this material as a solid could have wide applicability It could also play a crucial role as a mediator on biosensors for the analysis of biological molecules

3 14 References

(1) Kulesza, P J , Faulkner, L R *J Am Chem Soc* , **1993**, 115, 11878

(2) Keyes, T E , Forster, R J , Bond, A M , Miao, W *J Am Chem Soc* , **2001**, 123, 2877

(3) Moulzolf, S C , LeGore, L J , Lad, R *J Thin Solid Films*, **2001**, 400, 56

(4) Inoue, M , Cruz-Vazquez, C , Inoue, M B *Syn Metals*, **1993**, 57, 3748

(5) Quaranta, F , Rella, R , Siciliano, P , Capone, S , Epifani, M , Vasanelli, L , Licciulli, A , Zocco, A *Sensors and Actuators B* **1999**, 350

(6) Ni, J , Ju, H , Chen, H , Leech, D *Anal Chim Acta* **1999**, 378, 151

(7) Bond, A M , Cooper, J B , Marken, F , Way, D M *J Electroanal Chem* **1995**, 396, 407

(8) Wightman, R M , Wipf, D O *Electroanalytical Chemistry*, vol 15, Bard, A J Ed , Marcel Dekker, New York, 1989

(9) Deuber, R E , Bond, A M , Dickens, P G *J Electrochem Soc* **1992**, 139, 2363

(10) Forster, R J , Keyes, T E *Phys Chem Chem Phys* **2001**, 3, 1336

(11) Bard, A J , Faulkner, L R Electrochemical Methods Fundamentals and Applications, Wiley, New York, 1980

(12) Dostal, A , Schroder, U , Scholz, F *Inorg Chem* , **1995**, 34, 1711

(13) Bond, A M , Scholtz, F *Langmuir* **1991**, *7*, 3197

(14) Dostal, A , Meyer, B, Scholz, F , Schroder, U , Bond, A M , Marken, F , Shaw, S *J Phys Chem* **1995**, *99*, 2096

(15) Hong, S H , Evans, D H , Nelsen, S F , Ismagilov, R F *J Electroanal Chem* **2000**, *486*, 75

(16) Shklover V , Zakeeruddin, S M , Nesper, R , Fraser, D , Gratzel, M *Inorg Chim Acta* **1998**, *274*, 64

(17) Forster, R J , Keyes, T E , Bond, A M J Phys Chem B 2000, 104, 6389

(18)Zakeeruddin, S M , Fraser, D M , Nazeeruddin, M-K , Gratzel, M J *Electroanal Chem* **1992**, 337, 253

(19) Bond, A M , Marken, F *J Eolectroanal Chem* **1994**, 372, 125

(20) Forster, R J *Chem Soc Rev* **1994**, 289

(21) Whitely, L D , Martin, C R *J Phys Chem* **1989**, 93, 4650

(22) Forster, R J, Keyes, T E , Bond, A M *J Phys Chem B* **2000**, 104, 6389

(23) Shklover, V , Zakeeruddin, S M , Nesper, R , Fraser, D , Gratzel, M *Inorg Chim Acta* **1998**, 274, 64

(24) Juris, F , Balzani, V , Barigelletti, F , Campagna, S , Belser, P , Von Zelewsky, A Coord Chem Rev 1998, 82, 85

(25) Dahms, H *J Phys Chem* **1968**, *72*, 362

(26) Ruff, I , Friedrich, V J , Demeter, K , Csillag, K *J Phys Chem* **1971**, *75*, 3303

(27) Chan, M S , Wahl, A C *J Phys Chem* **1978**, *82*, 2542

(28) Charych, D H , Majda, *Thin Solid Films* **1992**, *210*, 348

(29) Charych, D H , Anvar D J , Majda, M *Thin Solid Films* **1994**, *242*, 1

(30) Lee, W –Y , Majda, M , Brezesinski, G , Wittek, M , Mobius, D *J Phys Chem B* **1999**, *103*, 6950

(31) Garay, F , Solis, V , Loviré, M *J Electroanal Chem* **1999**, 478, 17

(32) Forster, R J The Electrochemical Society *Interface,* Winter **2000**, 24

Chapter 4

Nanoparticle-Metallopolymer Assemblies Charge Percolation and Redox Properties

4 1 Introduction

The electrochemical properties of solid deposits of $[Os(OMe\text{-}bpy)_3]^{2+}$ were discussed in Chapter 3 The ingress/egress of counter ions to balance the charge created by the charging of the osmium center during electrochemical cycling changed the deposit morphology The protonated OMe substituents possibly create a network between the molecules thus promoting the formation of crystals when cycled in $HClO_4$ The protonation creates a hydrogen-bonded network that supports a rapid electron transfer between the redox sites as a result of the large self-exchange rate constant, k_{SE}, and diffusion coefficient, D_{CT}

The charge transport properties of polymers are pivotal to battery and molecular electronic research [1 2] The charge transport properties can be modified with the introduction of nanoparticles and can influence the research fields of catalytic synthesis and sensor development [3 4,5] Nanoparticles have unique optical,[6] electric[7] and magnetic properties [8] High reactivity and aggregation[9] issues have increased research of self-assembled monolayers[10 11 12] and functional polymers for controlling interparticle interactions [13] It has been known for a very long time, empirically, that the addition of certain natural biopolymers such as gelatine can stabilise colloidal dispersions The formation of a protective sheath around the each colloid particle prevents aggregation [14]

Polymers, such as poly-vinyl pyrrolidone,[15 16] that incorporate surface active functional groups[17] have proven to have useful properties not only in the production of tightly distributed nanoparticles of controlled size, but the resulting composite materials have attractive electrical and optical properties [18] However, the use of metallopolyers that contain not only surface active functional groups but also redox active centers, such as transition metal complexes, have not been widely explored in this context This situation is surprising given that the redox centers would be expected to influence nanoparticle growth, e g by mediating the reduction of the precursor salt, and the combination of both metal nanoparticles and complexes ought to lead to unique redox and conductivity effects In particular, the ability to modulate the local microenvironment of the nanoparticles and hence their reactivity by electrochemically switching the oxidation state of the redox centers is especially attractive

Charge transport through nanoparticle structures is of particular interest because of its importance in possible future device technologies Nanoparticles are referred to as artifical atoms because of their hydrogen like electronic structure due to the similarity in reactions of colloidal particles and are composed of thousands of metal atoms These tiny crystals range in size from 1 to 100 nanometers and confine electrons on the nanometer scale As a result these nanoparticles display unusual properties Single electron properties of nanoparticles have been examined through scanning tunneling microscopy measurements [19 20] Schiffrin et al have demonstrated that through STM, organic molecules containing redox centres can be used to attach metal nanoparticles to electrode surfaces and so control the electron transport between them [21]

In this chapter, the voltammetric properties of the redox active metallopolymer $[Os(bpy)_2\ (PVP)_{10}\ Cl]^+$, bpy is 2,2' bipyridyl and PVP is poly(4-vinly pyridine) are reported, as a coating on platinum disk and cylinder microelectrodes and as metallopolymer-nanoparticle composites The rigid nature of the metallopolymer were explored through the 'break in' and counterion ion effects The voltammetry of the metallopolymer on the platinum disk and cylinder microelectrode were compared Different diffusion charge transport coefficients were calculated for the two electrode types The similarity in the self exchange rate constants for the metallopolymer on the cylinder and disk electrode indicated that the inter redox active sites separation in the metallopolymer were indistinguishable on both electrode surfaces

Thin films of both the metallopolymer and composites exhibit nearly ideal voltammetric responses and cyclic voltammetry has been used to investigate their charge transport properties when in contact with an aqueous electrolyte solution Scan rates of 100 mVs^{-1} were utilized to determine the total surface area of the electrochemically active gold nanoparticles within the composites Probing the electrolyte concentration dependence on the formal potential of the metallopolymer-nanoparticle assembly can give insight to ion-pairing effects and the permeability towards counterions Analogous to the solid state $[Os(OMe\text{-}bpy)_3]^{2+}$ analyzed in Chapter 3, evaluating the homogeneous charge transport diffusion coefficient through the composites and metallopolymer was performed under semi-infimte linear diffusion conditions Polymer chains movement, [22] counterion diffusion/migration, [23,24] or electron hopping [25 26] could limit homogenous charge transport through the films and have been determined from observations of the

charge transport diffusion coefficient To gain an insight into the role of the osmium bipyridyl redox centers in electrical conduction, the dry state conductivity has been determined as a function of the nanoparticle loading for both the metallopolymer and PVP composite systems Both systems data can be described using the percolation theory[27 28] for a randomly dispersed electrically conducting filler, but the metallopolymer system exhibits significantly higher conductivity for all loadings investigated

Beyond probing the homogeneous charge transport diffusion coefficient as a function of nanoparticle loading and electrolyte concentration, the standard heterogeneous electron transfer rate, k° has also been determined These data are revealing of the differences between electrode/metallopolymer film and electrode/composite interfaces Heterogeneous electron transfer across the electrode/film interface depends on the electrode-reactant separation, the chemical composition, and the effective dielectric constant of the film, which are also influenced by the presence of the gold nanoparticles [29]

4 2 'Break In' and Counterion Effects of $[Os(bpy)_2 (PVP)_{10} Cl]^+$

Solvent transport studies of $[Os(bpy)_2 (PVP)_{10} Cl]^+$ have been undertaken previously [30] and Kelly et al have reported that the layers are rigid in $HClO_4$ electrolyte due to the chemical nature of both the electrolyte anion and the polymer backbone [31] 'Break-in' effect is an indication as to how solvated the material becomes when initially electrochemically cycled in supporting electrolyte and is a phenomena observed for the solid state, $[Os(OMe\text{-}bpy)_3]^{2+}$ in Chapter 3 Figure 4 1 illustrates that solvation effects are minimal when the metallopolymer is electrochemically cycled in the electrolyte as there is little or no voltammetric distortions evident

SEM imaging was performed on the polymer film to identify any morphology changes that may occur in the film after voltammetric cycling in perchloric acid Figure 4 2 is the image of the metallopolymer prior to cycling with no exposure to electrolyte and Figure 4 3 illustrates the film after cycling in 0 1 M $HClO_4$ for 200 cycles Unlike the SEM images of the solid $[Os(bpy\text{-}OMe)_3]^{2+}$ in Chapter 3 there is no appreciable change in film morphology prior to and following electrochemical cycling indicating that counterion/solvent movement or protonation within the layer does not cause appreciable structural changes to the metallopolymer The cracks evident in both images arise from the rapid solvent drying of the polymer after application on the graphite disks In conclusion, because of the chemical nature of both the electrolyte anion and polymer backbone, the layers are rigid in $HClO_4$ electrolyte

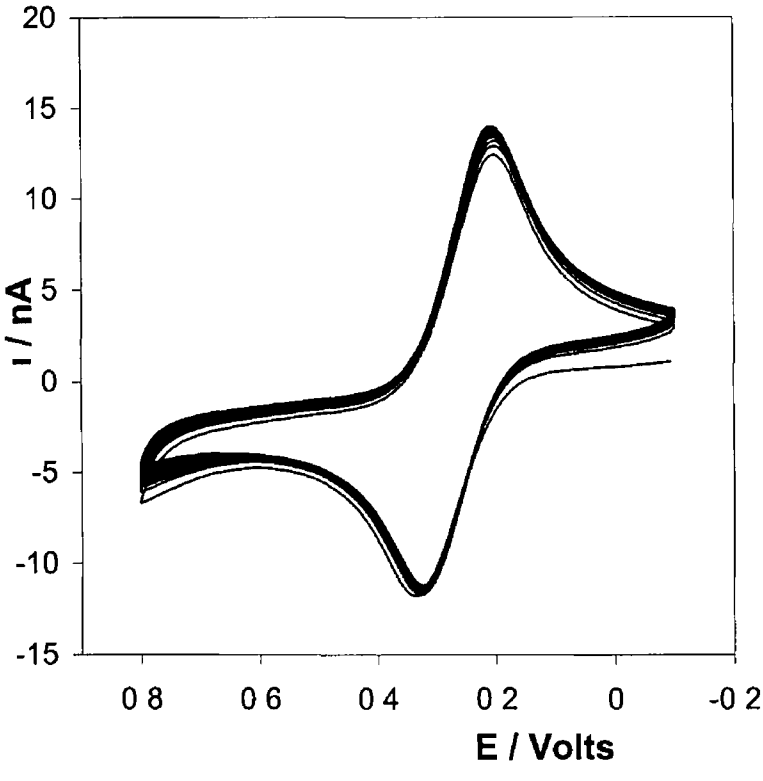

Figure 4 1 Initial cyclic voltammograms for $[Os(bpy)_2 (PVP)_{10} Cl]^+$ metallopolymer layer for 25 scans immobilized on a 25 μm platinum disk electrode The supporting electrolyte is 0 1 M $HClO_4$ and the scan rate is 100 mVs^{-1} Surface coverage is $1\ 5 \pm 0\ 2 \times 10^{-8}$ mol cm^{-2}

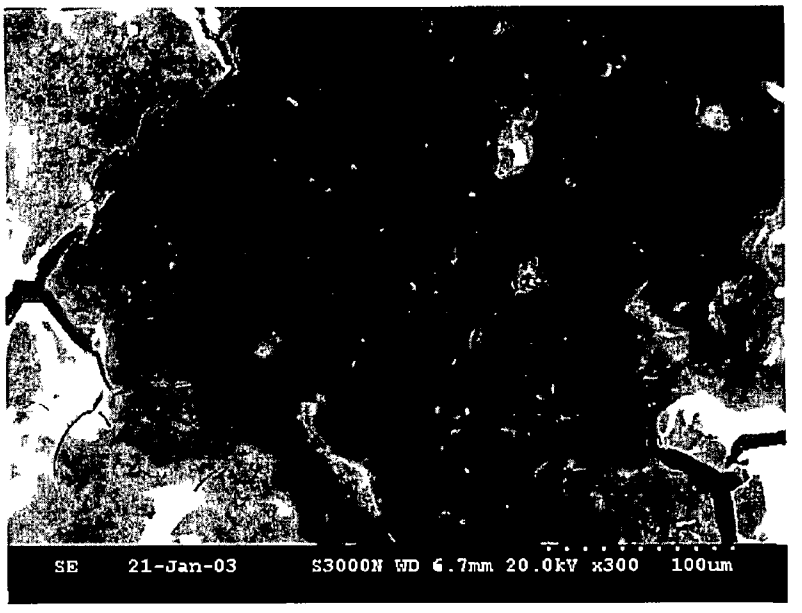

Figure 4 2 SEM image of $[Os(bpy)_2 (PVP)_{10} Cl]^+$ film as deposited as a paste in ethanol, before electrochemical cycling

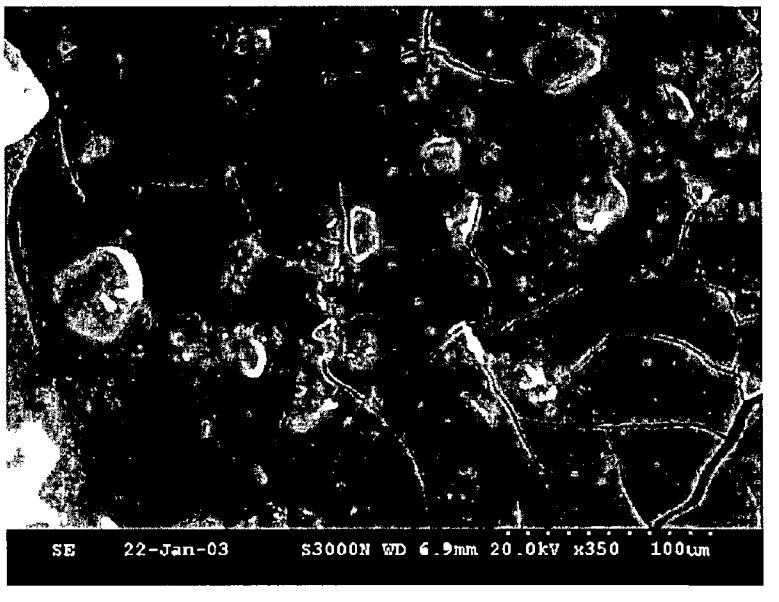

Figure 4 3 SEM image of $[Os(bpy)_2 (PVP)_{10} Cl]^+$ film after 200 voltammetric cycles between 0 and 0 8 V in 0 1 M $HClO_4$ at a scan rate of 0 1 Vs^{-1}

4 3 Metallopolymer and Metallopolymer Nanoparticle Redox Properties

Figure 4 4 illustrates the overlays of the electrochemical responses of the cylinder and disk electrodes modified with a layer of the metallopolymer $[Os(bpy)_2\ Cl\ (PVP)_{10}]^+$ in 0 1 M $HClO_4$ As expected the cyclic voltammograms of both electrode types are very similar with the formal potentials, $E^{0'}$, as given by the average of the anodic and cathodic peak potentials, 0 265 V and 0 263 V for the cylinder and disk electrode, respectively The peak-to-peak separation, ΔE_p, between the anodic and cathodic waves is 87 mV and 107 mV for the cylinder and disk electrode respectively According to the Nernst equation, ΔE_p of 59 mV is expected for an ideal for a one electron oxidation/reduction reaction The deviations from the ideal value are expected to be predominantly due to stray capacitance and double layer charging On the other hand, the ratio of the anodic peak current to the cathodic peak current in both cases, i_{pa}/i_{pc} is close to unity, which is expected for a chemically reversible, stable product Overall, because the cylinder microelectrode has greater surface area, there is a greater current signal for the immobilised metallopolymer The limits in the voltammograms are different but no other redox activity was detected beyond the Os^{2+}/Os^{3+} potentials

Figure 4 5 shows typical slow scan rate cyclic voltammograms for an $[Os(bpy)_2\ (PVP)_{10}\ Cl]^+$ metallopolymer film and for a nanoparticle metallopolymer composite electrode in which the mole fraction of the metallopolymer is 0 84 The mole fraction is defined ad the number of moles of a component of a solution divided by the total number of moles of all components In Figure 4 5, the supporting electrolyte is aqueous 0 1 M $HClO_4$ and the surface coverage is $2\ 0\pm0\ 2x10^{-8}$ mol cm^{-2} The surface coverage (Γ) is calculated from the area under the voltammetric peak [32]

$$\Gamma = \frac{Q}{nFA} \qquad (1)$$

where Q is the total charge required to reduce or oxidise the electroactive species, n is the number of electrons transferred, F is Faraday's constant and A is the area of the electrode For both the metallopolymer and the nanoparticle metallopolymer composite, the voltammetric response associated with the $Os^{2+/3+}$ couple centered at approximately

0 3 V is close to that expected for an immobilized, electrochemically reversible couple under finite diffusion conditions [33,34] For example, for the composite the peak shape is independent of the scan rate, υ, up to at least 25 mVs^{-1}, and the peak height scales linearly with scan rate from 1–25 mVs^{-1} The ratio of the anodic to cathodic peak currents is 1 0±0 05 Thus, beyond a persistent peak-to-peak separation, ΔE_p, of approximately 50 mV that is observed for both systems even at very slow scan rates, the voltammetric response is nearly ideal Also, some diffusion like tailing is observed especially for the pure metallopolymer which is attributed to spillover of the polymer film onto the non-conducting glass shroud

In strongly acidic media, the composite electrode exhibits well defined responses at positive potentials corresponding to the formation of gold oxide on the metal nanoparticles and its subsequent re-reduction For a polycrystalline gold surface, the charge passed during the reduction of a monolayer of gold oxide[35] is 390 $\mu F\ cm^{-2}$ Therefore, the area under the oxide reduction peak, Figure 4 6, has been used to determine the total surface area of the electrochemically active gold nanoparticles within the composite For the nanoparticle metallopolymer composite where the mole fraction of the metallopolymer is 0 84, the area obtained is $6\ 2x10^{-6}\ cm^2$ This area is indistinguishable from that expected, $6\ 8x10^{-6}\ cm^2$, on the basis of the known quantity of tetrachloroaurate reduced and the radius of the nanoparticle obtained from TEM (Section 4 5) This result suggests that even at low nanoparticle densities, an interconnected array is formed perhaps involving the osmium redox centers mediating electron transfer between the gold nanoparticles so that a gold oxide monolayer can be formed on nearly all of the particles The gold surface area as determined from the gold oxide reduction peak increases as the mole fraction of the metallopolymer is decreased, e g , where x is 0 02, the area is $1\ 2x10^{-5}\ cm^2$

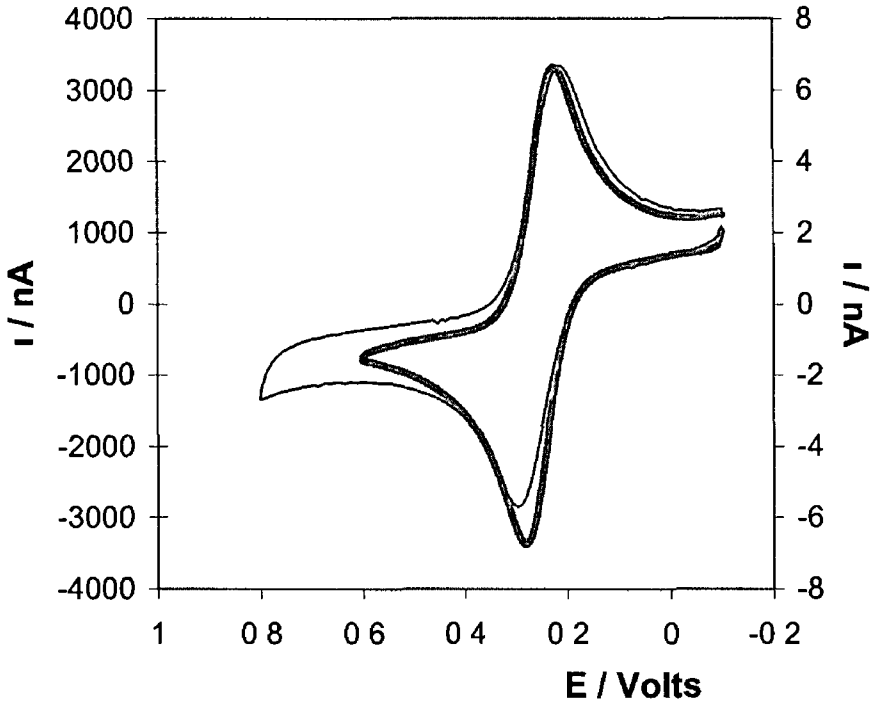

Figure 4 4 Cyclic Voltammograms for $[Os(bpy)_2\ Cl\ (PVP)_{10}]^+$ film coated on a 25 μm diameter platinum electrode disk electrode (thin line) and platinum cylinder microelectrode (thick line) The areas of the electrodes are $4\ 9 \times 10^{-6}$ cm^2 and $9\ 4 \times 10^{-3}$ cm^2 respectively where the cylinder length is 1 2 cm Surface coverages are $8\ 5 \times 10^{-9}$ mol cm^{-2} for the disk electrode and $9\ 9 \times 10^{-10}$ mol cm^{-2} for the cylinder electrode In both cases the supporting electrolyte is 0 1 M $HClO_4$ and the scan rate is 100 mVs^{-1}

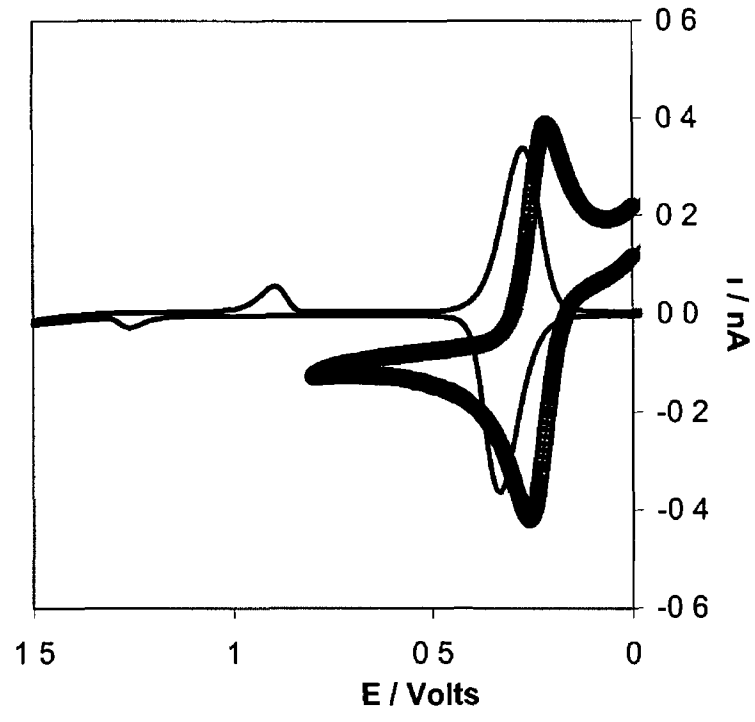

Figure 4 5 Cyclic voltammograms under finite diffusion conditions for an $[Os(bpy)_2 (PVP)_{10} Cl]^+$ film (thick line) and a nanoparticle metallopolymer composite film (thin line) where the mole fraction of metallopolymer is 0 84 In both cases, the supporting electrolyte is aqueous 0 1 M $HClO_4$, the surface coverage is $2\ 0\pm0\ 2x10^{-8}$ mol cm^{-2} and the working electrode is a 25 μm radius platinum microdisk The scan rate is 1 mVs^{-1} Extending the potential window for the metallopolymer on the disk electrode would reflect platinum oxidation / reduction activity

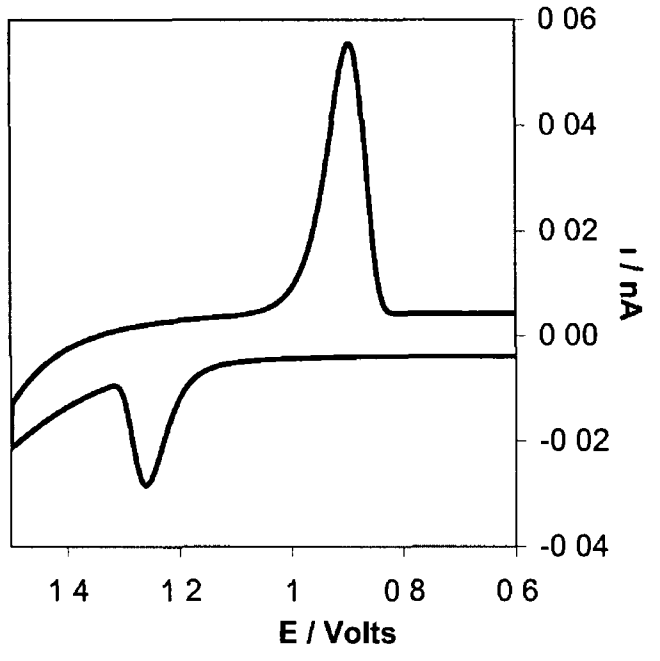

Figure 4 6 Enlargement of gold oxide formation / reduction region for the naoparticle metallopolymer composite from Figure 8 The supporting electrolyte is aqueous 0 1 M $HClO_4$, the surface coverage is 2 0±0 2x10 ^{8} mol cm ^{2} and the working electrode is a 25 μm radius platinum microdisk The scan rate is 1 mVs ^{1}

4 4 Film Resistance and Interfacial Capacitance

By examining the film resistance as a function of the supporting electrolyte concentration, it should be possible to probe the semi-permeable properties of the membrane [36 37] When a polyelectrolyte film is placed in a dilute solution of a strong electrolyte, the concentration of counterions within the film is typically considerably larger than that found in the contacting solution For these materials one might expect a high anion concentration (≈ 0 8 M) to be initially present in the film to compensate for the cationic osmium redox centers of the metallopolymer Thus, under the influence of the concentration gradient, counterions may diffuse from the film into the solution until the concentrations become equal in the two phases However, if diffusion of charged counterions occurs, then electroneutrality within the film would be violated, and an electrical potential would develop at the interface [38 39] This "Donnan potential" would then increase until an equilibrium was reached in which it completely opposed the tendency of the counterions to move down the concentration gradient Under these equilibrium conditions the net diffusion of counterions across the interface would be zero, and co-ions would be excluded from the polymer film [40]

The permselective response of the metallopolymer has been determined by measuring the total cell resistance as the supporting electrolyte concentration is changed In the case of an ideally permselective response, ions would be effectively excluded from the membrane, and the film resistance would be independent of the supporting electrolyte concentration Short timescale, small amplitude, potential step chronoamperometry was carried out to determine the total cell resistance of the metallopolymer film on the cylinder microelectrode The experiment involved stepping the potential from –60 mV to 0 mV at both bare and modified electrodes, and recording the resulting current over 40 μs, as shown in Figure 4 7 Figure 4 8 illustrates ln $i_c(t)$ vs time plots for the metallopolymer film as the $HClO_4$ concentration is adjusted from 0 1 to 0 6 to 1 0 M This response is described by Equation (3) [40]

$$i_c(t) = (\Delta E / R_u) \exp(-t / R_u C_{dl}) \qquad (2)$$

where ΔE is the pulse amplitude, R_u is the total cell resistance, i e , it includes contributions from both solution and film resistance, and C_{dl} is the integral double layer capacitance As shown in Figure 4 7 for the metallopolymer modified electrodes, the current decays in time according to a single exponential, which is consistent with double layer charging alone The absolute slope of these plots represents the reciprocal of the cell time constant R_uC_{dl} It is apparent from Equation (2) that R_u can be extracted from the intercepts of the insets of Figure 4 8

Table 1 presents R_uCdl values for a cylinder electrode before modification with the metallopolymer as a function of wire length and perchlorate concentration Table 2 represents R_uC_{dl} values for a cylinder electrode after modification with the metallopolymer Both tables show that both the bare and modified electrodes cell time constants decrease with increasing electrolyte concentration

Figure 4 9 shows the total cell resistance for a bare and modified electrode as the perchlorate concentration is systematically varied from 0 1 M to 1 0 M In both circumstances R_u is reduced at high electrolyte concentration reflecting a reduced solution resistance The cell resistance with the modified electrode is larger than that observed for the bare electrode over the range of electrolyte concentrations but the response time is more sensitive to the supporting electrolyte concentration for the microelectrode coated with the metallopolymer However, the cell resistance of the modified electrode is never more than 30 % larger for that observed with the bare electrode over the range of electrolyte concentrations This observation suggests that the solution resistance dominates the cell resistance for the modified electrode, and that the supporting electrolyte concentration within the film is relatively high

The dependence of the surface area of a bare and modified electrode at different electrode lengths with R_uC_{dl} is illustrated in Figure 4 10 In both cases the electrode surface area or the active electrode length is directly proportional to the cell time constant The R_uC_{dl} is more sensitive for the modified electrode at smaller surface areas The entire surface area of the electrode is active with the double layer capacitance increasing with the electrode length

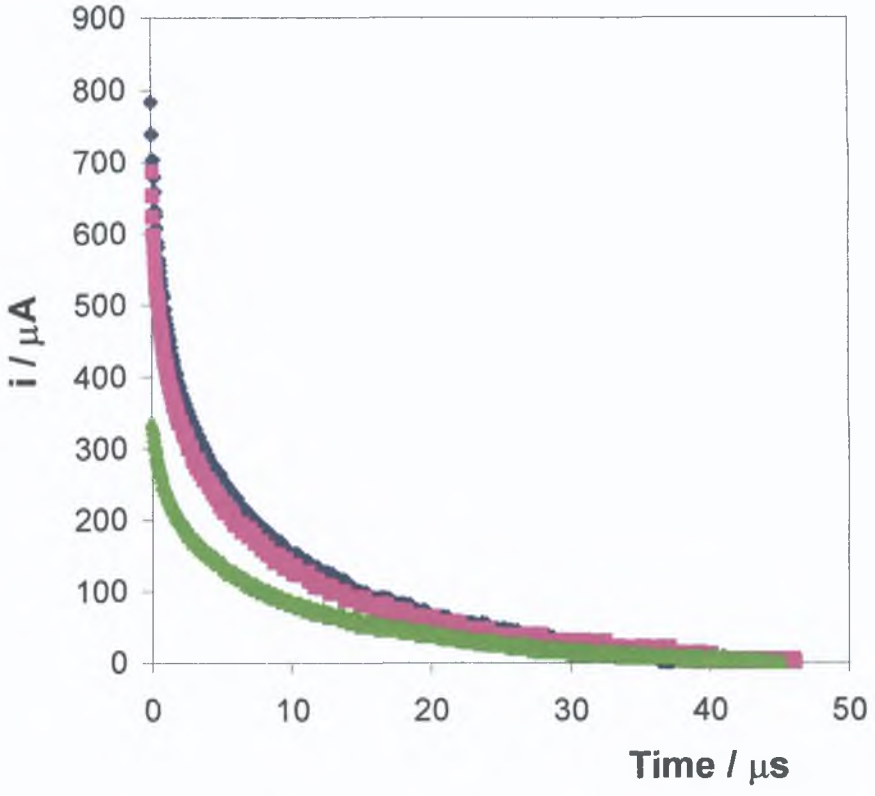

Figure 4.7. Current-time transients for a 25 μm diameter platinum microelectrode modified with metallopolymer following potential steps from –60 to 0 mV. The surface coverage is 1 x 10^{-9} mol cm^{-2}. The data correspond to aqueous 1.0 (♦), 0.6 (■) and 0.1 (▲) M $HClO_4$ as supporting electrolyte.

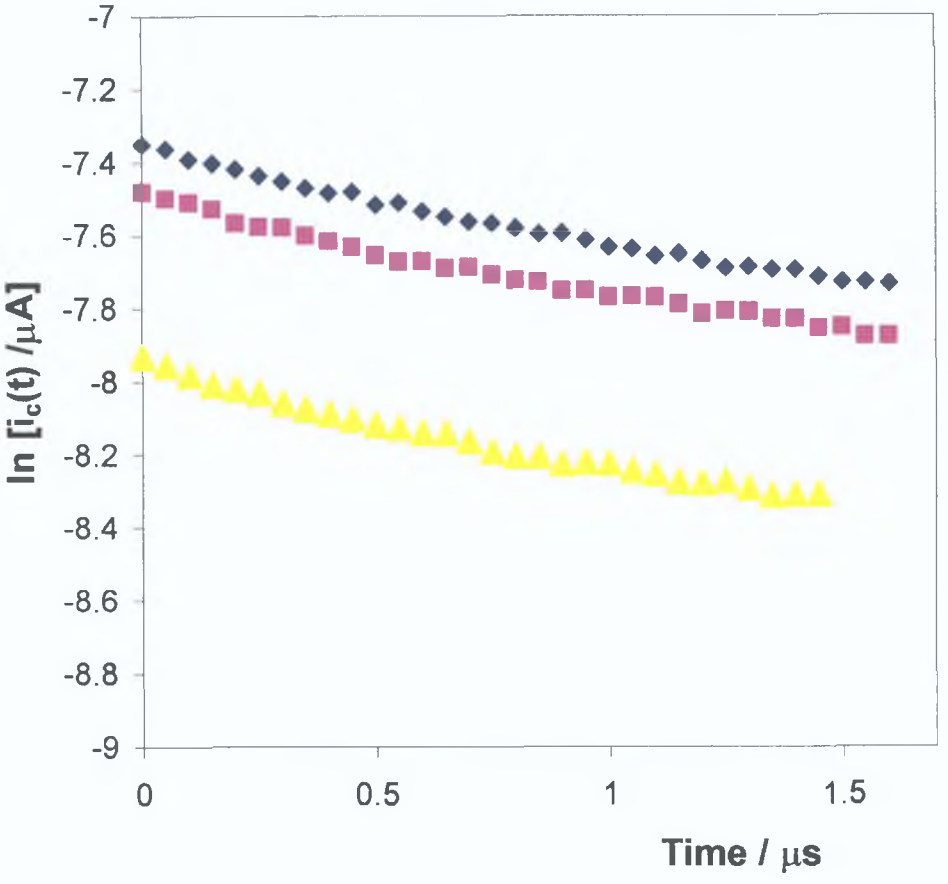

Figure 4.8. Semi-log current vs. time plots for a 25 μm diameter platinum microelectrode modified with metallopolymer following potential steps from –60 to 0 mV. The data correspond to aqueous 1.0 (♦), 0.6 (■) and 0.1 (▲) M $HClO_4$ as supporting electrolyte.

Table 1 Resistance, R_u, Double Layer Capacitance, C_{dl}, and electrode Response Times, R_uC_{dl} for 25 μm diameter platinum microelectrode before modification with film of $[Os(bpy)_2 (PVP)_{10} Cl]^+$ as the concentration of $HClO_4$ and cylinder length are varied

Bare				
$[HClO_4]$ / M	**Wire length / mm**	**R_u /10^{-4} Ω**	**C_{dl} /10^{-11}F**	**R_uCdl / μs**
0 1	3	6 6 (0 31)	4 6 (0 25)	3 02 (0 21)
	6	4 3 (0 21)	9 0 (0 50)	3 87 (0 19)
	12	3 5 (0 18)	13 5 (0 71)	4 71 (0 15)
0 2	3	4 5 (0 23)	4 8 (0 22)	2 16 (0 21)
	6	2 3 (0 12)	14 5 (0 83)	3 33 (0 18)
	12	1 8 (0 10)	21 1 (1 15)	3 79 (0 16)
0 6	3	4 0 (0 22)	5 0 (0 34)	1 99 (0 19)
	6	2 1 (0 12)	11 2 (0 68)	2 35 (0 17)
	12	1 7 (0 09)	19 2 (1 17)	3 26 (0 15)
0 8	3	2 2 (0 11)	5 9 (0 32)	1 31 (0 16)
	6	2 0 (0 10)	10 0 (0 61)	2 00 (0 15)
	12	1 7 (0 08)	18 0 (1 13)	3 06 (0 15)
1 0	3	2 0 (0 09)	5 9 (0 31)	1 18 (0 13)
	6	1 9 (0 09)	10 4 (0 55)	1 98 (0 12)
	12	1 6 (0 07)	17 6 (0 98)	2 82 (0 13)

* The numbers in parenthesis represent errors obtained by standard deviation from 3 independent experiments

Table 2 Resistance, R_u, Double Layer Capacitance, C_{dl}, and Electrode Response Times, R_uC_{dl} for 25 μm diameter platinum cylinder microelectrode after modification with film of $[Os(bpy)_2 (PVP)_{10} Cl]^+$ as the concentration of $HClO_4$ and cylinder length are varied

Modified				
$[HClO_4]$ / M	**Wire length / mm**	**R_u /10^{-4} Ω**	**C_{dl} /10^{-11} F**	**R_uC_{dl} / μs**
0 1	3	9 8 (0 5)	2 0 (0 1)	1 93 (0 09)
	6	7 8 (0 4)	2 8 (0 2)	2 21 (0 13)
	12	4 5 (0 3)	6 5 (0 3)	2 92 (0 16)
0 2	3	8 8 (0 5)	1 9 (0 1)	1 67 (0 09)
	6	5 4 (0 3)	3 6 (0 2)	1 96 (0 10)
	12	3 5 (0 2)	7 3 (0 4)	2 29 (0 12)
0 6	3	4 3 (0 3)	3 4 (0 2)	1 44 (0 08)
	6	3 1 (0 2)	6 2 (0 3)	1 91 (0 10)
	12	2 6 (0 1)	9 1 (0 5)	2 36 (0 12)
0 8	3	4 5 (0 2)	3 1 (0 2)	1 41 (0 07)
	6	3 0 (0 2)	6 3 (0 3)	1 86 (0 10)
	12	2 5 (0 1)	9 7 (0 4)	2 42 (0 11)
1 0	3	3 4 (0 2)	4 1 (0 2)	1 39 (0 07)
	6	2 5 (0 1)	7 4 (0 4)	1 85 (0 09)
	12	2 3 (0 1)	10 7 (0 6)	2 46 (0 12)

* The numbers in parenthesis represent errors obtained by standard deviation from 3 independent experiments

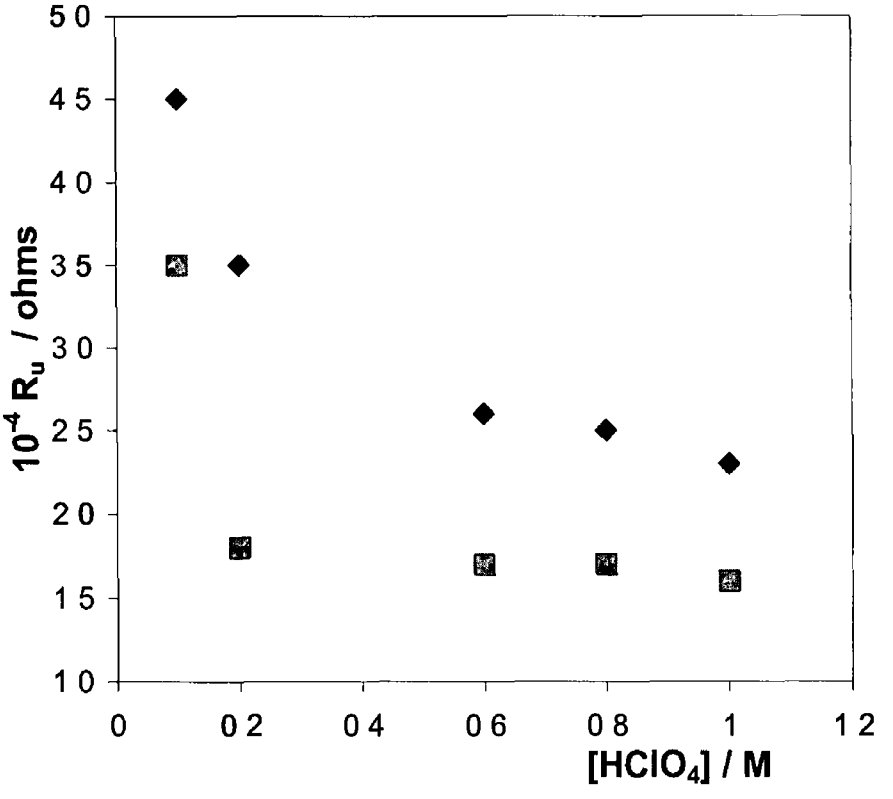

Figure 4 9 Dependence of the total cell resistance, R_u, on the concentration of $HClO_4$ as supporting electrolyte Data for a bare 25 μm diameter cylinder microelectrode are shown as (■) while (♦) represents the same microelectrode modified with an $[Os(bpy)_2 (PVP)_{10} Cl]^+$ film

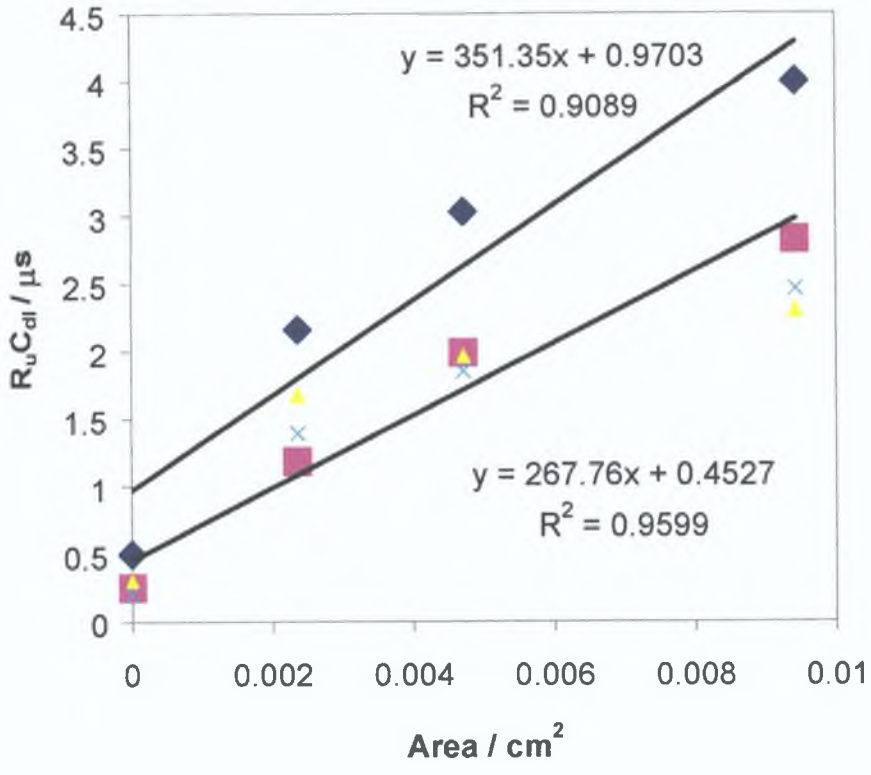

Figure 4.10. Dependence of the cell time constant R_uC_{dl} on the surface area of the electrode. Data for a bare 25 µm diameter electrode are (▲) in 0.2 M and (*) in 1.0 M $HClO_4$. (♦) and (■) represent the modified electrode in 0.2 M and 1.0 M $HClO_4$, respectively.

Likewise the total cell resistance of the nanoparticle metallopolymer composite was determined in a potential region where no Faradaic response is observed The potential was stepped from -100 mV to 0 mV at both bare and modified disk electrodes, and the resulting current was recorded over the following 5 μs, Figure 4 11 The presence of gold nanoparticles within the composite is likely to have a significant impact on the net diffusion of counterions across the interface as the nanoparticles may have negatively charged surfaces due to the borohydride reduction reaction used in their production

Figure 4 12 illustrates ln $i_C(t)$ vs t plots for a composite electrode in which the mole fraction of the metallopolymer is 0 02 as the $HClO_4$ concentration is systematically varied from 0 1 to 2 0 M Figure 4 12 shows the total cell resistance for a bare 12 5 μm radius microelectrode as well as a microelectrode coated with the metallopolymer and composite as the $HClO_4$ concentration is changed from 0 1 to 2 0 M It is apparent that in all circumstances R_u is reduced at high electrolyte concentrations reflecting a reduced solution resistance Significantly, the cell resistance for the metallopolymer coated electrode is consistently higher than that found for the bare or composite modified electrodes over the entire concentration range investigated This result suggests that the film resistance contributes to the overall cell resistance

However, in contrast to both the bare and composite modified electrodes, the metallopolymer film exhibits a pronounced sigmoidal dependence of R on [$HClO_4$] The inflection point, approximately 1 0 M, is consistent with the concentration of the osmium redox centers within the film and suggests that Donnan exclusion of co-ions breaks down in highly concentrated electrolytes The resistances observed for the composite are indistinguishable from those found for the bare electrode indicating that the contribution from film resistance is negligible for the metallopolymer nanoparticle material

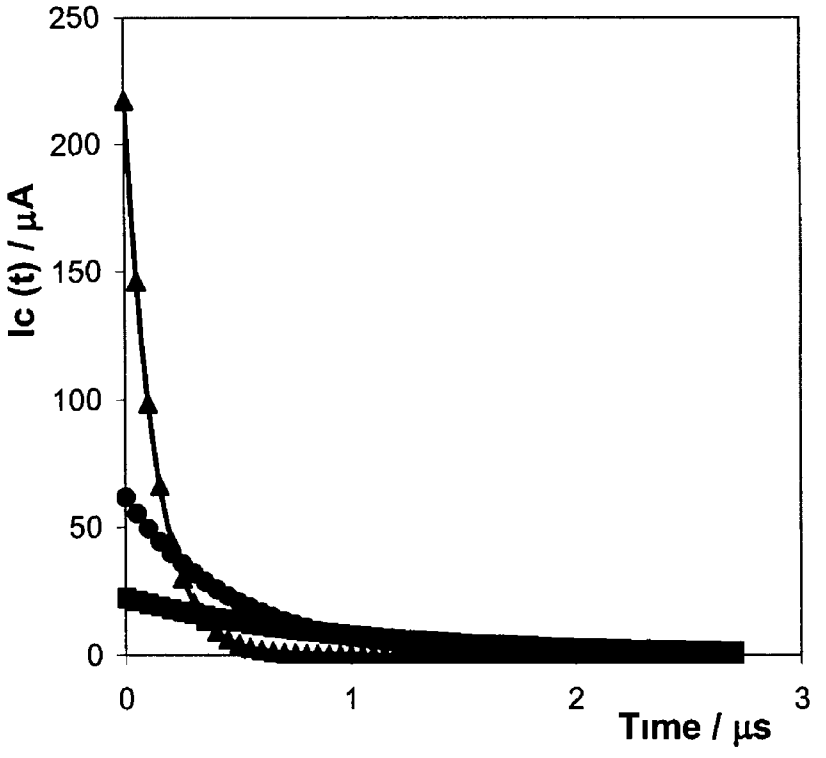

Figure 4 11 Current-time transients for a 25 μm diameter platinum microelectrode modified with a composite in which the mole fraction of metallopolymer is 0 2 following the potential steps from –0 050 to 0 000 V The data correspond to aqueous 0 1 (■), 0 5 (●) and 2 0 (▲) M $HClO_4$ as supporting electrolyte

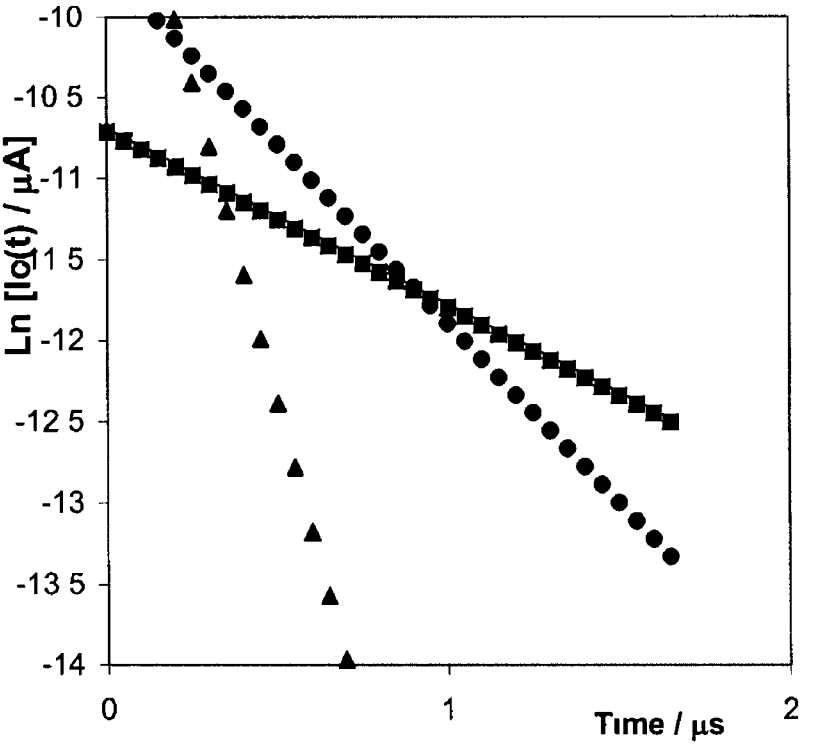

Figure 4 12 Semi-log current vs time plots for a 25 µm diameter platinum microelectrode modified with a composite m which the mole fraction of metallopolymer is 0 02 following the potential step from –0 050 to 0 000 V The data correspond to aqueous 0 1 (■), 0 5 (●) and 2 0 (▲) M $HClO_4$ as supporting electrolyte

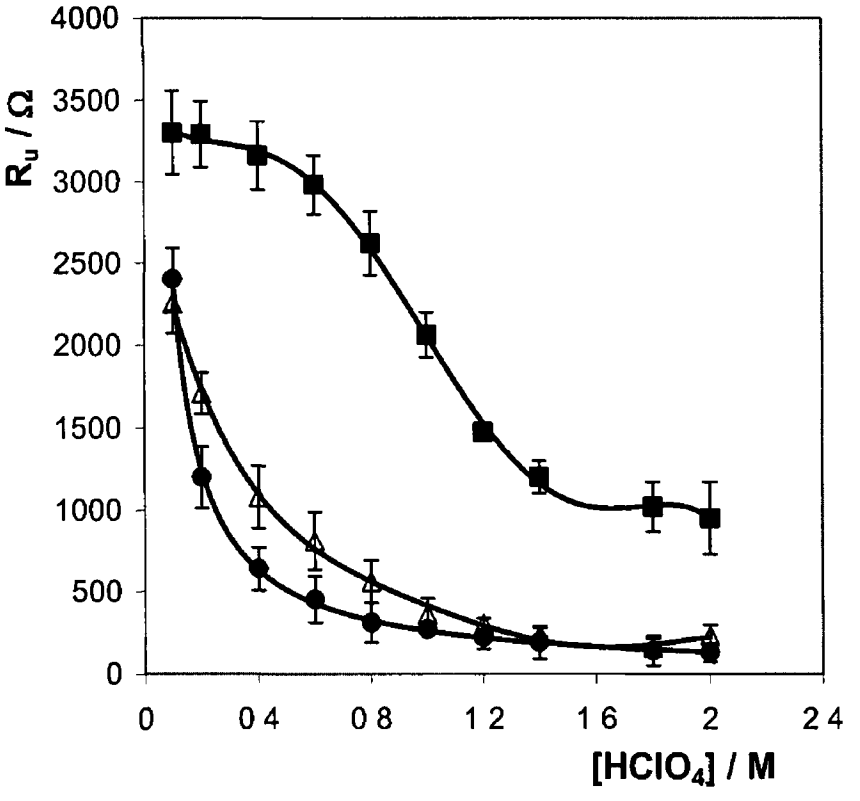

Figure 4 13 Dependence of the total cell resistance, R_u, on the concentration of $HClO_4$ as supporting electrolyte Data for a bare 25 μm diameter microelectrode are denoted by ●,■ denotes data for $[Os(bpy)_2 (PVP)_{10} Cl]Cl$ and Δ denotes data for a composite in which the mole fraction of metallopolymer 0 02

4 5 Enhanced Homogeneous Charge Transport

As illustrated in Figures 4 14 and 4 16, the cyclic voltammetry gives diffusion controlled responses for $50<\upsilon<500$ mVs^{-1} for the metallopolymer on the disk and cylinder electrode, respectively Figures 4 15 and 4 17 show that the peak current of the immobilised metallopolymer on the disk and cylinder electrode varies linearly with square root scan rate, $\upsilon^{1/2}$, up to 500 mVs^{-1} indicating that charge transport response is by semi-infinite diffusion According to the Randles-Sevçik equation,[40] the slope of these plots provides the product $D_{CT}{}^{1/2}C_{Os}$, from which D_{CT} has been determined using an osmium redox center concentration of 0 8 M D_{CT} for the disk electrode is 5 3±2 x 10^{-10} cm^{2}s^{-1} and 2 2 ±0 5 x 10^{-11} cm^{2}s^{-1} for the cylinder electrode In another investigation, the D_{CT} for the metallopolymer immobilised on a disk electrode in 0 1 M H_2SO_4 was 2 5 x 10^{-10} cm^{2}s^{-1} [41]

If ion transport limits the rate of homogeneous charge transport through the films, the difference in the polymer diffusional charge transport between the disk and cylinder electrode can be attributed to electrode diffusional fields [40] Diffusion occurs in two dimensions when considering the disk electrode, radially and linearly to the plane of the electrode Whereas, the cylindrical electrode involves only a single dimension of diffusion, the radial position normal to the axis of symmetry Since uniformity is assumed along the length of the cylinder, diffusion to the plane of the electrode (along the length) is omitted Therefore, D_{CT} is apparently greater for the metallopolymer film on the disk electrode than it is immobilised on the cylinder electrode

However, Figure 4 18 illustrates the independence of D_{CT} on the $HClO_4$ concentration for both the disk and cylinder electrode immobilised with a film of the metallopolymer From this, the rate of homogeneous charge transport could be affected by a combination of factors including large-scale movement of polymer chains,[22] counterion diffusion,[23 24] or electron hopping [25 26] In the case of electron hopping, counterions are freely available within the metallopolymer structure and D_{CT} is assumed to depend slightly upon the electrolyte concentration The Dahms-Ruff equation can be used to determine the electron self-exchange rate constant assuming that electron hopping represents the rate-

determining step where the intersite separation is taken to be 5 nm [41] As expected, the difference in the self-exchange rate constants of 1 9 x 10^6 $M^{-1}s^{-1}$ and 1 69 x 10^6 $M^{-1}s^{-1}$ for the disk and cylinder electrode, respectively, was minimal due to fixed inter-redox site separation

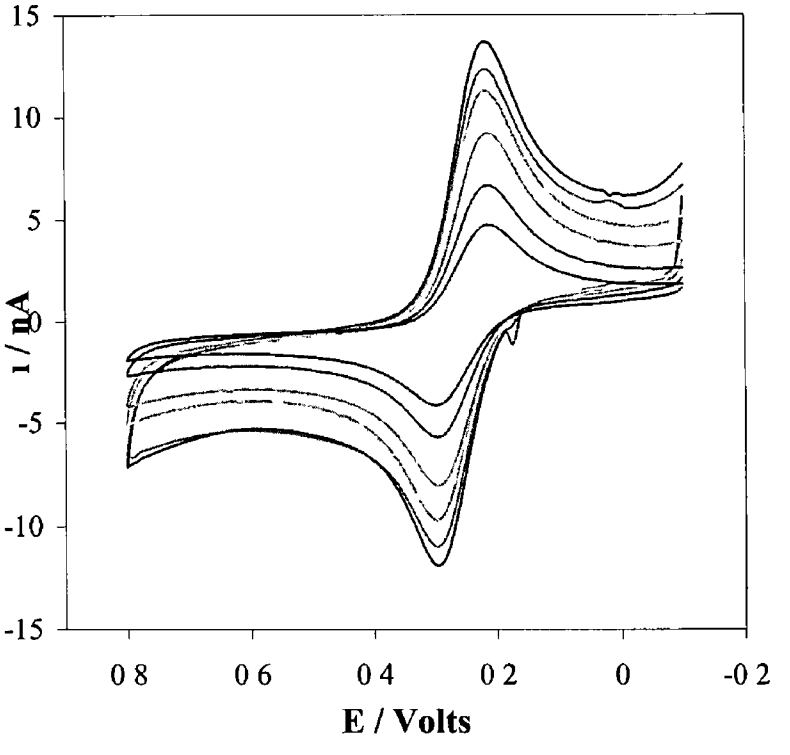

Figure 4 14 Scan rate dependence for an $[Os(bpy)_2 (PVP)_{10} Cl]^+$ film on a 25 μm diameter platinum microelectrode Sweep rates (top to bottom) 500, 400, 300, 200, 100 and 50 mVs^{-1} Surface coverage is 1 8 x 10^{-8} mol cm^{-2} and the electrolyte is 0 1 M $HClO_4$

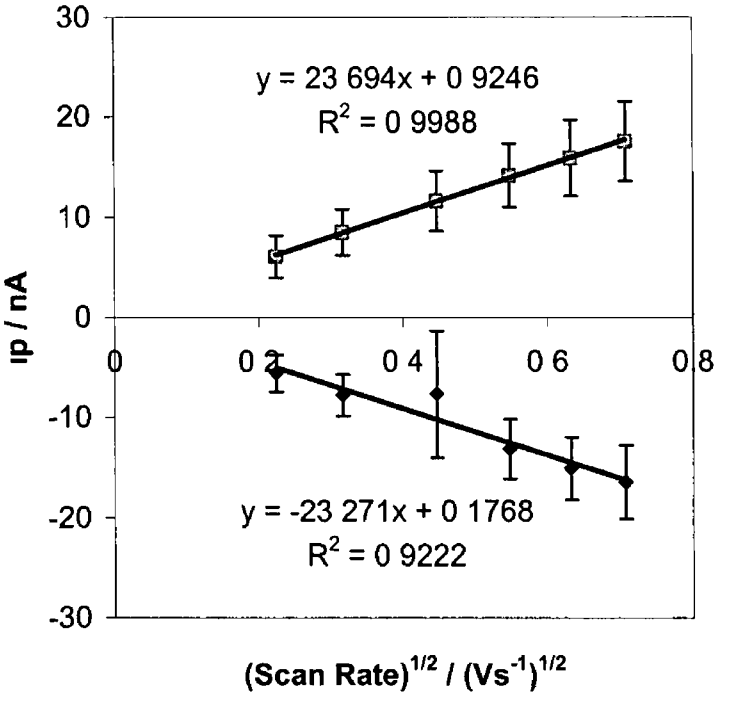

Figure 4 15 The dependence of the peak current on square root scan rate for the metallopolymer $[Os(bpy)_2(PVP)_{10}Cl]^+$ coated on a 25 μm disk microelectrode in 0 1 M $HClO_4$ The surface coverage is 8 5 x 10^{-9} mol cm^{-2}

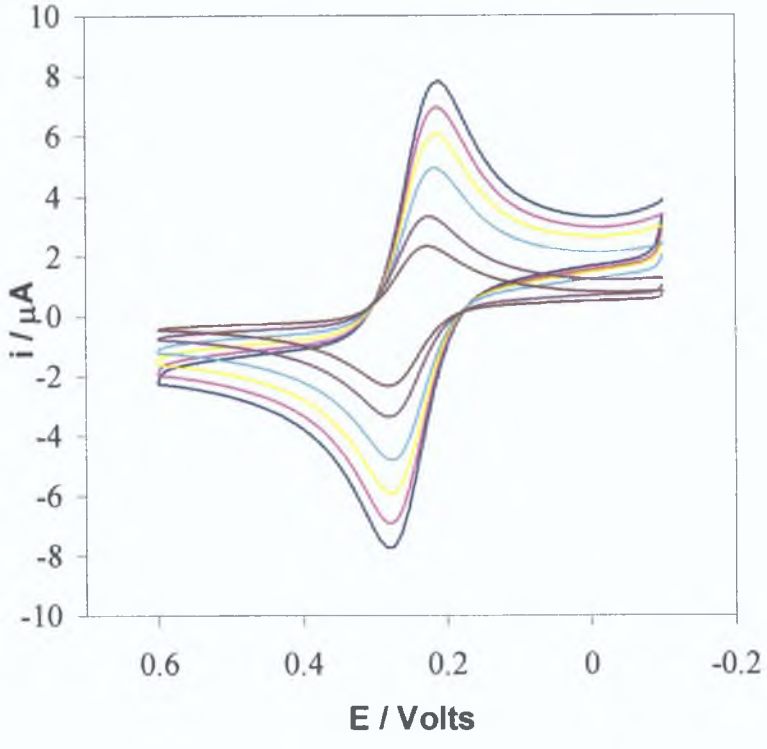

Figure 4.16. Cyclic voltammograms of $[Os(bpy)_2\ Cl\ (PVP)_{10}]^+$ film coated on a 25 µm platinum cylinder electrode of length 1.2 cm in 0.1 M $HClO_4$. From top to bottom, the scan rates are 500, 400, 300, 200, 100 and 50 mVs^{-1}. The surface coverage is 9.9×10^{-10} mol cm^{-2}

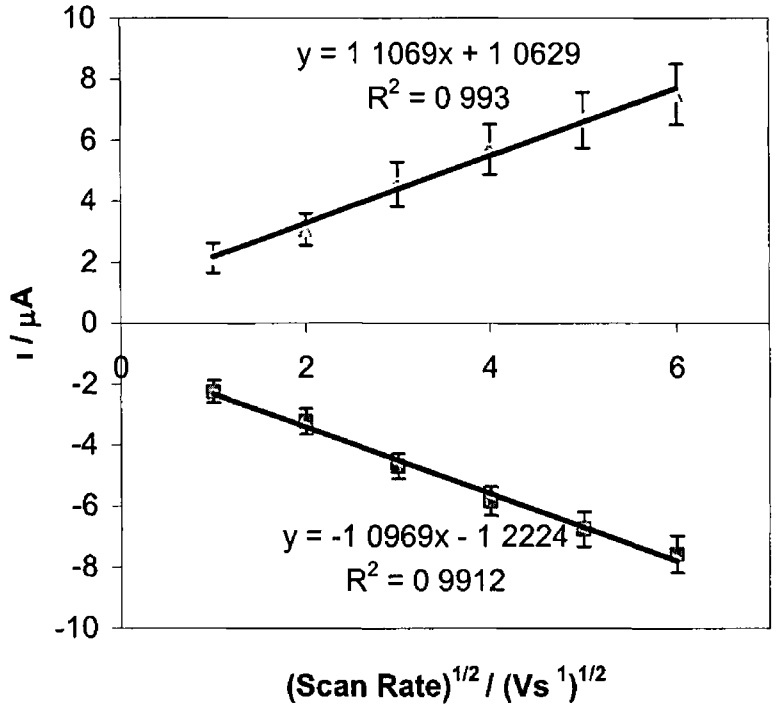

Figure 4 17 The dependence of the peak current on square root scan rate for the metallopolymer $[Os(bpy)_2(PVP)_{10}Cl]^+$ coated on a 25 µm cylinder microelectrode of length 1 2 cm in 0 1 M $HClO_4$

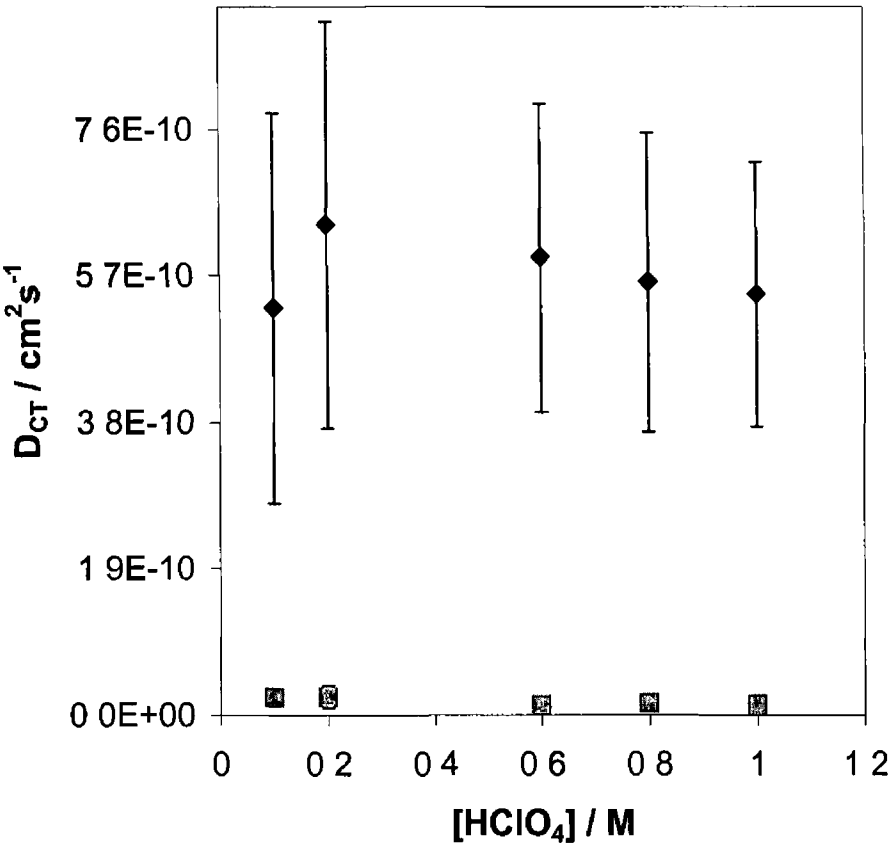

Figure 4 18 Dependence of the homogeneous charge transport diffusion coefficient of $[Os(bpy)_2\ Cl\ (PVP)_{10}]^+$ film on a platinum disk (♦) and cylinder electrode (■) on the concentration of $HClO_4$ as supporting electrolyte The error bars are obtained from 3 independent experiments

Figure 4 19 illustrates the diffusional responses for the metallopolymer nanoparticle composite and Figure 4 20 shows the linear dependence plot of the peak current vs the square root of the scan rate This is also consistent with an electrochemically reversible reaction under semi-infinite linear diffusion control as described by the Randle-Sevçik equation The diffusion coefficient, D_{CT}, is 5 8x10 ^{9} cm^2s^{1}

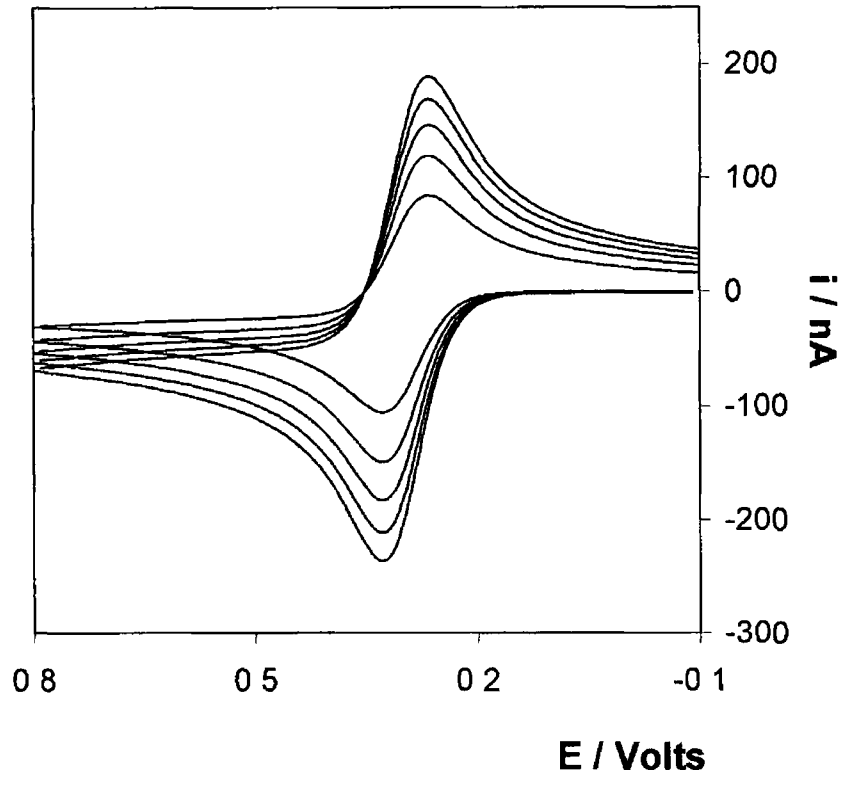

Figure 4.19. Scan rate dependence of cyclic voltammograms under semi-infinite diffusion conditions for a composite film in which the mole fraction of the metallopolymer is 0 02 on a 12 5 μm radius platinum microelectrode Sweep rates (top to bottom) 500, 400, 300, 200 and 100 mVs^{1} Surface coverage is 2 1 x 10^{-8} mol cm^{-2} Supporting electrolyte is aqueous 0 1 M $HClO_4$

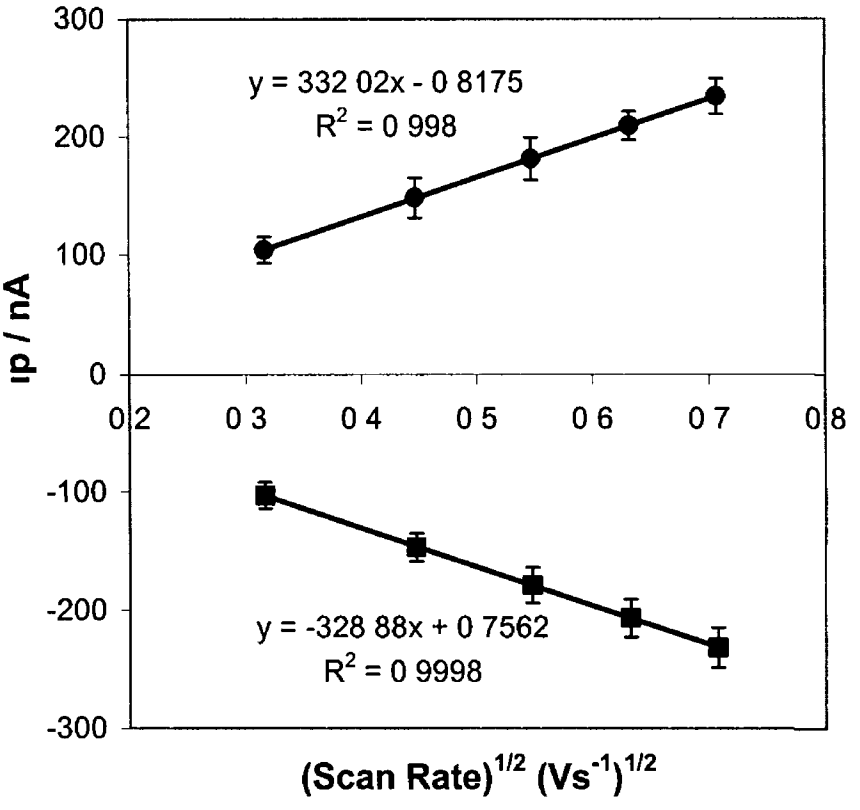

Figure 4 20 Plot of i_p vs $\upsilon^{1/2}$ for the composite film in which the mole fraction of the metallopolymer is 0 02 on a 12 5 μm radius platinum microelectrode

Figure 4 21 illustrates the dependence of D_{CT} on the $HClO_4$ concentration for both metallopolymer and nanoparticle metallopolymer composite films in which the mole fraction of the polymer is 0 02 As mentioned previously, there are three processes that could limit the rate of homogeneous charge transport through these films namely, large scale movement of polymer chains,[42] counterion diffusion/migration,[43] or electron hopping [44 45] The observation that D_{CT} is approximately independent of the supporting electrolyte concentration, coupled with the low film resistance data which indicated that the films contain a relatively high concentration of electrolyte, suggests that counterion diffusion does not represent the rate determining step The Dahms-Ruff equation was used to determine the electron self-exchange rate constant of 1 7 x 10^7 $M^{-1}s^{-1}$, assuming that electron hopping represents the rate determining step

Incorporating a relatively high loading of gold nanoparticles promotes a faster rate of homogeneous charge transport through the film Thus, for high nanoparticle loadings it appears that electron transfer between the osmium redox centers is mediated by the gold nanoparticles causing D_{CT} to increase by approximately an order of magnitude on going from the metallopolymer to the composite

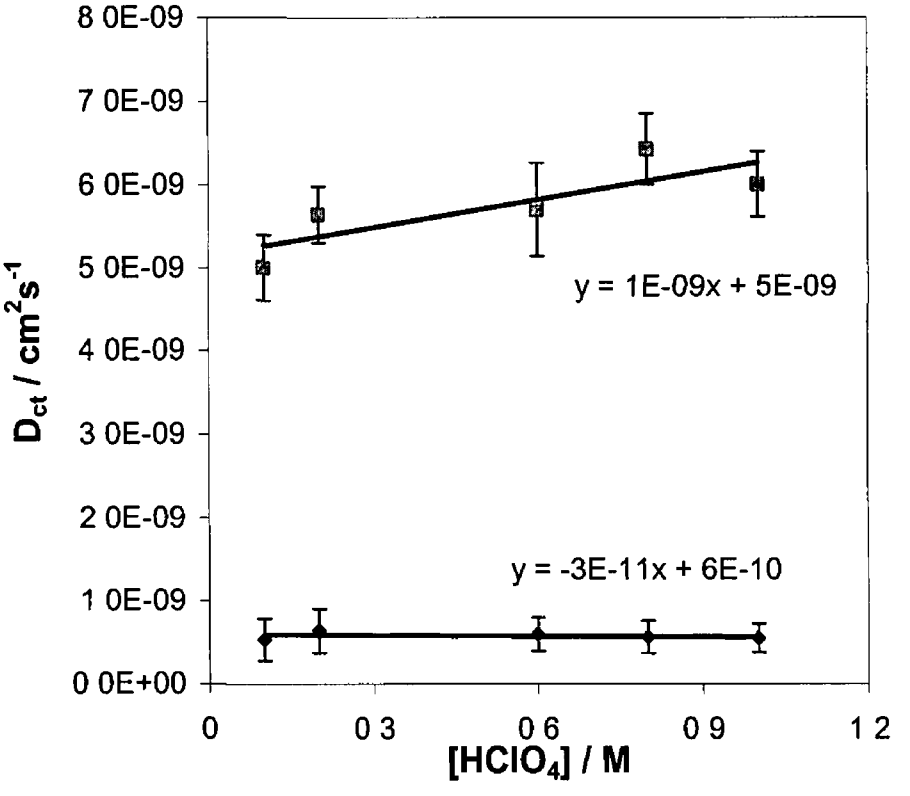

Figure 4 21 The effect of the concentration of $HClO_4$ as supporting electrolyte on the rate of homogeneous charge transport, D_{CT}, through an $[Os(bpy)_2 (PVP)_{10} Cl]Cl$ metallopolymer film (●) and through a composite film in which the mole fraction of the metallopolymer is 0 02 (■)

4 6 Metallopolymer Nanoparticle Composite Structure

The TEM images, Figures 4 22 and 4 23, show gold nanoparticles prepared in the presence of $[Os(bpy)_2 (PVP)_{10} Cl]Cl$ where the mole fraction of the metallopolymer is 0 84 and 0 02, respectively Both systems produce well defined nanoparticles with the approximately spherical shape of the gold nanoparticles suggests that the particles are not monocrystalline However, the most striking result of Figure 4 23 is that decreasing the amount of metallopolymer increases the average particle size from 1 6±0 3 to 5 2±0 6 nm This result suggests that a greater availability of surface binding pyridine groups inhibits growth and efficiently blocks particle aggregation This behavior is similar to that reported previously for poly-vinylpyrrohdone where larger quantities of polymer lead to the formation of smaller nanoparticles [46]

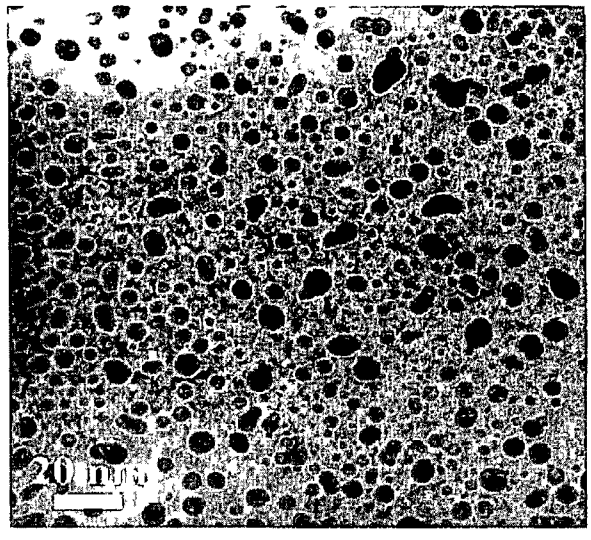

Figure 4 22 TEM of gold nanoparticles in which the mole fraction of $[Os(bpy)_2 (PVP)_{10} Cl]Cl$ is 0 02 Magnification is $1\ 25x10^6$

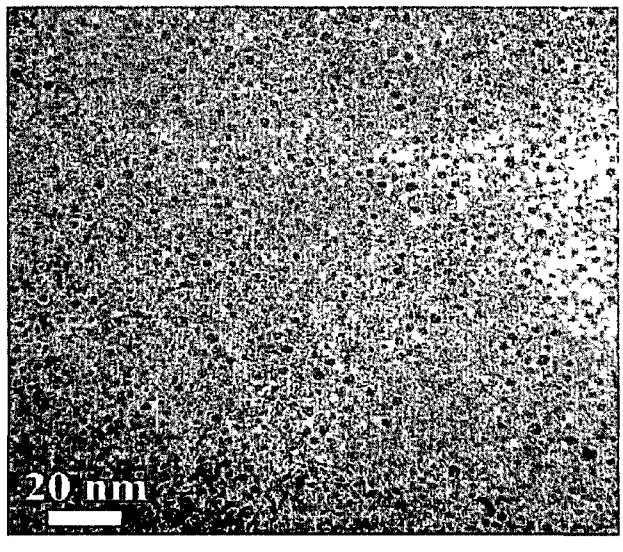

Figure 4 23 Transmission electron micrograph of gold nanoparticles in which the mole fraction of $[Os(bpy)_2 (PVP)_{10} Cl]Cl$ is 0 84 Magnification is $8\ 0x10^5$

4.7 Metallopolymer:Nanoparticle Electrical Conductivity

The possibility of controlling the electrical characteristics of polymers by systematically varying the loading of nanoparticles is important for a range of applications ranging from molecular electronic devices to sensors. When nanoparticles of conductivity σ_n are blended with a polymer matrix to a loading φ, having a conductivity σ_p, the conductivity of the resulting composite, σ, typically increases dramatically.[27,28] Specifically, when the percolation threshold, φ_c, is reached an infinite conductive cluster is formed and the composite may become highly conducting. As the filler concentration increases from φ_c to the limiting value F, the conductivity of the composite increases rapidly over several orders of magnitude, from the value σ_c at the percolation threshold to the maximal value σ_m. Below the percolation threshold, the conductivity change is negligible and the conductivity of the composite is equal to the polymer conductivity σ_p or slightly higher. While it does not consider the effects of particle shape, variable particle size, contact phenomena, the distribution of particles within the polymer etc, the dependence of the conductivity on the nanoparticle loading can be described by Equation 3 to a first order of approximation:

$$\sigma = \sigma_c + (\sigma_m - \sigma_c)[(\varphi - \varphi_c)/(F - \varphi_c)]^t \qquad (3)$$

where t is the critical exponent[47] and is typically between 1.6 and 1.9.

Figure 4.24 illustrates the dependence of the composite electrical conductivity on the nanoparticle loading for both metallopolymer and poly-4-vinyl pyridine matrices. In both cases, the solid curves represent the best fits of Equation 3 to the experimental data and the data are given in Table 3. These percolation curves reveal that the conductivity of the metallopolymer is approximately 1×10^{-3} S m^{-1} and for the unlabelled poly-4-vinylpyridine is 3.16×10^{-5} S m^{-1}. Both the pure PVP and metallopolymer composites exhibit a sharp increase in conductivity for a critical loading of the gold nanoparticles. However, the percolation threshold is dramatically lower for the metallopolymer based composite, 0.07±0.01, compared to 0.31±0.04 for the PVP matrix. The filling limit in both cases is 0.7±0.1, which is indistinguishable from the value of 0.64 expected for a

0 64 expected for a random distribution of conductive spheres in a non-electronically conducting matrix [48] Assuming a random dispersion, the average interparticle separation, d, at the percolation threshold is estimated as 2 6±0 1 and 5 0±0 1 nm for the PVP and metallopolymer composites, respectively The observation that the metallopolymer system is highly conducting for a larger interparticle separation suggests the osmium bisbipyridyl centers mediate electron transfer between adjacent metal particles over much greater distances than the pure poly-4-vinylpyridine material This conclusion is consistent with the observation that the maximum conductivity, σ_m, differs by only a factor of 4 for the two composites suggesting that particle-to-particle contact is the limiting factor on conductivity at the highest loadings investigated While the value of the critical exponent, t, for PVP is close to the range typically found for random dispersions,[27 49] 1 6-1 9, the value obtained for the metallopolymer matrix is significantly higher at 2 5 Large t values have been reported previously[50] and assumed to be associated with contributions from tunneling conductivity or complicated conduction pathways through the composite In the present case, it most likely arises because of specific interactions between the cationic redox centers and the surface of the gold nanoparticles

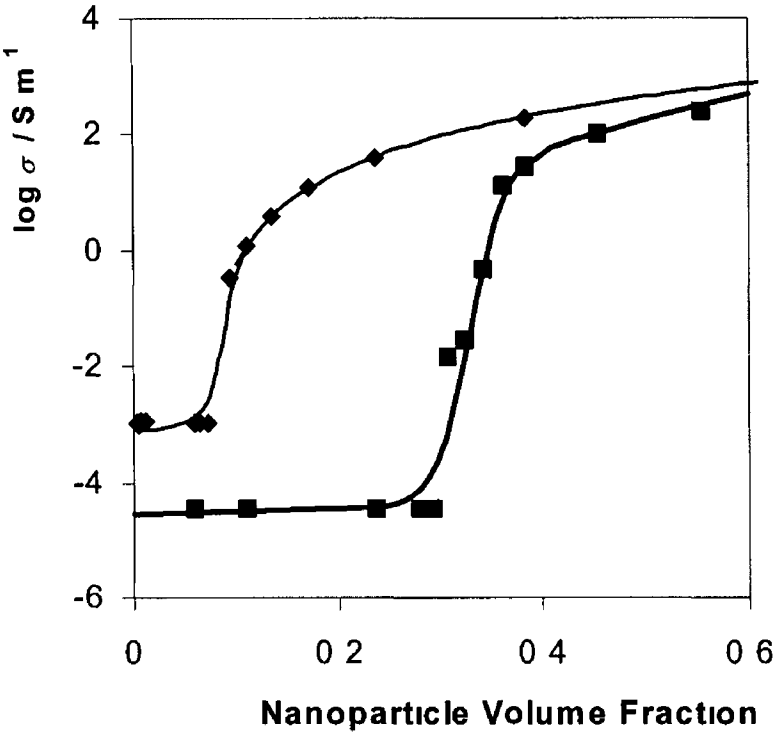

Figure 4 24 Dependence of composite electrical conductivity on the loading of gold nanoparticles ■ denotes composites where the polymer matrix is poly(4-vinylpyridine) and ♦ denotes composites where the matrix is $[Os(bpy)_2 (PVP)_{10} Cl]Cl$ The solid curves denote best fits to the percolation theory and the parameters are given in Table 3

Table 3 Electrical Conductivity Parameters for Composites Based on Gold Nanoparticle- Poly-4-vinylpyridine and Metallopolymer Matrices

Matrix	**Log (σ_P / Sm^{-1})**	**Log (σ_c / Sm^{-1})**	**Log (σ_m / Sm^{-1})**	φ_c	**F**	**t**	**d / nm**
Poly-4-vinylpyridine	-4 45(0 07)	-3 96(0 11)	3 55(0 04)	0 31 (0 04)	0 7 (0 1)	1 9(0 2)	4 9(0 4)
$[Os(bpy)_2(PVP)_{10}Cl]Cl$	-2 96(0 03)	-2 02(0 03)	2 94(0 05)	0 07 (0 01)	0 7 (0 1)	2 5(0 2)	12 0(0 3)

a Numbers in parentheses represent the standard deviations of three independent composite samples

4 8 Ion Pairing Effects

The formal potential of an immobilized electroactive group is sensitive to both the solvation shell of the redox center and to the extent of ion-pairing [51,52 53] It is therefore a sensitive probe of the local microenvironment within the polymer film Therefore, by examining the electrolyte concentration dependence of E^{o}, information about the extent of ion-pairing and the film's permeability towards anions can be obtained The plots of E^{o} vs the logarithm of the $HClO_4$ and $NaClO_4$ concentration for both the disk and cylinder electrodes immobilised with the metallopolymer are represented in Figures 4 25 and 4 26, respectively The sensitivity of the formal potential to the concentration of supporting electrolyte can be used to probe ionic interactions and differences in the relative stability between the two-redox states The plots show that the $E^{o'}$ for the metallopolymer on both the disk and cylinder electrodes shifts in a negative potential direction with increasing electrolyte concentration

This negative shift indicates that oxidation of the redox center becomes thermodynamically more facile at high electrolyte concentrations, and is consistent with ion-pairing between the electrolyte anion and the redox centers

The situation is summarized in the following Nernstian reaction

$$[Os(bpy)2\ (PVP)_n\ Cl]^{+}\ (X^{-})_{\rho} - e^{-} + p\ (X^{-}) \leftrightarrow [Os(bpy)2\ (PVP)_n\ Cl]^{2+}\ (X^{-})_{\rho+p}$$

where both redox forms are considered to participate in the ion-pairing equilibria The slopes observed for the metallopolymer film in Figure 4 25 are 73 8±0 1 mV dec^{-1} and 71 4±0 2 mV dec^{-1} for the modified disk and cylinder electrode in $HClO_4$, respectively, are larger than that predicted by theory for the pairing of an additional anion in the oxidized state, 59 mV dec^{-1} These deviations most likely arise because of differences in the ionic strength of the solutions and liquid junction effects Likewise, the slopes of the metallopolymer for the electrodes in $NaClO_4$ electrolyte, Figure 4 26, deviate from the true Nernstian slope of 59 mV dec^{-1} with 61 1±0 3 mV dec^{-1} and 46 3±0 4 mV dec^{-1} recorded for the disk and cylinder electrode, respectively This indicates that cation and pH effects on the metallopolymer layer can be disregarded

Figure 4 27 illustrates a plot of E° vs the logarithm of the $HClO_4$ concentration for a disk electrode modified with the metallopolymer and composite in which the mole fraction of the metallopolymer is 0 02 The most significant result is that $E°_{Os2+/3+}$ for the composite is completely insensitive to the perchlorate concentration This result suggests that additional perchlorate anions do not become paired with the Os^{3+} centers most likely because of strong interactions with the gold nanoparticles, which may also have an internal buffering role because of their surface charges

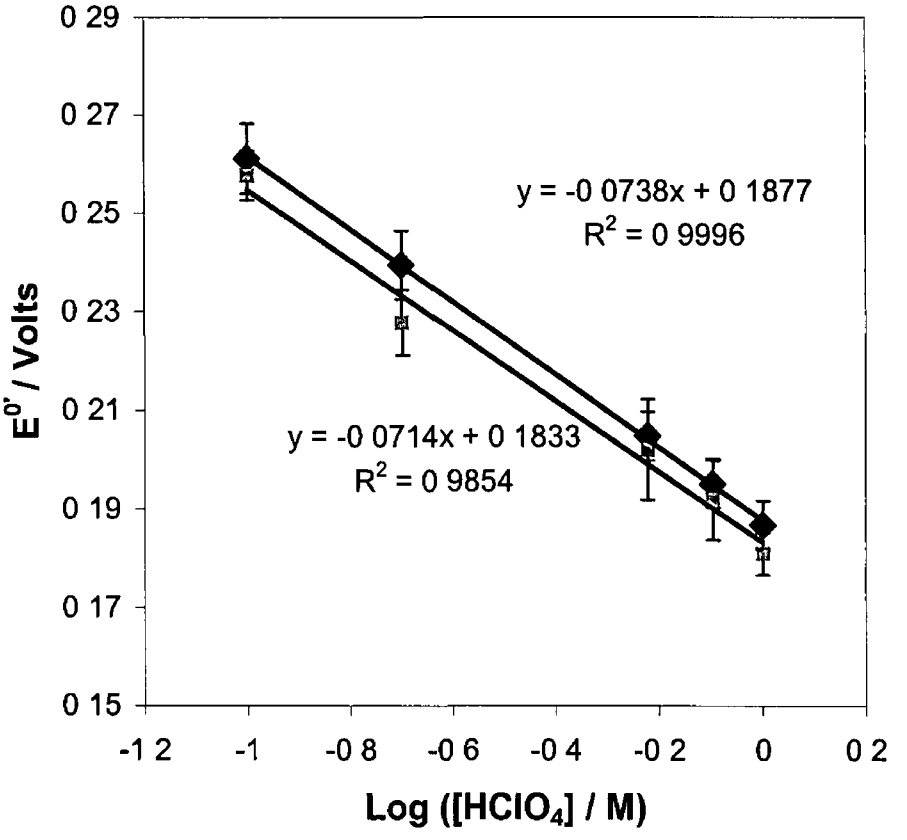

Figure 4 25 Dependence of the formal potential of $[Os(bpy)_2\ Cl\ (PVP)_{10}]^+$ on the concentration of $HClO_4$ as supporting electrolyte for films on a 25μm diameter disk (♦) and 25μm cylinder electrode (■) Cylinder length is 1 2 cm

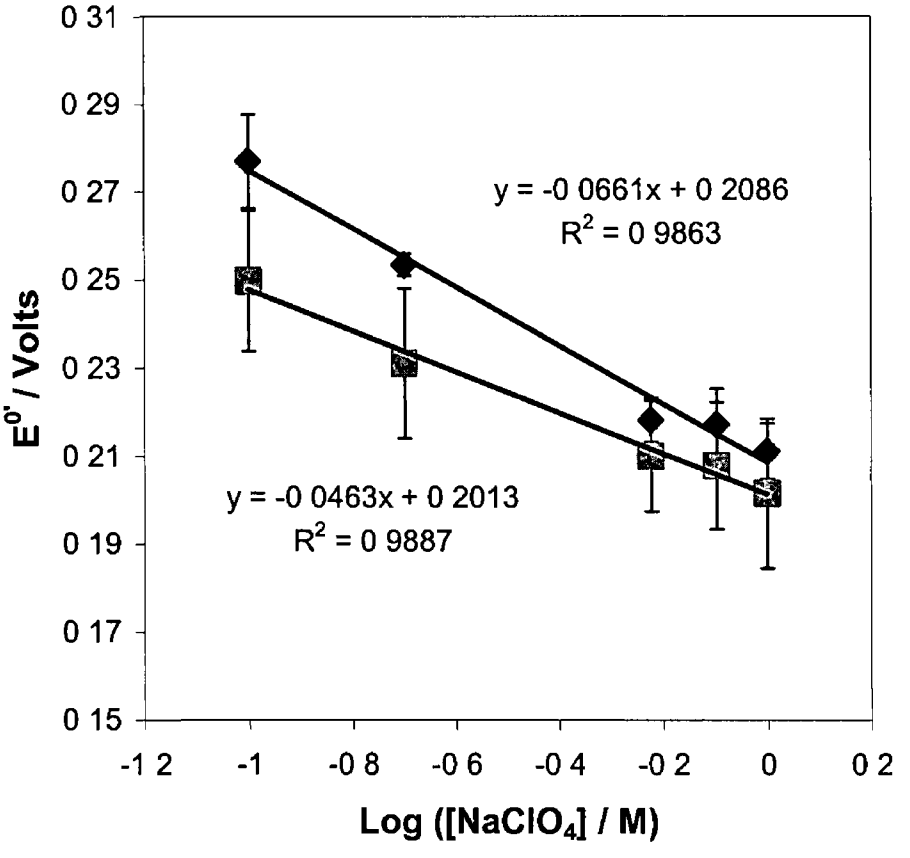

Figure 4 26 Dependence of the formal potential on the concentration of $NaClO_4$ as supporting electrolyte for $[Os(bpy)_2\ Cl\ (PVP)_{10}]^+$ films on a 25 μm diameter disk (♦) and cylinder electrode (■) Cylinder length is 1 2 cm

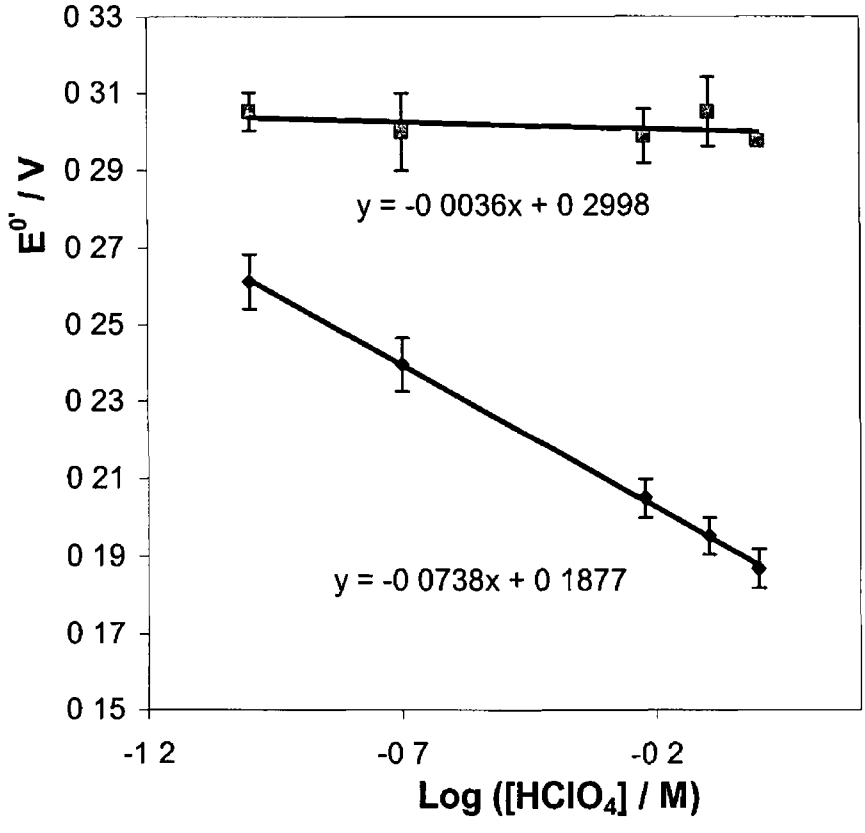

Figure 4 27 Dependence of the formal potential for the $Os^{2+/3+}$ process within an $[Os(bpy)_2(PVP)_{10}Cl]Cl$ metallopolymer film ● and within a composite in which the mole fraction of metallopolymer is 0 02 ■ on the concentration of $HClO_4$ as supporting electrolyte

4 9 Heterogeneous Electron Transfer

Fast scan rate cyclic voltammetry was used to determine the standard heterogeneous electron transfer rate constant, k°, describing the dynamics of electron transfer across the electrode/film interface Electrochemically cycling the cylinder electrode with metallopolymer film at fast scan rates to determine the heterogeneous electron transfer did not cause sufficient peak-to-peak separation, ΔE_p, for the rate constant calculation Figure 4 28 illustrates representative cyclic voltammograms at scan rates of 10, 100 and 500 Vs^{-1}, which show minimal ΔE_p ΔE_p is 98 mV at scan rate 10 Vs^{-1} and 148 mV for 500 Vs^{-1} Taking the high resistance values of Table 3 into consideration for the metallopolymer film on the cylinder microelectrode, the Ohmic iR drop is larger than 5-10% relative to ΔE_p This result is consistent with a large surface area of the cylinder electrode where there is greater double layer charging

Figure 4 21 clearly demonstrates that the rate of homogeneous charge transport through these metallopolymer based films can be significantly enhanced by incorporating gold nanoparticles within the matrix Heterogeneous electron transfer across the electrode/film interface depends on the electrode-reactant separation, the chemical composition, and the effective dielectric constant of the film, which are also influenced by the presence of the gold nanoparticles [54]

Figure 4 29 illustrates cyclic voltammograms for a metallopolymer film and a composite where the mole fraction of metallopolymer is 0 02 at scan rates of 10 and 100 Vs^{-1}, respectively The supporting electrolyte is 1 0 M $HClO_4$ in which, as shown in Figure 4 13, the total cell resistance does not exceed 2000 Ω even for the pure metallopolymer Thus, even though these experiments employ a relatively high scan rate, the iR drop is less than 5 mV, which is negligible compared to the peak-to-peak separations, ΔE_p, observed Despite the scan rate being an order of magnitude larger, the ΔE_p value for the composite is smaller (110 mV) than that found for the metallopolymer (250 mV) This result indicates that the rate of heterogeneous electron transfer is significantly faster for the composite than for the metallopolymer

Figure 4 29 also illustrates theoretical fits to the experimental cyclic voltammograms generated according to the Butler-Volmer formalism of electrode kinetics [40] In fitting these voltammograms, the residual sum of squares between the experimental and theoretical oxidation currents were minimized and then the reduction branch of the voltammogram was predicted The satisfactory agreement observed between theory and experiment suggests that the voltammograms for both metallopolymer and composite films can be approximately described by conventional solution phase models based on semi-infinite linear diffusion

Moreover, the satisfactory fits suggest that the films are solvated and that electrochemical double layer sets up at the electrode/layer interface For the metallopolymer film for $5<\upsilon<30$ Vs^{1}, the best fit simulated voltammogram is obtained where D_{CT} is $5\ 0x10^{10}$ cm^2s^{1} and a standard heterogeneous electron transfer rate constant, k°, is $8\ 25\pm1\ 75x10^{5}$ cms^{1} The diffusion coefficient obtained by fitting the complete voltammogram is identical to that found using the Randle-Sevçik analysis to within 5% Significantly, the standard heterogeneous electron transfer rate constant for the composite is almost two orders of magnitude higher at $4\ 0\pm0\ 2x10^{3}$ cms^{1} This result most likely arises because the gold nanoparticles mediate electron transfer between the underlying electrode surface and the osmium redox centers thus decreasing the electron transfer distance

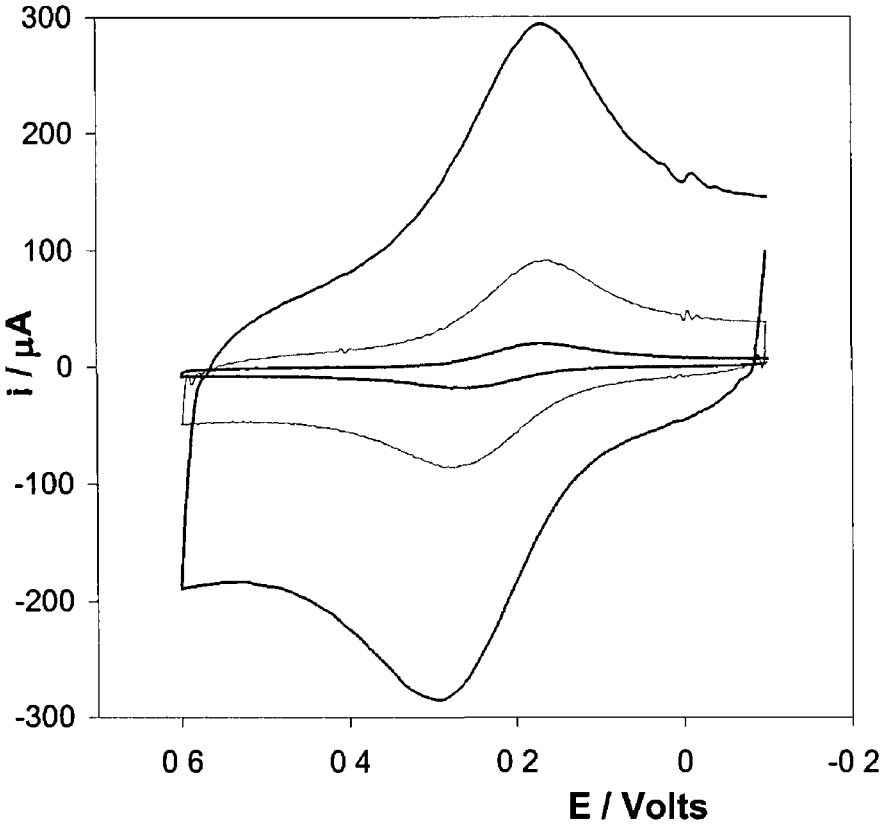

Figure 4 28 Cyclic voltammograms for a film of $[Os(bpy)_2 (PVP)_{10} Cl]^+$ on a 25 µm diameter platinum cylinder microelectrode From top to bottom the scan rates are 500, 100 and 50 Vs^{-1}, respectively The supporting electrolyte is 1 0 M $HClO_4$

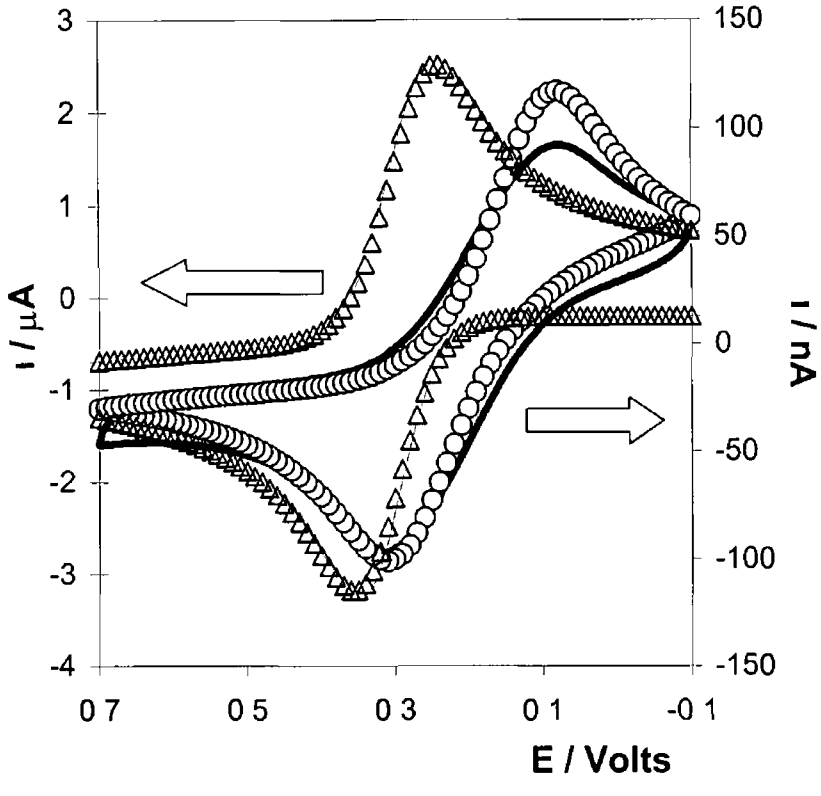

Figure 4 29 Cyclic voltammograms for an $[Os(bpy)_2 (PVP)_{10} Cl]Cl$ metallopolymer film (——) and a composite film (– – –) in which the mole fraction of the metallopolymer is 0 02 The scan rates are 10 and 100 Vs^{-1}, respectively Theoretical voltammograms obtained generated according to the Butler-Volmer formalism of electrode kinetics are denoted by the open symbols The supporting electrolyte is 1 0 M $HClO_4$

4 10 Ligand Exchange Study

Another approach explored where nanoparticles act as charge compensators was the formation of citrate based nanoparticles metallopolymer composites The nanoparticles are aqueous based whereas the metallopolymer is insoluble in aqueous media A study was undertaken on the nanoparticles to find the most suitable solvent in which the nanoparticles are stable towards aggregation and the metallopolymer is soluble

50 50 v/v sol and ethanol, acetomtrile and acetone as solvent were mixed for 15 minutes and the resulting UV-Vis spectra are shown in Figure 4 30 The peak at 530 nm corresponds to the distinctive surface plasmon band and the peaks that arise in the region of 750 to 760 nm are due to aggregation of nanoparticles [55] It is evident from the spectra that both ethanol and acetonitrile cause aggregation whereas acetone does not The citric acid may react with ethanol to form an ester and with acetomtrile forming a salt [56] These aggregates absorb at the longer wavelength [57] Acetone does not seem to cause nanoparticle aggregation and is therefore the most suitable solvent The metallopolymer is insoluble in acetone and as a result of the solvent limitations, no further experiments were carried out

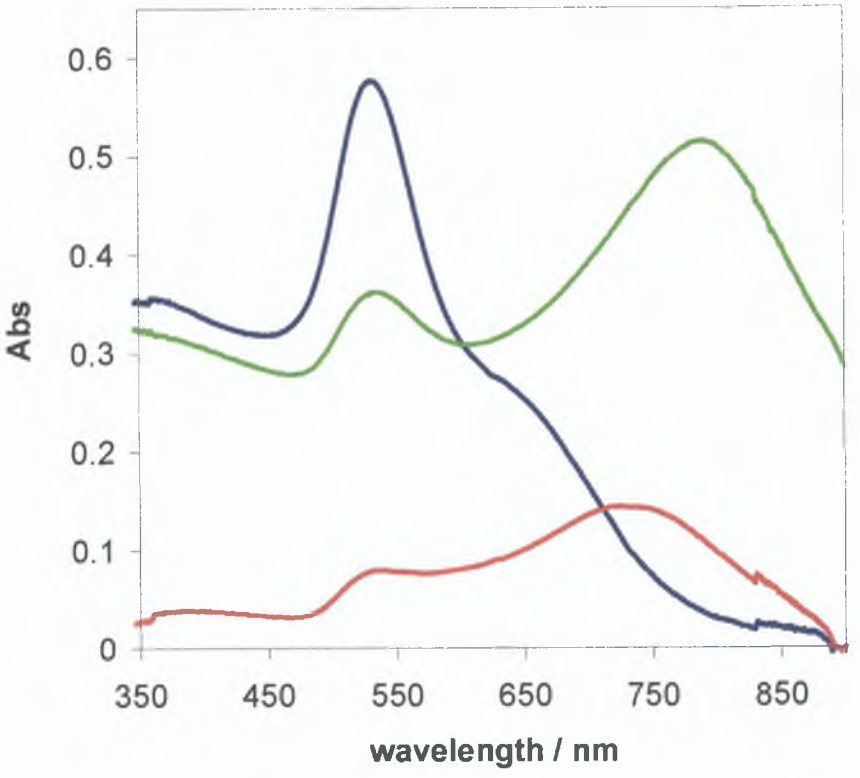

Figure 4.30. UV-Vis spectra of citrate protected gold nanoparticles in a 50:50 v/v with acetone (——), ethanol (——) and acetonitrile (——). Concentration is 3.2 x 10^{17} nanoparticles / cm^3

4 11 Characterization of Citrate Protected Gold Nanoparticles

TEM imaging of the gold nanoparticles was performed by Goran Karlsson at Uppsala University, Sweden and is greatly appreciated TEM images only the core of the nanoparticle [58] Figure 4 31 shows that the nanoparticles have diameters of ca 25 nm and an average intersite distance of 2 nm Consistent with other findings, some particles are irregularly shaped which may be a consequence of the particles growing in the water media [16]

Figure 4 32 represents the scan rate dependence on the gold nanoparticles from 50 to 500 mV^{1} using a glassy carbon electrode as the working electrode With an average diameter of 25 nm (from TEM data) the surface area of each nanoparticle core is approximately 1962 nm^2 The voltage is cycled from –0 1 V to 1 4 V Gold oxidation peak is obvious at 1 115 V with the corresponding symmetrical reduction peak at 0 7 V Upon the initial oxidation potential of –0 1 V, there is a reductive current recorded indicating that the nanoparticles are partially oxidised in the sol Figure 4 33 illustrates that the reductive charge is dependent of scan rate indicating that even at the slowest scan rate of 50 mVs^{1} the nanoparticles are fully oxidised At 50 mV^{1}, τ, the timescale of the experiment is 4 8 x 10^{5} s The number of nanoparticles oxidised is approx 8 x 10^{7}, on the basis of the known area of the gold oxide reduced and the radius of the nanoparticle obtained from TEM

Figure 4 34 represents the overlayed cyclic voltammograms of a bare gold macroelectrode and gold sol It is thermodynamically easier to oxidise the gold nanoparticles than the bulk gold and easier to reduce the oxidised bulk gold than the oxidised gold nanoparticles In spite of this, the voltammetries are very similar and is why nanoparticles are often referred to as microelectrodes The area of the gold electrode is 9 5 x 10^{3} cm^2 whereas the area from the TEM of a gold nanoparticle is 1 9 x 10^{11} cm^2 The area of the gold electrode is eleven orders of magnitude larger compared to the nanoparticle area However, when the charges of the gold reduction peak are compared the gold electrode charge is only one order of magnitude larger than the gold nanoparticle, the charges being 5 363 x 10^{6} C and 6 879 x 10^{7} C, respectively

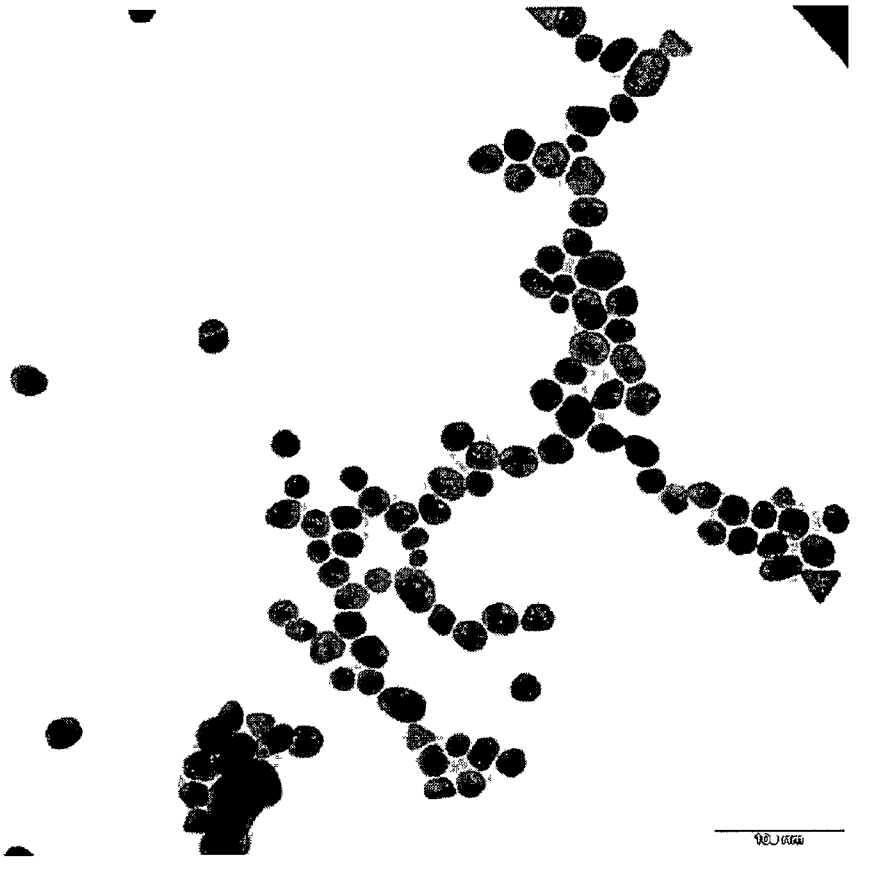

Figure 4 31 TEM image of gold nanoparticles

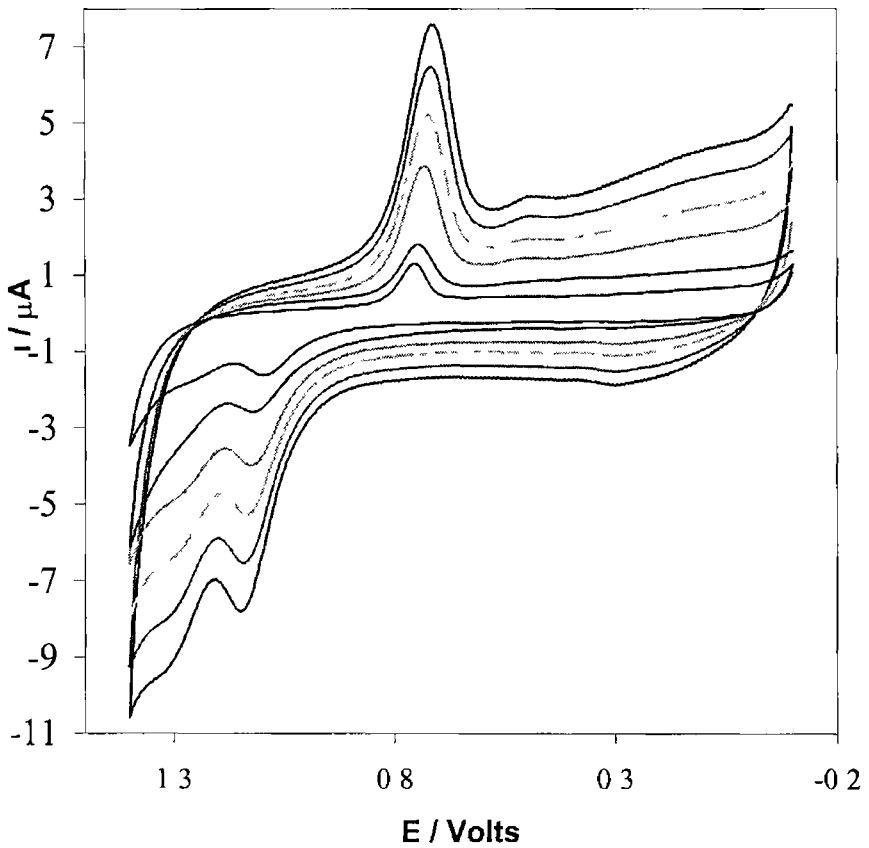

Figure 4 32 Cyclic voltammograms of a 3 mm glassy carbon electrode in gold nanoparticle sol From top to bottom, the scan rates are 500, 400, 300, 200, 100, 50 mVs^{1} Concentration is approx 3 17 x 10^{20} nanoparticles / 1000 cm^3

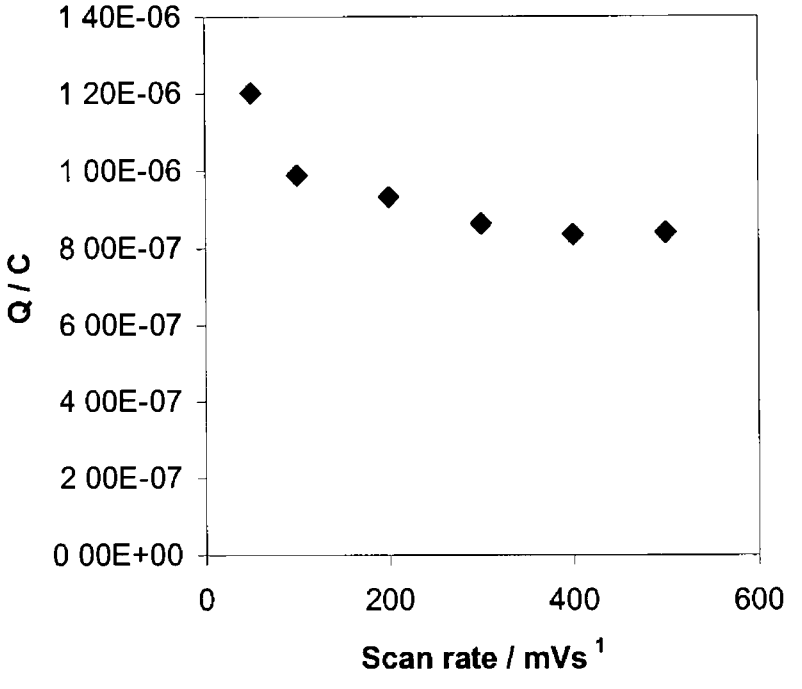

Figure 4 33 Dependence of the reductive gold nanoparticle charge on the scan rate at 0 7 V The concentration is approx 3 17 x 10^{20} nanoparticles / 1000 cm^3 and the working electrode is a 3 mm glassy carbon electrode

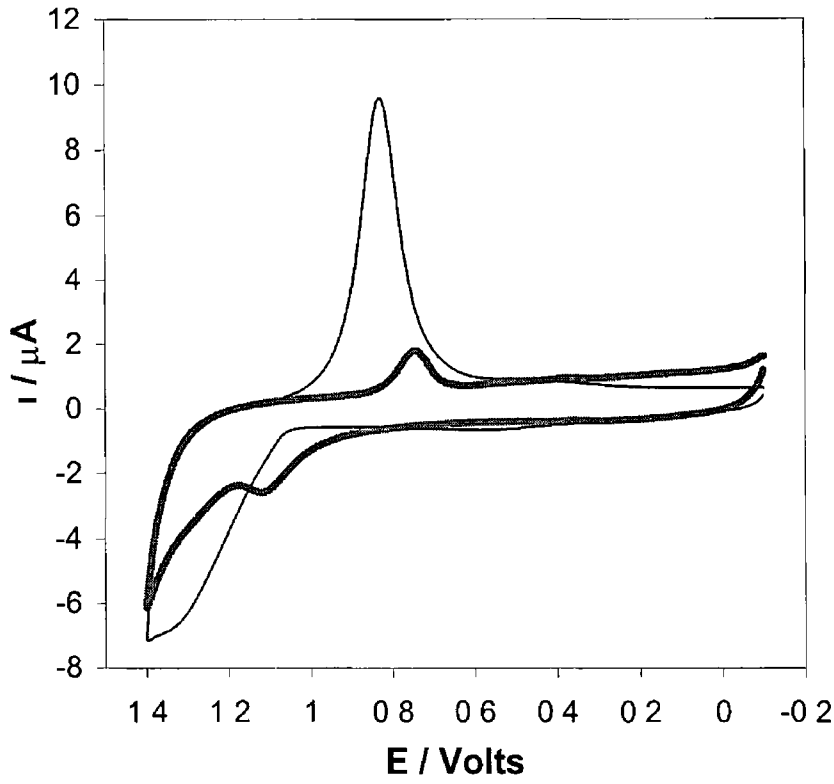

Figure 4 34 Cyclic Voltammograms of a bare 1 1 mm diameter gold macroelectrode cycled in 0 1 M H_2SO_4 (thin line) and gold nanoparticles with a 3 mm diameter glassy carbon electrode as the working electrode (thick line) Scan rate is 100 mVs ^{1}

4 12 Conclusion

'Break In' and counterion effects were not evident for the metallopolymer $[Os(bpy)_2(PVP)_{10}Cl]^+$ film indicating that the polymer contains a high water content and has a rigid structure The voltammetry of the metallopolymer is similar when immobilised on the disk and cylinder electrode an indication that the microenvironments seem comparable Introducing gold nanoparticles to the metallopolymer forming metallopolymer nanoparticle composites leads to nearly ideal voltammetry with the gold oxide reduction area close to that expected

The apparent homogeneous charge transport coefficients for the disk and cylinder electrode are 5 3±2 x 10^{-10} cm^2s^{-1} and 2 2 ±0 5 x 10^{-11} cm^2s^{-1}, respectively The apparent difference in D_{CT} can be attributed to differences in electrode diffusional fields and the difficulty in achieving true semi infinite linear diffusion conditions for both geometries at accessible timescales An enhanced D_{CT} value for the metallopolymer nanoparticle composites of 5 8 x 10^{-9} cm^2s^{-1} was obtained indicating that the rate of homogeneous charge transport increases with increasing nanoparticle loading The corresponding self exchange rate constant was 1 9 x 10^6 $M^{-1}s^{-1}$ for the metallopolymer and 1 7 x 10^7 $M^{-1}s^{-1}$ for the composite on a disk electrode These enhanced charge and electron transport values may indicate that, an interconnected network is formed possibly involving the osmium redox centers mediating electron transfer between the gold nanoparticles

Decreasing the mole fraction of metallopolymer in the nanoparticle metallopolymer composites increases the average particle size from 1 6±0 3 to 5 2±0 6 nm The percolation curves reveal that both the pure PVP and metallopolymer composites exhibit a sharp increase in conductivity for a critical loading of gold nanoparticles However, the percolation threshold is lower for the metallopolymer based composite, 0 07±0 01, compared to 0 31±0 04 for the PVP matrix The observation that the metallopolymer system is highly conducting suggests the osmium bisbipyridyl centers mediate electron transfer between adjacent metal particles over much greater distances than the pure poly-4-vinylpyridine material

Ion pairing in the metallopolymer film reveal nernstian slopes of 73 8±0 1 mV dec ^{1} and 71 4±0 2 mV dec ^{1} for the disk and cylinder electrode, respectively, are larger than that predicted by theory, 59 mV dec ^{1} pH and cation effects for the metallopolymer layer are negligible as the slopes of the metallopolymer in $NaClO_4$ electrolyte are 61 1±0 3 mV dec ^{1} and 46 3±0 4 mV dec ^{1} for the disk and cylinder electrode, respectively However, the metallopolymer nanoparticle composite is insensitive to the perchlorate concentration and implies that additional perchlorate anions do not become paired with the Os^{3+} centers most likely because of strong interactions of the osmium with the gold nanoparticles

However, k^{o} is 8 25±1 75x10 ^{5} cms ^{1} for the nanoparticle metallopolymer composite compared to 4 0±0 2x10 ^{3} cms ^{1} for the metallopolymer on the disk electrode This suggests that the gold nanoparticles probably mediate electron transfer between the underlying electrode surface and the osmium redox centers thus decreasing the electron transfer distance

The nanoparticle composites presented in this chapter could have wide applicability especially in the area of biological research Nanoparticles coated with fluorescent polymers based on transition metal complexes that are size manipulated could be tagged to sequences of DNA to produce specific coloured nanodots This kind of flexibility could lead to microarrays for genomics and proteomics and immunoassays for medical diagnostics

4 13 References

(1) Palacios, I , Castillo, R , Vargas, R A , *Electrochim Acta,* **2003**, 48, 2195

(2) Saxena, V , Malhotra, B D , *Current App Phys* , **2003**, 3, 293

(3) Cao, Y W C , Jin, R C , Mirkin, C A , *Science*, 2002, 297, 1536

(4) Katz, E , Willner, I , *J Am Chem Soc* , **2002**, 124, 10290

(5) Haes, A J , Van Duyne, R P , *J Am Chem Soc* , **2002**, 124, 10596

(6) Kreibig, U , Vollmer, M "Optical Properties of Metal Clusters", Ed Teonnies, J P 1995

(7) Aguila, A , Murray, R W , *Langmuir*, **2000**, 16, 5949

(8) Zhang, Z , Wan, M , *Syn Metals*, **2003**, 132, 205

(9) Park, S , Weaver, M J , *J Phys Chem B*, **2002**, 106, 8667

(10) Song, Y , Murray, R W , *J Am Chem Soc* , **2002**, 124, 7096

(11) Ziegler, K J , Doty, R C , Johnston, K P , Korgel, B A , *J Am Chem Soc* , **2001**, 123, 7797

(12) Kim, B , Tripp, S L , Wei, A , *J Am Chem Soc* , **2001**, 123, 7955

(13) von Werne, T , Patten, T E , *J Am Chem Soc* , **1999**, 121, 7409

(14) Everett, D H "Basic Principles of Colloid Science", Royal Society of Chemistry, 1988

(15) Jose, B , Ryu, J H , Kim, Y J , Kim, H , Kang, Y S , Lee, S D , H S Kim, *Chem Mater* , **2002**, 14, 2134

(16) Pastoriza-Santos, I , Liz-Marzan, L M , *Langmuir*, **2002**, 18, 2888

(17) Mandal, T K , Fleming, M S , Walt, D R , *Nanoletters*, **2002**, 2

(18) Minko, S , Kiriy, A , Gorodyska, G , Stamm, M , *J Am Chem Soc* , **2002**, 124, 10192

(19) Ingram, R S , Hostetler, M J , Murray, R W , Schaaff, T G , Khoury, J T , Whetten, R L , Bigioni, T P , Guthrie, D K , First, P N *J Am Chem Soc* **1997**, 119, 9279

(20) Andres, R P , Bein, T , Dorogi, M , Feng, S , Henderson, J I , Kubiak, C P , Mahoney, W , Osifchin, R G , Reifenberger, R *Science*, **1996**, 272, 1323

(21) Gittins, D I , Bethell, D , Schiffrin, D J , Nichols, R J *Nature*, **2000**, 408, 67

(22) Clarke, A P , Vos, J G , Hillman, A R , Glidle, A *J Electroanal Chem* **1995**, 389, 129

(23) Majda, M , Faulkner, L R , *J Electroanal Chem* **1984**, 169, 77

(24) Evans, C D , Chambers, J Q *J Am Chem Soc* **1994**, 116, 11052

(25) Blauch, D N , Saveant, J M *J Am Chem Soc* **1992**, 114, 3323

(26) Blauch, D N , Saveant, J M *J Phys Chem* **1993**, 97, 6444

(27) D Stauffer, Introduction to Percolation Theory, Taylor and Francis, London, 1985

(28) G Grimmet, Percolation, Springer-Verlag, Munich, 1989

(29) Forster, R J "Encyclopedia of Electrochemistry", Eds P A Unwin and A J Bard, Wiley, New York, 2000

(30) Kelly, A J , Ohsaka, T , Oyama, N , Forster, R J , Vos, J G *J Electroanal Chem* , **1990**, 287, 185

(31) Kelly, D M , Vos, J G , Hillman, A R *J Mater Chem* , **1997**, 7, 913

(32) Forster, R J *Anal Chem* , **1996**, 68, 3143

(33) Laviron, E , *J Electroanal Chem* , **1974**, 52, 395

(34) Brown, A P , Anson, F C *Anal Chem* , **1977**, 49, 1589

(35) Trasatti, S , Petrii, O A , *J Electroanal Chem* , **1992**, 327, 354

(36) Forster, R J , Keyes, T E , Bond, A M *J Phys Chem B* , **2000**, 104, 6389

(37) Walsh, D A , Keyes, T E , Hogan, C F , Forster, R J *J Phys Chem* , **2001**, 105, 2792

(38) Smith, C P , White, H S *Langmuir*, **1993**, 9, 1

(39) Smith, C P , White, H S *Anal Chem* , **1992**, 64, 2398

(40) Bard, A J , Faulkner, L R Electrochemical Methods Fundamentals and Applications, Wiley, New York, 1980

(41) Forster, R J , Vos, J G *J Electroanal Chem* , **1991**, 314, 135

(42) Karimi, H , Chambers, J Q *J Electroanal Chem* , **1987**, 217, 313

(43) Mathias, M , Haas, O *J Phys Chem* **1993**, 97, 9217

(44) R J Forster and J G Vos, J G Comprehensive Analytical Chemistry, Vol XXVII, Ed G Svehla, Elsevier, Amsterdam, 1992, 465

(45) R W Murray, Molecular Design of Electrode Surfaces, R W Murray, Ed , Wiley, New York, 1992, Chapter I

(46) Bonet F , Delmas, V , Grugeon, S , Herrera Urbina, R , Silvert, P-Y , Tekaia-Elhsissien, K *Nanostruc Mats* , **1999**, 11, 1277

(47) Mamunya, Y P , Davydenko, V V , Pissis, P , Lebedev, E V *Eur Polym J* , **2002**, 38, 1887

(48) Lux, F J , *J Mater Sci* ,**1993**, 28, 285

(49) Wu, J , McLachlan, D S *Phys Rev B*, **1997**, 56, 1236

(50) Carmona, F , Mouney, C J *Mater Sci* , **1997**, 27, 1322

(51) Creager, S E , Rowe, G K *Anal Chim Acta* , **1991**, 246, 233

(52) Rowe, G K , Creager, S E *Langmuir*, **1991**, 7, 2307

(53) Nagamura, T , Sakai, K , *J Chem Soc , Faraday Trans* , **1988**, 84, 3529

(54) R J Forster, Encyclopedia of Electrochemistry, Eds P A Unwin and A J Bard, Wiley, New York, 2000

(55) Yonezawa, T , Onoue, S-y , Kimizuka, N *Langmuir*, **2000**, 16, 5218

(56) McMurry, Organic Chemistry, 3rd Edition, Brooks/Cole Publishing Company

(57) Chen, S , Murray, R W *Langmuir*, **1999**, 15, 682

(58) Reetz, M T , Helbig, H , Quaiser, S A , Stimmmg, U , Bruer, N , Vogel, R , *Science*, **1995**, 267, 367

Chapter 5

Photoinduced Electron Transfer in Solution

5 1 Introduction

The results presented in Chapters 3 and 4 demonstrate that the physical properties, e g , crystallinity or nanoparticle loading, of redox active solid deposits and polymeric species can be changed so as to modulate the rate of homogeneous charge transport Materials with enhanced charge transport have wide applicability especially in areas such as battery,[1] sensor[2] and electronic device development [3] The studies of charge transport and electron self-exchange reported in Chapters 3 and 4 all exploit a potential to create a concentration gradient so as to drive charge transport However, light induced electron transfer represents an attractive alternative to ground state, potential driven processes in that the dynamics of excited state electron transfer can be probed Prior work within our group has demonstrated that even under identical driving force conditions, the rates of ground and excited state electron transfer for adsorbed monolayers can be markedly different because of the different mediating orbitals involved [4 5] Although not fully realised, the objective in this section of the thesis is to measure the rate of electron exchange between an excited state Os^{2+*} centre and an Os^{3+} site for both solid and solution phase reactants and to compare these rates with those reported in Chapter 3 using electrochemical, ground state approaches Success in this area places particularly stringent demands on the properties of the complexes For example, the excited state lifetime of the Os^{2+*} species has to be sufficiently long to allow sufficient time for interaction with the quenching Os^{3+} unit Moreover, the solid deposits must be sufficiently insoluble and stable under pulsed laser illumination

Osmium polypyridyl complexes are well suited for probing redox processes in both the ground and excited states and have long lived excited states [6] Fluorescence quenching is a process which decreases the intensity of the fluorescence emission and investigations into the quenching mechanism of osmium complexes have been carried out previously [7 8] Fluorescence quenching reactions are of great importance in such areas of molecular electronic systems [9] This interest is driven in part by the pivotal role that quenching reactions play in diverse areas including sensors,[10 11 12] optical devices[13] and information storage [14 15] Fluorescence quenching is also a valuable tool for the study of biological molecules such as protein/complex interactions [16 17 18]

The quenching of emission by addition of substrates may proceed by an energy transfer mechanism or by oxidation or reduction of the complex Both collisional and dynamic quenching have been discussed previously in Chapter 1 and require molecular contact between the fluorophore and quencher For collisional quenching the quencher must diffuse to the fluorophore during the lifetime of the excited state Upon contact, the fluorophore returns to the ground state , without emission of a photon In the case of static quenching, a complex is formed between the fluorophore and the quencher, and this complex is non-fluorescent For either static or dynamic quenching to occur, the fluorophore and quencher must be in contact

If redox activity and fluorescence originate in the same moiety of a molecule, only one member of the redox couple will usually be luminescent Electronic excitation of any species results in increased electron affinity and depends on the excitation energy The excited state is both a better reductant and a better oxidant than its ground state precursor, hence the electron exchange between the ground state redox form is always a quenching channel for the excited redox form

This chapter presents an investigation into the photoinduced and quenching processes of the osmium complex, $[Os(bpy)_3]^{2+}$ where bpy is 2,2'-bipyridyl, in solution phase This molecule was chosen over the methoxy derivative of Chapter 3 because of the increased luminescent lifetime Addition of ammonium cerium nitrate provides a convenient and rapid way to produce controlled ratios of Os^{2+} and Os^{3+} within the same solution $[Os(bpy)_3]^{2+}$ can luminesce whereas $[Os(bpy)_3]^{3+}$ is non-luminescent but is capable of quenching the emission of the Os^{2+} centre by energy or electron transfer

5 2 Emission Spectroscopy of $[Os(OMe\text{-}bpy)_3]^{2+}$ and $[Os(bpy)_3]^{2+}$

Figure 5 1 illustrates the UV-Vis spectra of $[Os(bpy)_3]^{2+}$ and $[Os(OMe\text{-}bpy)_3]^{2+}$ in acetonitrile at 298 K Details of the band assignments are presented in section 2 4 4 of Chapter 2 Both complexes exhibit intense bands representing ligand – based $\pi \rightarrow \pi^*$ transitions in the high-energy UV region of the spectrum and metal – to – ligand charge transfer (MLCT) bands in the low – energy visible region The bands of $[Os(OMe\text{-}bpy)_3]^{2+}$ are shifted to longer wavelengths when compared to $[Os(bpy)_3]^{2+}$ and is consistent with the electron donating properties of the methoxy substituent

Figure 5 2 illustrates the emission spectra of $[Os(OMe\text{-}bpy)_3]^{2+}$ and $[Os(bpy)_3]^{2+}$ at room temperature in acetonitrile $[Os(bpy)_3]^{2+}$ is highly luminescent arising from the photophysical properties of $[Os(N)_6]^{2+}$ complexes, where N represents a nitrogen donating group such as bpy [19] By comparison the emission intensity from $[Os(OMe\text{-}bpy)_3]^{2+}$ is only approximately 3% of that found for $[Os(bpy)_3]^{2+}$ This decrease in emission intensity arises predominantly from a significantly shorter luminescent lifetime for the methoxy derivative For these reasons, the electron quenching effects of $[Os(bpy)_3]^{2+}$ have only been investigated Both complexes have different maximum emission wavelength and indicates that even though the emission in both species is originating from the same chromophore, $[Os(bpy)_3]^{2+}$, the methoxy substituents shifts $[Os(OMe\text{-}bpy)_3]^{2+}$ to longer wavelengths

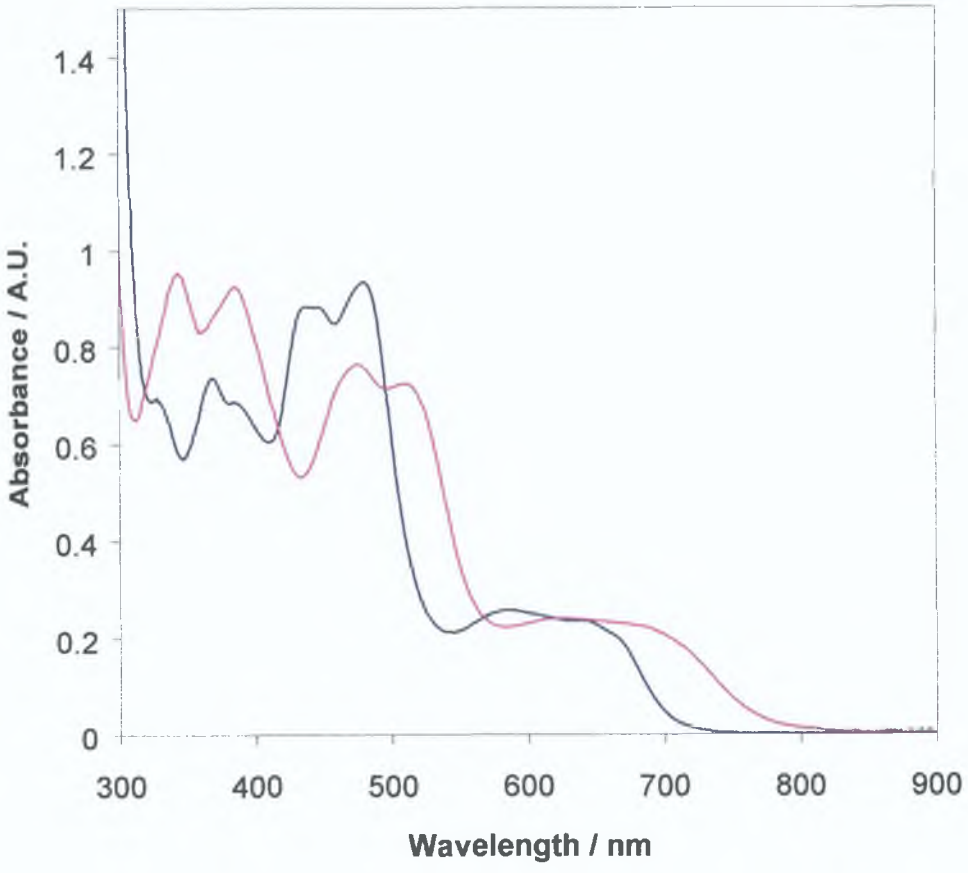

Figure 5.1. UV-Vis Absorbance spectra of $[Os(bpy)_3]^{2+}$ (———) and $[Os(OMe\text{-}bpy)_3]^{2+}$ (———). The concentration of both is 0.2 mM in acetonitrile.

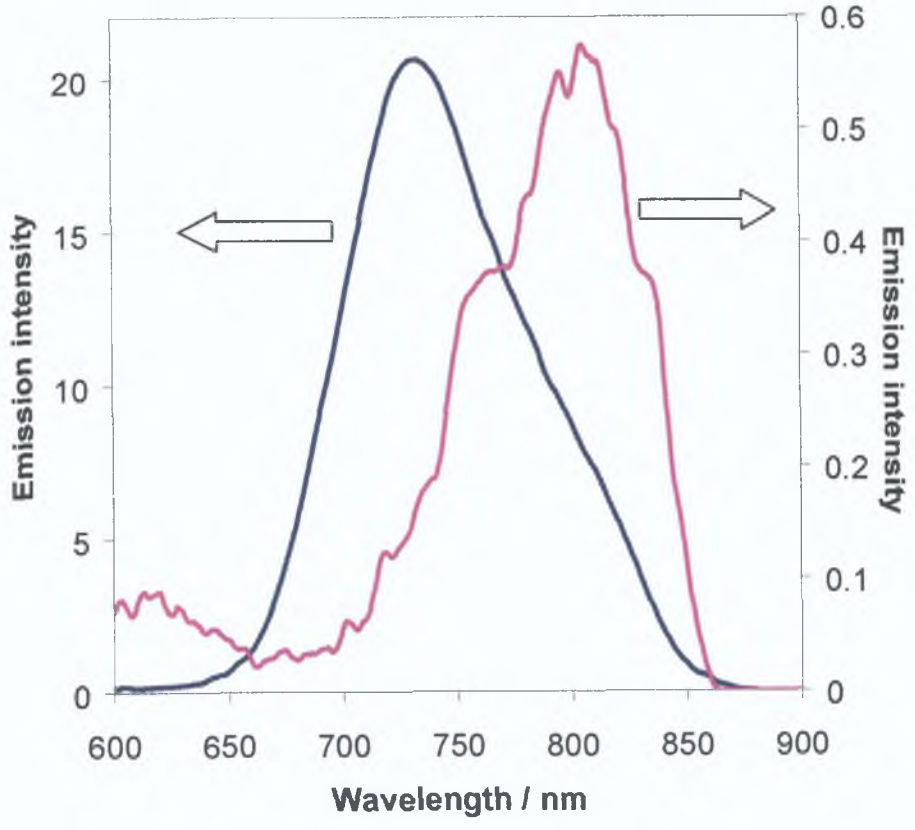

Figure 5.2. Emission spectra of $[Os(OMe\text{-}bpy)_3]^{2+}$ (——) and $[Os(bpy)_3]^{2+}$ (——) in acetonitrile at room temperature. The concentration of each complex is 10 μM. The excitation wavelength is 350 nm.

5 3 Photoinduced Charge Transfer

The fluorescence lifetime of a substance represents the average amount of time the species remains in the excited state prior to its return to the ground state Fluorescence is typically a unimolecular process and therefore the excited state population established by an impulse of exciting light will generally decay exponentially over time according to first order kinetics [20] The emission obtained for $[Os(OMe\text{-}bpy)_3]^{2+}$ using a 10 ns pulsed YAG laser were very poorly resolved which compromised the accuracy with which the emission lifetime could be determined To overcome this problem, Time-Correlated Single Photon Counting was used to determine the lifetime of $[Os(OMe\text{-}bpy)_3]^{2+}$ in deoxygenated acetonitrile This instrument is capable of picosecond time resolution enabling the short lifetime to be accurately measured

This technique counts photons which are time-correlated to the excitation pulse employed, building up a histogram of counts versus time channels, which represent the intensity decay of the sample TCSPC uses the rising edge of a photoelectron pulse for timing which allows phototubes of nanosecond width to provide sub-nanosecond resolution and therefore allows lifetimes of nanosecond timescale to be accurately determined As the method counts individual photons, rather than measuring the overall fluorescence intensity as a function of time as in transient laser spectroscopy, it can determine the lifetime of samples with relatively low fluorescence intensity [21] The transient achieved is produced in Figure 5 3 A lifetime of 4 89 ns for $[Os(OMe\text{-}bpy)]^{2+}$ was obtained by this method

For $[Os(bpy)_3]^{2+}$ the lifetime of the complex was estimated by monitoring the decay emission as a function of time and plotting the natural log of emission versus time The lifetime (τ) may be determined from the slope as follows

$$\ln(I/I_0) = -kt \qquad (1)$$

$$k = 1/\tau$$

The emission lifetime of $[Os(bpy)_3]^{2+}$ was obtained in deoxygenated acetonitrile at 248 K using transient laser spectroscopy The lifetime of the emission is the inverse of the slope of the semilog plot in the inset of Figure 4 and at 248 K is 470 ns In contrast, the lifetime of the complex obtained at 298 K is approximately 20 ns[22] indicating that as temperature increases, the emission lifetime decreases [23]

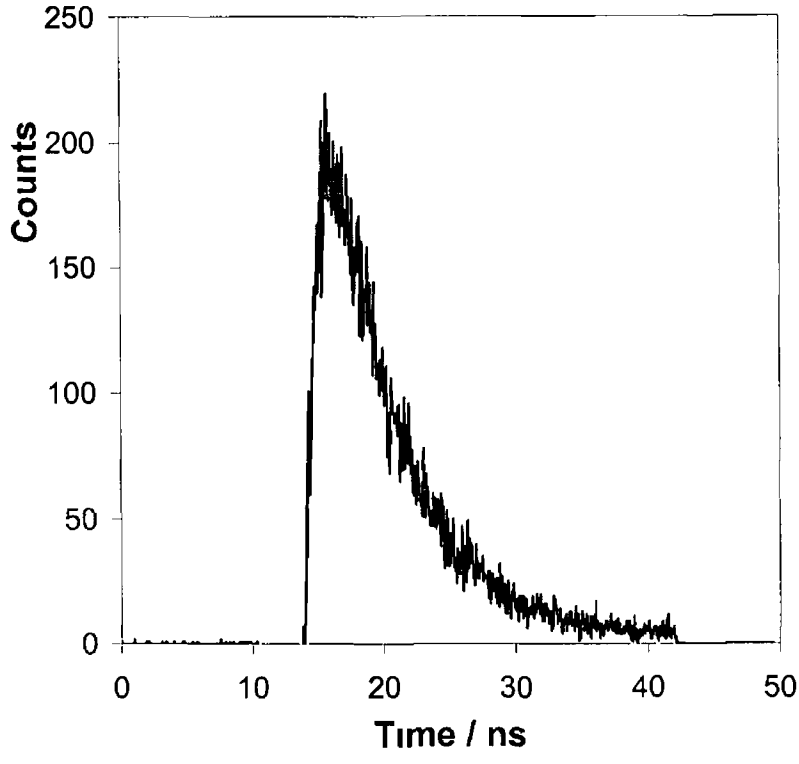

Figure 5 3 Emission transient for $[Os(OMe\text{-}bpy)_3]^{2+}$ following correction for the lamp profile recorded using time correlated single photon counting (TCSPC) approaches The concentration is 10 nM in deoxygenated acetonitrile The light source is an nF 900 Nanosecond Flashlamp filled with nitrogen, with a profile of 1 ns The excitation wavelength is 337 nm χ^2 is 1 338

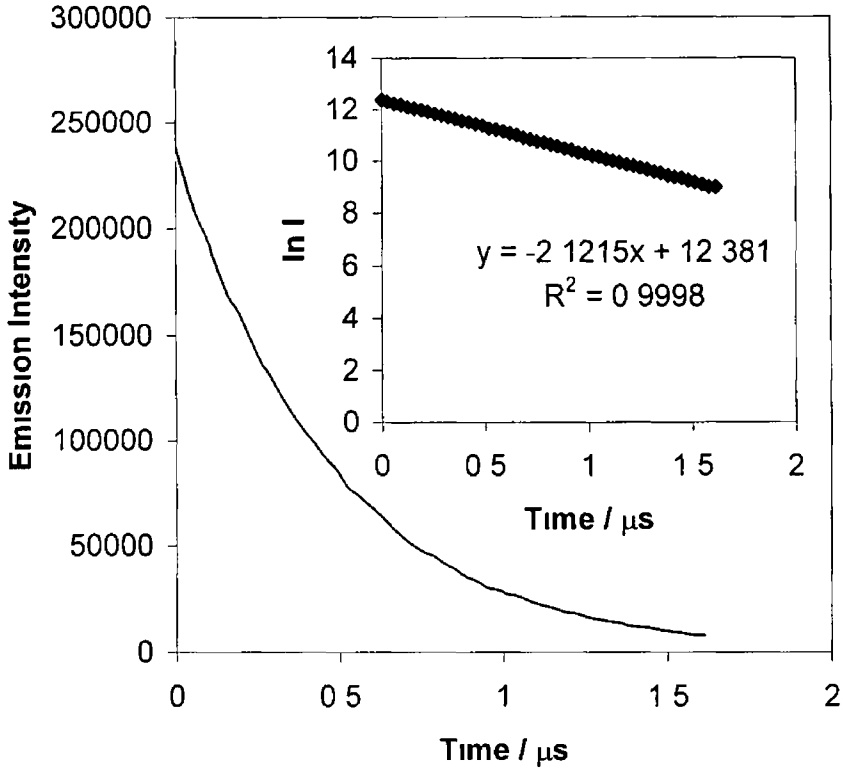

Figure 5 4 Emission decay for 0 6 nM $[Os(bpy)_3]^{2+}$ in deoxygenated acetonitrile at 248 K using transient emission spectroscopy The excitation wavelength is 400 nm (pulse duration 10 ns) and the detection wavelength is 800 nm Inset semilog plot of the decay

5 4 Electron Quenching Effects of $[Os(bpy)_3]^{3+}$

Fluorescence quenching is a process which decreases the intensity of the fluorescence emission by either an energy or electron transfer mechanism A wide variety of substances act as quenchers of fluorescence It has been demonstrated previously that adding ammonium cerium nitrate to solutions of $[Os(bpy)_3]^{2+}$ generates $[Os(bpy)_3]^{3+}$ that subsequently quench the excited state [24] Figure 5 5 shows the emission decay for the excited state $[Os(bpy)_3]^{2+*}$ and the decrease in intensity with increasing concentration of $[Os(bpy)_3]^{3+}$ The Os^{3+} state is non-emissive under experimental conditions and quenches the emissive Os^{2+} form upon contact

Both static and dynamic quenching require molecular contact between the fluorophore and quencher In the case of collisional quenching, the quencher must diffuse to the fluorophore during the lifetime of the excited state Upon contact, the fluorophore returns to the ground state by vibrational relaxation without emitting a photon Figure 5 6 illustrates the semilog plot of the decay of $[Os(bpy)_3]^{2+}$ with the addition of ammonium cerium nitrate For clarity only some of the quencher additions are shown The intercept decreases with increasing concentration of the quencher, which is also illustrated as an exponential decrease in Figure 5 7 Using Equation 1, the lifetime, τ, is 470 ± 12 ns for each of the slopes

The fact that τ is unchanged with increasing quencher concentration to the fluorophore indicates that static quenching is the dominant process [21] Static quenching removes a fraction of the fluorophores from observation The complexed fluorophores are non-fluorescent, and the only observed fluorescence is from the uncomplexed fluorophore The uncomplexed fraction is unperturbed, and hence the lifetime is τ_0 Therefore, for static quenching $\tau_0/\tau = 1$, where τ_0 is the lifetime in the absence of quencher and τ the lifetime in the presence of quencher The observation that quenching is predominantly static in nature contrasts sharply with previous investigations of this system where dynamic quenching was reported to have occured [22] This difference in quenching regime most likely arise because of the higher concentrations of fluorophore and quencher used here which will decrease the spatial separation of the fluorophore and quencher

Figure 5 8 illustrates that the osmium inter redox site separation of $[Os(bpy)_3]^{2+}$ decreases exponentially with increasing quencher concentration and is due to complex formation between the excited state $[Os(bpy)_3]^{2+}$ and the ground state $[Os(bpy)_3]^{3+}$

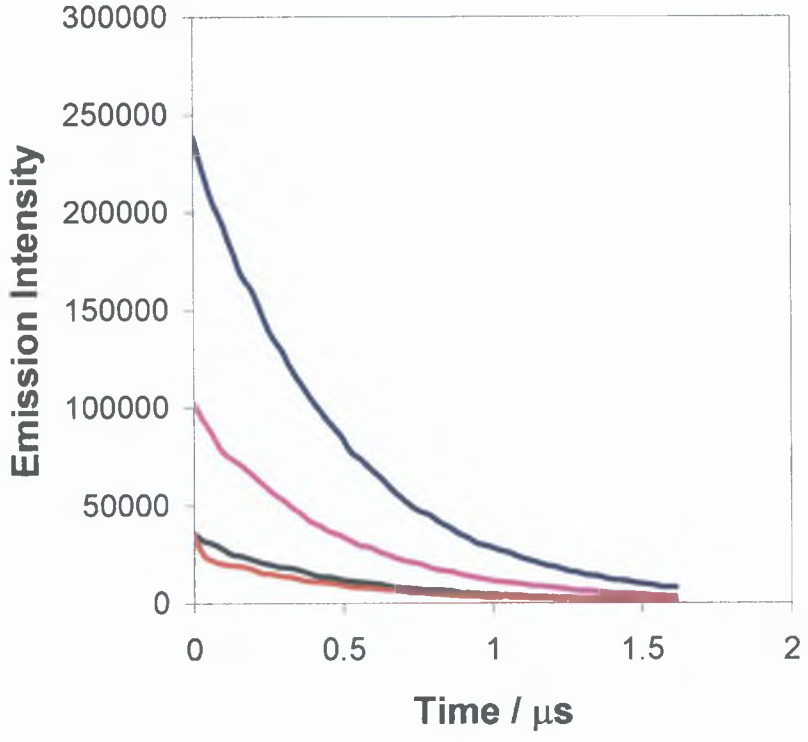

Figure 5.5. Emission decay for $[Os(bpy)_3]^{2+}$ (——) obtained in deoxygenated acetonitrile at 248 K using transient emission spectroscopy. The intensity of the decay decreases with additions of $[Os(bpy)_3]^{3+}$ generated chemically by addition of known quantities of 1 mM ammonium cerium nitrate; 10 μl (——), 20 μl (——), 30 μl (——). The excitation wavelength is 400 nm and the detection wavelength is 800 nm.

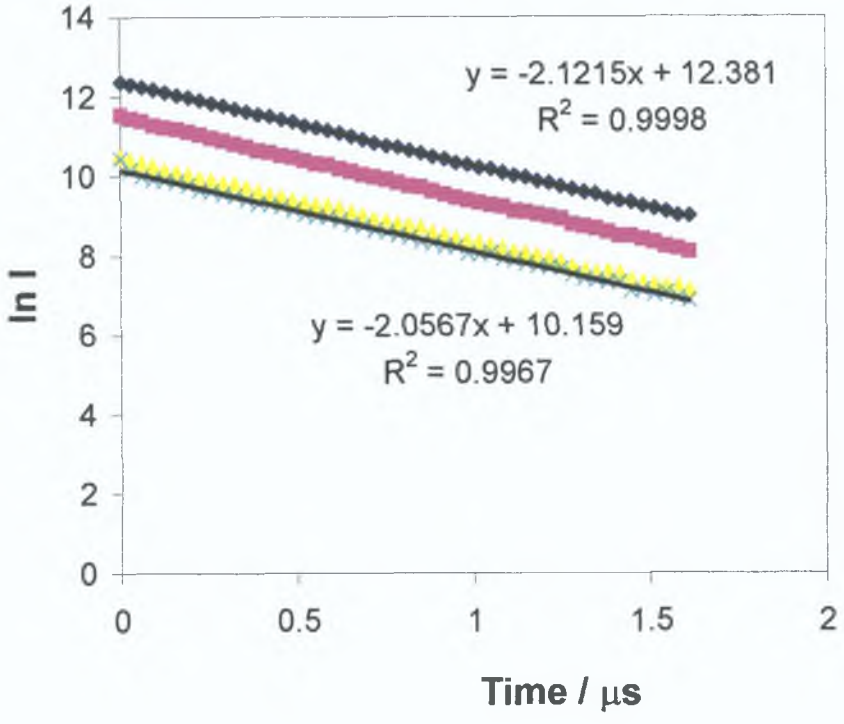

Figure 5.6. Semilog plot of the lifetime decay of $[Os(bpy)_3]^{2+}$ (♦) with additions of the quencher $[Os(bpy)_3]^{3+}$ upon additions of known quantities of 1 mM ammonium cerium nitrate; 10 μl (■); 20 μl (▲) and 30 μl (●). The y intercept decreases with increasing mole ratio of ammonium cerium nitrate.

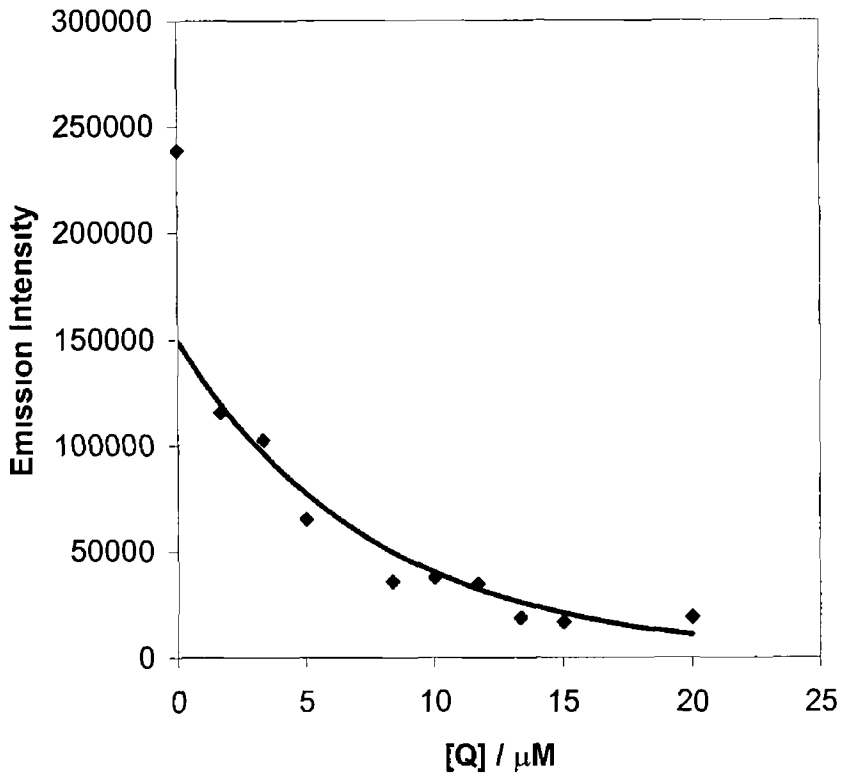

Figure 5 7 Decrease in emission intensity of $[Os(bpy)_3]^{2+}$ with [Q], quencher concentration Q is $[Os(bpy)_3]^{3+}$ and is generated upon addition of 1 mM ammonium cerium nitrate

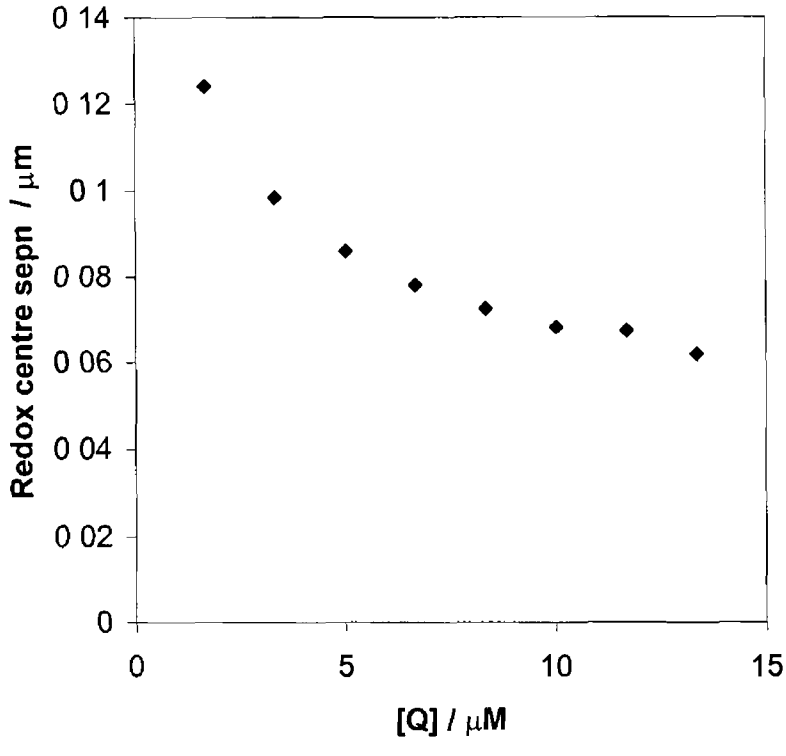

Figure 5 8 Decrease in Os^{2+} redox centre separation with increasing concentration of Q, $[Os(bpy)_3]^{3+}$, generated by the addition of 1 mM ammonium cerium nitrate

5 5 Stern-Volmer Effects

For static quenching of fluorescence, the dependence of the emission intensity, F on quencher concentration [Q] is given by the Stern-Volmer equation

$$F_0 / F = 1 + K_S[Q] \qquad (2)$$

where F_o is the emission in the absence of quencher and K_S is the Stern-Volmer constant Figure 5 9 illustrates the Stern-Volmer plot for solution phase $[Os(bpy)_3]^{2+}$ The slope of the plot reveals that K_S is 0 57 μM^{-1}

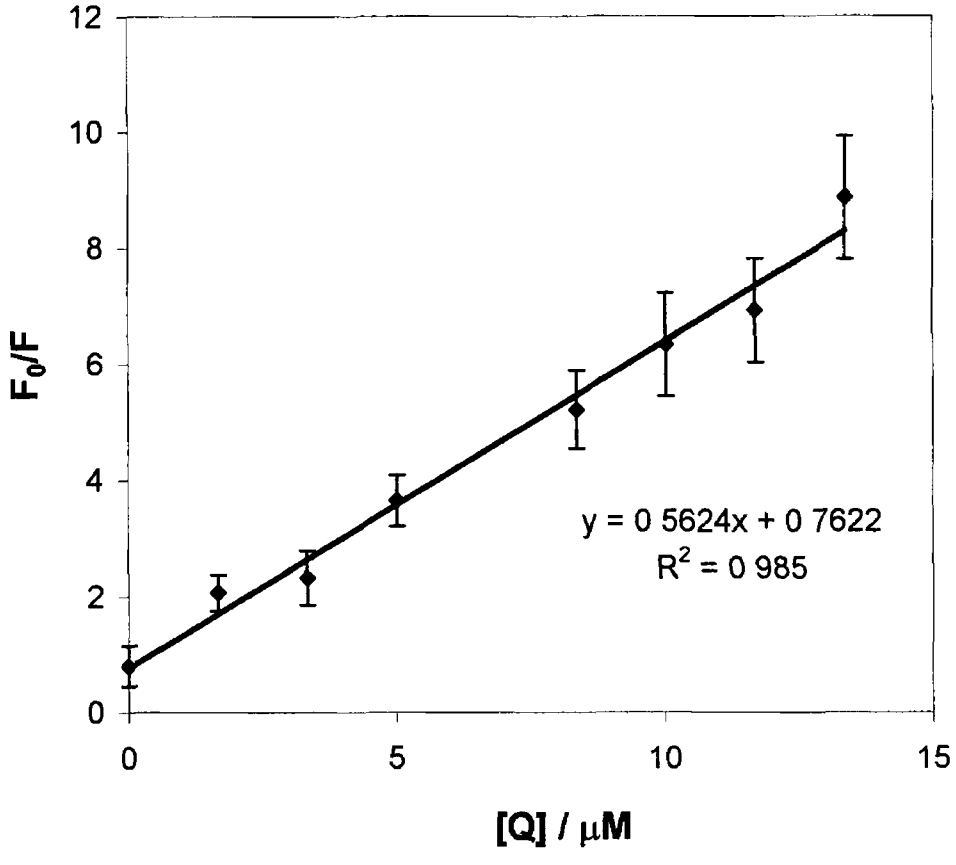

Figure 5.9. Stern-Volmer plot for quenching of $[Os(bpy)_3]^{2+}$ by the quencher $[Os(bpy)_3]^{3+}$ The quencher (Q) was generated chemically by the addition of ammonium cerium nitrate The error bars were obtained by standard deviation from 3 independent experiments

5 6 Conclusion

Excited state (photoinduced|) processes and fluorescence quenching are powerful experimental methods by which to investigate the parameters, which govern electron transfer Investigations into $[Os(bpy)_3]^{2+}$ could be useful in understanding electron transfer in redox active solid deposits and polymeric materials Transient emission spectroscopy and time-correlated single photon counting have been successfully used to determine the emission lifetime of $[Os(bpy)_3]^{2+}$ and $[Os(OMe\text{-}bpy)_3]^{2+}$ in solution The lifetime of $[Os(OMe\text{-}bpy)_3]^{2+}$ is 4 9 ns is significantly shorter than 470 ns for $[Os(bpy)_3]^{2+}$ For this reason, quenching experiments were only performed on $[Os(bpy)_3]^{2+}$

The quenching effects of $[Os(bpy)_3]^{3+}$ have been probed The observation that the lifetime of the complex, τ, is unchanged with increasing quencher concentration indicating that static quenching is present According to the Stern-Volmer equation, the Stern-Volmer constant, K_S, is 0 57 μM^{-1} for the quenching of $[Os(bpy)_3]^{2+}$ Experiments focused on elucidating the quenching mechanism and Stern-Volmer constant for solid deposits of $[Os(bpy)_3]^{2+}$ provided unreliable and inconclusive results because of dissolution especially in deposits of mixed redox composition and under laser irradiation Attempts to stabilise the deposits by changing the identity and concentration of the anion, or by applying a nafion overcoat, were not successful However, it is reasonable to expect that solid deposits can be formed that show the excellent stability towards dissolution of $[Os(OMe\text{-}bpy)_3]^{2+}$ and the long lived excited states of $[Os(bpy)_3]^{2+}$ Under these circumstances, the importance of static vs dynamic quenching for solid and solution phase reactants, as well as the dynamics of electron transfer between Os^{2+*} and Os^{3+} could be elucidated

5 7 References

(1) Palacios, I , Castillo, R , Vargas, R A *Electrochim Acta*, **2003**, 48, 2195

(2) Cao, Y W C , Jin, R C , Mirkin, C A *Science*, **2002**, 297, 1536

(3) Inoue, M , Cruz-Vazquez, C , Inoue, M B *Syn Metals*, **1993**, 57, 3748

(4) Brennan J L , Howlett, M , Forster, R J *Faraday Discuss* **2002**, 121, 391

(5) Forster, R J , Keyes, T E , *J Phys Chem B* **2001**, *105*, 8829

(6) Schanze, K S , Meyer, T J Inorg Chem , 1985, 24, 2123

(7) Hoselton, M A , Lin, C-T , Schwarz, H A , Sutin, N *J Am Chem Soc* **1978**, 100, 2383

(8) Pedinski, T , Marciniak, B , Hug, G L *J Photochem Photobiol A Chem* , **2002**, 150, 21

(9) Balzani, V , Juris, A , Venturi, M , Campagna, S , Serroni, S *Chem Rev* , **1996**, 96, 759

(10) Chang, Q , Murtaza, Z , Lakowicz, J R , Rao, G *Anal Chim Acta* , **1997**, 350, 97

(11) Jang, H , Pell, L E , Korgel, B A , English, D S *J Photochem Photobiol A Chem* , **2003**, 158, 111

(12) Voraberger, H S , Trettnak, W , Ribitsch, V *Sensors and Actuators B Chemical*, **2003**, 90, 324

(13) Brunel, M , Ozhul, C , Sanchez, F *Sensors and Actuators B Chemical*, **2000**, 62, 238

(14) Hopfield, J J Onuchic, J N , Beratan, D N *J Phys Chem* , **1989**, 93, 6350

(15) Goujon, A , Varret, F , Escax, V , Blauzen, A , Verdaguer, M *Polyhedron*, **2001**, 20, 1339

(16) Furue, M , Ishibashi, M , Satoh, A , Oguni, T , Maruyama, K , Sumi, K , Kamachi, M *Coord Chem Rev* , **2000**, 208, 103

(17) Lakowicz, J R , Malicka, J , D'Auria, S , Gryczynski, I *Anal Biochem* , **2003**, 320, 13

(18) Feng, J , Shan, G , Hammock, B D , Kennedy, I M *Biosensors and Bioelectronics*, **2003**, 18, 1055

(19) Meyer, T J *Acc Chem Res* **1978**, 11, 94

(20) Atkins, P W "Physical Chemistry", 1st Ed , Oxford University Press, London 1978

(21) Lakowicz, J R "Principles of Fluorescnece Spectroscopy", 2nd Ed , Kluwer Academic / Plenum Publishers, New York, 1999

(22) Turner Jones, E T , Faulkner, L R *J Electroanal Chem* , **1984**, 179, 53

(23) Brennan, J PhD Thesis, Dublin City University, **2002**

(24) Bilakhiya, A K , Tyagi, B , Paul, P *Polyhedron*, **2000**, 19, 1233

Chapter 6

Conclusions and Future Work

The focus of this thesis has been to investigate the charge transport properties in redox active solid state, metallopolymer and metallopolymer nanoparticles composite materials As discussed in Chapter 1, studying the charge transport properties is pivotal in the development of materials for technological devices as it is a direct indication of the efficiency of the material Even though charge transport properties of these materials have been well reported in the literature, very few deal with ways of enhancing charge transport and factors that affect it In particular, the development of metallopolymer nanoparticle composites have revealed very exciting and novel results detailing the increased charge transport rate by approximately an order of magnitude for the metallopolymer with the addition of gold nanoparticles These findings could certainly impact the development of materials for catalytic and sensor development

Chapter 2 describes the synthesis and characterisation of the osmium polypyridyl complexes as solid deposits, metallopolymer and metallopolymer nanoparticle composites Osmium polypyridyl complexes are excellent species for the study of charge transport as they exhibit nearly ideal electrochemical responses They could be examined in simple aqueous electrolytes and remained stable throughout experimentation

In Chapter 3, the voltammetric properties of solid deposits of $[Os(OMe\text{-}bpy)_3](PF)_6$ were reported These solid deposits were formed on platinum microelectrodes by mechanical abrasion 'Break in' effect or the degree of solvation was identified in the voltammetry when initially electrochemically cycled in the electrolyte This effect may arise from the close packing of the complex crystals resulting in a decreased internal free volume Electrochemically cycling the complex in low pH electrolyte resulted in more stable deposits with a change in film morphology With scanning electron microscopy, crystals with plate like structures were identified No noticeable changes were observed in the layer when cycled in neutral electrolyte It is probable that protonation of the methoxy groups encourages bonding between the complexes thus promoting the formation of crystals The rate of charge transport increased from $1\ 5\pm0\ 1 \times 10^{-9}$ cm^2s^{-1} for $0\ 1 \leq [HClO_4] \leq 0\ 6$ M to $13\pm1 \times 10^{-9}$ cm^2s^{-1} in 1 0 M $HClO_4$ However, conclusions cannot be drawn on whether counterion motion or electron transfer limited the overall rate of charge transport, as the diffusion coefficient was not totally

dependent/independent on the electrolyte concentration The heterogeneous electron transfer rate constants were calculated using a computer simulation based on the Butler-Volmer Theory and were indistinguishable for solid and solution phase reactants, being 1 0±0 05 x 10^{-4} cms ^{1} and 6 1±0 2 x 10^{5} cms ^{1}, respectively This result indicates that the electron transfer from the electrode to the redox species is similar in both cases

Future experiments in this area could focus on using solid deposits with bulkier side groups to encourage a higher free volume within the deposit This could allow comparisons to be made regarding side group size and any change in 'break in' effect as well as charge transport through the deposit The degree of counterion and solvent movement within the solid deposit could be monitored using electron probe microscopy and electrochemical quartz crystal microbalance techniques

In Chapter 4 the metallopolymer [Os(bpy)$_2$ PVP$_{10}$ Cl]Cl was drop cast on to the platinum microelectrode surface and electrochemical properties probed As discussed in the literature review, redox active polymeric materials can have different structural and electrochemical properties when compared to the solid state form The redox centres are further apart with the result that the charge transport properties can differ significantly 'Break in' was not apparent and may have been due to its high water content Polymeric materials are rigid and electrochemical cycling resulted in no morphological changes Introducing gold nanoparticles to the complex forming metallopolymer nanoparticle composites enhanced the charge transport rate The charge transport increased by approximately an order of magnitude from 5 3±2 x 10^{10} cm^{2}s ^{1} to 5 8 x 10^{9} cm^{2}s ^{1} corresponding to electron transfer rates between the redox centres of 1 9 x 10^{6} M ^{1}s ^{1} and 1 7 x 10^{7} M ^{1}s ^{1} These enhanced charge and electron transport values may indicate that, an interconnected network is formed possibly involving the gold nanoparticles mediating electron tunnelling between the osmium redox centres

Some size control exists when synthesising these metallopolymer nanoparticle composites as decreasing the mole fraction of metallopolymer increased the average particle size from 1 6±0 3 to 5 2±0 6 nm The percolation curves reveal that both the PVP and metallopolymer composites exhibit a sharp increase in conductivity for a critical loading of gold nanoparticles Conversely, the percolation threshold is lower for

the metallopolymer based composite compared to the PVP matrix, the values being 0 07±0 01 and 0 31±0 04, respectively The metallopolymer system seems to be highly conducting which suggests that the osmium bypyridyl centres mediate electron transfer between adjacent metal particles over much greater distances than the PVP material

The ion pairing properties of the metallopolymer were also affected with the introduction of the gold nanoparticles Nernstian type behaviour was observed for the pure metallopolymer with increasing $HClO_4$ concentration with a slope of 71 4±0 2 mV dec^{-1} reported In contrast, the metallopolymer nanoparticle composites were insensitive to the $HClO_4$ concentration and implies that perchlorate anions do not become paired with the Os^{3+} centres, most likely because of strong interactions of the osmium with the gold nanoparticles The heterogeneous rate constant for the metallopolymer increases from 8 25±1 75 x 10^{-5} cms^{-1} to 4 0±0 2 x 10^{-3} cms^{-1} for the metallopolymer nanoparticle composite suggesting that the gold nanoparticles may mediate electron transfer between the electrode surface and the osmium redox centres thus decreasing the electron transfer distance Experimental findings for the charge transport properties of metallopolymer nanoparticle composites have not been cited in the literature previously and could lead to some further exciting investigations with could influence research fields of molecular electronic research The size of the metallopolymer nanoparticle composites formed could be monitored using polymers of various backbone lengths in conjunction with charge transport investigations Further work in this area could also include exploring the optical properties and the conductivity of the metallopolymer nanoparticle composites at various sizes

Chapter 5 describes the investigation of $[Os(bpy)_3]^{2+}$ as a test species to investigate the rate of electron exchange between an excited state Os^{2+*} centre and an Os^{3+} site in solution phase which could be useful in understanding electron transfer in redox active solid deposits and polymeric materials The previous chapters describing the solid deposits and polymeric materials all exploit a potential to create a concentration gradient so as to drive charge transport However, light induced electron transfer represents an attractive alternative to ground state, potential driven processes where the dynamics of excited state electron transfer can be probed The results in this chapter indicate that certain demands on properties of redox compounds that have to be met before reliable

results can be reported For example, the excited state lifetime of the Os^{2+*} species has to be sufficiently long to allow sufficient time with the quenching Os^{3+} unit Also, both solid deposits and polymeric species must be sufficiently insoluble and stable under pulse laser illumination

The quenching effects of $[Os(bpy)_3]^{2+}$ were probed The observation that the lifetime of the complex, τ, was unchanged with increasing quencher concentration indicating that static quenching was present According to the Stern-Volmer equation, the Stern-Volmer constant, K_S was 0 57 μM^{-1} for the compound Elucidating the quenching mechanism for solid deposits of $[Os(bpy)_3]^{2+}$ proved inconclusive because of dissolution especially in deposits of mixed redox composition Future work in this area could provide interesting electron transfer comparisions with solution phase once stability of the solid state and polymeric species has been obtained

In conclusion, this thesis has demonstrated the profound contribution that redox active solid state, metallopolymer and metallopolymer nanoparticle composites can make to further understanding of charge transport Improving the factors affecting charge transport provides the necessary ways to control it to our advantage Investigating these factors is vital for the development of novel devices for chemical sensors, electrochromic materials, battery and molecular electronics

Appendix A

Dynamics of Charge Transport through Osmium Tris Dimethoxy Bipyridyl Solid Deposits

Lorraine Keane, Conor Hogan, and Robert J. Forster*

National Center for Sensor Research, School of Chemical Sciences, Dublin City University, Dublin 9, Ireland

Received June 19, 2001. In Final Form: October 23, 2001

Solid deposits of $[Os(OMe\text{-}bpy)_3](PF_6)_2$ have been formed on a platinum microelectrode, where OMe-bpy is 4,4′-dimethoxy, 2-2′-dipyridyl. The voltammetry associated with the $Os^{2+/3+}$ redox processes is nearly ideal where the supporting electrolyte is 0.1 M $HClO_4$ and suggests that the redox centers within the deposits are solvated. Scanning electron microscopy reveals that prior to voltammetric cycling, the deposits exist as an array of microscopic particles. In contrast, after voltammetric cycling in perchloric acid the deposit becomes microcrystalline in the form of thin plates. Electrocrystallization is not observed when the deposits are cycled in neutral electrolyte suggesting that protonation of the methoxy groups plays an important role in the process. Where the supporting electrolyte is $HClO_4$, voltammetry conducted under semi-infinite linear diffusion conditions yields a homogeneous charge transport diffusion coefficient, D_{CT}, of $1.5 \pm 0.1 \times 10^{-9}$ cm^2 s^{-1} for $0.1 \leq [HClO_4] \leq 0.6$ M. In contrast, above 0.6 M $HClO_4$ D_{CT} increases significantly reaching $13 \pm 1 \times 10^{-9}$ cm^2 s^{-1} in 1.0 M $HClO_4$. Analysis of these data according to the Dahms−Ruff equation yields a self-exchange rate constant of 5.7×10^6 M^{-1} s^{-1}. High scan rate voltammetry, $5 \leq \upsilon \leq 100$ V s^{-1}, has been used to determine the standard heterogeneous electron transfer rate constant, $k°$, as $1.0 \pm 0.05 \times 10^{-4}$ and $6.1 \pm 0.2 \times 10^{-5}$ cm s^{-1} for solid and solution phase, respectively.

Introduction

The local microenvironment of reactants can significantly affect the dynamics of electron transfer by changing the electron transfer distance, the local dielectric constant, or the rate-determining step in the overall process. In contrast to solution phase investigations, electron transfer processes within solids have only been investigated relatively recently.[1,2] This situation is surprising given the pivotal roles that solid state redox active materials play in devices ranging from optical detectors,[3] batteries,[4] redox supercapacitors and sensors.[5−7] However, to be technologically useful, it must be possible to quickly switch the redox composition of the solid. Osmium complexes are particularly attractive in this regard because of their stability of numerous oxidation states and very large self-exchange rate constants.[8,9] However, charge transport through solids can be controlled either by the rate of electron self-exchange between the redox sites or by the movement of charge-compensating counterions.[10] Recently, we demonstrated that solid deposits of [Os(bpy)$_2$ bpt Cl] deposits, where bpy is 2,2′-bipyridyl and bpt is 3,5-bis(pyridin-4-yl)-1,2,4,-triazole, exhibit nearly ideal reversible voltammetric responses.[11] In this system, the rate of charge-compensating counterion motion rather than electron hopping between the redox centers limits the overall rate of charge propagation. This situation arises because close packing of the complexes in the electrocrystallized deposit limits the free volume causing slow counterion diffusion. One approach to creating solids that facilitate more rapid ion transport is to encourage a higher free volume in the solid deposit by using complexes with bulkier side groups.

Chart 1

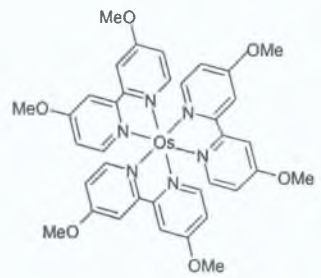

In this contribution, we consider the voltammetric properties of solid deposits of $[Os(OMe\text{-}bpy)_3](PF_6)_2$, where OMe-bpy is 4,4′-dimethoxy, 2-2′-dipyridyl (Chart 1). To facilitate dynamic measurements, these solid deposits have been formed on platinum microelectrodes by mechanical abrasion of the solid onto the electrode surface. The complex is insoluble in water allowing the electrochemistry to be investigated in aqueous electrolyte. The methoxy oxygen groups are capable of undergoing protonation/deprotonation reactions that give rise to a hydrogen-bonded structure in low pH media. There have been surprisingly few studies on the impact of hydrogen bonding on the structure of solid state materials. This

* To whom correspondence should be addressed.

(1) Scholz, F.; Nitschke, L.; Henrion, G. *Electroanalysis* **1990**, *2*, 85.
(2) Scholz, F.; Lange, B. *Trends Anal. Chem.* **1992**, *11*, 359.
(3) Yang, C.; He, G.; Wang, R.; Li, Y. *J. Electroanal. Chem.* **1999**, *471*, 32.
(4) Nazar, L. F.; Goward, G.; Leroux, M.; Duncan, H.; Kerr, T.; Gaubicher, J. *Int. J. Inorg. Mater.* **2001**, *3*, 191.
(5) Wrighton, M. S. *Science* **1986**, *231*, 32.
(6) Chidsey, C. E. D.; Murray, R. W. *Science* **1986**, *231*, 25.
(7) Tredicucci, A.; Gmachi, C.; Capasso, F.; Sivco, D. L.; Hutchinson, A. L.; Cho, A. Y. *Nature* **1998**, *396*, 350.
(8) Quaranta, F.; Rella, R.; Siciliano, P.; Capone, S.; Epifani, M.; Vasanelli, L.; Licciulli, A.; Zocco, A. *Sens. Actuators, B* **1999**, 350.
(9) Ni, J.; Ju, H.; Chen, H.; Leech, D. *Anal. Chim. Acta* **1999**, *378*, 151.
(10) Deuber, R. E.; Bond, A. M.; Dickens, P. G. *J. Electrochem. Soc.* **1992**, *139*, 2363.
(11) Forster, R. J.; Keyes, T. E. *Phys. Chem. Chem. Phys.* **2001**, *3*, 1336.

10.1021/la010927s CCC: $22.00
Published on Web 00/00/0000 PAGE EST: 7.5

situation is striking because careful studies on biosystems have proven that both the secondary structure and hydrogen bonding play critical roles in dictating the efficiency of long-range electron transfer.[12] In the investigations reported here, we have used scanning electron microscopy to probe the effect of voltammetric cycling on the structure of the solid deposit in contact with both neutral and acidic electrolytes.

Cyclic voltammetry under semi-infinite linear diffusion conditions has been used to measure the rate of homogeneous charge transport through the deposits.[13] By systematically varying the concentration of the supporting electrolyte, we have obtained an insight into whether electron transfer or counterion transport limits the rate at which the redox composition can be switched.

For technological applications ranging from molecular electronics to sensors, it is important to understand those factors that control the rate of electron transfer across the interface between a metal substrate and a molecular material. Therefore, we have probed the rate of heterogeneous electron transfer for this complex as both a solid deposit and as a solution phase reactant. These investigations into homogeneous charge transport and heterogeneous electron transfer for solid deposits will underpin developments ranging from electrocatalysis to redox switchable nonlinear optical materials.

Experimental Section

Chemicals. All chemicals were of analytical grade and were obtained from Sigma-Aldrich. All aqueous solutions were prepared using Milli-Q water and were thoroughly deoxygenated using nitrogen for 15 min prior to performing the electrochemical experiments.

Preparation of $[Os(OMe\text{-}bpy)_3](PF_6)_2$. The complex $[Os(OMe\text{-}bpy)_3](PF_6)_2$ was prepared from $[Os(OMe\text{-}bpy)_2\ Cl_2]$ which was synthesized as described by Heller and co-workers.[14] $[Os(OMe\text{-}bpy)_2\ Cl_2]$ (208 mg, 0.3 mmol) was placed in 40 cm^3 of methanol and refluxed for 10 min to ensure complete dissolution. A solution of 65 mg (0.3 mmol) of 4,4′-dimethoxy, 2-2′-dipyridyl dissolved in 10 cm^3 of methanol was added, and the solution was refluxed for 15 h. The progress of the reaction was monitored using HPLC and cyclic voltammetry. After the reaction was complete, the volume was reduced to 5 cm^3 by rotary evaporation. Ammonium hexafluorophosphate (95+%, Aldrich) was then added, and the dark green/black product was collected by filtration and washed with diethyl ether. The product was recrystallized from aqueous methanol to give dark purple-black crystals; yield: 295 mg, 88%. Elemental analysis calculated for $C_{36}H_{36}O_6N_6OsP_2F_{12}$: C, 38.29%; H, 3.19%; N, 7.44%. Found: C, 38.7%; H, 3.3%; N, 7.2%. The complex was further characterized using IR, UV−vis, NMR, and cyclic voltammetry. $^1H_{nmr}$ (CD_3CN): H3, 8.2 (d, 3H); H4, 6.9 (dd, 3H); H5, 7.4 (d, 3H); OMe, H1′, H2′, H3′, 4.05, (s, 3H).

Instrumentation. Cyclic voltammetry was performed using a CH Instrument model 660 Electrochemical Workstation and a conventional three-electrode cell. The platinum working electrodes used in these experiments ranged in radii dimensions from 25 μm to 3 mm. Microelectrodes were prepared using platinum microwires of radii between 1 and 25 μm sealed in a glass shroud as described previously.[15] The working electrodes were polished successively with 1.0, 0.3, and 0.05 μm aqueous alumina slurries and sonicated in distilled water and rinsed with acetone after each polishing step. The electrodes were then electrochemically cleaned by cycling in deoxygenated 0.1 M H_2SO_4 from −0.3 to 1.5 V until a voltammogram characteristic of a clean platinum electrode was obtained.[16] Before modification, the electrodes were cycled in 0.1 M $LiClO_4$ until hydrogen desorption was complete. Potentials are quoted with respect to a BAS Ag/AgCl gel-filled electrode, and all experiments were performed at room temperature (22 ± 3 °C).

For short time scale experiments (<250 μs), that were designed to probe the cell resistance and the interfacial capacitance, a custom-built programmable function generator−potentiostat was used.[17] This instrument had a rise time of less than 10 ns and was used to apply potential steps of variable pulse width and amplitude directly to a two-electrode cell. A large area Pt foil and an SSCE reference electrode were combined to form a counter electrode. The foil lowered the resistance and provided a high-frequency path. The current to voltage converter was based on a Comlinear CLC 203 AI operational amplifier with a 1500 Ω feedback resistance and a response time of less than 10 ns. The chronoamperograms were recorded using a HP54201A digital oscilloscope in 64X time-average mode. Cell time constants were extracted from the slope of ln $i(t)$ versus t plots using software routines written in Microsoft Excel.

Formation of Solid Deposits. For solid state voltammetric measurements,[18] two methods were used to transfer the solid onto the surface of the working electrode. In the first approach, the solid was transferred from a filter paper onto the surface of the working electrode by mechanical abrasion. This process caused some of the complex to adhere to the electrode surface as a random array of particles. In the second approach that was used to achieve surface coverages greater than approximately 10^{-7} mol cm^{-2}, a drop of Milli-Q water was first added to the complex before transferring the material onto the electrode surface as a paste. Prior to electrochemical measurements, the coating was allowed to dry. Beyond minor differences in the initial scans, films prepared by both methods give indistinguishable voltammetric responses. Films prepared using either approach show comparable stability toward dissolution. After use, the electrode surface was renewed by polishing using an aqueous slurry of 0.05 μm alumina.

Scanning Electron Microscopy. Scanning electron microscopy (SEM) was performed using a Hitachi S-3000N system. For SEM investigations, films were formed on 3 mm radius carbon disks. In electrochemical investigations, the modified disks were electrochemically cycled and then the layers were copiously washed in electrolyte-free Milli-Q water and then dried in a vacuum desiccator for several hours. Control experiments consisted of exposing the samples to electrolyte or Milli-Q water without electrochemical cycling.

Results and Discussion

Electrochemical Properties of $[Os(OMe\text{-}bpy)_3]^{2+}$ Solid Deposits. Figure 1 illustrates repetitive cyclic voltammograms for an $[Os(OMe\text{-}bpy)_3]^{2+}$ solid deposit on a 25 μm platinum electrode where the supporting electrolyte is 0.1 M $HClO_4$ and the scan rate is 0.1 V s^{-1}. The voltammetry changes significantly during the initial scans with the oxidation peak current approximately doubling over the first 50 cycles before becoming constant. Also, the anodic peak potential, E_{pa}, shifts in a positive potential direction by approximately 75 mV during the first 25 cycles. In contrast, the peak currents and potentials associated with the reduction process remain virtually unchanged when the deposit is repeatedly cycled. Figure 2 illustrates cyclic voltammograms for the complex dissolved in acetonitrile and for a solid deposit that has been repeatedly cycled until an equilibrium response is obtained. The voltammogram of the solution phase reactant is electrochemically reversible with $i_{pa}/i_{pc} = 1.0 \pm 0.05$. However, the peak-to-peak separation, ΔE_p, of 100 ± 10 mV is larger than the 56 mV theoretically

(12) Gray, H. B.; Winkler, J. R. *Annu. Rev. Biochem.* **1996**, *65*, 537.
(13) Wightman, R. M.; Wipf, D. O. *Electroanalytical Chemistry*; Bard, A. J., Ed.; Marcel Dekker: New York, 1989; Vol. 15.
(14) Taylor, C.; Kenaussis, G.; Katakis, I.; Heller, A. *J. Electroanal. Chem.* **1995**, *396*, 511.
(15) Forster, R. J.; Faulkner, L. R. *J. Am. Chem. Soc.* **1994**, *116*, 5444.
(16) O'Hanlon, D. Ph.D. Thesis, Dublin City University, Dublin, Ireland, 1999.
(17) Xu, C. Ph.D. Thesis, University of Illinois at Urbana-Champaign, Champaign, IL, 1992.
(18) Bond, A. M.; Marken, F. *J. Electroanal. Chem.* **1994**, *372*, 125.

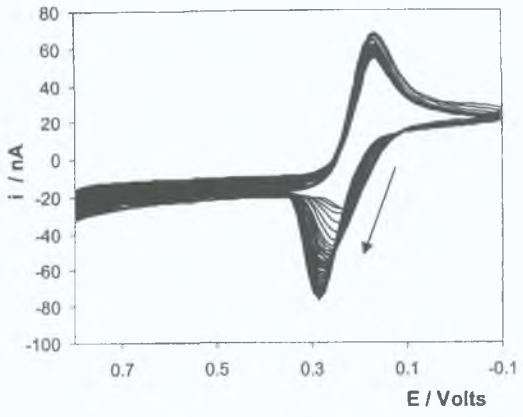

Figure 1. Repetitive cyclic voltammograms for an $[Os(OMe\text{-}bpy)_3]^{2+}$ solid deposit immobilized on a 25 μm platinum electrode. The supporting electrolyte is 0.1 M $HClO_4$, and the scan rate is 0.1 V s^{-1}. The initial potential is −0.100 V, and oxidation currents are negative.

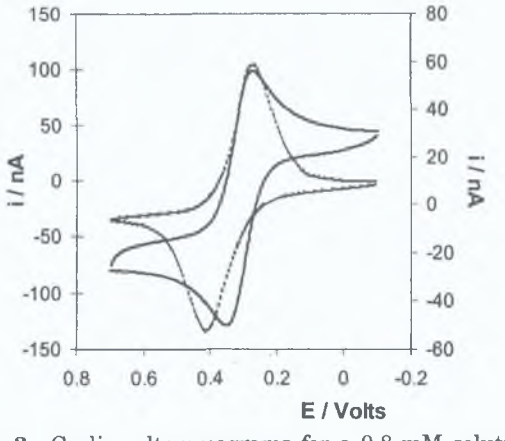

Figure 2. Cyclic voltammograms for a 0.8 mM solution of $[Os(OMe\text{-}bpy)_3]^{2+}$ dissolved in acetonitrile (solid line) and as a solid deposit (dashed line). In both cases, the supporting electrolyte is 0.1 M $HClO_4$, the working electrode is a 25 μm platinum electrode, and the scan rate is 0.1 V s^{-1}.

predicted for an ideally reversible reaction. The formal potentials, $E^{o\prime}$, as given by the average of the anodic and cathodic peak potentials, are 0.340 and 0.312 V for the solid deposit and solution phase reactants, respectively. This similarity in formal potentials is important and suggests that the local microenvironment of the redox center within the solid is quite similar to that found in acetonitrile.

Resistance and Interfacial Capacitance. When attempting to extract quantitative data from voltammetric data, for example, formal potential, charge transport diffusion coefficients, or heterogeneous electron transfer rate constants, it is important to consider the effects of both the electrode response time and ohmic effects. Also, by examining the resistance as a function of the supporting electrolyte concentration, it ought to be possible to obtain a limited insight into the permeability of the deposit. When a polycationic deposit is placed in a dilute solution of a strong electrolyte, the concentration of counterions (PF_6 in this case) within the deposit is typically considerably larger than that found in the contacting solution. For the films considered here, the anion concentration initially present in the deposit is expected to be of the order of 3 M. Thus, under the influence of the concentration gradient, counterions may diffuse from the deposit into the solution until the concentrations become equal in the two phases. However, if diffusion of charged counterions occurs, then electroneutrality within the film would be violated, and

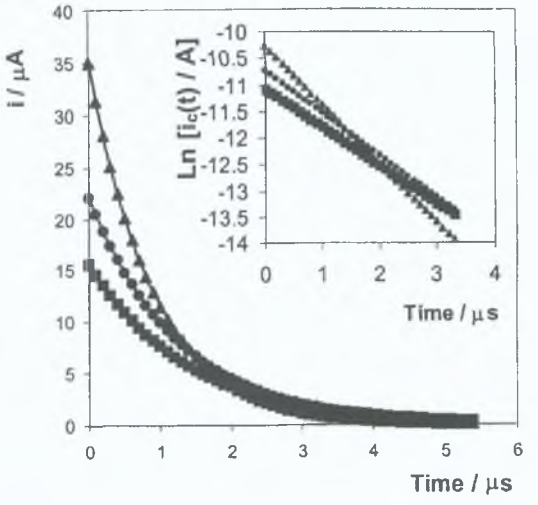

Figure 3. Current−time transients for a 25 μm radius platinum microelectrode modified with an $[Os(OMe\text{-}bpy)_3]^{2+}$ deposit following potential steps from −0.050 to 0.000 V. From top to bottom, the data correspond to 0.0, 0.4, and 1.0 M $NaClO_4$ in a fixed background of 0.1 M $HClO_4$ as supporting electrolyte. The inset illustrates the corresponding semilog current vs time plots.

an electrical potential would develop at the interface. This "Donnan potential" would then increase until an equilibrium was reached in which it completely opposes the tendency of the counterions to move down the concentration gradient. Under these equilibrium conditions, the net diffusion of counterions across the interface would be zero, and co-ions would be excluded from the solid deposit.[19]

We have probed the existence of such a permselective response for these solid deposits by determining the contribution of the film resistance to the total cell resistance as the supporting electrolyte concentration is changed. In the case of an ideally permselective response, ions would be effectively excluded from the membrane, and the film resistance would be independent of the supporting electrolyte concentration. To determine the total cell resistance, we have performed short time scale, small amplitude, potential step chronoamperometry, in a potential region where no Faradaic response is observed. In a typical experiment, the potential was stepped from −50 to 0 mV at both bare and modified microelectrodes, and the resulting current was recorded over the following 20 μs. This capacitive current versus time transient can be described by eq 1:[20]

$$i_c(t) = (\Delta E/R)\exp(-t/RC_{dl}) \qquad (1)$$

where ΔE is the pulse amplitude, R is the total cell resistance, and C_{dl} is the integral double-layer capacitance. For both modified and bare electrodes, the current decays in time according to a single exponential, which is consistent with double-layer charging alone.[19] Figure 3 illustrates $i_c(t)$ versus t and semilog current versus time plots for the solid deposits as the sodium perchlorate concentration is changed from 0 to 0.4 to 1.0 M in a fixed background of 0.1 M $HClO_4$. The absolute slope of the semilog plots represents the reciprocal of the cell time constant RC_{dl}. Table 1 presents RC_{dl} values for an electrode before and after modification with $[Os(OMe\text{-}bpy)_3]^{2+}$ as a function of the perchlorate concentration. This table shows

(19) Bard, A. J.; Faulkner, L. R. *Electrochemical Methods: Fundamentals and Applications*; Wiley: New York, 1980.

(20) Wightman, R. M.; Wipf, D. O. *Electroanalytical Chemistry*; Bard, A. J., Ed.; Marcel Dekker: New York, 1989; Vol. 15.

Table 1. Resistance, R, Double-Layer Capacitance, C_{dl}, and Electrode Response Times, RC, for 25 μm Radius Platinum Microelectrodes before and after Modification with a Solid Deposit of $[Os(OMe\text{-}bpy)_3]^{2+}$ as the Concentration of $NaClO_4$ Is Systematically Varied in a Background of 0.1 M $HClO_4$[a]

	bare			modified		
$[NaClO_4]$/M	R/Ω	$C_{dl}/\mu F$	$RC_{dl}/\mu s$	R/Ω	$C_{dl}/\mu F$	$RC_{dl}/\mu s$
0.0	2400(192)	5.89(0.53)	1.41(0.25)	3200(256)	4.32(0.21)	1.38(0.18)
0.1	2200(188)	6.28(0.50)	1.38(0.23)	2900(203)	4.71(0.23)	1.36(0.16)
0.2	2056(132)	6.48(0.58)	1.33(0.21)	2620(209)	5.10(0.31)	1.33(0.19)
0.4	1877(140)	7.06(0.14)	1.32(0.12)	2268(181)	5.49(0.32)	1.24(0.18)
0.6	1700(119)	7.06(0.28)	1.20(0.13)	1955(195)	5.31(0.15)	1.03(0.13)
0.8	1550(15.5)	7.46(0.74)	1.15(0.12)	1711(136)	5.89(0.58)	1.04(0.18)
1.0	1400(70)	8.24(0.49)	1.15(0.13)	1430(28)	6.28(0.37)	0.89(0.07)

[a] The numbers in parentheses represent errors obtained from at least three independent experiments.

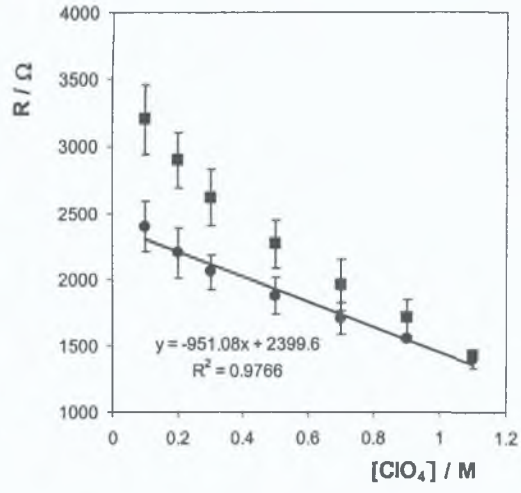

Figure 4. Dependence of the total cell resistance, R, on the concentration of $NaClO_4$ in a fixed background of 0.1 M $HClO_4$ as supporting electrolyte. Data for a bare 25 μm radius platinum microelectrode are shown on the lower curve (●), while the upper curves are for the same microelectrode modified with an $[Os(OMe\text{-}bpy)_3]^{2+}$ solid deposit (■).

that both the bare and the modified electrode cell time constants decrease with increasing electrolyte concentration as expected.[19] However, the response time is considerably more sensitive to the supporting electrolyte concentration for the microelectrode coated with the solid deposit. It is apparent from eq 1 that R can be extracted from the intercepts of the semilog plots shown in Figure 2. Figure 4 shows the total cell resistance for a bare and a coated electrode as the perchlorate concentration is changed from 0.1 to 1.0 M. It is apparent that in both circumstances R is reduced at high electrolyte concentrations reflecting a reduced solution resistance. Importantly, the cell resistance with the modified electrode is never more than 33% larger than that observed with a bare electrode over this range of electrolyte concentrations. This observation suggests that the cell resistance for the coated electrode is dominated by the solution resistance rather than the resistance of the deposit. These results suggest that these deposits do not contribute significantly to the overall cell resistance probably because electrolyte can permeate between the individual particles that exist on the microelectrode surface, vide infra.

Scanning Electron Microscopy. Given that oxidation of the deposit will be accompanied by the ingress of charge-compensating counterions, it is possible that the changes observed in the voltammetry illustrated in Figure 1 when the deposit is first cycled are associated with structural or solvation changes.[21-24] To address this issue, we have used scanning electron microscopy to image the deposits before and after voltammetric cycling in both acidic and near-neutral electrolytes.

Parts A and B of Figure 5 illustrate SEM images of the deposits before and after voltammetric cycling in 0.1 M $HClO_4$, respectively. The SEM image of the complex before cycling reveals particles of between approximately 1 and 20 μm. Given that crystallographic studies have been successfully performed on this material by other investigators, it is likely that the material is microcrystalline.[25] After cycling, the morphology and size of the crystal changes and they consist of very thin platelets. Significantly, cycling and its associated ion ingress and egress appear to play an important role in the electrocrystallization process. For example, bulk electrolysis at +0.800 V does not trigger any detectable change in the macroscopic structure of the material. Moreover, as illustrated in Figure 5C, electrocrystallization does not occur when the films are cycled in 0.1 M $NaClO_4$. These observations suggest that protonating the methoxy moieties induces hydrogen-bonding interactions between the complexes thus promoting the formation of crystals. Significantly, the pH protonation of all six of the methoxy groups would yield a highly polycationic layer with the overall charge on the reduced and oxidized forms of the complex being 8+ and 9+, respectively. Under these circumstances, electroneutrality will be maintained by the ingress of perchlorate anions that are likely to be mobile within the deposit. Anion incorporation is significant from the perspective of rapid charge transport since it will lead to a deposit that is porous on the molecular scale thus facilitating ion transport. In a later section, we use cyclic voltammetry to measure the rate of homogeneous charge transport and to probe the nature of the rate-determining step.

Ion Pairing Effects. The formal potential of the complex is sensitive to the concentration of the supporting electrolyte. Shifts in formal potential with changes in electrolyte concentration reflect differences in the relative stability between the two redox states and can be used to probe ionic interactions. Therefore, we have examined the electrolyte concentration dependence of $E^{o\prime}$ for reactants in solution and in the solid phase to obtain an insight into the effects of immobilization on the extent of ion pairing. Figure 6 shows that $E^{o\prime}$ for the solid deposits shifts in a negative potential direction with increasing $\log[ClO_4^-]$ where the pH of the supporting electrolyte is fixed at 1.0 ± 0.1. Consistent with ion pairing, this observation indicates that it becomes progressively easier to oxidize the deposits with increasing perchlorate con-

(21) Bond, A. M.; Scholtz, F. *Langmuir* **1991**, *7*, 3197.
(22) Dostal, A.; Meyer, B.; Scholz, F.; Schroder, U.; Bond, A. M.; Marken, F.; Shaw, S. *J. Phys. Chem.* **1995**, *99*, 2096.
(23) Hong, S. H.; Evans, D. H.; Nelsen, S. F.; Ismagilov, R. F. *J. Electroanal. Chem.* **2000**, *486*, 75.
(24) Forster, R. J.; Keyes, T. E.; Bond, A. M. *J. Phys. Chem. B* **2000**, *104*, 6389.
(25) Shklover, V.; Zakeerruddin, S. M.; Nesper, R.; Fraser, D.; Gratzel, M. *Inorg. Chim. Acta* **1998**, *274*, 64.

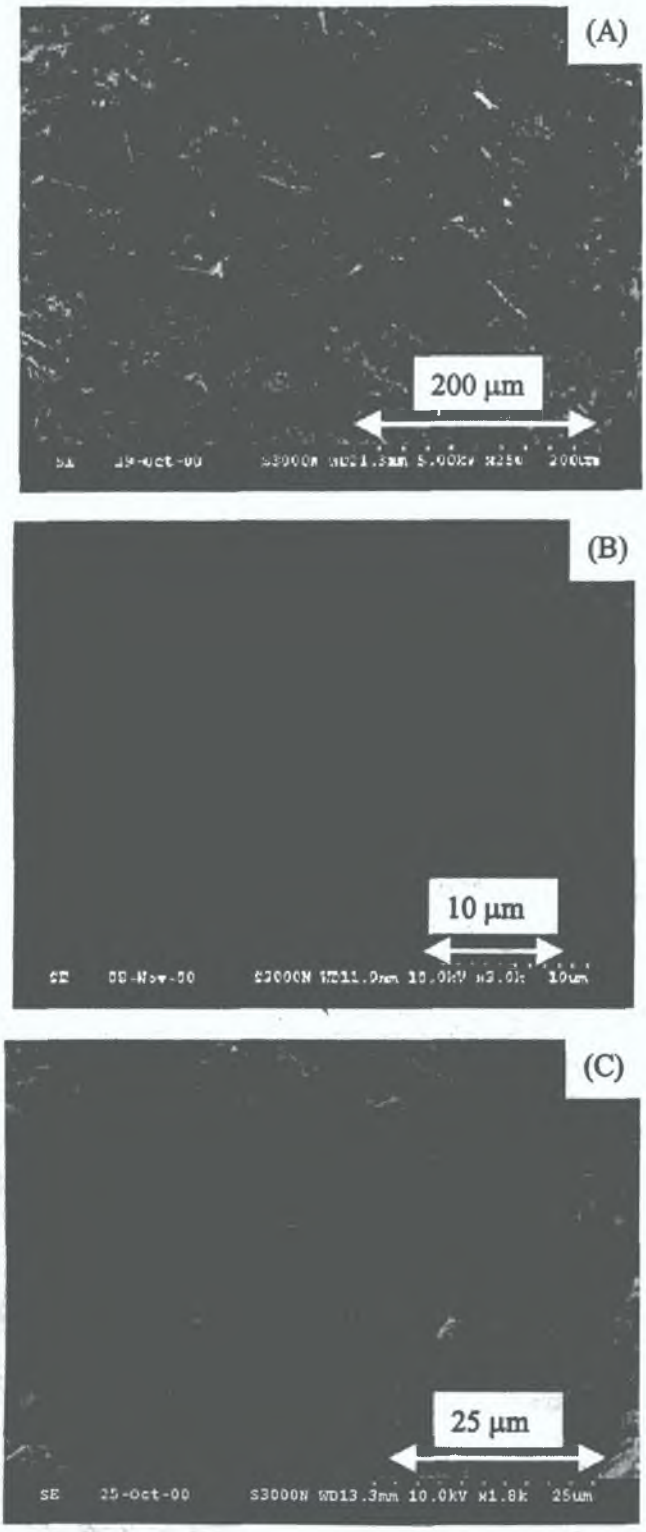

Figure 5. Scanning electron microscopy images of $[Os(OMe\text{-}bpy)_3]^{2+}$ solid deposits: (A) as deposited, before electrochemical cycling, (B) after 100 voltammetric cycles between −0.1 and 1.0 V in 0.1 M $HClO_4$ at a scan rate of 0.1 V s^{-1}, and (C) after 100 voltammetric cycles between −0.1 and 1.0 V in 0.1 M $NaClO_4$ at a scan rate of 0.1 V s^{-1}.

centration. This situation is summarized in the following reaction:

$$[Os(OMe\text{-}bpy)_3]^{2+}(X^-)_q - e^- + p(X^-) \leftrightarrow [Os(OMe\text{-}bpy)_3]^{3+}(X^-)_{q+p}$$

where both redox forms are considered to participate in

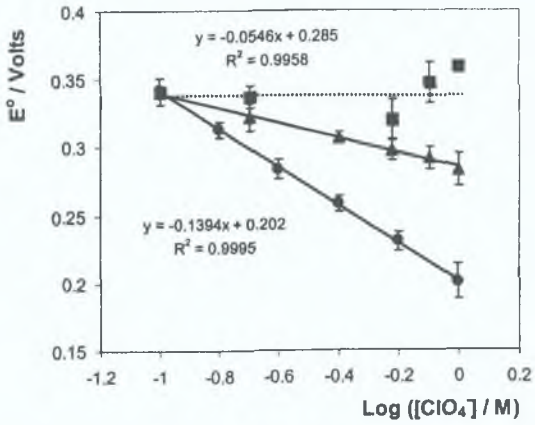

Figure 6. Dependence of the formal potential on the concentration of $HClO_4$ as supporting electrolyte for $[Os(OMe\text{-}bpy)_3]^{2+}$ solid deposits (■) and dissolved in acetonitrile (●) while (▲) denotes the effect of increasing the $NaClO_4$ concentration in a fixed background of 0.1 M $HClO_4$.

both the ion-pairing equilibria. The Nernst equation predicts a slope of −59/p mV per decade change in $[ClO_4^-]$. The experimentally observed slope, -55 ± 4 mV dec^{-1} is consistent with the Os^{3+} form becoming ion-paired with a single extra anion. However, as shown in the following reaction, the complexes used to form these deposits are also capable of undergoing acid/base reactions.

$$[Os(OMe\text{-}bpy)_3]^{2+}(X^-)_q + H^+ + r(X^-) \leftrightarrow [Os(H\ OMe\text{-}bpy)_3]^{3+}(X^-)_{q+r}$$

where both redox forms participate in the acid/base equilibrium. Therefore, if the oxidized form becomes ion-paired with two extra anions, one to compensate the charge on the electrochemically generated cation and a second to compensate for the protonated form, then the Nernst equation predicts a shift of −118 mV per decade change in the perchloric acid concentration. Figure 6 shows that the slope observed for the complex dissolved in solution is -139 ± 5 mV/decade which is somewhat larger than that predicted by the Nernst equation for the situation where both ion pairing and protonation reactions occur. The larger slope may reflect differences in the ionization constant for oxidized and reduced forms or several closely spaced methoxy pK_a values. In contrast, Figure 6 shows that $E^{\circ\prime}$ for the solid deposits remains constant as the perchloric acid concentration is increased from 0.1 to 1.0 M.

Charge Transport through the Deposits. In contrast to other solid state films, this material exhibits exceedingly well-defined metal-based oxidation processes across a wide range of electrolyte compositions making them attractive model systems for investigating the dynamics of charge transport. It is well-known that osmium polypyridyl complexes undergo fast electron self-exchange reactions.[26] However, the situation in solid films can be complicated by the ion movement necessary to maintain electroneutrality.

To address this issue, we have used cyclic voltammetry to measure the rate of homogeneous charge transport through the film.[27,28] For fast scan rates, only a small fraction of the total amount of material immobilized is

(26) Zakeeruddin, S. M.; Fraser, D. M.; Nazeeruddin, M.-K.; Grätzel, M. *J. Electroanal. Chem.* **1992**, *337*, 253.
(27) Bond, A. M.; Marken, F. *J. Electroanal. Chem.* **1994**, *372*, 125.
(28) Kuleszea, P. J.; Faulkner, L. R. *J. Am. Chem. Soc.* **1993**, *115*, 11878.

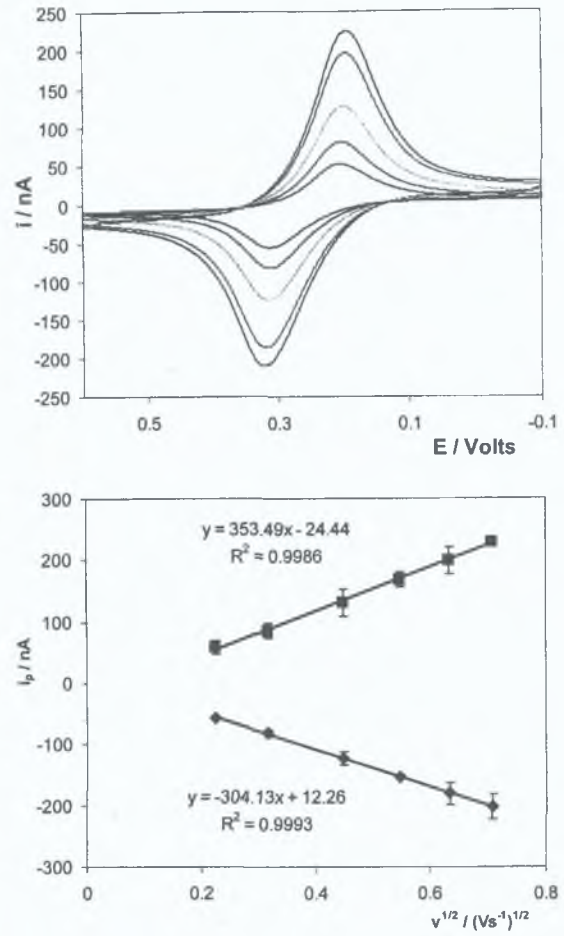

Figure 7. Cyclic voltammograms of $[Os(OMe\text{-}bpy)_3]^{2+}$ solid deposits on a 25 μm platinum electrode in 0.8 M $HClO_4$. From top to bottom, the scan rates are 0.05, 0.1, 0.2, 0.3, 0.4, and 0.5 V s^{-1}. The inset shows the dependence of the peak current on $v^{1/2}$.

electrolyzed and the depletion zone remains well within the deposit. Under these conditions, linear diffusion predominates and, in common with solution phase reactants, the peak current varies as $v^{1/2}$.[13,29,30] Figure 7 illustrates the effect of increasing the scan rate from 0.05 to 0.5 V s^{-1} on the voltammetry of $[Os(OMe\text{-}bpy)_3]$ deposits where the supporting electrolyte is 0.8 M $HClO_4$. The peak current does not exceed 250 nA which, when taken in conjunction with the data presented in Table 1, means that the ohmic drop is likely to be less than 1 mV. Moreover, Table 1 confirms that the electrode response time is very much shorter than the time constant for these experiments. The voltammograms are peak shaped similar to those obtained when the complex is dissolved in solution. However, modeling of the voltammetric response, vide infra, indicates that the experimental current beyond the peak potential is lower than that predicted by classical solution phase models based on semi-infinite linear diffusion. This observation suggests that finite diffusion may contribute to the observed response. This behavior is not entirely unexpected since these deposits are not monolithic and the time scale at which finite diffusion becomes important depends on the particle size. However, Figure 7 shows that the peak current, i_p, increases linearly with increasing $v^{1/2}$ indicating that semi-infinite linear diffusion dominates the observed response. Under these circumstances, the peak current, i_p, can be described in

(29) Forster, R. J. *Chem. Soc. Rev.* **1994**, 289.
(30) Whitely, L. D.; Martin, C. R. *J. Phys. Chem.* **1989**, *93*, 4650.

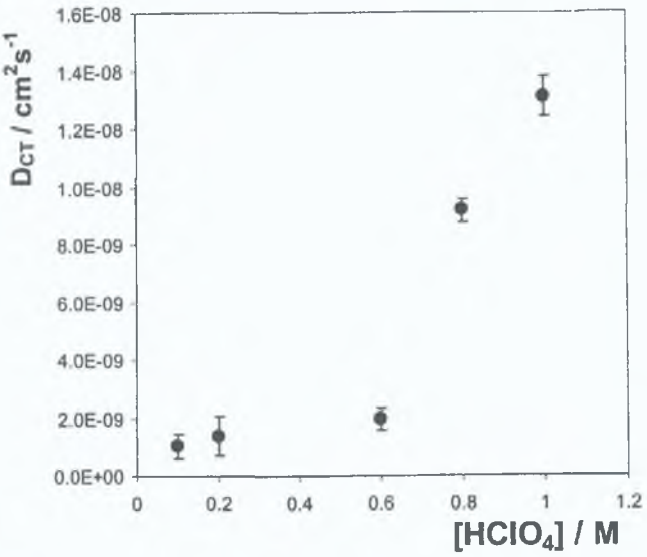

Figure 8. Dependence of the homogeneous charge transport diffusion coefficient of solid state $[Os(OMe\text{-}bpy)_3]^{2+}$ on the concentration of $HClO_4$ as supporting electrolyte.

terms of the Randles–Sevçik equation:

$$i_p = 2.69 \times 10^5 n^{3/2} A D_{CT}^{1/2} C_{eff} v^{1/2} \quad (2)$$

where n is the number of electrons transferred, A is the area of the electrode, D_{CT} is the apparent charge transport diffusion coefficient, and C_{eff} is the effective fixed site concentration. Previous investigations on related systems indicate that the fixed site concentration in systems is of the order of 1.5 M[11,24] and this concentration is consistent with X-ray crystallographic studies on osmium and ruthenium poly-pyridyl complexes.[25,31] Using this fixed site concentration, the data illustrated in Figure 7 yield a D_{CT} value of $1.8 \pm 0.1 \times 10^{-10}$ cm^2 s^{-1} for both oxidation and reduction processes.

Effect of Perchloric Acid Concentration on D_{CT}. The rate of homogeneous charge transport through these solid state deposits could be limited either by electron hopping between the sites or by the counterion diffusion/migration necessary to maintain electroneutrality.[10] In the case of electron hopping, charge-compensating counterions are freely available within the structure and D_{CT} is expected to depend weakly on the electrolyte concentration. As illustrated in Figure 8, D_{CT} is approximately independent of the perchloric acid concentration maintaining a value of $1.5 \pm 0.4 \times 10^{-9}$ cm^2 s^{-1} for $0.1 \leq [HClO_4] \leq 0.6$ M. Above 0.6 M electrolyte, D_{CT} increases significantly reaching a value of 13.1×10^{-9} cm^2 s^{-1} in 1.0 M $HClO_4$.

The Dahms–Ruff equation[32,33] can be used to calculate the electron self-exchange rate constant from the maximum D_{CT} value assuming that electron hopping represents the rate-determining step. This equation is given by

$$D_{CT} = D_{Phys} + 1/6\, k_{SE} \delta^2 C \quad (3)$$

where D_{Phys} describes physical diffusion in the absence of electron hopping, C is the fixed site concentration of the osmium complex, and δ is the intersite separation between adjacent Os^{2+}/Os^{3+} moieties. Given that we are dealing

(31) Juris, F.; Balzani, V.; Barigelletti, F.; Campagna, S.; Belser, P.; von Zelewsky, A. *Coord. Chem. Rev.* **1988**, *82*, 85.
(32) Dahms, H. *J. Phys. Chem.* **1968**, *72*, 362.
(33) Ruff, I.; Friedrich, V. J.; Demeter, K.; Csillag, K. *J. Phys. Chem.* **1971**, *75*, 3303.

with crystalline solid deposits, D_{Phys} is assumed to be zero. On the basis of crystallographic data for $[Os(OMe\text{-}bpy)_3]^{2+}$, the intersite separation was taken to be 9.6 Å.[25]

The maximum D_{CT} value yields a self-exchange rate constant of $5.7 \times 10^6\ M^{-1}\ s^{-1}$. This value is approximately an order of magnitude smaller than the values typically reported for osmium poly-pyridyl complexes in solution[34] or within monolayers.[24,35-37] Given the assumptions made in the calculation of k_{SE}, the value obtained does not allow an unambiguous determination of whether counterion motion or electron transfer limits the overall rate of charge transport. However, the data indicate that the rate of charge transport is significantly higher than that found in structurally related systems, for example, for solid deposits of $[Os(bpy)_2$ 3,5-bis(pyridin-4-yl)-1,2,4,-triazole $Cl]$ D_{CT} is $6.3 \times 10^{-12}\ cm^2\ s^{-1}$ in 1.0 M $HClO_4$, that is, more than 3 orders of magnitude smaller than those found here.[11] It is perhaps significant that the elemental analysis indicates a relatively higher carbon and hydrogen content than expected suggesting that the solid produced during synthesis contains solvent of crystallization, for example, diethyl ether or methanol. This solvent is likely to be mobile within the deposits leading to the facile ion transport behavior observed. The relatively large k_{SE} most likely arises because the redox centers are immobilized within an ordered crystalline array in which individual sites are linked by hydrogen bonds between protonated and deprotonated methoxy groups. The ability to rapidly switch the redox composition of these solid deposits in a highly reversible way makes them attractive for electrochromic and supercapacitor applications. It is important to consider the sensitivity of D_{CT} to the concentration of the supporting electrolyte. While we do not know the pK_a of the methoxy groups within the solid layer, this sensitivity most likely arises because the methoxy groups are deprotonated for $[HClO_4] \leq 0.6$ M but tend to become protonated at higher concentrations. This protonation reaction will create a hydrogen-bonded network that supports more rapid electron transfer between the sites.

Heterogeneous Electron Transfer. As discussed above, the voltammograms illustrated in Figure 7 are controlled by homogeneous charge transport through the deposit. At higher scan rates, the rate of heterogeneous electron transfer across the electrode/deposit interface influences the voltammetric response causing the peak-to-peak separation to increase significantly.[38] Figure 9 illustrates representative cyclic voltammograms in 0.8 M $HClO_4$ at scan rates of 5 and 100 V s^{-1} which show that the ΔE_P values increase with increasing scan rate. In attempting to use cyclic voltammetry to measure heterogeneous electron transfer rate constants, it is essential to ensure that ohmic loss, given by the product of the total current, i, and cell resistance, R, does not compromise the observed response. Ohmic effects represent a serious problem, not only because they will cause a significant E_P to be observed even when heterogeneous electron transfer is fast but also because the magnitude of the ohmic effect depends on the experimental time scale. In the experiments reported here, we have used microelectrodes and relatively high concentrations of supporting electrolyte to avoid iR drop. For example, as indicated in Table 1, the total resistance in this solution even with the modified electrode is 1430 Ω. Therefore, even for the highest scan rate investigated, 100 V s^{-1}, where the peak current is approximately 2 μA, the iR drop is less than 3 mV.

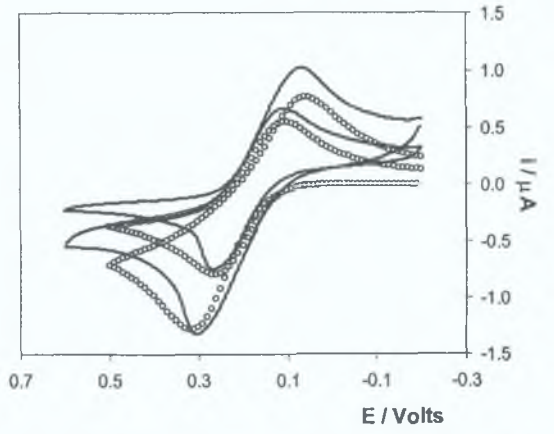

Figure 9. Cyclic voltammograms for a solid deposit of $[Os(OMe\text{-}bpy)_3]^{2+}$ on a 25 μm radius platinum microdisk electrode. From top to bottom, the scan rates are 30 and 5 V s^{-1}, respectively. Experimental data are denoted by the solid lines while the open circles represent theoretical fits generated according to the Butler–Volmer formalism of electrode kinetics where D_{CT} and $k°$ are $1.1 \times 10^{-9}\ cm^2\ s^{-1}$ and 1.0×10^{-4} cm s^{-1}, respectively. The supporting electrolyte is 0.8 M $HClO_4$.

Figure 9 illustrates theoretical fits to the experimental cyclic voltammograms generated according to the Butler–Volmer formalism of electrode kinetics.[39] In fitting these voltammograms, the residual sum of squares between the experimental and theoretical oxidation currents was minimized and then the reduction branch of the voltammogram was predicted. The satisfactory agreement observed between theory and experiment suggests that the voltammograms for the solid films be approximately described by conventional solution phase models based on semi-infinite linear diffusion. Moreover, the satisfactory fits suggest that the films are solvated and that an electrochemical double layer sets up at the electrode/layer interface. This conclusion is consistent with our observation that the formal potentials of solution phase and solid deposits are similar. For $5 < v < 100$ V s^{-1}, the best-fit simulated voltammogram is obtained where D_{CT} is $1.1 \times 10^{-9}\ cm^2\ s^{-1}$ and a standard heterogeneous electron transfer rate constant, $k°$, is $1.0 \pm 0.05 \times 10^{-4}$ cm s^{-1}. The diffusion coefficient obtained by fitting the complete voltammogram is identical to that found using the Randle–Sevçik analysis to within 5%. Significantly, the standard heterogeneous electron transfer rate constant is independent of the scan rate indicating that the layers are kinetically homogeneous. The observation that the rate constants for all redox centers capable of undergoing heterogeneous electron transfer are experimentally indistinguishable suggests that the local microenvironments, electron transfer distances, and reorganization energies are identical for individual redox centers.

Immobilizing the complex as a solid layer on an electrode surface could alter the microenvironment of the redox centers, for example, by changing the dielectric constant or the electron transfer distance. An insight into the importance of these effects for the $[Os(OMe\text{-}bpy)_3]^{2+}$ system can be obtained by comparing $k°$ values obtained for solid and solution phase reactants. Figure 10 illustrates cyclic voltammograms for the complex dissolved

(34) Chan, M. S.; Wahl, A. C. *J. Phys. Chem.* **1978**, *82*, 2542.
(35) Charych, D. H.; Majda, M. *Thin Solid Films* **1992**, *210*, 348.
(36) Charych, D. H.; Anvar, D. J.; Majda, M. *Thin Solid Films* **1994**, 2, 1.
(37) Lee, W.-Y.; Majda, M.; Brezesinski, G.; Wittek, M.; Möbius, D. *Phys. Chem. B* **1999**, *103*, 6950.
(38) Montenegro, M. I. Applications of Microelectrodes in Kinetics. *search in Chemical Kinetics*; Compton, R. G., Hancock, G., Eds.; sevier: New York, 1994; Vol. 2, p 1.
(39) Garay, F.; Solis, V.; Loviré, M. *J. Electroanal. Chem.* **1999**, *478*, 17.

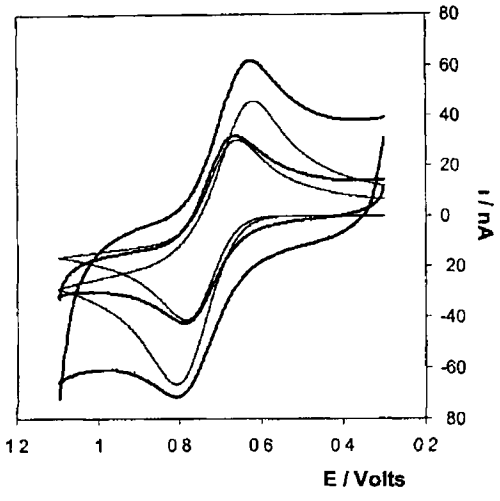

'igure 10 Cyclic voltammograms for a 5 mM solution of Os(OMe-bpy)$_3$]$^{2+}$ in acetonitrile The working electrode is a 25 m radius platinum microdisk From top to bottom, the scan ates are 30 and 5 V s^{-1}, respectively Experimental data are enoted by the thick solid lines, while thin lines are theoretical its generated using the Butler–Volmer formalism of electrode inetics D_{Soln} and $k_{Soln}°$ are 5 0 × 10^{-6} cm^2 s^{-1} and 6 1 ± 0 2 < 10^{-5} cm s^{-1}, respectively

n acetonitrile where the scan rate is sufficiently large so is to influence the voltammetry Fitting these solution phase voltammograms reveals diffusion coefficients, D_{Soln}, and standard heterogeneous electron transfer rate constants, $k_{Soln}°$, of 5 0 ± 0 3 × 10^{-6} cm^2 s^{-1} and 6 1 ± 0 2 × 10^{-5} cm s^{-1}, respectively Our present data do not allow is to directly compare the $k°$ values for the solid and solution phase reactants because of the different double-ayer structures and reactant mobilities under the two ircumstances However, it is striking that the $k°$ values obtained for solution and solid phase reactants are very similar with $k_{Soln}°$ being only 30% smaller than that found for the solid layer

Conclusions

Mechanically attached, solid deposits of [Os(OMe-bpy)$_3$](PF$_6$) where OMe-bpy is 4,4′ dimethoxy, 2-2′-dipyridyl have been formed on platinum microelectrodes The voltammetric response arising from the $Os^{2+/3+}$ redox reaction is close to ideally reversible for both solid and solution phase reactants, and similar formal potentials are observed Scanning electron microscopy reveals that electrochemically cycling the deposits in $HClO_4$ triggers electrocrystallization into a microcrystalline platelike structure In $HClO_4$, the diffusion coefficient is 1 5 ± 0 1 × 10^{-9} cm^2 s^{-1} for 0 1 ≤ [$HClO_4$] ≤ 0 6 M, and above 0 6 M $HClO_4$ it increases to 13 ± 1 × 10^{-9} cm^2 s^{-1} in 1 0 M $HClO_4$ A self-exchange rate constant of 5 7 × 10^6 M^{-1} s^{-1} was sought for the deposit, a value that is approximately an order of magnitude smaller than for related complexes in solution The heterogeneous electron transfer rate constants are indistinguishable for solid and solution phase reactants The charge transport activities of this material as a solid deposit could have wide applicability as a mediator in biosensors for the analysis of biological molecules

Acknowledgment The financial support from Enterprise Ireland, Ireland's Science and Technology Agency, is gratefully acknowledged The generous loan of potassium hexachloroosmate(IV) by Johnson Matthey under the loan scheme is deeply appreciated The insight of Dr Graeme Snook on the interpretation of the formal potential data is deeply appreciated

LA010927S

Y /Elsevier Science/Amsterdam/JEC/articles/JEC10065/Jec10065 3d[x] 6 May 2003 8 39 32

Available online at www sciencedirect com

SCIENCE DIRECT®

Journal of Electroanalytical Chemistry

ELSEVIER

Journal of Electroanalytical Chemistry 00 (2003) 1–10

www elsevier com/locate/jelechem

Nanoparticle–metallopolymer assemblies charge percolation and redox properties

Robert J Forster *, Lorraine Keane

School of Chemical Sciences National Centre for Sensor Research Dublin City University Dublin 9 Ireland

Received 9 December 2002 received in revised form 20 February 2003 accepted 29 March 2003

Abstract

Stable gold nanoparticles have been prepared by the chemical reduction of tetrachloroaurate in the presence of PVP and the metallopolymer $[Os(bpy)_2(PVP)_{10}Cl]^+$ films, where bpy is 2 2′ dipyridyl and PVP is poly(4 vinylpyridine) The maximum dry state conductivity observed is $3\,5\pm0\,3\times10^{3}$ and $8\,7\pm0\,1\times10^{2}$ S m^{-1} where the polymer matrix is PVP and the metallopolymer, respectively The percolation threshold is significantly lower for the nanoparticle loaded metallopolymer, $0\,07\pm0\,01$ compared with PVP, $0\,31\pm0\,04$ This result suggests that the osmium centers provide an enhanced conductivity pathway in the dry state The redox properties of thin films of the composites deposited on microdisk platinum electrodes in contact with aqueous electrolyte have been investigated The charge transport diffusion coefficient D_{CT} is approximately an order of magnitude larger for the composite containing the highest nanoparticle loading $5\,7\pm0\,4\times10^{-9}$ cm^2 s^{-1} than that found for the pure metallopolymer, $5\,7\pm0\,2\times10^{-10}$ cm^2 s^{-1} A nanoparticle loading above the percolation threshold also promotes faster heterogeneous electron transfer increasing from $8\,2\pm1\,7\times10^{-5}$ to $4\,0\pm0\,2\times10^{-3}$ cm s^{-1}

Keywords Gold nanoparticles Poly(4 vinylpyridine) Metallopolymer Heterogeneous electron transfer

1 Introduction

The unique optical, electric and magnetic properties of nanoparticles continues to drive intense research in fields as diverse as catalytic synthesis and sensor development [1–3] Driven by issues such as high reactivity and aggregation [4], there is an increasing recognition that self-assembled monolayers [5–7] and functional polymers represent important matrices for controlling interparticle interactions [8] Polymers, such as poly-vinyl pyrrolidone [9,10], that incorporate surface active functional groups [11] has proven to have useful properties not only in the production of tightly distributed nanoparticles of controlled size, but the resulting composite materials have attractive electrical and optical properties [12] Combining redox active materials with nanoparticles is attractive because the redox centers would be expected to influence nanoparticle growth, e g by mediating reduction of the precursor salt, and the combination of both metal nanoparticles and complexes ought to lead to unique redox and electrical conductivity effects In particular, the ability to modulate the local microenvironment of the nanoparticles and hence their reactivity by electrochemically switching the oxidation state of the redox centers is especially attractive Thin redox-active composite films with a layered hybrid structure have been created using palladium [13] and gold nanoparticles coated with biferrocene-terminated thiolates [14 15] However, the use of metallopolymers that contain not only surface active functional groups but also redox active centers, such as transition metal complexes, has not been widely explored in this context [16]

This contribution reports on the preparation of dispersed nanoparticle–metallopolymer composites in which the gold nanoparticle loading within an $[Os(bpy)_2(PVP)_{10}Cl]^+$ polymer is systematically varied, bpy is 2,2′-bipyridyl and PVP is poly(4-vinyl pyridine) Scheme 1 illustrates a conceptual representation that emphasizes binding of the nine free pyridine moieties to

* Corresponding author Tel +353 1 7045 943 fax +353 1 7045 503

E mail address robert forster@dcu ie (R J Forster)

0022 0728/03/$ see front matter © 2003 Published by Elsevier Science B V
doi 10 1016/S0022 0728(03)00258 4

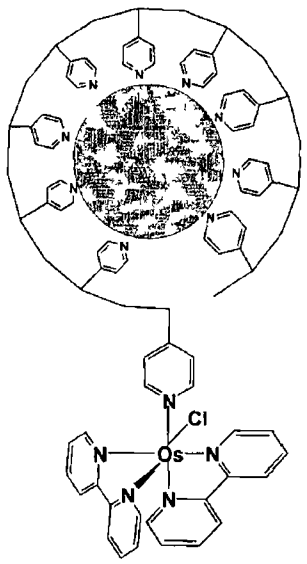

Scheme 1

the nanoparticle surface The ratio of redox centers to pyridine monomer units is 1 10 The composites are prepared by chemically reducing gold tetrachloroaurate in the presence of various mole fractions, x, of the metallopolymer or the unlabelled PVP The effect of changing the mole fraction of the metallopolymer on the size distribution of the nanoparticles has been investigated and reveals that the average particle size depends on the mole fraction of metallopolymer present in the reaction solution with particle diameters ranging from $1\,6\pm0\,3$ to $5\,2\pm0\,6$ nm as the mole fraction of metallopolymer is systematically varied from 0 84 to 0 02 To gain an insight into the role of the osmium bipyridyl redox centers in electrical conduction, the dry state conductivity has been determined as a function of the nanoparticle loading for both the metallopolymer and PVP systems The data of both systems data can be described using the percolation theory [17 18] for a randomly dispersed electrically conducting filler, but the metallopolymer system exhibits significantly higher conductivity for all loadings investigated Thin films of both the metallopolymer and composites exhibit nearly ideal voltammetric responses and cyclic voltammetry has been used to investigate their charge transport properties when in contact with an aqueous electrolyte solution The ionic interactions have been probed by monitoring the effect of the supporting electrolyte concentration on the formal potential of the $Os^{2+/3+}$ redox reaction

Beyond probing the homogeneous charge transport diffusion coefficient as a function of nanoparticle loading and electrolyte concentration we have also determined the standard heterogeneous electron transfer rate, k° These data are revealing of the differences between the electrode | metallopolymer film and electrode | composite interfaces

2 Experimental

2 1 Materials

A detailed description of the synthesis and characterization of the metallopolymer has been reported previously [19] The gold precursor tetrachloroauric acid, $HAuCl_4$, and the reducing agent potassium borohydride, KBH_4, were obtained from Aldrich An aqueous solution of KBH_4 was prepared just before use and rapidly added to the stirred solutions containing $HAuCl_4$ and either PVP or the metallopolymer To avoid difficulties in defining the polymer molar mass, the mole fraction of the polymer is defined in terms of the number of moles of pyridine groups and gold ions prior to production of the gold nanoparticles UV–vis spectra were taken before and after the reduction reaction Millipore water (18 MΩ) was used to prepare electrolytic solutions

2 2 Apparatus and procedures

Transmission electron micrographs were taken with a JEOL-100 CX II transmission electron microscope in order to obtain the particle sizes, morphologies, and particle-size distributions of the gold nanoparticles The samples were prepared by placing a drop of the colloid on a carbon-coated copper grid and allowing the solvent to evaporate The particle sizes of at least 100 individual particles were measured to obtain information about the size distribution

2 3 Film preparation

Adherent layers of the composites were obtained by evaporation of the required volume of a 1% solution of the material in methanol on the electrode, which was placed in a methanol saturated chamber, followed by air drying for several hours For macroscopic electrodes, the resulting films were visibly smooth and shiny, and were free from any obvious aggregates when viewed under an optical microscope at magnifications up to 40 × In the case of the metallopolymer, the solid was dissolved in a minimum volume of ethanol and applied to the electrode surface as a paste The adherent layer was air dried for 30 min prior to measurement Beyond minor differences in the initial scans, the film preparation method had no impact on the formal potential, diffusion coefficient or heterogeneous electron transfer rate constant obtained

2.4. Electrical conductivity

The specimens for measurements of electrical conductivity were prepared by applying 11 500 kg cm^{-2} of pressure to a finely ground (particle size <2 μm) composite within a 10 mm diameter die. Prior to application of pressure the die assembly was evacuated using a high vacuum pump for at least 5 min and evacuation was continued during pressurization. Sufficient material, typically 4 mg, was used to produce a disk approximately 1 mm thick. For highly resistive samples (σ values less than 10^{-2}–10^{-4} S m^{-1}), the dc conductivities were measured using a Guildline programmable digital teraohmmeter 6500A. For more highly conducting samples, specimens in the form of plates were used. Irrespective of the nature of the sample, to reduce the complications arising from electrode-specimen contact resistance, the four-electrode method was used [20].

2.5. Electrochemical measurements

Cyclic voltammetry was performed using a CH Instrument Model 660 electrochemical workstation and a conventional three-electrode cell. The platinum working electrodes used in these experiments ranged in radii from 1 to 3 mm. Microelectrodes were prepared using platinum microwires of radii between 1 and 25 μm sealed in a glass shroud as described previously [21]. The working electrodes were polished successively with 1.0, 0.3 and 0.05 μm aqueous alumina slurries and sonicated in distilled water and rinsed with acetone after each polishing step. The electrodes were then electrochemically cleaned by cycling in deoxygenated 0.1 M H_2SO_4 from -0.3 to 1.5 V until a voltammogram characteristic of a clean platinum electrode was obtained [22]. Before modification, the electrodes were cycled in 0.1 M $LiClO_4$ until hydrogen desorption was complete. Potentials are quoted with respect to a BAS Ag | AgCl | 3 M NaCl gel-filled electrode and all experiments were performed at room temperature (22 ± 3 °C)

For short timescale experiments (<250 μs), that were designed to probe the cell resistance and the interfacial capacitance, a custom built programmable function generator-potentiostat was used. This instrument had a rise time of less than 10 ns and was used to apply potential steps of variable pulsewidth and amplitude directly to a two-electrode cell. A large area Pt foil and a reference electrode were combined to form a counter electrode. The foil lowered the resistance and provided a high frequency path. The current to voltage converter was based on a Comlinear CLC 203 AI operational amplifier with a 1500 Ω feedback resistance and a response time of less than 10 ns. The chronoamperograms were recorded using a HP54201A digital oscilloscope in 64 × time-average mode. Cell time constants were extracted from the slope of ln $I(t)$ versus t plots using software routines written in Microsoft QuickBASIC.

3. Results and discussion

3.1. Composite structure

Fig. 1A,B show TEM images of gold nanoparticles prepared in the presence of $[Os(bpy)_2\ (PVP)_{10}\ Cl]Cl$ where the mole fractions of the metallopolymer are 0.84 and 0.02, respectively. Both systems produce well-defined nanoparticles with the approximately spherical shape of the gold nanoparticles suggesting that the particles are not monocrystalline. However, the most striking result of Fig. 1 is that decreasing the amount of metallopolymer increases the average particle size from 1.6 ± 0.3 to 5.2 ± 0.6 nm. This result suggests that a greater availability of surface binding pyridine groups inhibits growth and efficiently blocks particle aggregation. This behavior is similar to that reported previously for poly-vinylpyrrolidone where larger quantities of polymer lead to the formation of smaller nanoparticles [23].

3.2. Electrical conductivity

The possibility of controlling the electrical characteristics of polymers by systematically varying the loading of nanoparticles is important for a range of applications ranging from molecular electronic devices to sensors. When nanoparticles of conductivity σ_n are blended with a polymer matrix to a loading φ, having a conductivity σ_p, the conductivity of the resulting composite, σ, typically increases dramatically [17,18]. Specifically, when the percolation threshold, φ_c, is reached an infinite conductive cluster is formed and the composite may become highly conducting. As the nanoparticle loading increases from φ_c to the limiting value F, the conductivity of the metallopolymer–nanoparticle composite increases rapidly by several orders of magnitude, from the value σ_c at the percolation threshold to the maximal value σ_m. Below the percolation threshold, the conductivity change is negligible and the conductivity of the composite is equal to the polymer conductivity σ_p or slightly higher. While it does not consider the effects of particle shape, variable particle size, contact phenomena, the distribution of particles within the polymer, etc. the dependence of the conductivity on the nanoparticle loading can be described by Eq. (1) to a first order of approximation:

$$\sigma = \sigma_c + (\sigma_m - \sigma_c)[(\varphi - \varphi_c)/(F - \varphi_c)]^t \quad (1)$$

where t is the critical exponent [24] and is typically between 1.6 and 1.9.

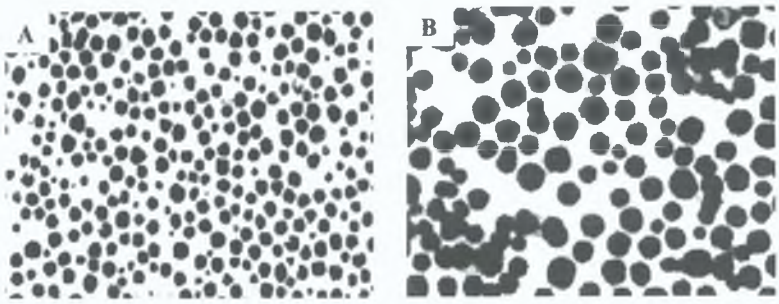

Fig. 1. Transmission electron micrographs of gold nanoparticles in which the mole fraction of $[Os(bpy)_2(PVP)_{10}Cl]Cl$ is (A) 0.84 (magnification 1.25×10^6) and (B) 0.02 (magnification 8.0×10^5). The films were prepared by dissolving the composite in ethanol and drop casting onto a TEM minigrid.

Fig. 2 illustrates the dependence of the composite electrical conductivity on the volume fraction of the nanoparticles for both metallopolymer and poly-4-vinyl pyridine matrices. In this plot the volume fraction of the gold nanoparticles is calculated from the known densities of metallic gold, PVP [25] and the metallopolymer [19] assuming that all of the tetrachloroaurate is reduced to metallic gold during nanoparticle synthesis. In both cases, the solid curves represent the best fits of Equation 1 to the experimental data and the data are given in Table 1. These percolation curves reveal that the conductivity of the metallopolymer is approximately 30 times greater than that found for the unlabelled poly-4-vinylpyridine material. Both the pure PVP and metallopolymer composites exhibit a sharp increase in conductivity for a critical loading of the gold nanoparticles. However, the percolation threshold is dramatically lower for the metallopolymer based composite, 0.07 ± 0.01, compared to 0.31 ± 0.04 for the PVP matrix. The filling limit in both cases is 0.7 ± 0.1 which is indistinguishable from the value of 0.64 expected for a random distribution of conductive spheres in a non-electronically conducting matrix [26]. Assuming a random dispersion, the average edge-to-edge interparticle separation, d, at the percolation threshold is estimated as 2.6 ± 0.1 and 5.0 ± 0.1 nm for the PVP and metallopolymer matrices, respectively. The observation that the metallopolymer system is highly conducting for a larger interparticle separation suggests the osmium bisbipyridyl centers mediate electron transfer between adjacent metal particles over much greater distances than the pure poly-4-vinylpyridine material. This conclusion is consistent with the observation that the maximum conductivity, σ_m, differs by only a factor of 4 for the two composites suggesting that particle-to-particle contact is the limiting factor on conductivity at the highest loadings investigated. While the value of the critical exponent, t, for PVP is close to the range typically found for random dispersions [17,27], 1.6–1.9, the value obtained for the metallopolymer matrix is significantly higher at 2.5. Large t values have been reported previously[28] and assumed to be associated with contributions from tunneling conductivity or complicated conduction pathways through the composite. In the present case, it most likely arises because of specific interactions between the cationic redox centers and the surface of the gold nanoparticles.

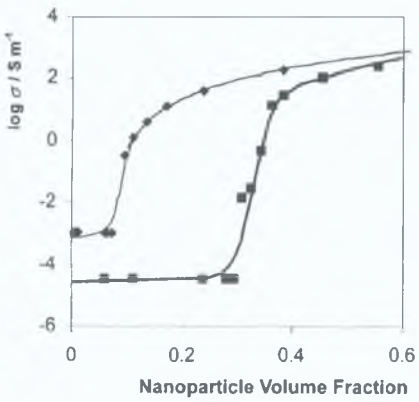

Fig. 2. Dependence of composite electrical conductivity on the loading of gold nanoparticles. ■ denotes composites where the polymer matrix is poly(4-vinylpyridine) and ◆ denote composites where the matrix is $[Os(bpy)_2(PVP)_{10}Cl]Cl$. The solid curves denote best fits to the percolation theory and the parameters are given in Table 1.

3.3. Redox properties

Fig. 3 shows typical slow sweep cyclic voltammograms for an $[Os(bpy)_2(PVP)_{10}Cl]^+$ metallopolymer film and for a composite electrode in which the mole fraction of the metallopolymer is 0.84. In both cases, the supporting electrolyte is aqueous 0.1 M $HClO_4$ and the surface coverage is $2.0 \pm 0.2 \times 10^{-8}$ mol cm^{-2}. For both the metallopolymer and the composite, the voltammetric response associated with the $Os^{2+/3+}$ couple centered at approximately 0.3 V is close to that expected for an immobilized, electrochemically reversible couple under finite diffusion conditions [29,30]. For example, for the composite the peak shape is independent of the scan rate, v, up to at least 25 mV s^{-1}, and the peak height scales linearly with scan rate from 1 to 25 mV s^{-1}. The ratio of the anodic to cathodic peak currents is

Table 1
Electrical conductivity parameters for composites based on gold nanoparticle–poly 4 vinylpyridine or metallopolymer matrices

Matrix	$\text{Log}(\sigma_p/\text{S m}^{-1})$	$\text{Log}(\sigma_c/\text{S m}^{-1})$	$\text{Log}(\sigma_m/\text{S m}^{-1})$	φ_c	F	t	d/nm
Poly 4 vinylpyridine	−4 45 (0 07)	−3 96 (0 11)	3 55 (0 04)	0 31 (0 04)	0 7 (0 1)	1 9 (0 2)	4 9 (0 4)
$[Os(bpy)_2(PVP)_{10}Cl]Cl$	−2 96 (0 03)	−2 02 (0 03)	2 94 (0 05)	0 07 (0 01)	0 7 (0 1)	2 5 (0 2)	12 0 (0 3)

Numbers in parentheses represent the standard deviations of at least three independent composite samples

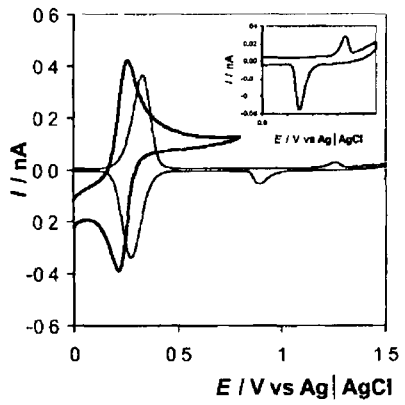

Fig 3 Cyclic voltammograms under finite diffusion conditions for—an $[Os(bpy)_2(PVP)_{10}Cl]^+$ film and—a composite film in which the mole fraction of metallopolymer is 0 84 In both cases the supporting electrolyte is aqueous 0 1 M $HClO_4$ the surface coverage is $2\ 0 \pm 0\ 2 \times 10^{-8}$ mol cm^{-2} For the metallopolymer and composite films the working electrodes are 12 5 μm radius platinum and carbon micro disks respectively The scan rate is 1 mV s^{-1} The inset shows an expanded view of the gold oxide formation/reduction region for the composite

$1\ 0 \pm 0\ 05$ the FWHM is 110 ± 10 mV A persistent peak-to-peak separation, ΔE_p, of approximately 50 mV is observed for both systems even at very slow scan rates Also, some diffusion like tailing is observed especially for the pure metallopolymer which is attributed to spillover of the polymer film onto the non-conducting glass shroud

As illustrated in the inset of Fig 3, in strongly acidic media the composite electrode exhibits well defined responses at positive potentials corresponding to the formation of gold oxide on the metal nanoparticles and its subsequent re-reduction The charge under these waves depends on the nanoparticle size and loading but the peak potentials and shape are independent of loading and particle size Under identical conditions, the potential at which gold oxide formation and re-reduction are observed for polycrystalline gold, 1 36 and 0 90 V, respectively, compares favorably with the values found for the gold nanoparticles, 1 27 and 0 88 V, respectively This result suggests that the gold nanoparticles are polycrystalline and have similar electrochemical properties to bulk gold Repetitive cycling through the gold oxide formation region leads to significant loss of the apparent surface area e g for the highest loading investigated at 100 mV s^{-1} the apparent surface area decreases by 25% after 25 cycles This decrease in surface area is consistent with TEM investigations which reveal that the gold nanoparticles are not entirely stable during gold oxide formation but coalesce to give larger particles of smaller surface area It is important to note that cycling the composites through the $Os^{2+/3+}$ process does not trigger coalescence of the nanoparticles or a change in their surface areas

For a polycrystalline gold surface, the charge passed during the reduction of a monolayer of gold oxide [31] is 390 μF cm^{-2} Therefore, the area under the oxide reduction peak (inset of Fig 3) has been used to determine the total surface area of the electrochemically active gold nanoparticles within the composite For the composite where the mole fraction of the metallopolymer is 0 84, the area obtained is $6\ 2 \times 10^{-6}$ cm^2 This area is indistinguishable from that expected, $6\ 8 \times 10^{-6}$ cm^2, on the basis of the known quantity of tetrachloroaurate reduced and the radius of the nanoparticle obtained from TEM This result suggests that even at low nanoparticle densities, an interconnected array is formed perhaps involving the osmium redox centers mediating electron transfer between the gold nanoparticles so that a gold oxide monolayer can be formed on nearly all of the particles The gold surface area as determined from the gold oxide reduction peak increases as the mole fraction of the metallopolymer is decreased, e g where x is 0 02, the area is $1\ 2 \times 10^{-5}$ cm^2

3 4 Film resistance and interfacial capacitance

Previous investigations into related metallopolymers have revealed that ion transport into the film typically limits the rate at which the redox composition of the film can be switched [32 33] Therefore the film resistance is expected to be dominated by the ionic rather than electronic resistance By examining the film resistance as a function of the supporting electrolyte concentration, it should be possible to probe the semi-permeable properties of the membrane [34 35] When a polyelectrolyte film is placed in a dilute solution of a strong electrolyte, the concentration of counterions within the film is typically considerably larger than that found in the contacting solution For these materials one might expect a high anion concentration ($\approx 0\ 8$ M) to be initially present in the film to compensate for the cationic osmium redox centers

Thus, under the influence of the concentration gradient, counterions may diffuse from the film into the solution until the concentrations become equal in the two phases. However, if diffusion of charged counterions occurs, then electroneutrality within the film would be violated, and an electrical potential would develop at the interface [36,37]. This 'Donnan potential' would then increase until an equilibrium was reached in which it completely opposes the tendency of the counterions to move down the concentration gradient. Under these equilibrium conditions the net diffusion of counterions across the interface would be zero, and co-ions would be excluded from the polymer film. The presence of gold nanoparticles within the composite that may have negatively charged surfaces due to the borohydride reduction is likely to have a significant impact on this behavior. Moreover, the resistance of the composite films would be anticipated to change as the percolation threshold is crossed and a significant electronic conductivity is achieved.

The permselective response of the composites has been determined by measuring the total cell resistance as the supporting electrolyte concentration is changed. In the case of an ideally permselective response, ions would be effectively excluded from the membrane, and the film resistance would be independent of the supporting electrolyte concentration. To determine the total cell resistance, we have performed short timescale, small amplitude, potential step chronoamperometry, in a potential region where no Faradaic response is observed. In a typical experiment, the potential was stepped from −100 to 0 mV at both bare and modified electrodes, and the resulting current was recorded over the following 5 μs. This capacitive current versus time transient can be described by Eq. (2):

$$I_c(t) = (\Delta E/R_u)\exp(-t/R_u C_{dl}) \quad (2)$$

where ΔE is the pulse amplitude, R_u is the total cell resistance, i.e. it includes contributions form both solution and film resistance, and C_{dl} is the integral double layer capacitance. As shown in Fig. 4 for the composite modified electrodes, the current decays in time according to a single exponential, which is consistent with double layer charging of the underlying electrode alone. Fig. 4 also illustrates $\ln I_c(t)$ versus t plots for a composite electrode in which the mole fraction of the metallopolymer is 0.02 as the $HClO_4$ concentration is systematically varied from 0.1 to 2.0 M. The absolute slope of these plots represents the reciprocal of the cell time constant $R_u C_{dl}$. It is apparent from Eq. (2) that R_u can be extracted from the intercepts of the insets of Fig. 4. Fig. 5 shows the total cell resistance for a bare 12.5 μm radius microelectrode as well as a microelectrode coated with the metallopolymer and composite as the $HClO_4$ concentration is changed from 0.1 to 2.0 M. It is apparent that in all circumstances R_u is reduced at high electrolyte concentrations reflecting a reduced solution resistance. Significantly, the cell resistance for the metallopolymer coated electrode is consistently higher than that found for the bare or composite modified electrodes over the entire concentration range investigated. This result suggests that the film resistance contributes to the overall cell resistance. However, in contrast to both the bare and

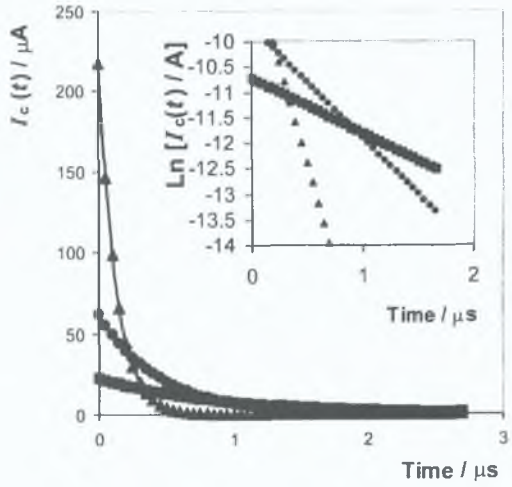

Fig. 4. Current–time transients for a 12.5 μm radius platinum microelectrode modified with a composite in which the mole fraction of the metallopolymer is 0.84 following potential steps from −0.050 to 0.000 V. From top to bottom, the data correspond to aqueous 0.1 (■), 0.5 (●) and 2.0 (▲) M $HClO_4$ as supporting electrolyte. The inset illustrates the corresponding semi-log current vs. time plots.

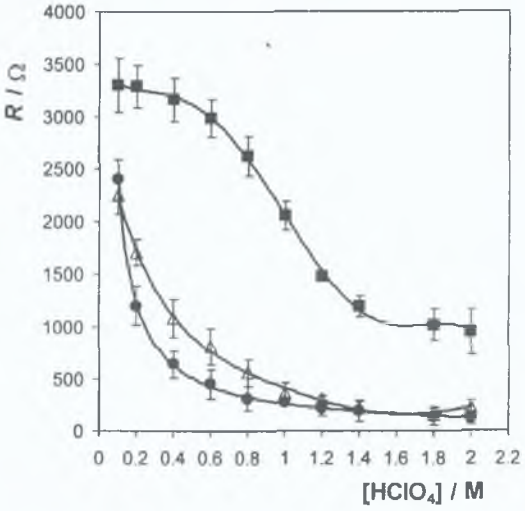

Fig. 5. Dependence of the total cell resistance, R_u, on the concentration of $HClO_4$ as supporting electrolyte. Data for a bare 12.5 μm radius platinum microelectrode are denoted by ●, ■ denotes data for $[Os(bpy)_2(PVP)_{10}Cl]Cl$ and △ denotes data for a composite in which the mole fraction of metallopolymer is 0.02. The surface coverage of the $[Os(bpy)_2PVPCl]^+$ centers was kept constant at $2.0 \pm 0.2 \times 10^{-10}$ mol cm^{-2} irrespective of the nanoparticle loading.

composite modified electrodes, the metallopolymer film exhibits a pronounced sigmoidal dependence of R_u on $[HClO_4]$ The inflection point, approximately 1 0 M, is consistent with the concentration of the osmium redox centers within the film and suggests that Donnan exclusion of co-ions breaks down in highly concentrated electrolytes [22 38] The resistances observed for the composite are indistinguishable from those found for the bare electrode indicating that the contribution from the film resistance is negligible for this material in which the nanoparticle loading is above the percolation threshold

The chronoamperometry data reveal that the absolute double layer capacitance increases from 4 1 to 6 4 × 10^{-10} F as the concentration of the supporting electrolyte is increased from 0 1 to 1 0 M Given that the microscopic area of the 12 5 μm radius microdisk is 7 8 × 10^{-6} cm^2 (corresponding to a roughness factor of 1 6), these absolute capacitances yield area normalized double layer capacitances of 52 and 81 μF cm^{-2} for the 0 1 and 1 0 M electrolytes These values are consistent with those expected for a modified electrode in contact with a concentrated aqueous electrolyte [22] Significantly, this analysis strongly suggests that the nanoparticles do not undergo double layer charging presumably because the compressed nature of the double layer means that the majority of the approximately 1 μm thick film does not experience the interfacial electric field

3 5 *Ion pairing effects*

The formal potential of an immobilized electroactive group is sensitive to both the solvation shell of the redox center and to the extent of ion-pairing [39–41] It is therefore a sensitive probe of the local microenvironment within the polymer film Shifts in formal potential with changes in electrolyte concentration reflect differences in the relative stability between the two redox states, and can be used to probe ionic interactions Therefore by examining the electrolyte concentration dependence of $E^{\circ\prime}$, information about the extent of ion-pairing and the film's permeability towards anions can be obtained

Fig 6 illustrates a plot of $E^{\circ\prime}$ versus the logarithm of the $HClO_4$ concentration for an electrode modified with the metallopolymer and composite in which the mole fraction of the metallopolymer is 0 02 This figure reveals that, for the metallopolymer coating, $E^{\circ\prime}$ shifts progressively in a negative potential direction with increasing electrolyte concentration This negative shift indicates that oxidation of the redox center becomes thermodynamically more facile at high electrolyte concentrations and is consistent with ion-pairing between the electrolyte anion and the redox centers

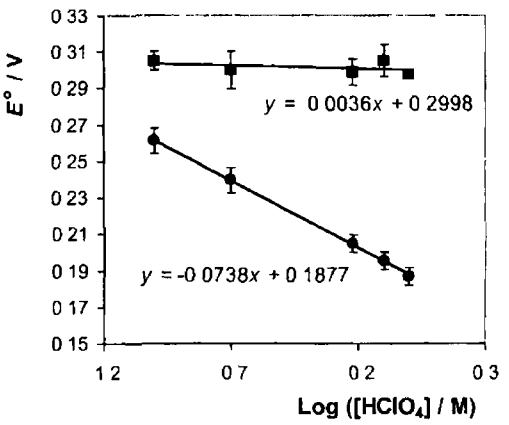

Fig 6 Dependence of the formal potential for the $Os^{2+/3+}$ process within an $[Os(bpy)_2(PVP)_{10}Cl]Cl$ metallopolymer film ● and within a composite in which the mole fraction of the metallopolymer is 0 02 ■ on the concentration of $HClO_4$ as supporting electrolyte

This situation is summarized in the following Nernstian reaction

$$[Os(bpy)_2(PVP)_nCl]^+(X^-)_p - e^- + p(X^-) \leftrightarrow [Os(bpy)_2(PVP)_nCl]^{2+}(X^-)_{p+p}$$

where both redox forms are considered to participate in the ion-pairing equilibria While the slope observed for the metallopolymer film, 73 8 ± 0 1 mV dec^{-1}, is rather larger than that predicted by theory for the pairing of an additional anion in the oxidized state, 59 mV dec^{-1}, these deviations most likely arise because of differences in the ionic strength of the solutions and liquid junction effects The most significant result of Fig 6 is that $E^{\circ\prime}_{Os^{2+/3+}}$ for the composite is completely insensitive to the perchlorate concentration This result suggests that additional perchlorate anions do not become paired with the Os^{3+}, centers most likely because of strong interactions with the gold nanoparticles which may also have an internal buffering role because of surface charges

3 6 *Charge transport diffusion coefficients*

In systems of this kind, for intermediate scan rates the electrochemical response becomes dominated by semi-infinite linear diffusion which can be identified by the appearance of diffusional tails, a ΔE_p value of 57 mV and a linear dependence of the peak current on $v^{1/2}$ As illustrated in Fig 7, cyclic voltammetry gives diffusional responses for $50 < v < 500$ mV s^{-1} for the $Os^{2+/3+}$ couple within the metallopolymer For the composites, the lower scan rate at which semi-infinite linear diffusion becomes dominant is always higher than that found for the composites and depends on the nanoparticle loading For example, for the composite in which the mole fraction of the metallopolymer is 0 84, semi-infinite

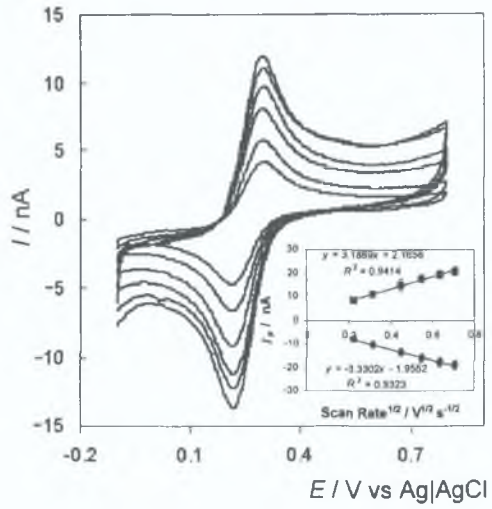

Fig. 7. Scan rate dependence of cyclic voltammograms under semi-infinite diffusion conditions for an $[Os(bpy)_2(PVP)_{10}Cl]^+$ film on a 12.5 μm radius platinum microelectrode. Sweep rates (top to bottom) 500, 400, 300, 200, 100 and 50 mV s^{-1}. Surface coverage is 1.8×10^{-8} mol cm^{-2}. Supporting electrolyte is aqueous 0.1 M $HClO_4$. The inset illustrates a plot of I_p vs. $v^{1/2}$.

diffusion is observed for $v > 25$ mV s^{-1} whereas the scan rate must be increased to 100 mV s^{-1} where the mole fraction of the metallopolymer is reduced to 0.02. This observation indicates that the rate of homogeneous charge transport increases with increasing nanoparticle loading. As illustrated in the insets of Figs. 7 and 8, plots of the peak current versus the square-root of the scan rate are linear, which is consistent with an electrochemically reversible reaction under semi-infinite linear diffusion control as described by the Randles-Ševčik

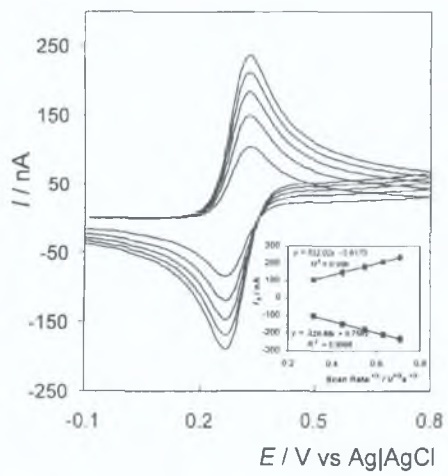

Fig. 8. Scan rate dependence of cyclic voltammograms under semi-infinite diffusion conditions for a composite film in which the mole fraction of the metallopolymer is 0.02 on a 12.5 μm radius platinum microelectrode. Sweep rates (top to bottom) 500, 400, 300, 200 and 100 mV s^{-1}. Surface coverage is 2.1×10^{-8} mol cm^{-2}. Supporting electrolyte is aqueous 0.1 M $HClO_4$. The inset illustrates a plot of I_p vs. $v^{1/2}$.

equation [22]. The slope of these plots provides the product $D_{CT}^{1/2}c_{Os}$, from which D_{CT} has been determined using an osmium redox center concentration of 0.8 M. The charge transport diffusion coefficients thus obtained represent a lower limit since the effective osmium concentration within the film may be reduced by swelling when it is in contact with the aqueous electrolyte.

Fig. 9 illustrates the dependence of D_{CT} on the $HClO_4$ concentration for both metallopolymer and composite films in which the mole fraction of the polymer is 0.02. There are three processes that could limit the rate of homogeneous charge transport through these films namely, large scale movement of polymer chains, counterion diffusion/migration, or electron hopping [42,43]. The observation that D_{CT} is approximately independent of the supporting electrolyte concentration, coupled with the low film resistance data which indicated that the films contain a relatively high concentration of electrolyte, suggests that counterion diffusion does not represent the rate determining step. What is apparent from Fig. 9 is that incorporating a relatively high loading of gold nanoparticles (in this composite the edge to edge inter-particle separation will be of the order of 2.6 nm compared to the average inter-redox site separation of 5 nm in the pure metallopolymer) promotes a faster rate of homogeneous charge transport through the film. This result is consistent with the percolation curve shown in Fig. 2 which demonstrates that metal like conductivity through the dispersed nanoparticles is achieved at high loadings. Thus, for high nanoparticle loadings it appears that electron transfer between the osmium redox centers is mediated by the gold nanoparticles causing D_{CT} to increase by approximately an order of magnitude on going from the metallopolymer to a composite with a nanoparticle loading above the percolation threshold.

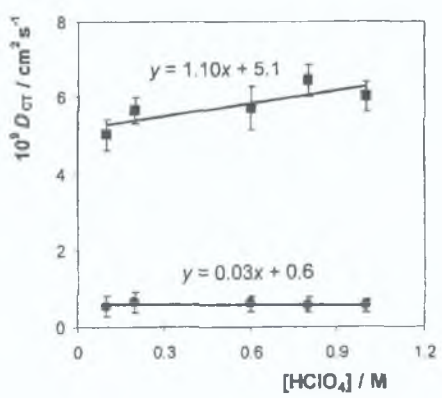

Fig. 9. The effect of the concentration of $HClO_4$ as supporting electrolyte on the rate of homogeneous charge transport, D_{CT}, through an $[Os(bpy)_2(PVP)_{10}Cl]Cl$ metallopolymer film (●) and through a composite film in which the mole fraction of the metallopolymer is 0.02 (■).

3 7 Heterogeneous electron transfer kinetics

Fig 8 clearly demonstrates that the rate of homogeneous charge transport through these metallopolymer based films can be significantly enhanced by incorporating gold nanoparticles within the matrix Heterogeneous electron transfer across the electrode | film interface depends on the electrode-reactant separation, the chemical composition, and the effective dielectric constant of the film which are also influenced by the presence of the gold nanoparticles [44] Therefore, beyond evaluating D_{CT} we have used high scan rate cyclic voltammetry to determine the standard heterogeneous electron transfer rate constant, k°, describing the dynamics of electron transfer across the electrode | film interface Fig 10 illustrates cyclic voltammograms for a metallopolymer film and a composite where the mole fraction of metallopolymer is 0 02 at scan rates of 10 and 100 V s^{-1}, respectively The supporting electrolyte is 1 0 M $HClO_4$ in which, as shown in Fig 4, the total cell resistance does not exceed 1000 Ω even for the pure metallopolymer Thus, even though these experiments employ a relatively high scan rate, the *IR* drop is less than 5 mV which is negligible compared to the peak-to-peak separations, ΔE_p, observed Under these fast scan conditions, ΔE_p exceeds the 57 mV expected for an electrochemically reversible process indicating that the time constants for the experiment and heterogeneous electron transfer are comparable Despite the scan rate being an order of magnitude larger, the ΔE_p value for the composite is smaller (110 mV) than that found for the metallopolymer (250 mV) This result indicates that the rate of heterogeneous

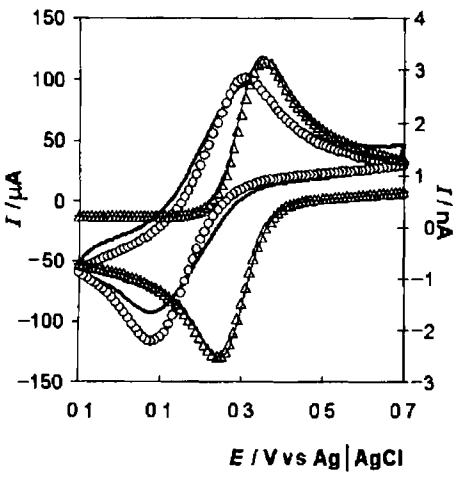

Fig 10 Cyclic voltammograms for an $[Os(bpy)_2(PVP)_{10}Cl]Cl$ metallopolymer film (—) and a composite film (—) in which the mole fraction of the metallopolymer is 0 02 The scan rates are 10 and 100 V s^{-1} respectively Theoretical voltammograms obtained generated according to the Butler–Volmer formalism of electrode kinetics are denoted by the open symbols The supporting electrolyte is 1 0 M $HClO_4$

electron transfer is significantly faster for the composite than for the metallopolymer

Fig 10 also illustrates theoretical fits to the experimental cyclic voltammograms generated according to the Butler–Volmer formalism of electrode kinetics [22] In fitting these voltammograms, the experimental diffusion coefficient was used, the transfer coefficient was taken as 0 5 and the standard heterogeneous electron transfer rate constant was systematically varied so as to minimize the residual sum of squares between the experimental and theoretical oxidation currents Using these best-fit parameters, the reduction branch of the voltammogram was then simulated The satisfactory agreement observed between theory and experiment suggests that the voltammograms for both metallopolymer and composite films can be approximately described by conventional solution phase models based on semi-infinite linear diffusion Moreover, the satisfactory fits suggest that the films are solvated and that the electrochemical double layer sets up at the electrode | layer interface For the metallopolymer film for $5 < v < 30$ V s^{-1}, the best fit simulated voltammogram is obtained where D_{CT} is $5\,0 \times 10^{-10}$ cm^2 s^{-1} and a standard heterogeneous electron transfer rate constant, k°, is $8\,25 \pm 1\,75 \times 10^{-5}$ cm s^{-1} The diffusion coefficient obtained by fitting the complete voltammogram is identical to that found using the Randles-Sevčik analysis to within 5% Significantly, the standard heterogeneous electron transfer rate constant for the composite is significantly higher at $4\,0 \pm 0\,2 \times 10^{-3}$ cm s^{-1} This increased rate most likely arises because electron transfer to redox centers located relatively far away from the electrode surface, e g greater than 50 A, proceeds as a two-stage process involving electron hopping to a gold nanoparticle followed by transfer to the redox center In this way, the presence of gold nanoparticles provides stronger electronic coupling giving rise to fast electron transfer rates The ability to modulate the dynamics of interfacial electron transfer in this way while preserving the physico-chemical properties of the immobilized redox center is attractive for applications ranging from energy storage to sensors and electrocatalysis

4 Conclusions

The electrochemical responses of composite films based on poly(4-vinylpyridine) covalently labeled with osmium bisbipyridyl complexes and loaded with gold nanoparticles are nearly ideal The size and interparticle separation can be systematically varied by changing the mole fraction of metallopolymer in the initial synthesis Dry state conductivity measurements reveal that the electrical conductivity depends markedly on the nanoparticle loading with a percolation threshold of approximately 7% by volume being observed This loading

corresponds to an interparticle separation of approximately 2 6 nm These materials have been used to obtain an insight into how the presence of metallic nanoparticles influences the dynamics of electron self-exchange between the Os^{2+} and Os^{3+} sites within the 3-dimensional structure When in contact with a solution containing supporting electrolyte the composites appear to exist as hydrogels on the electrode surface that contain excess salt and water The rate of homogeneous charge transport, D_{CT}, through the materials depends on the loading of the metal nanoparticles reaching a maximum of $6\,0\pm0\,4\times10^{-9}$ cm^2 s^{-1} when the mole fraction of the metallopolymer is 0 02, i e when the nanoparticle loading is above the percolation threshold This D_{CT} value is approximately an order of magnitude larger than that found for the metallopolymer in the absence of nanoparticles

Acknowledgements

The financial support of Enterprise Ireland, the Irish Science and Technology Agency, the Higher Education Authority under the Programme for Research in Third Level Institutions and the generous loan of potassium hexachloro osmate by Johnson-Matthey are gratefully acknowledged The useful suggestions of the referees during review of this manuscript are deeply appreciated

References

[1] Y W C Cao R C Jin C A Mirkin Science 297 (2002) 1536
[2] E Katz I Willner J Am Chem Soc 124 (2002) 10290
[3] A J Haes R P Van Duyne J Am Chem Soc 124 (2002) 10596
[4] S Park M J Weaver J Phys Chem B 106 (2002) 8667
[5] Y Song R W Murray J Am Chem Soc 124 (2002) 7096
[6] K J Ziegler R C Doty K P Johnston B A Korgel J Am Chem Soc 123 (2002) 7797
[7] B Kim S L Tripp A Wei J Am Chem Soc 123 (2002) 7955
[8] T von Werne T E Patten J Am Chem Soc 121 (2002) 7409
[9] B Jose J H Ryu Y J Kim H Kim Y S Kang S D Lee H S Kim Chem Mater 14 (2002) 2134
[10] I Pastoriza Santos L M Liz Marzan Langmuir 18 (2002) 2888
[11] T K Mandal M S Fleming D R Walt Nanoletters (2002) 2
[12] S Minko A Kiriy G Gorodyska M Stamm J Am Chem Soc 124 (2002) 10192
[13] I Quiros M Yamada K Kubo J Mizutani M Kurihara H Nishihara Langmuir 18 (2002) 1413
[14] M Yamada H Nishihara H Chem Commun 21 (2002) 2578
[15] M Yamada I Quiros J Mizutani K Kubo H Nishihara Phys Chem Chem Phys 3 (2001) 3377
[16] M Kurihara K Kubo T Horikoshi M Kurosawa T Nankawa T Matsuda H Nishihara Macromol Symp 156 (2000) 21
[17] D Stauffer Introduction to Percolation Theory Taylor and Francis London 1985
[18] G Grimmet Percolation Springer Verlag Munich 1989
[19] R J Forster J G Vos Macromolecules 23 (1990) 4372
[20] L A Geddes IEEE Eng Med Biol (1996) 133
[21] R J Forster L R Faulkner J Am Chem Soc 116 (1994) 5444
[22] A J Bard L R Faulkner Electrochemical Methods Fundamentals and Applications Wiley New York 1980
[23] F Bonet V Delmas S Grugeon R Herrera Urbina P Y Silvert K Tekaia Elhsissien Nanostruc Mater 11 (1999) 1277
[24] Y P Mamunya V V Davydenko P Pissis E V Lebedev Eur Polym J 38 (2002) 1887
[25] V Frosini S Petris Chim Ind 49 (1967) 1
[26] F J Lux J Mater Sci 28 (1993) 285
[27] J Wu D S McLachlan Phys Rev B 56 (1997) 1236
[28] F Carmona C J Mouney Mater Sci 27 (1997) 1322
[29] E Laviron J Electroanal Chem 52 (1974) 395
[30] A P Brown F C Anson Anal Chem 49 (1977) 1589
[31] S Trasatti O A Petrii J Electroanal Chem 327 (1992) 354
[32] R J Forster J G Vos J Electroanal Chem 314 (1991) 135
[33] R J Forster J G Vos Electrochim Acta 37 (1992) 159
[34] R J Forster T E Keyes A M Bond J Phys Chem B 104 (2000) 6389
[35] D A Walsh T E Keyes C F Hogan R J Forster J Phys Chem 105 (2001) 2792
[36] C P Smith H S White Langmuir 9 (1993) 1
[37] C P Smith H S White Anal Chem 64 (1992) 2398
[38] K J Vetter Electrochemical Kinetics Academic Press New York 1967
[39] S E Creager G K Rowe Anal Chim Acta 246 (1991) 233
[40] G K Rowe S E Creager Langmuir 7 (1991) 2307
[41] T Nagamura K Sakai J Chem Soc Faraday Trans 84 (1988) 3529
[42] R J Forster J G Vos in G Svehla (Ed) Comprehensive Analytical Chemistry vol XXVII Elsevier Amsterdam 1992 p 465
[43] R W Murray in R W Murray (Ed) Molecular Design of Electrode Surfaces (Ch I) Wiley New York 1992
[44] R J Forster in P A Unwin A J Bard (Eds) Encyclopedia of Electrochemistry Wiley New York 2000